frontiers
RESEARCH TOPICS

SCALE-FREE DYNAMICS AND CRITICAL PHENOMENA IN CORTICAL ACTIVITY

Topic Editors
Biyu J. He, Andreas Daffertshofer
and Tjeerd W. Boonstra

frontiers in
PHYSIOLOGY

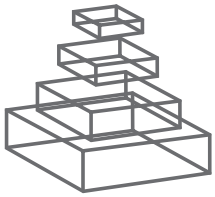

frontiers

Cover image provided by Ibbl sarl, Lausanne CH

ISSN 1664-8714
ISBN 978-2-88919-129-1
DOI 10.3389/978-2-88919-129-1

ABOUT FRONTIERS

Frontiers is more than just an open-access publisher of scholarly articles: it is a pioneering approach to the world of academia, radically improving the way scholarly research is managed. The grand vision of Frontiers is a world where all people have an equal opportunity to seek, share and generate knowledge. Frontiers provides immediate and permanent online open access to all its publications, but this alone is not enough to realize our grand goals.

FRONTIERS JOURNAL SERIES

The Frontiers Journal Series is a multi-tier and interdisciplinary set of open-access, online journals, promising a paradigm shift from the current review, selection and dissemination processes in academic publishing.
All Frontiers journals are driven by researchers for researchers; therefore, they constitute a service to the scholarly community. At the same time, the Frontiers Journal Series operates on a revolutionary invention, the tiered publishing system, initially addressing specific communities of scholars, and gradually climbing up to broader public understanding, thus serving the interests of the lay society, too.

DEDICATION TO QUALITY

Each Frontiers article is a landmark of the highest quality, thanks to genuinely collaborative interactions between authors and review editors, who include some of the world's best academicians. Research must be certified by peers before entering a stream of knowledge that may eventually reach the public - and shape society; therefore, Frontiers only applies the most rigorous and unbiased reviews.
Frontiers revolutionizes research publishing by freely delivering the most outstanding research, evaluated with no bias from both the academic and social point of view.
By applying the most advanced information technologies, Frontiers is catapulting scholarly publishing into a new generation.

WHAT ARE FRONTIERS RESEARCH TOPICS?

Frontiers Research Topics are very popular trademarks of the Frontiers Journals Series: they are collections of at least ten articles, all centered on a particular subject. With their unique mix of varied contributions from Original Research to Review Articles, Frontiers Research Topics unify the most influential researchers, the latest key findings and historical advances in a hot research area!
Find out more on how to host your own Frontiers Research Topic or contribute to one as an author by contacting the Frontiers Editorial Office: researchtopics@frontiersin.org

SCALE-FREE DYNAMICS AND CRITICAL PHENOMENA IN CORTICAL ACTIVITY

Topic Editors:
Biyu J. He, NIH, NINDS, USA
Andreas Daffertshofer, VU University Amsterdam, Netherlands
Tjeerd W. Boonstra, University of New South Wales, Australia

Adapted from http://commons.wikimedia.org/wiki/File:Cauliflower_romanesco.JPG

The brain is composed of many interconnected neurons that form a complex system, from which thought, behavior, and creativity emerge through self-organization. By studying the dynamics of this network, some basic motifs can be identified. Recent technological and computational advances have led to rapidly accumulating empirical evidence that spontaneous cortical activity exhibits scale-free and critical behavior. Multiple experiments have identified neural processes without a preferred timescale in the avalanche-like spatial propagation of activity in cortical slices and in self-similar time series of local field potentials. Even at the largest scale, scale-free behavior can be observed by looking at the power distributions of brain rhythms as observed by neuroimaging. These findings may indicate that brain dynamics are always close to critical states – a fact with important consequences for how brain accomplishes information transfer and processing. Capitalizing on analogies between the collective behavior of interacting particles in complex physical systems and interacting neurons in the cortex, concepts from non-equilibrium thermodynamics can help to understand how dynamics are organized. In particular, the concepts of phase transitions and self-organized criticality can be used to shed new light on how to interpret collective neuronal dynamics. Despite converging support for scale-free and critical dynamics in cortical activity, the implications for accompanying cognitive functions are still largely unclear. This Research Topic aims to facilitate the discussion between scientists from different backgrounds, ranging from theoretical physics, to computational neuroscience, brain imaging and neurophysiology. By stimulating interactions with the readers of Frontiers in Physiology, we

hope to advance our understanding of the role of scale-freeness and criticality in organizing brain dynamics. What do these new perspectives tell us about the brain and to what extent are they relevant for our cognitive functioning?

For this Research Topic, we therefore solicit reviews, original research articles, opinion and method papers, which address the principles that organize the dynamics of cortical activity. While focusing on work in the neurosciences, this Research Topic also welcomes theoretical contributions from physics or computational approaches.

Table of Contents

frontiers in
PHYSIOLOGY

EDITORIAL
published: 10 April 2013
doi: 10.3389/fphys.2013.00079

Scale-free dynamics and critical phenomena in cortical activity

***Tjeerd W. Boonstra*[1,2,3]*, *Biyu J. He*[4] *and Andreas Daffertshofer*[3]**

[1] *School of Psychiatry, University of New South Wales, Sydney, NSW, Australia*
[2] *Black Dog Institute, Sydney, NSW, Australia*
[3] *Research Institute MOVE, VU University Amsterdam, Netherlands*
[4] *National Institute of Neurological Disorders and Stroke, National Institutes of Health, Bethesda, MD, USA*
**Correspondence: t.boonstra@unsw.edu.au*

Edited by:
Bruce J. West, US Army Research Laboratory, USA

Reviewed by:
Bruce J. West, US Army Research Laboratory, USA

The brain is composed of many interconnected neurons that form a complex system, from which thought, behavior, and creativity emerge. The organizing principles of complex networks can be investigated using approaches developed by modern complexity science (Albert and Barabási, 2002). Activity in many large networks including the brain has been shown to be scale-free, e.g., the spatiotemporal propagation of activity in multi-electrode local field potentials (LFP) obeys a power-law distribution—termed "neuronal avalanches" (Beggs and Plenz, 2003). Moreover, fluctuations in electrophysiological and neuroimaging signals reveal prevalent scale-free dynamics (Linkenkaer-Hansen et al., 2001; He, 2011). These studies have sparked resurgent interests in scale-free brain dynamics and raise the question whether the brain might be operating in a permanently critical state (Chialvo, 2004). These topics were discussed in a symposium at the 17th Annual Meeting of the Organization for Human Brain Mapping in Quebec City in 2011 and form the basis of this Research Topic in *Frontiers in Fractal Physiology*.

Notwithstanding recent advances, whether the brain is in a critical state remains unanswered. In a Socratic dialog, Beggs and Timme (2012) review recent literature providing evidence for this hypothesis. A central issue is whether power-law scaling can be convincingly shown in neural data and whether this is sufficient proof for criticality, as other processes may also produce power-law distributions. Solutions may include experimentally steering the system away from the critical point and investigating changes in scaling behavior. Despite increasing evidence supporting this hypothesis, the presence of critical states in the awake brain remains controversial.

Indeed, using high-density electrode array recordings of cortical activity in cats, monkey, and human subjects, Dehghani et al. (2012) showed that avalanche sizes derived from spiking data never revealed clear power-law scaling but scaled exponentially or displayed intermediate scaling. In contrast, simultaneously recorded LFPs did reveal evidence for power-law scaling in local peak sizes. Although their finding does not contradict those for criticality in neuronal slices (Beggs and Plenz, 2003) and anesthetized states (Hahn et al., 2010), it clearly argues against criticality as an encompassing principle for different brain systems.

The Research Topic revealed a broad range of recording techniques to assess scale-free dynamics. Monto (2012) investigated the dynamics of phase synchrony in magnetoencephalography (MEG). Nested synchrony was investigated by considering the phase coupling between faster oscillations in two distinct brain regions as a function of the phase of slow oscillations. Nested synchrony was sparsely but robustly present in MEG recordings of human brain activity. Although these data do not directly speak to the presence of scale-free dynamics, nested synchrony may be a candidate for organizing neuronal oscillations across time and spatial scales.

Hemodynamic responses are also a candidate modality for testing the presence of criticality in the brain. Ciuciu et al. (2012) examined the scaling properties of the temporal dynamics of fMRI signals. They employed multi-fractal analysis that quantifies a collection of scaling exponents rather than a single exponent. Scaling behavior during rest was compared to brain activity in an auditory detection task and revealed multi-fractal dynamics in functional networks as well as in artifacts. However, only functional components showed significant modulations of the multi-fractal attributes between rest and task.

Fraiman and Chialvo (2012) investigated the statistical properties of spatio-temporal dynamics in fMRI data. They considered three novel statistical features, which reveal the type of fluctuations generated by systems in a critical state. Their results showed that the variance of the fMRI signal remained constant across a wide range of observed cluster sizes, that this behavior originated from bursts of synchronized activity across regions, and that correlation length diverged so that clusters of different sizes exhibit the same collective dynamics.

The development of analytical techniques for the detection of scale invariance played a central role in many contributions. The review article by Hardstone et al. (2012) provides a comprehensive account of detrended fluctuation analysis (DFA), a method that has been widely used for analyzing scaling behavior. The review gives a detailed explanation of the underlying concepts and provides basic examples to clarify different types of scaling behavior. They then applied DFA to amplitude fluctuations in EEG data and provided an open-source software toolbox to encourage further use of this technique.

Several models have been investigated to understand mechanisms that may underlie scale-free dynamics. In a review article, de Arcangelis and Herrmann (2012) considered a new family of networks, the Apollonian networks (Andrade et al., 2005), which

are scale-free and have small-world topology. Integrate-and-fire type neurons were connected as an Apollonian, a scale-free, or a fully connected network and synaptic strengths were modified according to a Hebbian learning rule. Once a percentage of connections were pruned, plastic adaption was stopped and the avalanche statistics and power spectral densities were assessed. Power-law behavior was observed for all models except for the fully connected networks showing supercritical behavior.

Aburn et al. (2012) investigated the scaling behavior of the Jansen-Rit model, a mean-field model that describes the average firing rate of interconnected neural populations. The bifurcation dynamics was studied as extrinsic input was delivered to different subpopulations. Long-range temporal correlations were assessed as a statistical indicator of linear instability and showed an increase of the autocorrelation length depended on the direction of the input fluctuations. Hence the detection of scale-free dynamics was dependent on the subpopulation that was stochastically perturbed, which has implications for applying these indicators to EEG recordings.

Finally, Van Orden et al. (2012) investigated the functional implications of critical brain dynamics by considering the body-brain relationship. Haken (1977) described that close to a phase transition, the components partition in two distinct groups in which slow macroscopic processes enslave fast microscopic processes. Hence the authors speculated that slow bodily processes may in fact control faster brain processes. They reviewed studies showing power-law scaling in human performance data and concluded that "metastable system can commit to a region of the state space of possibilities for action, without otherwise narrowing its options."

This Research Topic reflects the heterogeneity of research on critical phenomena in cortical activity. The studies point out that the wide-ranging findings may not be reconciled with a single unifying theory. The theory of critical brain dynamics may be more like a searchlight theory (Popper, 1972), shedding new light on well-known things and creating new problems and observations. We should hence anticipate that the current theory may prove too coarse and requires further adjustments. The emphasis on network dynamics and the statistics of spatiotemporal fluctuations have provided key insights in brain organization and inspired new research directions. Unfortunately not all of us will be able to explore these new exciting possibilities. Guy van Orden passed away on 11 May 2012 while working on his manuscript for this Research Topic. His contributions will be truly missed.

ACKNOWLEDGMENTS

Tjeerd W. Boonstra acknowledges the support of the Netherlands Organisation for Scientific Research (NWO #451-10-030). Biyu J. He is supported by the Intramural Research Program of the National Institutes of Health/National Institute of Neurological Disorders and Stroke.

REFERENCES

Aburn, M. J., Holmes, C. A., Roberts, J. A., Boonstra, T. W., and Breakspear, M. (2012). Critical fluctuations in cortical models near instability. *Front. Physiol.* 3:331. doi: 10.3389/fphys.2012.00331

Albert, R., and Barabási, A.-L. (2002). Statistical mechanics of complex networks. *Rev. Mod. Phys.* 74, 47–97.

Andrade, J. S. Jr., Herrmann, H. J., Andrade, R. F., and Da Silva, L. R. (2005). Apollonian networks: simultaneously scale-free, small world, euclidean, space filling, and with matching graphs. *Phys. Rev. Lett.* 94:018702. doi: 10.1103/PhysRevLett.94.018702

Beggs, J. M., and Plenz, D. (2003). Neuronal avalanches in neocortical circuits. *J. Neurosci.* 23, 11167–11177.

Beggs, J. M., and Timme, N. (2012). Being critical of criticality in the brain. *Front. Physiol.* 3:163. doi: 10.3389/fphys.2012.00163

Chialvo, D. R. (2004). Critical brain networks. *Physica A* 340, 756–765.

Ciuciu, P., Varoquaux, G., Abry, P., Sadaghiani, S., and Kleinschmidt, A. (2012). Scale-free and multifractal time dynamics of fMRI signals during rest and task. *Front. Physiol.* 3:186. doi: 10.3389/fphys.2012.00186

de Arcangelis, L., and Herrmann, H. J. (2012). Activity-dependent neuronal model on complex networks. *Front. Physiol.* 3:62. doi: 10.3389/fphys.2012.00062

Dehghani, N., Hatsopoulos, N. G., Haga, Z. D., Parker, R. A., Greger, B., Halgren, E., et al. (2012). Avalanche analysis from multielectrode ensemble recordings in cat, monkey, and human cerebral cortex during wakefulness and sleep. *Front. Physiol.* 3:302. doi: 10.3389/fphys.2012.00302

Fraiman, D., and Chialvo, D. R. (2012). What kind of noise is brain noise: anomalous scaling behavior of the resting brain activity fluctuations. *Front. Physiol.* 3:307. doi: 10.3389/fphys.2012.00307

Hahn, G., Petermann, T., Havenith, M. N., Yu, S., Singer, W., Plenz, D., et al. (2010). Neuronal avalanches in spontaneous activity *in vivo*. *J. Neurophysiol.* 104, 3312–3322.

Haken, H. (1977). *Synergetics. An Introduction.* Berlin: Springer.

Hardstone, R., Poil, S. S., Schiavone, G., Nikulin, V. V., Mansvelder, H. D., and Linkenkaer-Hansen, K. (2012). Detrended fluctuation analysis: a scale-free view on neuronal oscillations. *Front. Physiol.* 3:450. doi: 10.3389/fphys.2012.00450

He, B. J. (2011). Scale-free properties of the functional magnetic resonance imaging signal during rest and task. *J. Neurosci.* 31, 13786–13795.

Linkenkaer-Hansen, K., Nikouline, V. V., Palva, J. M., and Ilmoniemi, R. J. (2001). Long-range temporal correlations and scaling behavior in human brain oscillations. *J. Neurosci.* 21, 1370–1377.

Monto, S. (2012). Nested synchrony–a novel cross-scale interaction among neuronal oscillations. *Front. Physiol.* 3:384. doi: 10.3389/fphys.2012.00384

Popper, K. R. (1972). *Conjectures and Refutations: The Growth of Scientific Knowledge*. London: Routledge.

Van Orden, G., Hollis, G., and Wallot, S. (2012). The blue-collar brain. *Front. Physiol.* 3:207. doi: 10.3389/fphys.2012.00207

Received: 22 March 2013; accepted: 23 March 2013; published online: 10 April 2013.

*Citation: Boonstra TW, He BJ and Daffertshofer A (2013) Scale-free dynamics and critical phenomena in cortical activity. Front. Physiol. **4**:79. doi: 10.3389/fphys.2013.00079*

This article was submitted to Frontiers in Fractal Physiology, a specialty of Frontiers in Physiology.

frontiers in
PHYSIOLOGY

REVIEW ARTICLE
published: 07 June 2012
doi: 10.3389/fphys.2012.00163

Being critical of criticality in the brain

John M. Beggs*[1,2] *and* ***Nicholas Timme*[1]**

[1] *Department of Physics, Indiana University, Bloomington, IN, USA*
[2] *Biocomplexity Institute, Indiana University, Bloomington, IN, USA*

Edited by:
Tjeerd W. Boonstra, University of New South Wales, Australia

Reviewed by:
Alain Destexhe, Information and Complexité Centre National de la Recherche Scientifique, France
Woodrow Shew, University of Arkansas, USA

***Correspondence:**
John M. Beggs, Department of Physics, Indiana University, 727 East, 3rd Street, Bloomington, IN 47405-7105, USA.
e-mail: jmbeggs@indiana.edu

Relatively recent work has reported that networks of neurons can produce avalanches of activity whose sizes follow a power law distribution. This suggests that these networks may be operating near a critical point, poised between a phase where activity rapidly dies out and a phase where activity is amplified over time. The hypothesis that the electrical activity of neural networks in the brain is critical is potentially important, as many simulations suggest that information processing functions would be optimized at the critical point. This hypothesis, however, is still controversial. Here we will explain the concept of criticality and review the substantial objections to the criticality hypothesis raised by skeptics. Points and counter points are presented in dialog form.

Keywords: criticality, scale-free, avalanche, network, multi-electrode array, statistical physics, Ising model

INTRODUCTION

The scene: Two scientists, Critio and Mnemo, are attending a neuroscience conference. They happen to sit at the same table for lunch and strike up a conversation. This paper contains a record of that conversation. In turn, the scientists discuss criticality, evidence for criticality in neural data, various objections to this evidence, and several responses to those objections.

Critio: Hello professor. I enjoyed your presentation this morning. Your group is doing some fascinating work on synaptic plasticity. I was particularly interested in your thoughts on how synaptic changes underlie memory.

Mnemo: Thank you! I can see from your badge that you are in a physics department. What brings you to a neuroscience conference?

Critio: Well, I have been using ideas from statistical mechanics to try to explain how groups of neurons collectively behave. One of my primary research interests is determining whether or not the brain is operating at a critical point.

Mnemo: I've seen several papers in that area and they seem to show some interesting results. There also appears to be a great deal of controversy about criticality in biology (Gisiger, 2001; Mitzenmacher, 2004) and in neural systems (Bedard et al., 2006; Touboul and Destexhe, 2010; Dehghani et al., 2012). However, I must admit that I haven't had the time to follow that research topic very closely.

Critio: It is definitely true that there is significant disagreement in the research community about the role criticality plays in neural dynamics (Stumpf and Porter, 2012). I happen to believe that criticality plays an important role, but other researchers disagree.

Mnemo: Well, that's to be expected. Many topics in science are hotly debated and that's part of the fun of being a scientist!

Critio: Oh, I agree! I just want to say that, even given my view that criticality does play an important role in neural dynamics, I recognize that it is completely possible that criticality, in fact, does not play an important role in neural dynamics. Other methodologies, such as non-linear systems might better explain neural dynamics (May, 1976; Nicolis and Prigogine, 1989).

Mnemo: Well, this certainly sounds like an interesting topic. But since we have a few minutes here, why don't you give me a quick description of your research? I probably won't read a review, but I could learn a few things from you over lunch. Do you mind if I pick your brain, so to speak?

Critio: Not at all! I guess I could give you an overview of criticality and how it might apply to the brain. I am somewhat biased, but I'll do my best to present arguments from researchers who disagree with my view of criticality in neural systems. You can help me by being as skeptical of my arguments as possible.

TOPOLOGY AND CRITICALITY

Mnemo: That sounds great! But before we get started, I would like to clear one thing up that has been bugging me. Several of the other researchers at my institution study network topology. I always hear them talking about scale-free networks, power laws, and criticality. Are those all the same thing?

Critio: That is an excellent question and I think it gets at a point that isn't widely made in the literature. If we're interested in network topology, we're interested in how the nodes of a network are connected to each other. A scale-free network has nodes that are connected in a certain way. If we're interested in criticality, we're interested in how the network behaves. The two topics are certainly related, but it is possible for non-scale-free networks to exhibit critical behavior and it is possible for scale-free networks to not exhibit critical behavior. The network connectivity affects the critical behavior of that network (Haldeman and Beggs, 2005; Beggs et al., 2007; Gray and Robinson, 2007; Hsu et al., 2007; Teramae and Fukai, 2007; Larremore et al., 2011; Rubinov et al., 2011), as we can discuss if you have the time, but network connectivity and criticality are conceptually quite different.

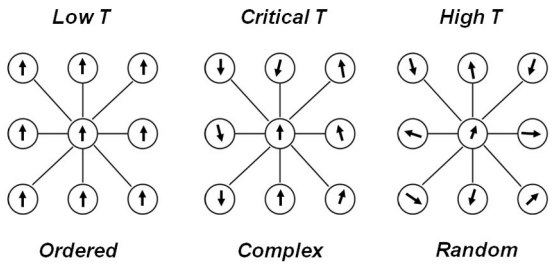

FIGURE 1 | A simple diagram of spins in the Ising model. (Left) At low temperature, nearest neighbor interactions dominate over thermal fluctuations. As a result, almost all the spins align in the same direction, producing a very ordered state. (Right) At high temperature, thermal fluctuations dominate over nearest neighbor interactions. As a result, the spins point in different directions, producing a very disordered state. (Center) At some critical temperature, nearest neighbor interactions and thermal fluctuations balance to produce a complex state.

EXPLAINING CRITICALITY

Mnemo: That sounds complicated! But, since I hear most people discussing criticality, let's discuss that first. So, what is criticality?

Critio: Criticality is a phenomenon that has been observed in physical systems like magnets, water, and piles of sand. Many systems that are composed of large numbers of interacting, similar units can reach the critical point. At that point, they behave in some very unusual ways. Some people, including myself, suspect that cortical networks within the brain may be operating near the critical point.

Mnemo: This all sounds intriguing, but I have no idea what you mean by the critical point. Can you give me a simple example?

Critio: Sure, let's use a well explored model in this field: the Ising model (Brush, 1967; Cipra, 1987). [Critio grabs a napkin and sketches the left panel of **Figure 1**.]

This model will illustrate the critical point pretty well. See these circles? They represent lattice sites in a piece of iron. At each site, there is an electron whose "spin" is either up or down. You can think of these arrows as little bar magnets, with the arrowhead being the North pole of the magnet. In a piece of iron, these bar magnets influence their nearest neighbors to align in the same direction. I will represent their influence on each other by drawing lines between the circles. So, when the temperature T is low, as in the left panel of **Figure 1**, these nearest neighbor interactions dominate and all the spins point in the same direction. This gives the piece of iron a net magnetization, and makes it behave like a magnet, sticking to your refrigerator. It is extremely ordered, almost boringly so. I have a movie here on my laptop from a talk I gave recently. [Critio opens up his laptop and plays Movie S1 in Supplementary Material.]

This movie shows a simulated piece of iron as the temperature is cooled. Each black square represents a spin pointed up, and each white square is a spin pointed down. See how, over time, all of the spins begin to point in the same direction? Pretty soon the whole sample will be either all black or all white. That behavior is caused by the nearest neighbor interactions.

Mnemo: So all iron is magnetic?

Critio: No, certainly not. Being ordered like that is just one phase that the piece of iron can be in. And that happens only at low T. If you heat it up, you can make it change into another phase.

Mnemo: Oh, I have heard some things about a "phase transition." Is that where this is going?

Critio: Well, yes. If you heat up the iron quite a lot, then this increased thermal energy will begin to "jostle around" the spins. Even though they still have a tendency to align with each other, this will be overwhelmed by the added heat. [Critio sketches the right panel of **Figure 1**.] Now you have no order at all and things look like random static on a TV screen when it is disconnected from a cable. Here is the movie of the disordered phase. [Critio plays Movie S2 in Supplementary Material from his laptop.]

Mnemo: So is this why a magnet loses its ability to stick when it is heated up too much?

Critio: Exactly. All the spins are pointing in different directions and they cancel each other. There is no net magnetic field produced by the sample any more.

Mnemo: So now you have shown me the ordered and the disordered phases. What happens between them, at the so called "phase transition point?" Is this the same thing as the "critical point?"

Critio: Yes it is. If you add just the right amount of heat to get to the critical temperature, then the tendency for the spins to align is exactly counterbalanced by the jostling caused by the heat. Now you no longer have global order. Instead, there will be local domains where a group of spins are pointed up, and other domains where the spins are pointed down (Stanley, 1971; Yeomans, 1992). [Critio sketches the middle panel of **Figure 1** above.] The sizes of these domains vary widely at this temperature; many are small but a few are quite large. So, this state is an interesting mix of order and disorder, and constantly changing over time. You can see that in this movie of a simulated piece of iron at the critical temperature. [Critio plays Movie S3 in Supplementary Material from his laptop.]

Mnemo: Wow, that is really interesting – some of the domains almost look like amoeba crawling across the screen, with boundaries that are extending and contracting. I can see that there are many different sized domains too. OK, you have been telling me a lot about this piece of iron, but how does this relate to the brain?

CRITICALITY AND COMMUNICATION

Critio: Good question, but before we get to neural data, we need to understand a few more things about criticality. You certainly must agree that communication between neurons is very important for the brain. If we continue with the magnet analogy, we could ask how two spins at different lattice sites might communicate with each other.

Mnemo: Ok, go on. . .

Critio: A simple way to measure this would be to look at the dynamic correlation between two lattice sites. This is not the correlation that is usually used in statistics, but something that depends on coordinated fluctuations. Here is the equation for the dynamic correlation. Critio then writes down Eq. 1:

$$C_{ij} = \langle (i - \langle i \rangle)(j - \langle j \rangle) \rangle \quad (1)$$

The angled brackets here indicate a time average, so $\langle i \rangle$ is the average value of the spin at site i. If the spin is pointed up, we

could represent the state of the lattice site with a +1. Similarly, if the spin is pointed down, it would be represented with a −1. The average over a long time might be something like +0.2, say. So the term in the left parenthesis, $(i - \langle i \rangle)$, represents the amount by which the spin at site i fluctuates from its average at a given time. Likewise, the term $(j - \langle j \rangle)$ represents the amount by which site j fluctuates from its average at a given time. To make C_{ij} large, both i and j must fluctuate, and they must do so in a coordinated manner, at the same time and in the same direction. So you need both fluctuations and coordination to have a large dynamic correlation.

Mnemo: Ok, that seems to make sense. Now I see why it is called the dynamic correlation – if both i and j are stuck pointing up, the dynamic correlation would be 0, but a static correlation would still give 1.

Critio: Great, you get it! Now let's take a look at what happens to the dynamic correlation for the three different cases we talked about: low T, high T, and critical T. In the low T case, the piece of iron is extremely ordered and all the spins are pointed in the same direction. The dynamic correlation is low because there are no fluctuations and the terms in parentheses are both nearly 0 all the time. In contrast, for the high T case, there are plenty of fluctuations, as the spins are constantly deviating from their averages, but there is no coordination between sites i and j. One term in parenthesis might be positive, while the other might be negative. On another occasion, they might both be positive. So on average the dynamic correlation is again low. But at critical T, there is enough heat to allow fluctuations, but not so much heat that it destroys coordination between spin sites. The spins deviate from their averages, and they often do so together because the nearest neighbor influence is not completely overwhelmed by the added heat. Here, there is both fluctuation and coordination. When one of those "amoeba-like" domains that you saw in Movie S3 in Supplementary Material crawls across the screen, it might cause nearby spins to flip one after the other, setting up a dynamic correlation. I could sketch the positions of the spins, either up or down or in between, over time for the three different cases. [Critio now pulls out red and green markers, grabs another napkin and sketches **Figure 2**.]

Mnemo: So there is dynamic correlation between spins only at the critical temperature?

Critio: Well, there might be some dynamic correlation in all three cases, but it is certainly strongest at the critical temperature. Another key difference is that the distance over which these correlations extend is greatest at the critical temperature.

Mnemo: Can you show me what you mean by that?

Critio: Sure. If we were to measure the dynamic correlation between two spin sites i and j as a function of distance, we would find out that it decreases with distance in all cases. Remember that in this model, we have only built in connections between nearest neighbor spins. So you wouldn't expect the correlation to extend much beyond that, at least when the temperature is very high or very low. But at the critical temperature, we find that the dynamic correlation is above 0 well beyond the nearest neighbor distance. [Critio sketches **Figure 3**.]

Critio: In this example from a simulation, the dynamic correlation at the critical temperature extends about 15 lattice sites before it drops down to near 0. We call the distance at which the dynamic correlation first reaches 0 the "correlation length" and it is often

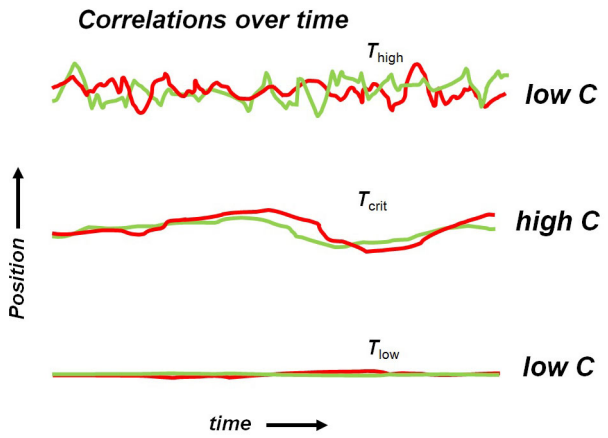

FIGURE 2 | Hypothetical positions of two spins as a function of time. (Top) At high temperature, the spin orientations fluctuate greatly, but independently of one another, producing a low dynamic correlation value. (Middle) At the critical temperature, the spin orientations fluctuate somewhat and the fluctuations are coordinated, producing a high dynamic correlation value. (Bottom) At low temperature, the spin orientations do not fluctuate very much, yielding a low dynamic correlation value.

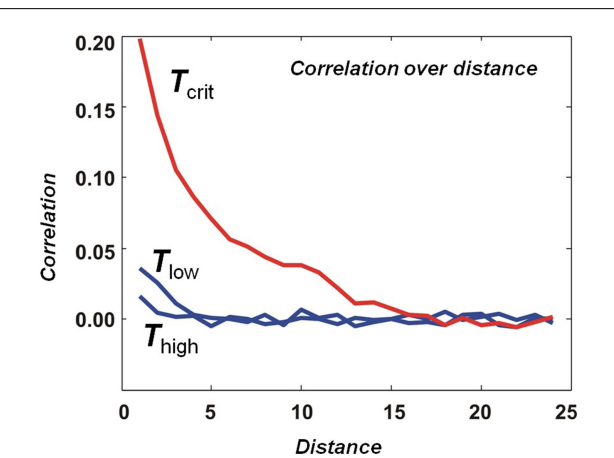

FIGURE 3 | Average dynamic correlation as a function of distance. At high and low temperatures, the average dynamic correlation between two lattice sites decreases rapidly toward 0 as the distance between the lattice sites is increased. At the critical temperature, the average dynamic correlation also decreases toward 0 as the distance is increased, but much more gradually.

given by the Greek capital letter gamma, Γ; in this case the correlation length is 15 lattice sites long. We didn't build this length into the model – it merely emerged at the critical temperature. At this temperature, when one spin flips from down to up, for example, it might influence one of its nearest neighbors to also flip, which might in turn influence one of its nearest neighbors and so on. In this way, the movement at one lattice site can propagate beyond the nearest neighbor length. You could draw the correlation length as a function of temperature, and it would show a sharp peak at

the critical point. [Critio asks another person sitting at the table for a fresh napkin and draws **Figure 4**.]

Critio: Again, this shows the separation of phases nicely. On the left you have the ordered phase, with low temperature. This is sometimes called the subcritical regime. On the right you have the disordered phase, with high temperature, and this is sometimes called the supercritical regime. Between them you have the phase transition region, which is very narrow and occurs at the critical temperature.

Mnemo: I think I see what is going on. Only at the critical temperature can you have communication that spans large distances. So if I were to make an analogy with a neural network, it would be that at the critical point, the neurons can communicate most strongly and over the largest number of synapses, right?

Critio: Exactly!

Mnemo: But wait, what do you mean by "communication?" When the model is at low temperatures, the state of one lattice site strongly influences the state of lattice sites throughout the whole network. So, it would seem to me that communication is maximized when the temperature is low, not when the system is at the critical point.

Critio: Ah, that is a subtle point. Clearly, we haven't been very rigorous with our definition of "communication," but let me see if I can clarify my point. When the model is at low temperatures, the coupling between the lattice sites is strong, so coordination is high. However, the state of each lattice site doesn't change very much through time, so fluctuations are low. Communication requires both coupling and variability, or in other words, both coordination and fluctuation. If communication is to take place, lattice sites must be able to influence each other and that influence must actually affect changes. Does that make more sense?

Mnemo: Yes, I see your point about the distinction between communication and coupling.

Critio: Great! So, at the critical point these two qualities of the system – coupling and variability – are balanced to produce long distance communication. And it turns out that it is not just communication that would be optimized at the critical point (Beggs and Plenz, 2003; Bertschinger and Natschlager, 2004; Maass et al., 2004; Ramo et al., 2007; Tanaka et al., 2009; Chialvo, 2010; Shew et al., 2011). Many other researchers have pointed out, with very general models, that information storage (Socolar and Kauffman, 2003; Kauffman et al., 2004; Haldeman and Beggs, 2005) and computational power (Bertschinger and Natschlager, 2004) are expected to be optimized there as well (Chialvo, 2004, 2010; Plenz and Thiagarajan, 2007; Beggs, 2008). In addition, the ability of the network to respond to inputs of many different sizes, called its dynamic range, is expected to be optimal at the critical point (Kinouchi and Copelli, 2006; Shew et al., 2009). Phase synchrony also appears to be optimized at the critical point (Yang et al., 2012).

Mnemo: So this sounds pretty reasonable to me so far. But it is only an analogy. You haven't shown me any evidence to suggest that the brain might be doing this. What evidence, if any, do you have to make me think that this is connected to real neurons?

CRITICALITY AND POWER LAWS

Critio: Again, a very fair question. Before we can get to the neural data, I first need to show you how I got interested in this topic. Let me return for a moment to the plot of the average dynamic correlation length. If I were to change the axes by making them both logarithmic, then I would get something like this for the dynamic correlation, plotted now only for the critical case. [Critio draws **Figure 5**.]

Critio: When plotted this way, the dynamic correlation approximates a straight line over part of its range. This suggests that it could be described by a so-called "power law," where the dynamic correlation, C, is related to the distance, D, raised to some negative power, say $-\alpha$. Note that the slope of the power law line when plotted logarithmically is given by $-\alpha$. Well, the physics of critical phenomena tells us that near the critical point, a system will have many variables that can be described by power law functions (Stanley, 1971; Goldenfeld, 1992; Yeomans, 1992; Nishimori and Ortiz, 2011). In addition to the dynamic correlation as a function

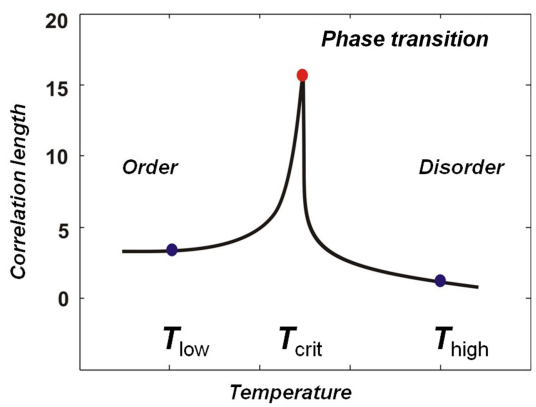

FIGURE 4 | Correlation length as a function of temperature for a simulation of the Ising Model. Near the critical temperature the correlation length rapidly approaches a maximum value. This sharp peak separates the ordered phase from the disordered phase and occurs at the phase transition point.

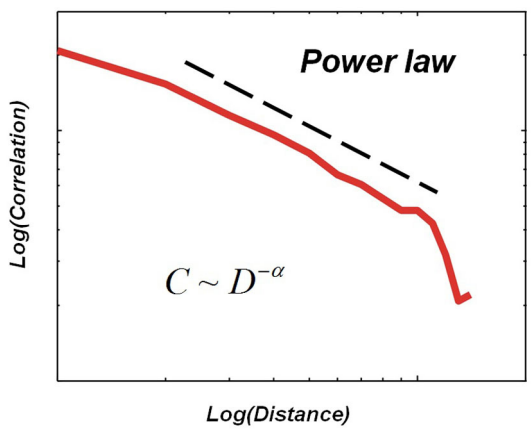

FIGURE 5 | Hypothetical relationship between the average dynamic correlation between two lattice sites and the distance between those lattice sites at the critical temperature in a small simulation of the Ising model.

of distance, the distribution of domain sizes that we talked about earlier would also follow a power law at the critical point. The reason the straight line does not extend to larger distances is because the simulation had a limited size. The bigger the simulation, the further the power law line would extend.

Mnemo: Ok, for the moment I will assume you are right that this power law would extend to indefinitely large distances if the system were large enough. What is so special about a power law, besides the fact that it might suggest your system is critical?

Critio: An interesting feature of power laws is that they show no characteristic scale. When plotted in log-log coordinates, they produce a straight line that has the same slope everywhere. This implies that the data will have a fractal structure. For example, imagine what the distribution of correlation strength would look like if you were only able to sample separation distances from 10^1 to 10^2 units. It would be a straight line with a slope of $-\alpha$ when plotted logarithmically. Interestingly, this would look just like the distribution that you would observe if you were only able to sample separation distances from 10^2 to 10^3 units. Again, the exponent would be $-\alpha$. This has caused some people to use the phrase "scale-free" when describing power law distributions (Stam and de Bruin, 2004). If you zoom in or zoom out, things look very similar (Teich et al., 1997). This self-similarity is a characteristic of fractals.

Mnemo: So is where the name "scale-free" network comes from?

Critio: Yes! In scale-free networks, the degree distribution – the distribution of the number of connections each node possesses – follows a power law. But notice, in the Ising model, the nodes are connected in a lattice and the Ising model exhibits critical behavior. So, here we can see the distinction between criticality and scale-free networks in action. The nodes are not connected as in a scale-free network, yet the activity is scale-free.

Mnemo: That is certainly interesting, but I am still searching for a strong argument, not nice pictures. So power laws are an indicator of criticality? And you are going to tell me that you see some power laws in your neural data? This is the argument? It must be more substantial than that! After all, this is science, not just loose associations!

Critio: A critical system will produce power laws, yes, but power laws do not prove criticality! There are many ways to get power laws, and I can tell you more about that in a minute. The key thing to remember here is that exhibiting power laws is strongly suggestive of criticality. However, power laws alone are not sufficient to establish criticality.

Mnemo: Ok, I want to ask about these other ways to get power laws in a minute. But to return to the issue I raised earlier, you are going to tell me about some neural data that display power laws?

Critio: Yes, I can tell you about that first and then we can get to all the potential objections.

Mnemo: That sounds fine. Proceed with the data.

POWER LAWS AND NEURAL DATA

Critio: Well, there were several early reports that the nervous system could produce power law distributions (Chen et al., 1997; Teich et al., 1997; Linkenkaer-Hansen et al., 2001; Worrell et al., 2002). These data all came from "one-dimensional" measurements, were a single variable, like spike count, temporal correlation, or total energy, was found to follow a power law distribution. While these important findings were very suggestive, they did not immediately provide insight as to what the underlying network was doing to produce these distributions. The earliest data to explore power law distributions at the network level came from recordings from microelectrode arrays that had 60 electrodes. There, the experimenters were able to observe bursts of spontaneous activity. They found that if they counted the number of electrodes activated in each distinct burst, that the burst sizes were distributed according to a power law (Beggs and Plenz, 2003). Because the statistics of these bursts followed the same equations used to describe avalanche sizes in critical systems, they called these events "neuronal avalanches." I have on my laptop here a figure from one of their papers that shows the power law distribution of avalanche sizes, measured either as the total number of electrodes activated per avalanche, or as the total amplitude of local field potential (LFP) signal measured at all the electrodes involved in the avalanche. [Critio shows **Figure 6** to Mnemo.]

Since these initial results, power law distributions of avalanche sizes have been reported in awake monkeys (Petermann et al., 2006, 2009), anesthetized rats (Gireesh and Plenz, 2008), isolated leech ganglion (Mazzoni et al., 2007), and dissociated cultures (Mazzoni et al., 2007; Pasquale et al., 2008), suggesting that this is a very general and robust phenomenon. It is interesting to mention that some of these reports have relied on spike data, and not just LFP data (e.g., Beggs, 2007, 2008; Mazzoni et al., 2007; Pasquale et al., 2008; Hahn et al., 2010; Friedman et al., 2011, 2012). Avalanche dynamics also have been reported in human brain oscillations (Poil et al., 2008) and there are several reports of power law scaling (Miller et al., 2009) even though these are not necessarily attributed to avalanches. In addition, the size of phase locking intervals in human fMRI has been reported to follow a power law, and the authors have related this to criticality in the awake, healthy human brain (Kitzbichler et al., 2009). This is intriguing, despite the fact that the temporal resolution of fMRI is much lower than that of

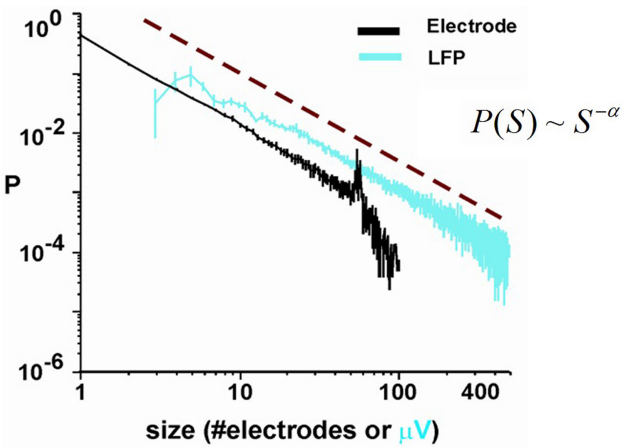

FIGURE 6 | Probability distribution of neuronal avalanche size. (Black) Size measured using the total number of activated electrodes. (Teal) Size measured using total LFP amplitude measured at all electrodes participating in the avalanche (Beggs and Plenz, 2003).

electrophysiological signals from extra-cellular electrodes, so it is not yet clear if these power laws are directly related to neuronal avalanches at the local network scale.

MNEMO's FIRST OBJECTION: DO THE NEURAL DATA REALLY SHOW POWER LAWS?

Mnemo: That is an impressive list of neural systems in which power laws have been observed. However, I seem to recall hearing that other researchers have found that these power laws were actually better fit by exponentials. Is that true?

Critio: That is true. Using sophisticated statistical tests, several researchers have shown that some data sets, none of which were from neuroscience, that were previously thought to be power law distributed are actually better fit by an exponential distribution (Clauset et al., 2009). Using analysis methods from that work, some researchers in neuroscience have argued that the supposed power laws associated with neural activity are not actually power laws, or that the power laws that have been found are artifacts (Bedard et al., 2006; Bedard and Destexhe, 2009; Touboul and Destexhe, 2010; Dehghani et al., 2012).

Mnemo: How do you escape that objection? It seems like so much of your argument is based on power laws. If those really aren't there or if they are artifacts, then your system certainly isn't operating at the critical point, is it?

Critio: You are right; this is a very important part of my argument. Let's talk about each paper separately since they present distinct arguments and evidence. First, let's discuss the papers that argue the observed power laws are artifacts. Some researchers have produced strong theoretical models that indicate that the extra-cellular medium may behave as a $1/f$ filter (Bedard and Destexhe, 2009). If the extra-cellular medium does, in fact, behave this way, that only explains the observed power law distribution in the LFP spectrum. But it does not necessarily explain the power law distribution in other neural phenomena, like the size distribution of neuronal avalanches. Another paper has made a notable argument that the power laws observed in avalanche size distributions are actually artifacts (Touboul and Destexhe, 2010). In that work, the authors analyzed avalanches using both positive and negative LFP peaks and found that both were fit by power laws. However, positive LFP peaks are significantly less correlated with neuron spiking activity than negative LFP peaks. So, those authors concluded that the power law avalanche size distribution is not associated with neuron spiking activity. In response, I think it is important to point out that the form of this argument is fallacious. The power law observed in the positive LFP peaks avalanche size distribution may be due to some other phenomenon and it could still be the case that the power law observed in the negative LFP peaks avalanche size distribution is related to spiking activity.

Mnemo: I see your point, what about the other papers?

Critio: Those papers argue that the power laws associated with neural phenomena that have been observed are not actually present. Several of the investigators who claimed to show that neural event size distributions were better fit by exponentials did not use many electrodes in their recordings. In some of their papers, they only had about eight electrodes (Bedard et al., 2006; Touboul and Destexhe, 2010). To really assess whether or not something follows a power law, you should have many closely-spaced electrodes. A recent paper showed that if you under-sample a critical process, you can get distributions that deviate substantially from power laws (Priesemann et al., 2009). The basic idea is that if your electrodes are too far apart, it will be extremely rare for an avalanche to occur that will span the distance between them. This will make it look like all the events are occurring independently, and this leads to a distribution with a short tail that is not a power law, even if the underlying process is indeed critical (Ribeiro et al., 2010). When people who do have data sets from large numbers of electrodes tested their data, they found contradictory results. A paper from 2011 showed that the data were better fit by power laws than by exponential distributions using the advanced statistical method I mentioned before (Clauset et al., 2009; Klaus et al., 2011). They performed this analysis using recordings taken from acute slices, *in vivo* recordings from rats, and *in vivo* recordings from primates. A more recent work used the same analysis method and found the opposite result using *in vivo* data from cats, monkeys, and humans (Dehghani et al., 2012). That study used a closely spaced 96 electrode array. So, at least for that study, it is very unlikely that under-sampling prevented the appearance of a power law. Therefore, it seems that this point about power laws is still somewhat controversial, and may take a few years to resolve. But remember, power laws are suggestive of criticality. They are not proof, and there may be better ways to establish criticality than by looking only at power laws. Hopefully we can talk later about these other ways of testing whether a system is critical or not.

MNEMO's SECOND OBJECTION: THE ISING MODEL IS AN EQUILIBRIUM MODEL, BUT NEURAL NETWORKS ARE DYNAMIC

Mnemo: Ok, but first let me understand this a bit more. You just told me about a magnetic model – the Ising model – and how that would settle into different equilibrium states at different temperatures. Now you are jumping to a network of neurons, where things do not settle at all. In fact, the Ising model seems like it would be pretty poor at describing how one neuron excites another, leading to cascades of activity spreading through the network.

Critio: As a neuroscientist, you have a very keen intuition for the physics! You are absolutely right to point out the potential problem. The Ising model is an equilibrium model, appropriate for describing how the system will settle at different temperatures, but this model does not explicitly account for time. To try to extend the Ising model into the range of dynamics, some people have applied a perturbation to the model – a slowly changing magnetic field for example – and watched how the system responds. Typically, when the model is at the critical temperature, applying a local magnetic field will cause several nearby spins to flip, so as to align with the applied field. These spins will in turn cause a change in the orientation preference for other nearby spins, and so will cause them to flip, leading to avalanches of spin flips. This is called the Barkhausen effect. In both theoretical work (Sethna et al., 2001) and in experiments (Papanikolaou et al., 2011), the sizes of these avalanches are distributed according to a power law when the system is at the critical temperature (Perkovic et al., 1995). Also, the exponents found in neuronal avalanches, typically near -1.5, are solidly in the range of exponents reported for the Barkhausen

effect, which range from −1 to −2.8. These Barkhausen exponents vary because they apply to many different metals under various geometries and different models. It seems that there is a reasonable connection, then, between the equilibrium Ising model and dynamic avalanches (Liu and Dahmen, 2009).

Mnemo: So to follow your analogy, the neurons in the brain could be thought of as spins in a magnet at the critical point. When something comes along and delivers an input, this propagates through the system with maximum distance, because the correlation length is greatest at the critical point. The avalanches of activity have sizes distributed as a power law, and you mentioned that some experimenters have observed power law distributions of avalanche sizes in neural tissue as well.

Critio: That is a good summary of what I have said so far. Even though impressive progress has been made recently in applying the Ising model to neuronal activity patterns found in actual data (Schneidman et al., 2006; Shlens et al., 2006, 2009; Tang et al., 2008; Yu et al., 2008, 2011; Tkacik et al., 2009; Yeh et al., 2010) you are entirely right to say that the Ising model is far too simple to completely capture all neural phenomena. One problem with the Ising model is that, without applying an external magnetic field, all states of an individual lattice site are equally likely. Real neurons are far more likely to be in one state (quiescent) over another state (spiking). Researchers have developed many models to attempt to more fully incorporate neural behavior, and specifically to deal with temporal dynamics (Maass et al., 2002). Also, models have been created to better simulate damaged or malfunctioning neural behavior, such as models to simulate Alzheimer's disease (Horn et al., 1993) and epilepsy (Netoff et al., 2004; Hsu et al., 2008)[1]. However, I believe the Ising model serves as an excellent introductory system for the topic of criticality.

Mnemo: I understand that no model is perfect and that it is easier to start with a simplified system, but I'm still dissatisfied.

Critio: What's bothering you?

MNEMO's THIRD OBJECTION: POWER LAWS DO NOT PROVE CRITICALITY

Mnemo: You've given me a nice story, but this is hardly proof. As you said, the existence of power laws is a necessary, but not sufficient condition for criticality. So, just because we've found some power laws in neural data, the existence of those power laws not prove that the neural systems are operating at the critical point. I don't know about you, but I don't like to affirm the consequent.

Critio: You are right to be skeptical. As I said, the power laws are *consistent* with the idea that the neural networks that have been studied are operating near the critical point, but the existence of these power laws is not proof.

Mnemo: Sure, it seems like now would be a good time for you to tell me about the many other ways in which power laws can be generated.

[1]Critio: As a brief aside, I'm very interested in models of Epilepsy. In epileptic tissue, seizures exist that take the form of widespread coordinated activity. So, when modeling epileptic neural activity, we must be careful to incorporate seizures into our understanding of when the model is critical. For instance, during seizures, the activities of many neurons are highly correlated, so the dynamic correlation between model neurons is very high, but, by examining other parameters of the network, the network is not at a critical point.

Critio: There are so many ways to generate power laws that it is hard to know where to begin. People have written entire articles devoted largely to this topic (Mitzenmacher, 2004; Newman, 2005; Stumpf and Porter, 2012). Perhaps the simplest mechanism to start with would be successive fractionation. Consider a stick of some length. Now break it into two parts at a randomly chosen location. Then break each of these parts in two, again at randomly chosen locations. If you keep successively doing this, you will eventually produce a power law distribution of fragment lengths. Related to this, multiplicative noise can also produce power laws (Sornette, 1998). In one of the papers that challenged the existence of power laws in neural data that we discussed earlier, the authors used a random process that, when thresholded, also produced power law distributions (Touboul and Destexhe, 2010). Another way to get power laws is through a combination of exponentials (Reed and Hughes, 2002). As you know, exponential processes are ubiquitous. If you have a process that grows exponentially over time, but is terminated at random times drawn from a negative exponential distribution, then you will also get a power law distribution of sizes. Reed and Hughes explored this in a paper whose title included "...Why power laws are incredibly common in nature" (Reed and Hughes, 2002). As just one more example, consider an array of processes that all decay exponentially, but with different time constants. Under the right conditions you can add these decay processes together and they will produce a power law as well (Fusi et al., 2005). There are several other mechanisms proposed to generate power laws (Mitzenmacher, 2004). So you are completely right to be skeptical. Just showing a power law by itself doesn't tell you all that much.

Mnemo: It now seems that you have dug yourself into a hole from which you cannot escape. If power laws are so unexceptional, then why should I be so excited about seeing them in neural data?

CRITIO's RESPONSE TO MNEMO's THIRD OBJECTION: EVIDENCE FOR CRITICALITY BEYOND POWER LAWS

Critio: The fact that other non-critical systems also produce power laws is very important. Fortunately, recent experiments by several groups have addressed this issue directly. There are three main ways to demonstrate that the power laws observed in neural tissue are the result of a critical mechanism: the ability to tune the network from a subcritical regime through criticality to a supercritical regime, the existence of mathematical relationships between the exponents of the power laws for a system, and the existence of a data collapse within neural data.

Tuning the network through criticality

Critio: First, recall that in a system that displays criticality, the power law will only occur when the system is between phases, in other words, at the phase transition point. So, for systems that really are critical, we should be able to observe different phases on either side of the critical point and get distributions there that do not follow power laws.

Mnemo: And you have evidence of this?

Critio: Actually, yes. By blocking excitatory synaptic transmission, you can dampen network excitability, leading to smaller avalanches (Mazzoni et al., 2007). Here is a figure I saw from a

poster at the conference. [Critio pulls out a small copy of the poster and points to **Figure 7**.]

In **Figure 7A**, the resulting distribution of avalanche sizes is curved downward and has a smaller mean than in the control case shown in **Figure 7B**. In **Figure 7A**, the distribution is beginning to deviate from a power law. This looks like the subcritical or damped phase of the system, where activity dies out quickly. Conversely, by blocking inhibitory synaptic transmission, in **Figure 7C**, it is possible to make the tissue hyperexcited, leading to larger avalanches (Beggs and Plenz, 2003). The resulting distribution here is not a power law either, but has a big bump out in the tail, indicating that many extremely large avalanches occur. This looks like the supercritical phase, where activity is often amplified until it spans the entire system. The existence of these two phases, on either side of the critical point, which is shown in **Figure 7B**, strongly suggests that the power law arises from a mechanism that is related to a phase transition.

Critio: Related to this, there have been some very elegant experiments that have shown how information processing functions in the tissue approach optimal behavior near the critical point (Shew et al., 2009, 2011). This also suggests that different phases can be produced in the network.

Mnemo: What do you mean by that? And how is it related to the idea of phases?

Critio: Shew and colleagues looked at information transmission through cortical slice networks under three different conditions: where excitatory transmission is reduced; where there is no manipulation; and where inhibitory transmission is reduced. They showed that there was a peak in information transmission in the unperturbed condition, and that information transmission fell to either side of this point as perturbations increased. In many ways, they observed behavior just like that seen in the correlation function in the Ising model that we talked about earlier from **Figure 4**. Remember the plot that showed a sharp peak in the middle? – Their results are similar. In other experiments from the same group, they demonstrated that dynamic range in the network – similar to susceptibility in the Ising model – peaks in the unperturbed condition and declines as perturbations are increased. All of this suggests that these networks can be tuned from one phase to another, or left between phases at the critical point. And it underscores why it would be advantageous for brains to operate near the critical point, because that is where information processing is optimal. The presence of different phases indicates that the power law is related to a phase transition, because the power law is only seen between the phases. These peaks in information processing functions also occur between the phases, under the same conditions where the power law occurs.

Mnemo: So it seems that you need to be able to move the system from one phase to another if it is going to show a critical point. What you have been telling me is that these neural systems can be moved in this way.

Critio: That's right. If a system displays criticality, then it must be tunable in some sense. Typically, a "control parameter" can be adjusted to determine the phase of the system. In the Ising model that we discussed earlier, the temperature is the control parameter. Sweeping the temperature from 0 to some high value would bring the system from the subcritical, ordered, phase, up to the critical point, and then into the supercritical, disordered, phase. The "order parameter" is what tells you the phase. In the case of the Ising model, the order parameter would be the net magnetic field produced by all the spins, called the magnetization. In the subcritical phase, all the spins are aligned and the magnetization has a large magnitude. In the supercritical phase, all the spins are pointing in random directions and the magnetization is 0. Near the critical point, we see the transition of the magnetization from some large magnitude toward 0. If a system is indeed critical, then all of the variables that could indicate its phase will depend on the control parameter.

Mnemo: To continue with the analogy, what would be the control parameter in neural systems?

Critio: That is a very good question. At the moment, it seems that the balance between excitation and inhibition can serve as a control parameter (Mazzoni et al., 2007; Shew et al., 2009; Benayoun et al., 2010; Hobbs et al., 2010). Too much inhibition will cause the system to be subcritical. Too much excitation will cause the system to be supercritical. A balance between them would lead to the critical point. But I must say that there is still a lot of work to be done in this area. Other things, like connection strengths

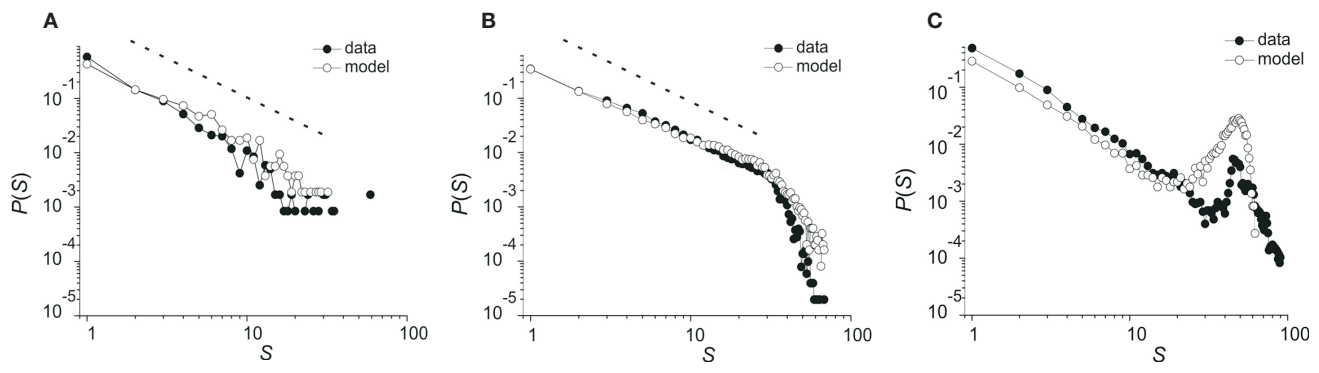

FIGURE 7 | Avalanche size distributions in local field potential data collected with a 60-channel microelectrode array from rat cortical slice networks. (A) Subcritical regime; excitatory antagonist (3 mM CNQX) applied. **(B)** Critical regime; normal network. **(C)** Supercritical regime; inhibitory antagonist (2 mM PTX) applied (Haldeman and Beggs, 2005).

(Haldeman and Beggs, 2005; Beggs et al., 2007; Chen et al., 2010), or the density or pattern of connections in the network (Gray and Robinson, 2007; Larremore et al., 2011; Rubinov et al., 2011), might also serve as control parameters. The key point is that experiments have shown the system can indeed display different phases, so it is tunable.

Mnemo: So you cannot tune the other, non-critical stochastic systems, like successive fractionation, or a combination of exponentials?

Critio: Well, you could tune them in some sense, but such tuning would only change the exponent of the resulting power law distribution. For example, let's return to the combination of exponentials model proposed by Reed and Hughes (2002). Recall that there is a process that grows exponentially, let's say with exponent α, and it is terminated at random times that are drawn from a distribution that has exponential decay, let's say with exponent β. If you increase α or decrease β, you will decrease the exponent of the size distribution (thereby making the slope of the size distribution less steep when plotted logarithmically), but it will still be a power law. As long as such a process is adequately sampled, it will never curve downward or curve upward to produce a hump at the end of the distribution. So this type of non-critical process fails to show different phases. Therefore it cannot serve as a good model for what has been observed in the neural data, where clear phases exist. All of the non-critical models that have been proposed to generate power laws are like this – they fail to show phases.

Mnemo: I think I get it: if they don't have different phases, then they are not operating at a phase transition point, even though they may produce power laws. That all sounds reasonable. But you told me that there were additional arguments to support your point, right?

Mathematical relationships between power law exponents

Critio: Yes, the second main argument comes from a slightly different aspect of critical phenomena. It will take me a minute or two to explain, but I think it will be helpful. As I said previously, if a system is truly critical, it will display power law distributions in more than one variable of interest (Stanley, 1971, 1999; Goldenfeld, 1992; Nishimori and Ortiz, 2011). For example, recall that in the Ising model the correlation as a function of distance followed a power law at the critical point. The domain size distribution also follows a power law at the critical point. Also, the susceptibility, the specific heat, and other variables will exhibit power laws as well. All of these power laws may have different exponents, and so will have different "characteristic" exponents. Far away from the critical point, these power laws break down. Right near criticality, though, there are multiple power laws.

Mnemo: Why are there multiple power laws?

Crito: Remember how I said that the phase of a critical system can be determined by a control parameter? Let me describe how important that parameter is. If we go back to that curve of the correlation length, recall that it had a sharp peak near T_c, the critical temperature. This type of curve is observed experimentally in diverse critical systems (Stanley, 1971; Yeomans, 1992) and would be expected to go to infinity right at T_c if you had an infinitely large system. A simple way to describe such a curve would be with an equation like this:

$$\Gamma = \left[\frac{T_c}{T - T_c}\right]^{\xi} \tag{2}$$

As T approaches T_c, the denominator goes to 0, and the correlation length, Γ, shoots up to infinity. The exponent ξ is another value that would be obtained from experimental data, and in general it would not always be 1. For convenience, physicists often use something called the "reduced temperature" given here by t, in describing critical phenomena:

$$t \equiv \frac{T - T_c}{T_c} \tag{3}$$

In general, we don't know precisely how the correlation length will depend on the reduced temperature, but I am able to write the correlation length as a power series in t, like this:

$$\Gamma = At^{\lambda}\left(1 + Bt^{\lambda_2} + Ct^{\lambda_3} + \cdots\right) \tag{4}$$

Near the critical point, the reduced temperature t approaches 0, so all the higher-order terms of this series become very small. We can then approximate the whole power series by something like this:

$$\Gamma \approx At^{\lambda} \tag{5}$$

And you should recognize that this as a power law relationship. Using similar methods, other power laws can be found that relate other variables associated with the system, such as the relationship between the dynamic correlation value and distance between lattice sites in the Ising model (**Figure 6**). Furthermore, in the process of deriving these power laws, mathematic relationships between the exponents of the power law distributions can also be derived. It would take me a while to explain the details of how these exponent relationships come to be (Griffiths, 1965; Stanley, 1971; Yeomans, 1992), but for now it should be enough to say that near the critical point, many power laws exist, and they are mathematically related to one another.

Mnemo: Why wouldn't successive fractionation produce a relationship between exponents?

Critio: In that simple, one-dimensional system, there is only one power law, and that is related to the lengths of the sticks. There is only one exponent, so it can't be related to other exponents.

Mnemo: But what about something like a combination of exponentials?

Critio: Recall that in that model the exponents α and β are the rates at which exponential processes increase and decrease, not exponents of power laws observed in variables associated with the system. The event size distribution is a power law whose exponent is related to the ratio of α/β. So, again there is only one exponent, so it can't be related to other exponents. In addition, α and β are independent input parameters in the model, so there can be no relationship between them.

Mnemo: Let us assume for the moment that I agree that you should have exponent relationships if your system is truly critical.

Is there any evidence for this type of relationship in neural data collected so far?

Critio: In fact there is. There is a recent article (Friedman et al., 2012) where the investigators were recording neuronal avalanches of spikes from individual neurons. They showed that the exponent for the avalanche size distribution, α, and the exponent for the avalanche lifetime distribution, β, could be used to predict the exponent of the power law that related avalanche size to avalanche lifetime, γ, using Eq. 6.

$$\gamma = \frac{(\beta - 1)}{(\alpha - 1)} \tag{6}$$

They found that the exponent γ, predicted in this way, fit reasonably well to the actual data. So, this is another piece of evidence suggesting that the system can display critical behavior (Friedman et al., 2011, 2012).

Mnemo: Alright, this makes sense. It seems to be another way to assess whether or not the system is critical. But I would still like to hear more. What is your third argument that the neural data are collected from a critical process?

Data collapse

Critio: Remember when I said that power law distributions were scale-free? Recall that this was related to fractals that showed self-similarity?

Mnemo: Yes, I do. I have read some popular articles about fractals, so I am not completely new to this (Mandelbrot, 1982; Stewart, 2001).

Critio: Good, then I can build on your existing knowledge to explain my last argument about why the neural data suggest criticality. It goes like this: The critical point is characterized by power laws in many variables, all of which express fractal relationships. We know that neural activity propagates dynamically through networks of neurons in cascades of activity. If these cascades, or avalanches, are truly critical then there should be some way to capture a relationship between the avalanches in a fractal way. What if we could take something like avalanche shapes and show that they were fractal? If we could do this, it would allow us to go beyond power laws, and show a scaling relationship that captured the dynamics of these non-equilibrium systems.

Mnemo: This sounds pretty abstract! Could you give me a more concrete example of what you are talking about?

Critio: Yes, of course. Let me describe what I mean by the avalanche shape. Consider how an avalanche of neural activity might evolve. It could start with one or a few spiking neurons. These could activate others, so the number of active neurons would increase over time. Eventually this would decline to 0, marking the end of the avalanche. If we plotted the average number of active neurons over time, we might get something that looked like an inverted parabola. This is what I mean by the average avalanche shape. Now if the network is at the critical point, then I should be able to take average avalanche shapes from different durations and show that they are all fractal copies of each other. In other words, I should be able to rescale them with the appropriate critical exponents and get them all to lie on top of each other, in what is called a data collapse. [Critio sketches **Figure 8**.]

Critio: These are average avalanche shapes taken from avalanches of different durations. See how they look like they might have roughly the same shape?

Mnemo: Yes, sort of. They could be copies of one another at different scales, but how are you going to show this?

Critio: Well, if we divide each curve by its duration, then they will be rescaled to all have the same length. Then if we rescale their heights by their duration raised to an exponent, γ from Eq. 2, that is related to the critical exponents α and β that we discussed earlier, then we get a picture that looks like this. [Critio draws **Figure 9**.]

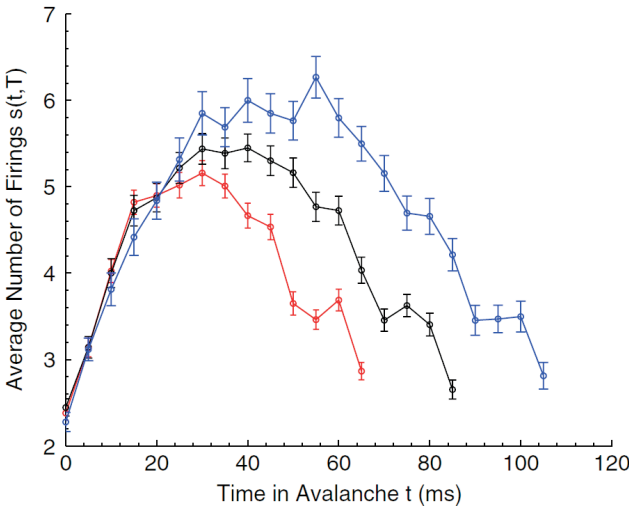

FIGURE 8 | Average avalanche shapes for avalanches of three distinct durations (Friedman et al., 2012).

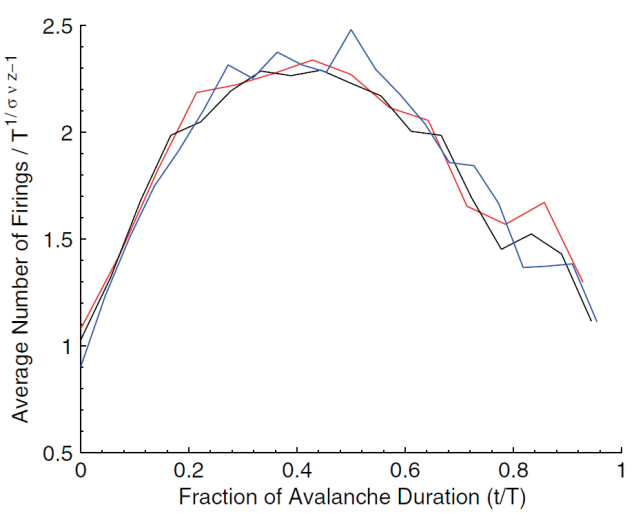

FIGURE 9 | Rescaled avalanche shapes from Figure 8 (Friedman et al., 2012).

Mnemo: The curves do seem to lie on top of one another pretty closely. Each curve is an average of how many avalanches?

Critio: Yes, each average avalanche shape is produced by hundreds of avalanches. So this data collapse is highly unlikely to have occurred by chance. In fact, when the spike train times from the original data are randomly jittered by 50 ms, the curves no longer look like copies of each other, suggesting that this scaling relationship has relatively tight temporal precision (Friedman et al., 2012). This type of data collapse, based on average avalanche shape, has been explored for several years in a variety of different systems (Perkovic et al., 1999; Kuntz and Sethna, 2000; Mehta et al., 2006), and has recently been applied to Barkhausen noise experiments with good success (Papanikolaou et al., 2011). The fact that it also can be applied to some neural networks strongly suggests that these networks are operating near the critical point.

Mnemo: Although I can't claim to understand all the math behind this, it certainly seems like your argument does not now rest on power laws alone. You have shown me a fractal relationship that ties together both space and time in the dynamic evolution of the avalanches. From all that you have told me, this should only occur near the critical point.

Critio: Yes, but it again sounds like you are not fully convinced!

MNEMO's FOURTH OBJECTION: INFLUENCE OF LOWER LEVEL PROCESSES THAT EXHIBIT POWER LAWS

Mnemo: You are correct – I still have another question about all this. In particular, I seem to recall reading somewhere that fractals are everywhere in neuroscience.

Critio: That's right. Some have shown that a plot of the number of spikes produced by a neuron looks roughly the same at all intervals (Teich et al., 1997). When you zoom out to very large time scales, this pattern of on and off firing appears to be just a copy of the pattern you see at short intervals. In addition, researchers have found that neurotransmitter secretion is fractal (Lowen et al., 1997), and that intervals between sodium channel openings follow a power law (Toib et al., 1998).

Mnemo: If all this is true, then I guess I shouldn't be so surprised when you tell me that some networks of neurons also display fractal behavior. The activity in the network could just be reflecting power law statistics that appear at other scales below it.

Critio: You are right to bring this up – with so many fractals out there, why should I get excited about a power law distribution of activity in small, local networks of neurons? Well, I have two answers to this. First, I could say that all the evidence I just mentioned about fractals in phenomena related to individual neurons is actually in favor of my general argument. We might expect the brain and its underlying systems to operate near a critical point to optimize information processing. However, the existence of the expectation is certainly not an argument against that which is expected. It seems that many biological systems would approach optimality by operating in a regime where they produce power laws (Mora and Bialek, 2011). That could be why so many biological systems exhibit power laws. To give my second answer to your point, I first want to clarify what I think you are saying. It sounds like you are saying that these power laws at other scales might not be produced by criticality, and that the power laws that have been observed in neuronal avalanches are just a reflection of these non-critical processes at other scales. Is that what you are saying?

Mnemo: Yes, I think that is a fair description of my objection.

Critio: Ok, let us assume for the sake of argument that power laws in spike counts, transmitter secretion and channel dynamics are all produced by processes that are not critical. Is it really clear that if we combined such processes that the resulting cascades of activity on a network also would have to follow a power law? Would the resulting network therefore not be critical? We know from computer simulations that the pattern of network connectivity can have a profound effect on whether the network produces power laws or not (Teramae and Fukai, 2007; Tanaka et al., 2009; Rubinov et al., 2011). Not every pattern of connections leads to a power law. In addition, from experiments we know that the relative strength of inhibition to excitation can influence whether or not a network produces power law distributions (Beggs and Plenz, 2003; Stewart and Plenz, 2006; Shew et al., 2009). These manipulations are done globally at the network level, not at the lower levels, and yet they seem to have the effect of tuning the network. If it were true that power law behavior at the network level was simply a result of power law behavior on the cellular level, then we shouldn't observe such effects by altering network level parameters. Furthermore, if the power law behavior observed at the network level is found to be critical using the methods discussed previously, then the network level behavior is critical regardless of whether or not the power law behavior of the underlying systems is also critical. Still, we don't know why the network level behavior is critical, or at the very least why it exhibits power laws. Nor do we know how this behavior is related to network structure and the underlying systems.

Mnemo: Oh, is this where all that "self-organized criticality" literature comes in (Bak et al., 1987; Bak, 1996; Jensen, 1998)? I have heard that some physicists are extremely skeptical of that work. So I suppose I should approach your work with similar caution.

Critio: It is still an open question as to how the network operates at the critical point, if it is indeed operating a critical point, and there have been several interesting proposals and experiments related to this topic (Bienenstock, 1995; Chialvo and Bak, 1999; de Carvalho and Prado, 2000; Bak and Chialvo, 2001; Eurich et al., 2002; Freeman, 2005; Kozma et al., 2005; de Arcangelis et al., 2006; Hsu and Beggs, 2006; Abbott and Rohrkemper, 2007; Buice and Cowan, 2007, 2009; Juanico et al., 2007; Levina et al., 2007, 2009; Pellegrini et al., 2007; Hsu et al., 2008; Stewart and Plenz, 2008; Allegrini et al., 2009; Magnasco et al., 2009; Tanaka et al., 2009; Buice et al., 2010; de Arcangelis and Herrmann, 2010; Kello and Mayberry, 2010; Millman et al., 2010; Tetzlaff et al., 2010; Rubinov et al., 2011; Droste et al., 2012). Whether the network gets to criticality through self-organization or not, it does seem that at least some networks of neurons can operate at the critical point. But I would be surprised if this does not involve some form of self-organization, as synaptic strengths are constantly in flux.

Mnemo: I suppose we will have to settle this over another lunch, as I have to go to another talk!

Critio: Wow, it is late! Hey, do you mind if I write this up and submit it to a journal? I think you have raised some very interesting objections, and you have forced me to think through my positions more thoroughly.

Mnemo: Sure, go ahead. But I am still skeptical, so don't plan to include me as a co-author.

Critio: Not a problem. Thanks for sharing lunch.

Mnemo: My pleasure. Good bye.

SUPPLEMENTARY MATERIAL

The Movies S1–S3 for this article can be found online at http://www.frontiersin.org/Fractal_Physiology/10.3389/fphys.2012.00163/abstract

Movie S1 | Simulation of an Ising model at low temperature.

Movie S2 | Simulation of an Ising model at high temperature.

Movie S3 | Simulation of an Ising model at the critical temperature.

REFERENCES

Abbott, L. F., and Rohrkemper, R. (2007). A simple growth model constructs critical avalanche networks. *Prog. Brain Res.* 165, 13–19.

Allegrini, P., Menicucci, D., Bedini, R., Fronzoni, L., Gemignani, A., Grigolini, P., West, B. J., and Paradisi, P. (2009). Spontaneous brain activity as a source of ideal 1/f noise. *Phys. Rev. E* 80, 061914. doi: 10.1103/PhysRevE.80.061914

Bak, P. (1996). *How Nature Works: The Science of Self-Organized Criticality*. New York, NY: Copernicus.

Bak, P., and Chialvo, D. R. (2001). Adaptive learning by extremal dynamics and negative feedback. *Phys. Rev. E. Stat. Nonlin. Soft Matter Phys.* 63, 031912.

Bak, P., Tang, C., and Wiesenfeld, K. (1987). Self-organized criticality: an explanation of the 1/f noise. *Phys. Rev. Lett.* 59, 381–384.

Bedard, C., and Destexhe, A. (2009). Macroscopic models of local field potentials and the apparent 1/f noise in brain activity. *Biophys. J.* 96, 2589–2603.

Bedard, C., Kroger, H., and Destexhe, A. (2006). Does the 1/f frequency scaling of brain signals reflect self-organized critical states? *Phys. Rev. Lett.* 97, 118102.

Beggs, J. M. (2007). *Neuronal Avalanche*. Available at: http:www.scholarpedia.org/article/Neuronal_avalanche [accessed on May 1, 2012].

Beggs, J. M. (2008). The criticality hypothesis: how local cortical networks might optimize information processing. *Philos. Trans. A Math. Phys. Eng. Sci.* 366, 329–343.

Beggs, J. M., Klukas, J., and Chen, W. (2007). "Connectivity and dynamics in local cortical networks," in *Handbook of Brain Connectivity*, ed. R. M. V. Jirsa (Berlin: Springer), 91–116.

Beggs, J. M., and Plenz, D. (2003). Neuronal avalanches in neocortical circuits. *J. Neurosci.* 23, 11167–11177.

Benayoun, M., Cowan, J. D., Van Drongelen, W., and Wallace, E. (2010). Avalanches in a stochastic model of spiking neurons. *PLoS Comput. Biol.* 6, e1000846. doi:10.1371/journal.pcbi.1000846

Bertschinger, N., and Natschlager, T. (2004). Real-time computation at the edge of chaos in recurrent neural networks. *Neural. Comput.* 16, 1413–1436.

Bienenstock, E. (1995). A model of neocortex. *Netw. Computat. Neural Syst.* 6, 179–224.

Brush, S. G. (1967). History of Lenz-Ising model. *Rev. Modern Phys.* 39, 883–893.

Buice, M. A., and Cowan, J. D. (2007). Field-theoretic approach to fluctuation effects in neural networks. *Phys. Rev. E. Stat. Nonlin. Soft Matter Phys.* 75, 051919.

Buice, M. A., and Cowan, J. D. (2009). Statistical mechanics of the neocortex. *Prog. Biophys. Mol. Biol.* 99, 53–86.

Buice, M. A., Cowan, J. D., and Chow, C. C. (2010). Systematic fluctuation expansion for neural network activity equations. *Neural. Comput.* 22, 377–426.

Chen, W., Hobbs, J. P., Tang, A. N., and Beggs, J. M. (2010). A few strong connections: optimizing information retention in neuronal avalanches. *BMC Neurosci.* 11, 14. doi:10.1186/1471-2202-11-3

Chen, Y. Q., Ding, M. Z., and Kelso, J. A. S. (1997). Long memory processes (1/f(alpha) type) in human coordination. *Phys. Rev. Lett.* 79, 4501–4504.

Chialvo, D. R. (2004). Critical brain networks. *Phys. Stat. Mech. Appl.* 340, 756–765.

Chialvo, D. R. (2010). Emergent complex neural dynamics. *Nat. Phys.* 6, 744–750.

Chialvo, D. R., and Bak, P. (1999). Learning from mistakes. *Neuroscience* 90, 1137–1148.

Cipra, B. A. (1987). An introduction to the Ising-model. *Am. Math. Mon.* 94, 937–959.

Clauset, A., Shalizi, C. R., and Newman, M. E. J. (2009). Power law distributions in empirical data. arXiv:0706.1062v2.

de Arcangelis, L., and Herrmann, H. J. (2010). Learning as a phenomenon occurring in a critical state. *Proc. Natl. Acad. Sci. U.S.A.* 107, 3977–3981.

de Arcangelis, L., Perrone-Capano, C., and Herrmann, H. J. (2006). Self-organized criticality model for brain plasticity. *Phys. Rev. Lett.* 96, 028107.

de Carvalho, J. X., and Prado, C. P. C. (2000). Self-organized criticality in the Olami-Feder-Christensen model. *Phys. Rev. Lett.* 84, 4006–4009.

Dehghani, N., Hatsopoulos, N. G., Haga, Z. D., Parker, R. A., Greger, B., Halgren, E., Cash, S. S., and Destexhe, A. (2012). Avalanche analysis from multi-electrode ensemble recordings in cat, monkey and human cerebral cortex during wakefulness and sleep. arXiv:1203.0738v2.

Droste, F., Do, A. L., and Gross, T. (2012). Analytical investigation of self-organized criticality in neural networks. arXiv:1203.4942v1.

Eurich, C. W., Herrmann, J. M., and Ernst, U. A. (2002). Finite-size effects of avalanche dynamics. *Phys. Rev. E. Stat. Nonlin. Soft Matter Phys.* 66, 066137.

Freeman, W. J. (2005). A field-theoretic approach to understanding scale-free neocortical dynamics. *Biol. Cybern.* 92, 350–359.

Friedman, N., Butler, T., Deville, R. E. L., Beggs, J. M., and Dahmen, K. (2011). Beyond critical exponents in neuronal avalanches. *APS March Meeting*, Dallas.

Friedman, N., Ito, S., Brinkman, B. A. W., Shimono, M., Deville, R. E. L., Dahmen, K. A., Beggs, J. M., and Butler, T. C. (2012). Universal critical dynamics in high resolution neuronal avalanche data. *Phys. Rev. Lett.* 108, 208102.

Fusi, S., Drew, P. J., and Abbott, L. F. (2005). Cascade models of synaptically stored memories. *Neuron* 45, 599–611.

Gireesh, E. D., and Plenz, D. (2008). Neuronal avalanches organize as nested theta- and beta/gamma-oscillations during development of cortical layer 2/3. *Proc. Natl. Acad. Sci. U.S.A.* 105, 7576–7581.

Gisiger, T. (2001). Scale invariance in biology: coincidence or footprint of a universal mechanism? *Biol. Rev.* 76, 161–209.

Goldenfeld, N. (1992). *Lectures on Phase Transitions and the Renormalization Group*. Reading, MA: Addison-Wesley, Advanced Book Program.

Gray, R. T., and Robinson, P. A. (2007). Stability and spectra of randomly connected excitatory cortical networks. *Neurocomputing* 70, 1000–1012.

Griffiths, R. (1965). Ferromagnets and simple fluids near critical point - some thermodynamic inequalities. *J. Chem. Phys.* 43, 1958–1968.

Hahn, G., Petermann, T., Havenith, M. N., Yu, S., Singer, W., Plenz, D., and Nikolic, D. (2010). Neuronal avalanches in spontaneous activity in vivo. *J. Neurophysiol.* 104, 3312–3322.

Haldeman, C., and Beggs, J. M. (2005). Critical branching captures activity in living neural networks and maximizes the number of metastable States. *Phys. Rev. Lett.* 94, 058101.

Hobbs, J. P., Smith, J. L., and Beggs, J. M. (2010). Aberrant neuronal avalanches in cortical tissue removed from juvenile epilepsy patients. *J. Clin. Neurophysiol.* 27, 380–386.

Horn, D., Ruppin, E., Usher, M., and Herrmann, M. (1993). Neural-network modeling of memory deterioration in Alzheimers-disease. *Neural. Comput.* 5, 736–749.

Hsu, D., and Beggs, J. M. (2006). Neuronal avalanches and criticality: a dynamical model for homeostasis. *Neurocomputing* 69, 1134–1136.

Hsu, D., Chen, W., Hsu, M., and Beggs, J. M. (2008). An open hypothesis: is epilepsy learned, and can it be unlearned? *Epilepsy Behav.* 13, 511–522.

Hsu, D., Tang, A., Hsu, M., and Beggs, J. M. (2007). Simple spontaneously active Hebbian learning model: homeostasis of activity and connectivity, and consequences for learning and epileptogenesis. *Phys. Rev. E. Stat. Nonlin. Soft Matter Phys.* 76, 041909.

Jensen, H. J. (1998). *Self-Organized Criticality: Emergent Complex Behavior in Physical and Biological Systems.* Cambridge, NY: Cambridge University Press.

Juanico, D. E., Monterola, C., and Saloma, C. (2007). Dissipative self-organized branching in a dynamic population. *Phys. Rev. E. Stat. Nonlin. Soft Matter Phys.* 75, 045105.

Kauffman, S., Peterson, C., Samuelsson, B., and Troein, C. (2004). Genetic networks with canalyzing Boolean rules are always stable. *Proc. Natl. Acad. Sci. U.S.A.* 101, 17102–17107.

Kello, C. T., and Mayberry, M. R. (2010). "Critical branching neural computation," in *The 2010 International Joint Conference on Neural Networks*, Barcalona.

Kinouchi, O., and Copelli, M. (2006). Optimal dynamical range of excitable networks at criticality. *Nat. Phys.* 2, 348–352.

Kitzbichler, M. G., Smith, M. L., Christensen, S. R., and Bullmore, E. (2009). Broadband criticality of human brain network synchronization. *PLoS Comput. Biol.* 5, 13. doi:10.1371/journal.pcbi.1000314

Klaus, A., Yu, S., and Plenz, D. (2011). Statistical analyses support power law distributions found in neuronal avalanches. *PLoS ONE* 6, e19779. doi:10.1371/journal.pone.0019779

Kozma, R., Puljic, M., Balister, P., Bollobas, B., and Freeman, W. J. (2005). Phase transitions in the neuropercolation model of neural populations with mixed local and nonlocal interactions. *Biol. Cybern.* 92, 367–379.

Kuntz, M. C., and Sethna, J. P. (2000). Noise in disordered systems: the power spectrum and dynamic exponents in avalanche models. *Phys. Rev. B* 62, 11699–11708.

Larremore, D. B., Shew, W. L., Ott, E., and Restrepo, J. G. (2011). Effects of network topology, transmission delays, and refractoriness on the response of coupled excitable systems to a stochastic stimulus. *Chaos* 21, 025117. doi: 10.1063/1.3600760

Levina, A., Herrmann, J. M., and Geisel, T. (2007). Dynamical synapses causing self-organized criticality in neural networks. *Nat. Phys.* 3, 857–860.

Levina, A., Herrmann, J. M., and Geisel, T. (2009). Phase transitions towards criticality in a neural system with adaptive interactions. *Phys. Rev. Lett.* 102, 118110. doi: 10.1103/PhysRevLett.102.118110

Linkenkaer-Hansen, K., Nikouline, V. V., Palva, J. M., and Ilmoniemi, R. J. (2001). Long-range temporal correlations and scaling behavior in human brain oscillations. *J. Neurosci.* 21, 1370–1377.

Liu, Y., and Dahmen, K. A. (2009). Unexpected universality in static and dynamic avalanches. *Phys. Rev. E* 79, 061124. doi: 10.1103/PhysRevE.79.061124

Lowen, S. B., Cash, S. S., Poo, M., and Teich, M. C. (1997). Quantal neurotransmitter secretion rate exhibits fractal behavior. *J. Neurosci.* 17, 5666–5677.

Maass, W., Natschlager, T., and Markram, H. (2002). Real-time computing without stable states: a new framework for neural computation based on perturbations. *Neural. Comput.* 14, 2531–2560.

Maass, W., Natschlager, T., and Markram, H. (2004). Fading memory and kernel properties of generic cortical microcircuit models. *J. Physiol. Paris* 98, 315–330.

Magnasco, M. O., Piro, O., and Cecchi, G. A. (2009). Self-tuned critical anti-hebbian networks. *Phys. Rev. Lett.* 102, 258102. doi: 10.1103/PhysRevLett.102.258102

Mandelbrot, B. B. (1982). *The Fractal Geometry of Nature.* San Francisco: W.H. Freeman.

May, R. M. (1976). Simple mathematical-models with very complicated dynamics. *Nature* 261, 459–467.

Mazzoni, A., Broccard, F. D., Garcia-Perez, E., Bonifazi, P., Ruaro, M. E., and Torre, V. (2007). On the dynamics of the spontaneous activity in neuronal networks. *PLoS ONE* 2, e439. doi:10.1371/journal.pone.0000439

Mehta, A. P., Dahmen, K. A., and Ben-Zion, Y. (2006). Universal mean moment rate profiles of earthquake ruptures. *Phys. Rev. E* 73.

Miller, K. J., Sorensen, L. B., Ojemann, J. G., and Den Nijs, M. (2009). Power-law scaling in the brain surface electric potential. *PLoS Comput. Biol.* 5, e1000609. doi:10.1371/journal.pcbi.1000609

Millman, D., Mihalas, S., Kirkwood, A., and Niebur, E. (2010). Self-organized criticality occurs in non-conservative neuronal networks during 'up' states. *Nat. Phys.* 6, 801–805.

Mitzenmacher, M. (2004). A brief history of generative models for power law and lognormal distributions. *Internet Math.* 1, 226–251.

Mora, T., and Bialek, W. (2011). Are biological systems poised at criticality? *J. Stat. Phys.* 144, 268–302.

Netoff, T. I., Clewley, R., Arno, S., Keck, T., and White, J. A. (2004). Epilepsy in small-world networks. *J. Neurosci.* 24, 8075–8083.

Newman, M. E. J. (2005). Power laws, Pareto distributions and Zipf's law. *Contemp. Phys.* 46, 323–351.

Nicolis, G., and Prigogine, I. (1989). *Exploring Complexity: An Introduction.* New York: W.H. Freeman.

Nishimori, H., and Ortiz, G. (2011). *Elements of Phase Transitions and Critical Phenomena.* New York: Oxford University Press.

Papanikolaou, S., Bohn, F., Sommer, R. L., Durin, G., Zapperi, S., and Sethna, J. P. (2011). Universality beyond power laws and the average avalanche shape. *Nat. Phys.* 7, 316–320.

Pasquale, V., Massobrio, P., Bologna, L. L., Chiappalonea, M., and Martinoia, S. (2008). Self-organization and neuronal avalanches in networks of dissociated cortical neurons. *Neuroscience* 153, 1354–1369.

Pellegrini, G. L., de Arcangelis, L., Herrmann, H. J., and Perrone-Capano, C. (2007). Activity-dependent neural network model on scale-free networks. *Phys. Rev. E* 76.

Perkovic, O., Dahmen, K., and Sethna, J. P. (1995). Avalanches, Barkhausen noise, and plain old criticality. *Phys. Rev. Lett.* 75, 4528–4531.

Perkovic, O., Dahmen, K. A., and Sethna, J. P. (1999). Disorder-induced critical phenomena in hysteresis: numerical scaling in three and higher dimensions. *Phys. Rev. B* 59, 6106–6119.

Petermann, T., Lebedev, M., Nicolelis, M., and Plenz, D. (2006). Neuronal avalanches in vivo. *Soc. Neurosci. Abstr.* 531.

Petermann, T., Thiagarajan, T. C., Lebedev, M. A., Nicolelis, M. A. L., Chialvo, D. R., and Plenz, D. (2009). Spontaneous cortical activity in awake monkeys composed of neuronal avalanches. *Proc. Natl. Acad. Sci. U.S.A.* 106, 15921–15926.

Plenz, D., and Thiagarajan, T. C. (2007). The organizing principles of neuronal avalanches: cell assemblies in the cortex? *Trends Neurosci.* 30, 101–110.

Poil, S. S., Van Ooyen, A., and Linkenkaer-Hansen, K. (2008). Avalanche dynamics of human brain oscillations: relation to critical branching processes and temporal correlations. *Hum. Brain Mapp.* 29, 770–777.

Priesemann, V., Munk, M. H., and Wibral, M. (2009). Subsampling effects in neuronal avalanche distributions recorded in vivo. *BMC Neurosci.* 10, 40. doi:10.1186/1471-2202-10-40

Ramo, P., Kauffman, S., Kesseli, J., and Yli-Harja, O. (2007). Measures for information propagation in Boolean networks. *Phys. D Nonlin. Phenomena* 227, 100–104.

Reed, W. J., and Hughes, B. D. (2002). From gene families and genera to incomes and internet file sizes: why power laws are so common in nature. *Phys. Rev. E. Stat. Nonlin. Soft Matter Phys.* 66, 067103.

Ribeiro, T. L., Copelli, M., Caixeta, F., Belchior, H., Chialvo, D. R., Nicolelis, M. A. L., and Ribeiro, S. (2010). Spike avalanches exhibit universal dynamics across the sleep-wake cycle. *PLoS ONE* 5, e14129. doi:10.1371/journal.pone.0014129

Rubinov, M., Sporns, O., Thivierge, J. P., and Breakspear, M. (2011). Neurobiologically realistic determinants of self-organized criticality in networks of spiking neurons. *PLoS Comput. Biol.* 7, e1002038. doi:10.1371/journal.pcbi.1002038

Schneidman, E., Berry, M. J., 2nd, Segev, R., and Bialek, W. (2006). Weak pairwise correlations imply strongly correlated network states in a neural population. *Nature* 440, 1007–1012.

Sethna, J. P., Dahmen, K. A., and Myers, C. R. (2001). Crackling noise. *Nature* 410, 242–250.

Shew, W. L., Yang, H., Petermann, T., Roy, R., and Plenz, D. (2009). Neuronal avalanches imply maximum dynamic range in cortical networks at criticality. *J. Neurosci.* 29, 15595–15600.

Shew, W. L., Yang, H., Yu, S., Roy, R., and Plenz, D. (2011). Information capacity and transmission are maximized in balanced cortical networks with neuronal avalanches. *J. Neurosci.* 31, 55–63.

Shlens, J., Field, G. D., Gauthier, J. L., Greschner, M., Sher, A., Litke, A. M., and Chichilnisky, E. J. (2009). The structure of large-scale synchronized firing in primate retina. *J. Neurosci.* 29, 5022–5031.

Shlens, J., Field, G. D., Gauthier, J. L., Grivich, M. I., Petrusca, D., Sher, A., Litke, A. M., and Chichilnisky, E. J. (2006). The structure of multi-neuron firing patterns in primate retina. *J. Neurosci.* 26, 8254–8266.

Socolar, J. E. S., and Kauffman, S. A. (2003). Scaling in ordered and critical random Boolean networks. *Phys. Rev. Lett.* 90, 4.

Sornette, D. (1998). Multiplicative processes and power laws. *Phys. Rev. E* 57, 4811–4813.

Stam, C. J., and de Bruin, E. A. (2004). Scale-free dynamics of global functional connectivity in the human brain. *Hum. Brain Mapp.* 22, 97–109.

Stanley, H. E. (1971). *Introduction to Phase Transitions and Critical Phenomena.* New York: Oxford University Press.

Stanley, H. E. (1999). Scaling, universality, and renormalization: three pillars of modern critical phenomena. *Rev. Mod. Phys.* 71, S358–S366.

Stewart, C. V., and Plenz, D. (2006). Inverted-U profile of dopamine-NMDA-mediated spontaneous avalanche recurrence in superficial layers of rat prefrontal cortex. *J. Neurosci.* 26, 8148–8159.

Stewart, C. V., and Plenz, D. (2008). Homeostasis of neuronal avalanches during postnatal cortex development in vitro. *J. Neurosci. Methods* 169, 405–416.

Stewart, I. (2001). *What Shape is a Snowflake?* New York: W.H. Freedman.

Stumpf, M. P. H., and Porter, M. A. (2012). Critical truths about power laws. *Science* 335, 665–666.

Tanaka, T., Kaneko, T., and Aoyagi, T. (2009). Recurrent infomax generates cell assemblies, neuronal avalanches, and simple cell-like selectivity. *Neural. Comput.* 21, 1038–1067.

Tang, A., Jackson, D., Hobbs, J., Chen, W., Smith, J. L., Patel, H., Prieto, A., Petrusca, D., Grivich, M. I., Sher, A., Hottowy, P., Dabrowski, W., Litke, A. M., and Beggs, J. M. (2008). A maximum entropy model applied to spatial and temporal correlations from cortical networks in vitro. *J. Neurosci.* 28, 505–518.

Teich, M. C., Heneghan, C., Lowen, S. B., Ozaki, T., and Kaplan, E. (1997). Fractal character of the neural spike train in the visual system of the cat. *J. Opt. Soc. Am. A. Opt. Image Sci. Vis.* 14, 529–546.

Teramae, J. N., and Fukai, T. (2007). Local cortical circuit model inferred from power-law distributed neuronal avalanches. *J. Comput. Neurosci.* 22, 301–312.

Tetzlaff, C., Okujeni, S., Egert, U., Worgotter, F., and Butz, M. (2010). Self-organized criticality in developing neuronal networks. *PLoS Comput. Biol.* 6, e1001013. doi:10.1371/journal.pcbi.1001013

Tkacik, G., Schneidman, E., Berry, J., and Bialek, W. (2009). Spin glass models for a network of real neurons. arXiv:0912.5409v1.

Toib, A., Lyakhov, V., and Marom, S. (1998). Interaction between duration of activity and time course of recovery from slow inactivation in mammalian brain Na+ channels. *J. Neurosci.* 18, 1893–1903.

Touboul, J., and Destexhe, A. (2010). Can power-law scaling and neuronal avalanches arise from stochastic dynamics? *PLoS One* 5, 14. doi:10.1371/journal.pone.0008982

Worrell, G. A., Cranstoun, S. D., Echauz, J., and Litt, B. (2002). Evidence for self-organized criticality in human epileptic hippocampus. *Neuroreport* 13, 2017–2021.

Yang, H. D., Shew, W. L., Roy, R., and Plenz, D. (2012). Maximal variability of phase synchrony in cortical networks with neuronal avalanches. *J. Neurosci.* 32, 1061–1072.

Yeh, F. C., Tang, A. N., Hobbs, J. P., Hottowy, P., Dabrowski, W., Sher, A., Litke, A., and Beggs, J. M. (2010). Maximum entropy approaches to living neural networks. *Entropy* 12, 89–106.

Yeomans, J. M. (1992). *Statistical Mechanics of Phase Transitions.* Oxford: Oxford University Press.

Yu, S., Huang, D., and Singer, W. Nikolic, D. (2008). A small world of neuronal synchrony. *Cereb. Cortex* doi:10.1093/cercor/bhn047

Yu, S., Yang, H. D., Nakahara, H., Santos, G. S., Nikolic, D., and Plenz, D. (2011). Higher-order interactions characterized in cortical activity. *J. Neurosci.* 31, 17514–17526.

Conflict of Interest Statement: The authors declare that the research was conducted in the absence of any commercial or financial relationships that could be construed as a potential conflict of interest.

Received: 21 February 2012; accepted: 07 May 2012; published online: 07 June 2012.

Citation: Beggs JM and Timme N (2012) Being critical of criticality in the brain. Front. Physio. ***3****:163. doi: 10.3389/fphys.2012.00163*

This article was submitted to Frontiers in Fractal Physiology, a specialty of Frontiers in Physiology.

frontiers in
PHYSIOLOGY

ORIGINAL RESEARCH ARTICLE
published: 03 August 2012
doi: 10.3389/fphys.2012.00302

Avalanche analysis from multielectrode ensemble recordings in cat, monkey, and human cerebral cortex during wakefulness and sleep

Nima Dehghani[1]*, Nicholas G. Hatsopoulos[2], Zach D. Haga[2], Rebecca A. Parker[3], Bradley Greger[4], Eric Halgren[5], Sydney S. Cash[6] and Alain Destexhe[1]*

[1] *Laboratory of Computational Neuroscience, Unité de Neurosciences, Information et Complexité, CNRS, Gif-sur-Yvette, France*
[2] *Department of Organismal Biology and Anatomy, Committee on Computational Neuroscience University of Chicago, Chicago, IL, USA*
[3] *Interdepartmental Program in Neuroscience, University of Utah, Salt Lake City, UT, USA*
[4] *Department of Bioengineering, University of Utah, Salt Lake City, UT, USA*
[5] *Multimodal Imaging Laboratory, Departments of Neurosciences and Radiology, University of California San Diego, La Jolla, CA, USA*
[6] *Department of Neurology, Massachusetts General Hospital and Harvard Medical School, Boston, MA, USA*

Edited by:
Andreas Daffertshofer, VU University Amsterdam, Netherlands

Reviewed by:
Dante R. Chialvo, Northwestern University, USA
Chunhua Bian, Nanjing University, China

****Correspondence:***
Nima Dehghani and Alain Destexhe, Laboratory of Computational Neuroscience, Unité de Neurosciences, Information et Complexité, Centre National de la Recherche Scientifique, 1 Avenue de la Terrasse, Gif-Sur-Yvette, France.
e-mail: dehghani@unic.cnrs-gif.fr; destexhe@unic.cnrs-gif.fr

Self-organized critical states are found in many natural systems, from earthquakes to forest fires, they have also been observed in neural systems, particularly, in neuronal cultures. However, the presence of critical states in the awake brain remains controversial. Here, we compared avalanche analyses performed on different *in vivo* preparations during wakefulness, slow-wave sleep, and REM sleep, using high density electrode arrays in cat motor cortex (96 electrodes), monkey motor cortex and premotor cortex and human temporal cortex (96 electrodes) in epileptic patients. In neuronal avalanches defined from units (up to 160 single units), the size of avalanches never clearly scaled as power-law, but rather scaled exponentially or displayed intermediate scaling. We also analyzed the dynamics of local field potentials (LFPs) and in particular LFP negative peaks (nLFPs) among the different electrodes (up to 96 sites in temporal cortex or up to 128 sites in adjacent motor and premotor cortices). In this case, the avalanches defined from nLFPs displayed power-law scaling in double logarithmic representations, as reported previously in monkey. However, avalanche defined as positive LFP (pLFP) peaks, which are less directly related to neuronal firing, also displayed apparent power-law scaling. Closer examination of this scaling using the more reliable cumulative distribution function (CDF) and other rigorous statistical measures, did not confirm power-law scaling. The same pattern was seen for cats, monkey, and human, as well as for different brain states of wakefulness and sleep. We also tested other alternative distributions. Multiple exponential fitting yielded optimal fits of the avalanche dynamics with bi-exponential distributions. Collectively, these results show no clear evidence for power-law scaling or self-organized critical states in the awake and sleeping brain of mammals, from cat to man.

Keywords: criticality, self-organization, brain dynamics, scale invariance, complexity, power-law

INTRODUCTION

Self-organized criticality (SOC) is a dynamical state of a system which maintains itself at (or close to) a phase transition point. This family of systems were initially described by Bak et al. (1987), and have been found in many natural systems (reviewed in Bak, 1996; Jensen, 1998). SOC systems are characterized by scale invariance, which is usually identified as a power-law distribution of characteristics of the system's dynamics such as event size or the waiting time between events. The temporal fingerprint of SOC systems is often $1/f$ or $1/f^2$ noise. These features are interesting because they show the presence of long-lasting or long-range correlations in the system.

The dynamics of SOC systems are structured as "avalanches" of activity, separated by silent periods. Avalanche sizes are typically distributed as a power-law, where the probability of occurrence $p(x)$ of a given avalanche size x scales as:

$$p(x) \sim x^{-\alpha},$$

where α is the scaling exponent of the distribution.

SOC systems have been observed in many different natural phenomena, from sandpiles, to rice piles, in forest fires, and earthquakes (Bak and Paczuski, 1995; Bak, 1996; Frette et al., 1996; Jensen, 1998; Malamud et al., 1998; Peters and Neelin, 2006). Evidence of SOC was also demonstrated in circuits of neurons *in vitro* (Beggs and Plenz, 2003), where network activity was found to alternate between active and quiescent periods, forming "neuronal avalanches." The presence of avalanches, although clear *in vitro*, is more controversial *in vivo*. Since power-laws fit neuronal avalanches better than other alternative probability distributions (Klaus et al., 2011), their presence has been taken as evidence for neuronal avalanches *in vivo*. In anesthetized cats (Hahn et al., 2010) and awake monkeys (Petermann et al., 2009),

power-law distributed avalanches have been found in the peaks of local field potentials (LFP). However, LFP peaks are only statistically related to neuronal firing. In a study on awake and naturally sleeping cats, no sign of avalanches were found in neuronal firing (Bedard et al., 2006), and the apparent power-law scaling of LFP peaks could be explained as an artifact induced by the thresholding procedure used to detect LFP peaks. Previous studies have shown that even purely stochastic processes can display power-law scaling when subjected to similar thresholding procedures (Touboul and Destexhe, 2010). It was also stressed that power-law statistics can be generated by stochastic mechanisms other than SOC (Giesinger, 2001; Chialvo, 2010; Touboul and Destexhe, 2010). Similarly, if exponentially growing processes are suddenly killed (or "observed"), a power-law at the tail ends will emerge (Reed and Hughes, 2002). This case, would be similar to a non-stationary Poisson processes, or combining Poisson processes at different rates, a situation that is likely to happen in the nervous system. Such scenarios can give rise to spurious power-laws.

These contrasting results correspond to different preparations and recording techniques, single units or LFPs, or different species, so that it is difficult to compare them. In the present paper, we attempt to overcome these shortcomings by providing a systematic analysis of both units and LFPs for different species and different brain states.

MATERIALS AND METHODS

RECORDINGS

Cat

Recordings of local field potentials (LFPs) and action potentials (APs) were obtained from motor cortex in 2 felines (M1 and approximately hindlimb region). Commercially obtained 96 electrode sputtered iridium oxide film arrays (Blackrock Microsystems, Inc., Salt Lake City, UT, USA) were chronically implanted and recordings were performed in the awake, unrestrained feline (as described in Parker et al., 2011). Electrodes on the array were arranged in a square with 400 micron spacing and 1 mm shank length. LFPs and APs were recorded using a Cerebus data acquisition system (Blackrock Microsystems). Spike sorting on AP data was performed using the t-dist EM algorithm built into Offline Sorter (Plexon, Inc.). All animal procedures were performed in accordance with University of Utah Institutional Animal Care and Use Committee guidelines.

We also compared these data with previously published multielectrode data on cat parietal cortex (Destexhe et al., 1999). In this case, a linear array of 8 bipolar electrodes (separated by 1 mm) was chronically implanted in cortical area 5–7, together with myographic and oculographic recordings, to insure that brain states were correctly discriminated (quiet wakefulness with eyes-open, slow-wave sleep, REM sleep). Throughout the text, this cat will be referred to as "cat iii" LFP signals were digitized offline at 250 Hz using the Igor software package (Wavemetrics, OR, USA; A/D board from GW Instruments, MA, USA; low-pass filter of 100 Hz). Units were digitized offline at 10 kHz, and spike sorting and discrimination was performed with the DataWave software package (DataWave Technologies, CO, USA; filters were 300 Hz high-pass and 5 kHz low-pass).

Monkey

Recordings from three monkeys were used in this study. Each monkey was chronically implanted with 100-electrode Utah arrays (400 m inter-electrode separation, 1.0 mm electrode length; Blackrock Microsystems, Inc., Salt Lake City, UT, USA). In two monkeys (i) and (ii), we used recordings made during the performance of motor tasks. The motor tasks involved moving a cursor to visually presented targets in the horizontal plane by flexing and extending the shoulder and elbow of the arm contralateral to the cerebral hemisphere that was implanted. In monkey (iii), sleep recordings were used to test avalanche dynamics. Monkey i was implanted with one 96 electrode array in primary motor cortex (MI) and a second 96 electrode array in dorsal premotor cortex (PMd) from which recordings were made on 64 electrodes in each cortical area. Monkey ii had an array implanted in MI from which 96 electrodes were recorded and monkey iii had two arrays in MI and PMd from which 96 electrodes were recorded in PMd cortex and 32 electrodes were recorded in MI area. During a recording session, local field potential (LFP) signals were amplified (gain, 5000), band-pass filtered (0.3–250 or 0.3–500 Hz), and recorded digitally (14-bit) at 1 kHz per channel To acquire extracellular action potentials, signals were amplified (gain, 5000), band-pass filtered (250–7.5 kHz) and sampled at 30 kHz per channel. For each channel, a threshold was set above the noise band: if the signal crossed the threshold, a 1.6-ms duration of the signal – as to yield 48 samples given a sampling frequency of 30 kHz – was sampled around the occurrence of the threshold crossing and spike-sorted using Offline Sorter (Plexon, Inc., Dallas, TX, USA). All of the surgical and behavioral procedures performed on the non-human primates were approved by the University of Chicagos IACUC and conform to the principles outlined in the Guide for the Care and Use of Laboratory Animals (NIH publication no. 86–23, revised 1985).

Human

Recordings were obtained from two patients with medically intractable focal epilepsy using NeuroPort electrode array as discussed previously (Truccolo et al., 2010; Peyrache et al., 2012). The array, 1 mm in length, was placed in layers II/III of the middle temporal gyrus with informed consent of the patient and with approval of the local Institutional Review Board in accordance with the ethical standards of the Declaration of Helsinki. This array is silicon-based, made up of 96 microelectrodes with 400-μm spacing, covering an area of 4 mm $\times$ 4 mm. Since the corners are omitted from the array, the furthest separated contacts are 4.6 mm apart. Data were sampled at 30 kHz (Blackrock Microsystems, Salt Lake City, UT, USA). The continuous recording was downsampled to 1250 Hz to obtain LFPs. The dataset we analyzed was devoid of any form of identifiable epileptic activity (such as interictal spikes), and there was no seizure in the analyzed dataset. The implantation site was included in the therapeutic resection in both patients. For details on spike sorting, see Peyrache et al. (2012).

AVALANCHE DETECTION

Avalanches are defined by temporally contiguous clusters of activity among the different electrodes, separated by periods of silence. Either trains of neuronal action potentials (spikes) or LFP peaks

can be analyzed for the occurrence of avalanches. There are two empirical limits on bin duration. The smallest bin size is set by the duration of the action potential. The upper boundary, is limited by how many unique values of the aggregate ensemble activity occur in a window. When the number of unique values approaches 1, avalanche loses its definition, because there is no silent period left. In the cat data, where there are 160 cells, we reach this limit at a bin-width of 16 ms. So, we have stayed within the 1- to 15-ms regime in which an avalanche could be well defined.

Spike avalanche

In each set of recordings, regardless of the spatial location of a given electrode in the multielectrode array, its spiking activity was put in the same pool with all other spikes recorded from other electrodes of the same array. This ensemble trace was then binned and coarse grained for different δt ranging from 1 to 16 ms in 2 ms steps. This created a series of bins containing the ensemble of activity across all neurons for that δt. The sum of spiking in that bin represents the total bin activity. The sum of all bin activities between two quiescent bins, represents the avalanche size, which was later used for statistical analyses. Notice that in the case of the minimum $\delta t = 1$, avalanche size would range between 0 and maximum number of neurons present as this bin approximates the size unity of spiking period. **Figure 1A** shows the definition of avalanche in spike series from human recordings.

LFP avalanche

Each LFP trace was first detrended through a least-squares fit of a straight line to the data and subsequent subtraction of the resulting function from all the sample points. After this detrending removed the mean value or linear trend from a LFP vector, it was then normalized (Z score) to have a common reference frame for discretization across channels, recordings, states, and species. The z-scored LFP, was then discretized through a local maxima peak detection. An optimizing small running average filter was designed and 3 passes of the filter were applied to the data in order to remove small spurious peaks in each LFP deflection. Next, by comparing each element of data to its neighboring values, if that sample of data was larger than both of its adjacent ones, that element was considered as a local peak. Next, all the peaks were sorted in descending order, beginning with the largest peak, and all identified peaks not separated by more than minimum peak distance (of 3 samples) from the next local peak were discarded.

The threshold was fixed and defined as a multiple of the standard deviation (STD) of the LFP signal. Different thresholds were tested, starting at $1.25 \times$ STD and increasing in 0.25 steps up to $5 \times$ STD for both negative and positive maxima. This procedure was realized on each LFP channel, state, species (**Figure 1B**). Such matrix of discrete events (for a given polarity and a given threshold), was then treated the same way the spike matrix was used to create avalanche vectors of quiescent and active periods.

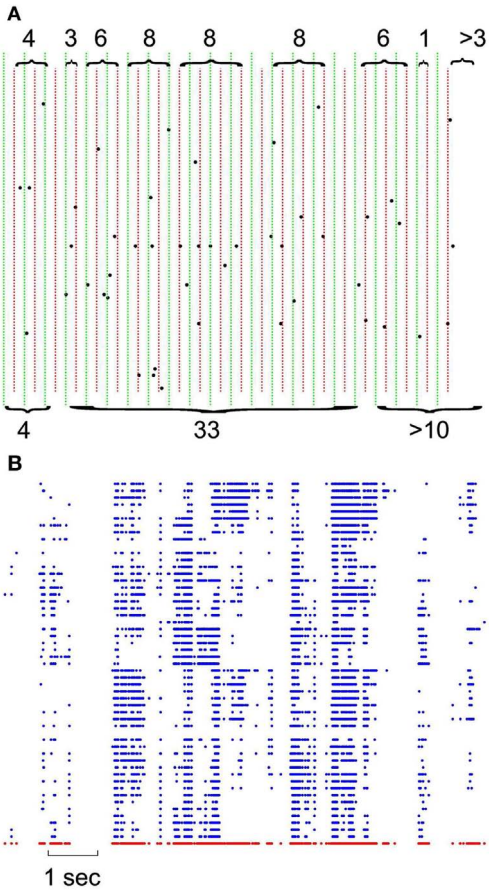

FIGURE 1 | Definition of avalanches. (A) Comparison of avalanche definition for 8 vs. 16 ms binning; green vertical lines define the boundaries of 16 ms binning; naturally, each 16 ms bin is composed of 2 independent 8 ms bin (depicted with red dotted lines). Accolades point to the avalanches, separated by quiescent periods. Top, 8 ms avalanches and their sizes, bottom, 16 ms avalanches and their corresponding size. Please note that last avalanche continues after of the limits in this figure. **(B)** Negative local maxima obtained from the grid of electrodes for a period of 10 s. Each row represents negative maxima of a single LFP channel of a selected threshold level $\geq 1.75 \times$ STD of the normalized LFP. The red dots in the bottom refer to ensemble presence of nLFP maxima.

LFP PEAK AND SPIKING RELATIONSHIP

Wave-triggered-average (WTA)

We used wave-triggered averaging (WTA) to analyze the differences in the relationships of spikes to nLFP vs. pLFP. In WTA, the individual negative LFP peaks (nLFP) were used to epoch the ensemble spike series. The epoched ensemble spike series were normalized by the number of epochs (triggered by nLFPs). This procedure was performed for the three different thresholds (low, medium, and high) and the results were averaged across these thresholds to obtain cross-threshold WTA percentage firing to quantify the spike-nLFP relationship. An identical procedure was applied to pLFPs. The red and blue solid lines in **Figure 6** refer to nLFP-spike and pLFP-spike WTA percentage firing, respectively.

Controls and randomization Methods

We used 4 methods of surrogate/randomization in order to evaluate the statistical robustness of the comparative relation of spike-nLFP vs. spike-pLFP. Each of the following 4 methods, was first performed on all 3 chosen thresholds and then the results were averaged to obtain the overall randomization effect.

Poisson surrogate data. At the first step, we wanted to test whether the observed nLFP and pLFP differences could be reproduced by surrogate spike series. For this type of control, first, each individual channel's spike rate was calculated. Then, using a renewal process, a surrogate Poisson spike series for that channel was created (matching the firing rate and duration of the experimental data from that channel). Then, all Poisson spike series (across all channels) were aggregated together to create the ensemble spike series (similar to the experimental data). Next, for each pLFP (or nLFP), the WTA of this Poisson aggregate series was created. This procedure was repeated 1000 times and then averaged across the 1000 trials. The results were close to a constant WTA percent firing and did not fluctuate according to the timing of the peak LFP that was used to epoch each individual WTA event. This control test showed that the simple aggregate of surrogate Poisson spikes can not reproduce the observed relation between nLFP and spikes in the WTA or mimic the behavior of natural peak(positive or negative)-induced percentage firing. This procedure was also repeated with Poisson spikes without a refractory period and provided similar results.

Random permutation. In a follow up test, we wanted to verify that randomizing the aggregate spike series by itself can not mimic the observed the LFP-spike relation. For this procedure, we performed a random permutation on the aggregate spike series and then calculated the nLFP(and pLFP)-based WTA. This procedure was repeated 1000 times. The observations are similar to the Poisson randomization, verifying that the nLFP peak is not reproducible by randomization of spikes and the fluctuations of WTA percentage firing are not results of random events.

Local jitter randomization of LFP peaks. Next, we wanted to evaluate the effects of randomization based on the statistics of the individual channel's LFP peak times (before aggregating them into the ensemble LFP peak train). First, each channel's nLFP IPI (inter-peak-interval) were calculated. Then these IPIs from all channels were put in the same pool and the, 0.25, 0.5, and 0.75 quantiles IPI for the aggregate nLFPs were extracted. Next, we created a normal distribution with 0.5 percentile as the mean, the interquartile range ($0.75 - 0.25$ quantile) as the standard deviation of the pdf, and N events matching the number of aggregate nLFPs. This set of values, were used to jitter nLFPs in the following manner. Each sample from the aggregates nLFP peak series was shifted according to one drawn sample (without replacement) from the nLFP jitter pool. The direction of the shift was to the right if the drawn jitter value was negative (and to the left for the positive value). The magnitude of the shift was defined by the value of the jitter itself. The same procedure was repeated for pLFPs. The results of this randomization are shown in **Figure 6A**. As can be appreciated, with this tightly regulated data-driven local randomization, the structure of the WTA is preserved except for the peak curve around 0 for the nLFP case.

Fixed-ISI circular shift of spikes. In this procedure, we kept the ISI (inter-spike interval) of the aggregate spike series as well as the IPI (inter-peak intervals) of the nLFP and pLFP intact but randomized the relation between the aggregate spike and aggregate peak series. In each of the 1000 trials, a circular shift with the magnitude chosen randomly between 1 and the range of the ISI, was performed. The results, shown in **Figure 6B**, show that by destroying the relation between ensemble spikes and ensemble peaks while preserving their internal structure, the observed fluctuations and most importantly, the tightly bound relation of nLFP and spikes, is lost.

TESTING POWER-LAW DISTRIBUTION IN EMPIRICAL DATA

For testing the power-law behavior, usually a simple least square method is applied to fit a power-law on the data. If such fit in a log-log scale, follows a straight line, the slope of the probability density function (PDF) line is taken as the scaling exponent. Such method is widely practiced but is highly inaccurate in its estimation of true existence of power-law in a given dataset. It has been argued that, for obtaining statistically sound results in estimating power-law in empirical data, one has to rely on rigorous statistical methods. In a detailed analysis of the problem (Newman, 2005; Clauset et al., 2009), it was proposed that the cumulative distribution function (CDF) is much more accurate to fit the power-law exponent, as well as to identify if the system obeys a power-law.

If the initial distribution of the PDF is power-law, i.e.,

$$p(x) = Cx^{-\alpha},$$

then CDF is defined as

$$Pr(X > x) = C\int_x^{inf} x'^{-\alpha}dx' = \frac{C}{\alpha - 1}x^{-(\alpha-1)}.$$

Thus, the corresponding CDF also behaves as a power-law, but with a smaller exponent

$$\alpha - 1$$

being 1 unit smaller than the original exponent (Newman, 2005).

Generally, in fitting the power-law to the empirical data, all the initial values (left hand of the distribution histogram, i.e., smallest sizes of avalanches) are included in the used decades to obtain the slope of the fit (scaling exponent α). The inclusion of these initial parts may cause significant errors, and should be removed (Goldstein et al., 2004; Bauke, 2007; Clauset et al., 2009). Thus, before calculating the scaling exponent, it is essential to discard the values below the lower bound (X_{min}). It is only above this lower bound that, a linear PDF or CDF can be reliably used for estimation of the scaling exponent. There are different methods for proper estimation of the X_{min}. We used a Kolmogorov-Smirnov (KS test) optimization approach that searches for the minimum "distance" (D) between the power-law model and the empirical, where for $Xi \geqslant X_{min}$, "D" is defined as

$$D = max|S(x) - P(x)|,$$

$S(x)$ the CDF of the empirical data and $P(x)$ the CDF of the best matching power-law model. The X_{min} value that yields the minimum D, is the optimal X_{min}. The X_{min} is used in a maximum likelihood estimate (MLE) of power-law fit to the CDF of the avalanches in order to obtain the scaling exponent. This fitting,

however, does not provide any statistical significance on whether the power-law is a plausible fit to the data or not. After the estimation of X_{min} and the exponent, we generated N (N = 1000) power-law distributed surrogate data with the exact same features of X_{min} and exponent. Each of these surrogate series are then fitted with power-law and KS-statistics of distance D (to the surrogate power-law), is performed. The fraction of N that the resultant statistics was bigger than the one obtained from the empirical data, comprises the p-value. If p-value $\leqslant 0.1$, the power-law is ruled out. However, even if p-value is larger than this threshold, the data is not necessarily guaranteed to be generated by a power-law process unless no better distribution is found to estimate the properties of the data. For this, the alternative test was adapted as following.

Generating power-law distributed random numbers with high precision

It is essential to use high precision and reliable algorithms to generate random numbers from a given probability distribution; otherwise the statistical tests based on such distributions may be erroneous. For initializing the generator with an "Integer Seed," we adapted the reliable Mersenne Twister algorithm (known as MT19937AR) with full precision of Mersenne prime $(2^{19937} - 1)$ (Matsumoto and Nishimura, 1998). This algorithm provides a proper method for running Monte Carlo simulations. After initialization, "Transformation algorithm" was used to generate the desired distribution (Press et al., 2007a; Clauset et al., 2009). All the random number generations and analyses were performed on a 16-core Intel 48 GB Linux platform equipped with 448 core Tesla C2050 GPU with double precision of 515 Gflop and single precision of 1.03 Tflops. The custom code was based on Matlab (Mathworks) and CUDA (NVIDIA) wrapper Jacket (Accelreyes) for parallel computing on GPU.

ALTERNATIVE FITS

The power-law fit was compared with alternative hypotheses to test which distribution best fits the data. The alternatives included exponential distribution (as predicted by a Poisson type stochastic process), "Discretized log-normal distribution" (which is represented as a linear fit in log-normal scale), as well as fit of "Discrete exponential distribution" nature. These fits had two general types of simple exponential, defined as: $f(x) = a\exp(bx)$ as well as sum of exponential set as: $f(x) = a\exp(bx) + c\exp(dx)$ In each case, residual analyses, goodness of fit as well as confidence and prediction bounds were used to evaluate the properties of each fit vs. power-law. In case of a good fit model, Residual, defined as the difference between data and fit, should approximate random error and behave randomly.

Goodness of fit comparison of exponential models

A measure of "goodness of fit," R-square, is the ratio of the sum of squares of the regression (SSR) and the total sum of squares (SST). This measure, represents the square of the correlation between the observed and predicted response values, and indicates what percentage of the variance of the data is explained by the chosen fit (values of R-square range from 0, worst fit, to 1, the best possible fit). If we have SSR as: $SS_{\text{reg}} = \sum_i (\hat{y}_i - \bar{y})^2$, and SSE as: $SS_{\text{err}} = \sum_i (y_i - \hat{y})^2$, and SST as: $SS_{\text{tot}} = \sum_i (y_i - \bar{y})^2$, where, $y_i, \bar{y}, \hat{y}$ are the original data values, their mean and modeled values respectively. Then, it follows that:

$$R^2 = SS_{\text{reg}}/SS_{\text{tot}} = 1 - \frac{SS_{\text{err}}}{SS_{\text{tot}}}.$$

Correction by "total degree of freedom" and "error degree of freedom," defines adjusted R-square:

$$\bar{R}^2 = 1 - \left(1 - R^2\right)\frac{N-1}{N-M-1} = 1 - \frac{SS_{\text{err}}}{SS_{\text{tot}}}\frac{df_t}{df_e}.$$

where "N" is the sample size, and "M" is the number of fitted coefficients (excluding constants). Usage of $\bar{R}^2$ in the comparison of "simple exponential" and "sum of exponential" is warranted by the fact that by an increase in the fitted number of the components, from one model to the other, the degrees of freedom changes. Both R^2 and $\bar{R}^2$ measures were estimated through nonlinear least square optimization of exponential curve fitting. In the optimization process for estimating the coefficients of the models, we adapted Levenberg-Marquardt algorithm with a tolerance of 10^{-8} (Press et al., 2007b).

Test of linearity in log-normal scale

Linearity in log-normal scale, is a hallmark of an exponential family process. In order to test the linearity of the PDF in log-normal scaling, we used Root mean square error (RMSE), $\text{RMSE}(\hat{\theta}) = \sqrt{\text{MSE}(\hat{\theta})}$ where MSE is: $\frac{SS_{\text{err}}}{df_e}$. This measure ranges from 0 to 1, where closer value to 0 is an indicator of a better fit.

This test was performed by fitting $y = log[P(x)]$ with a linear least square first degree polynomial. As shown in **Figure 13C**, sometimes, the initial values in the left tail may slightly deviate from a simple 1st degree polynomial. Therefore, we tested whether the linearity was improved or worsened when the data range was reduced to above some X_{min}. For doing so, we adapted a more stringent regression, bi-square robust 1st degree polynomial (Press et al., 2007b). This method is an iteratively reweighted least-squares, based on $\bar{R}^2$, and assigns less weight to the values farther from the line. This procedure was repeated after excluding consequent single values from the left tail (up to 20% of the points). For each new shortened series, the RMSE (based on bi-square method) was re-calculated. The rational behind using RMSE for testing the linearity range in these datasets (with variable N) is that when a distinct point is removed from the dataset, 2 other reductions follow: (a) the sum of squares and (b) degrees of freedom. Thus, if after limiting the range, the error remains the same, SS_{err} would increase. Similarly, when the error is significantly reduced, SS_{err} would increase. Therefore, any change in the error, should only be considered significant if it is compensated by the amount of change in the degree of freedom. For quantifying this, we defined two measures for linearity improvement after limiting the data above X_{min}. The first measure, "overall RMSE change" (oRMSE), was defined as:

$$oRMSE_i = \frac{RMSE_n - RMSE_{n-i}}{RMSE_n} * 100.$$

In parallel, "relative RMSE change" (rRMSE), was defined as:

$$rRMSE_i = \frac{RMSE_{n-i+1} - RMSE_{n-i}}{RMSE_n} * 100,$$

where $RMSE_n$ was the RMSE of the full length data. Next standard deviation of the, these measures were normalized to their maximum (*noRMSE* and *nrRMSE*) and a 3rd dimension was created by the distance of each pair ($noRMSE_i$, $nrRMSE_i$), from the geometrical diagonal defined as

$$D = \frac{det\,[(Q2 - Q1) \cdot (P - Q1)]}{\|(Q2 - Q1)\|}$$

where P was the coordinates of a point ($noRMSE_i$, $nrRMSE_i$) while Q1 = [0 0] and Q2 = [1 1] were the vertices of the geometrical diagonal of the RMSEs pair space. The point that had the maximum "$(1 - D_i) + noRMSE_i + nrRMSE_i$" (this value can range between 0 and 3), was taken as the optimal linearizing shortening index (X_{min}; **Figure 13D**). Next, we fitted all data ranges (from N sample points to $N - X_{min}$) with the two exponential models as described above.

RESULTS

In this study, we used data from multielectrode recordings in 3 species: cat motor cortex (cats i and ii with a 96 channel multielectrode array in primary motor cortex, hindlimb area), cat parietal cortex (cat iii, 8 bipolar electrodes), monkey motor cortex (three monkeys with a 64 or 96 recordings from 96 channel multielectrode arrays in motor and/or premotor cortex), and humans (2 patients with a 96 multielectrode array in middle temporal gyrus). In the following, we briefly address definition of avalanche, then describe the results of power-law analyses on spike avalanche, state-dependence, regional differences, and polarity-dependence of LFP maxima avalanche. At the end, we briefly discuss alternative fits to the data.

AVALANCHE DEFINITION

Figure 1 illustrates the definition of avalanche for discrete (spike) and continuous (LFP) data, as they are used in this study. For both spikes and LFP, we used bins of 1–15 ms (in 2 ms steps) for defining the quiescent vs. active periods. Avalanches are defined by contiguous bins of non-zero activity, separated by periods of quiescence (empty bins). The size of the avalanche is defined as the sum of all activities (spikes or LFP peaks) within that active period. Thus, the avalanches depend on the bin size (as illustrated in **Figure 1A** for spikes). For LFPs, we first discretized the continuous data based on its local maxima. Both positive and negative maxima were examined in our study. For each polarity, 17 levels of thresholds were chosen (see Methods for details). After discretization, the obtained matrix (**Figure 1B**) was used for the same binning and avalanche definition as used for spike series.

POWER-LAW FIT

It has been shown that that CDF provides a better measure than PDF as it avoids erroneous measures at the far end of the distribution tail of probability curve (Newman, 2005; Clauset et al., 2009). It is also necessary to exclude the values below the valid lower bound, or else the calculated coefficient could be highly biased (Clauset et al., 2009). In each of the following estimates of power-law distribution, based on the methods described previously, we adapted the following steps on analyzing the CDF of avalanches: Values above a given X_{min} are used in a maximum likelihood estimate (MLE) of the exponent α. For each CDF, the proper lower bound of X_{min} is selected using a KS test. We also used 1000 semi-parametric repetitions of the fitting procedure for obtaining estimates of uncertainty and goodness of fit.

AVALANCHE ANALYSIS FROM SPIKES

Next, we studied whether the spike avalanches follow power-law distributions.

Avalanche analysis in wakefulness

We first studied avalanche dynamics in awake resting recordings from cats and humans. As depicted in **Figure 2**, neither of these species, showed a dominant power-law behavior in their spike avalanche size distribution. The average scaling exponent of awake recordings for the decades that could be considered to follow power-law (i.e., $>X_{min}$), was to high to be related to SOC systems (see **Tables 1** and **2**; **Figures 2i,ii,iii**). These values not only are distant from those of $1/f$ noise, but also only apply to partial parts of the CDF (cumulative distribution function) of avalanche sizes. These lack of clear power-law characteristics is shown with X_{min} lower boundary (green dotted lines in **Figure 2**). Only values above X_{min} could "statistically" follow a power-law regime and as mentioned, even in those cases, the exponent values were too high to be considered a signature of SOC systems. It is important to note that the CDF representation is cumulative, and thus the left tail is not excluded from the data but its influence is shifted to the right (see details in Clauset et al., 2009; see also Methods).

Interestingly, representing the size distributions in log-linear scale revealed a scaling very close to linear for all species (**Figure 3**), indicating that avalanches defined from spikes scale close to an exponential, as would be predicted by a Poisson type stochastic process. This conclusion was also reached previously by analyzing units and LFP recordings in cats (Bedard et al., 2006). Also, as can be seen in the inset of **Figure 2A**, the same analyses done on the awake recording from the parietal cortex (albeit spatially sampled at only 8 electrodes) shows similar scaling behavior.

In addition to wake resting recordings, we also considered recordings made while monkeys engaged in cognitive motor tasks. Similar to awake resting recordings in cat and man, the lower bound was variable between different binning sizes, thus excluding parts of the "invalid" initial avalanche sizes, which are usually used as evidence of existence of power-law (Beggs and Plenz, 2003; Petermann et al., 2009; Klaus et al., 2011). The inclusion of these initial parts may cause errors, and were removed here; however, their cumulative effects are still present in the tested regimen above X_{min} of the analyzed "cumulative distribution function" (Goldstein et al., 2004; Newman, 2005; Bauke, 2007; Clauset et al., 2009). Above the lower bound value, all the CDF curves showed significant high exponent values. Interestingly, the MI (in both monkeys A and B) had similar mean to PMd (**Table 1**; **Figures 2D–F**), suggesting similar dynamics in the two areas.

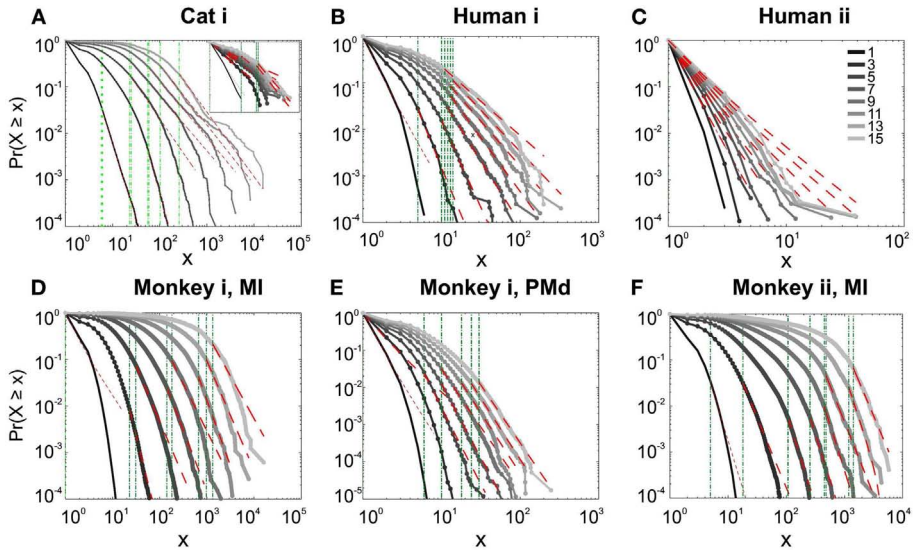

FIGURE 2 | Avalanche analysis on spiking activity during wakefulness. In idle awake **(A)**. Cat i (96 electrode array) and Cat iii (inset, 8 electrode array). **(B)** Human i (96 electrode array). **(C)** Human ii (96 electrode array). Different line colors refer to different bin sizes as shown in the legend. The lower bound (X_{min}, shown in green dotted line), shows that the CDF of avalanche size, only partially, may follow power-law distribution. Even in such cases, the exponents had very high values, well above the criticality regime that is hypothesized for $1/f$ noise. **(D–F)** Show the same type of curves for monkeys engaged in cognitive motor task (96 electrode array; augmented with a 64 electrode array). Same pattern is observed; it also seems MI has slightly higher values than PMd in the plausible power-law regime. For the mean/STD exponent values, see **Tables 1** and **2**.

Table 1 | Summary spike avalanche.

Species	Loc	State	CDF exponent	Pval	gof
Monkey i	MI	Awake	3.4413 ± 0.7616	0.0419 ± 0.1152	0.0442 ± 0.0216
Monkey i	Pmd	Awake	4.1660 ± 0.6590	0.1130 ± 0.2140	0.0180 ± 0.0050
Monkey ii	MI	Awake	4.6250 ± 0.4730	0.4550 ± 0.3600	0.0330 ± 0.0120
Monkey iii	MI	SWS	4.5560 ± 0.7980	0.0030 ± 0.0100	0.0220 ± 0.0080
Monkey iii	Pmd	SWS	3.7760 ± 0.8660	0 ± 0	0.0430 ± 0.0170
Cat ii	MI	Awake	2.8412 ± 1.2184	0.3056 ± 0.3844	0.0599 ± 0.0368
Cat iii	Parietal	Awake	3.1410 ± 0.8720	0.2010 ± 0.3680	0.0270 ± 0.0180
Cat iii	Parietal	SWS	4.2110 ± 0.7930	0.3290 ± 0.3620	0.0350 ± 0.0140
Cat iii	Parietal	REM 1	3.3240 ± 0.8150	0.2990 ± 0.2170	0.0290 ± 0.0110
Cat iii	Parietal	REM 2	3.4050 ± 0.8250	0.4250 ± 0.4470	0.0230 ± 0.0140
Human i	Temporal	Awake	3.5490 ± 0.8790	0.3870 ± 0.3650	0.0210 ± 0.0080
Human i	Temporal	SWS 1	3.6340 ± 0.6410	0.3790 ± 0.3150	0.0250 ± 0.0100
Human i	Temporal	SWS 2	3.2550 ± 0.5770	0.1710 ± 0.2670	0.0330 ± 0.0150
Human i	Temporal	REM 1	3.3740 ± 0.8560	0.0930 ± 0.1720	0.0300 ± 0.0090
Human i	Temporal	REM 2	3.6430 ± 0.5540	0.0960 ± 0.1950	0.0320 ± 0.0170
Human i	Temporal	Awake	3.9200 ± 0.7970	0.0080 ± 0.0230	0.0090 ± 0.0070
Human i	Temporal	SWS	3.8950 ± 0.7630	0.0070 ± 0.0140	0.0100 ± 0.0070

Cross species summary of spike avalanche.

Avalanche analysis during natural sleep

It has been claimed that wakefulness may not be the best state to display SOC, and that avalanches may be more naturally related to brain states with oscillations, and slow-wave oscillations in particular (Hahn et al., 2011). In contrast to this, a previous study in cat found that like wakefulness, slow-wave sleep (SWS) did not display power-law scaling as defined from spike avalanches (Bedard et al., 2006), but this latter study suffered from a limited spatial sampling. To further investigate the issue, we have examined SWS and Rapid Eye Movement (REM) sleep periods with more dense sampling of spike activity. **Figures 4** and **5**, show the analyses for cat, human i and ii as well as monkey iii (MI and PMd) for SWS and REM periods. In none of these cases we, see clear sign of power-law scaling. In all cases (except human ii), the

variability of lower bound between different bin sizes is robust. All the curves represent "partiality of power-law" with high exponent values. During SWS, cat, human subjects, and monkey iii (MI and PMd) all manifested either lack of significant power-law scaling, or had such higher exponent values that makes it highly unlikely for power-law to be the generating process of spike dynamics (**Table 1**). Similarly, in REM periods, there was no evidence for power-law scaling in human i's first and second REM episodes. Together, with Cat REMs' high exponents values, power-law scaling appears to be an unlikely candidate to describe the statistics of neural firing (**Table 1**). Taken together, these various tests all based on proper statistical inferences, show that spike avalanches do not follow power-law scaling, for any brain state or sampling density.

Detailed numerical values for spike avalanche CDF exponents and their goodness of fit are provided in **Tables 1** and **2**.

Table 2 | Detailed awake spike avalanche.

Loc	Bin size (ms)	CDF exponent	Pval	gof
MI	1	2.5	0	0.036
MI	3	5	0.008	0.020
MI	5	3.36	0	0.029
MI	7	3.63	0	0.039
MI	9	3.03	0	0.047
MI	11	3.83	0.327	0.034
MI	13	3.35	0	0.060
MI	15	2.83	0	0.089
PMd	1	4.1	0	0.006
PMd	3	2.81	0	0.021
PMd	5	5	0	0.018
PMd	7	4.85	0.061	0.017
PMd	9	4.03	0	0.022
PMd	11	4.21	0.018	0.024
PMd	13	4.25	0.216	0.019
PMd	15	4.08	0.61	0.017

Monkey i detailed table.

AVALANCHE DYNAMICS FROM LOCAL FIELD POTENTIALS

Next, we investigated the occurrence of avalanche type of dynamics from the local field potentials, which were simultaneously recorded with unit activity, in all datasets.

Relation between LFP peaks and spiking activity

Calculation of neuronal avalanches from LFP data is based on the assumption that statistically speaking, in comparison with the positive LFPs (pLFP), the negative LFP (nLFP) peaks are more strongly related to neuronal activity (e.g., see Destexhe et al., 1999 and references therein). Indeed, the 8-electrode cat LFP data analyzed here show such a relation (Destexhe et al., 1999; Touboul and Destexhe, 2010). To further test this relation, we also examined the simultaneous LFP and unit recordings in the ensemble recordings in cat, man, and monkey. We used a wave-triggered-average (WTA) procedure, where the ensemble of nLFPs were used to epoch the ensemble spike activity. Averaging across these WTAs across different thresholds, show that there is indeed a weak relationship between nLFP and spiking (**Figure 6A**). However, repeating the

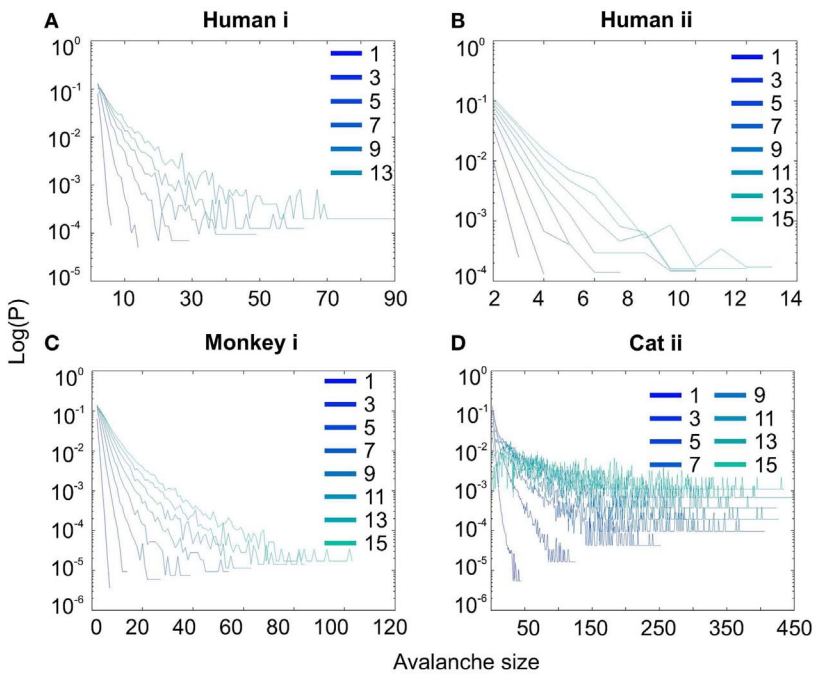

FIGURE 3 | Spike avalanche distributions in log-linear representation. (A–D) Show results for different subjects. Different line colors refer to different bin sizes as shown in the legend. An exponential process has a linear trend in log-linear scale. Spike avalanches for all coarse graining levels, showed a linear trend. Please notice that bin sizes 11 and 15 are not shown because for the clarity in the line plot, but showed similar linear trend in this scale (not shown).

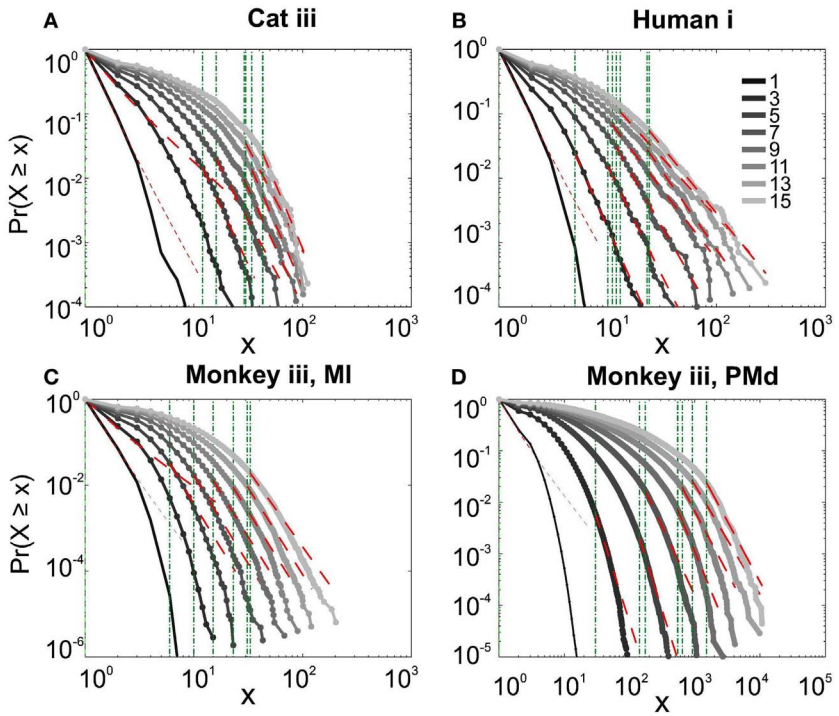

FIGURE 4 | Avalanche analysis of spiking activity during slow-wave sleep. (A) Cat iii, **(B)** Human i, **(C)** monkey iii MI, and **(D)** monkey iii PMd. Different line colors refer to different bin sizes as shown in the legend. In parallel to awake dynamics (**Figure 2**), there is no sign of criticality, the curves follow different partial power-law with high exponents and variable lower bound values. The avalanche dynamics do not show a state-dependent trend. For the mean/STD exponent values, see **Table 1**.

same procedure for positive LFP (LFP) peaks, did not display any relation (**Figure 6B**), in agreement with the same analysis in cats (Touboul and Destexhe, 2010). Through four different types of control and randomization, we show that the relation between nLFP and spike is robust and is not attributable to randomness of the spiking events or spurious fluctuations in the LFPs. For details of these control/randomization, see methods and **Figure 6**. This fundamental difference between nLFP and pLFP peaks provides a very important test to infer if a given power-law observation from LFPs is related to the underlying neuronal activity, as we will, see below.

nLFP avalanches

Similar to previous studies, we investigated the avalanche dynamics from nLFPs. The nLFPs were detected using a fixed threshold, defined as a multiple of the standard deviation (STD) of the LFP signal (see Methods), and several thresholds were tested. In the following, we use "high," "medium" and "low" thresholds, which correspond to 2.25, 1.75, and 1.25 multiples of the standard deviation, respectively. As shown in **Figures 7** and **8**, the distributions defined for avalanches at different bin sizes and thresholds seem to display power-law scaling, both for human and monkey. This result seems to be in agreement with similar analyses done on awake monkey (Petermann et al., 2009). However, plotting the same data as CDF revealed that the scaling as power-law was very narrow (**Figure 9**). While Monkey ii displayed apparent power-law over more than one decade, the other cases from cats and humans, did not display any convincing power-law scaling. For details of nLFP avalanches for an example subject, and its comparison with pLFP avalanches, see **Table 3**. One can also note that in some of the CDFs (and their counterpart PDF), there is a possibility that the distribution can be segmented into two regions each covering certain decades of avalanche size. In such cases, relying on a single scaling exponent to describe the totality of the functional dynamics of the network does not seem adequate. This could be an indication that the space of the distributions is not uniform and the underlying mechanisms could be of metastability nature (Mastromatteo and Marsili, 2011). In such scenario, interaction with the external world could push the system from the "currently most stable state" to a new "most stable state." Such constant changes may lead to the formation of non-uniform distribution of the neural events at different temporal scales. Therefore it is essential to emphasize that, in some cases, one scaling exponent may not be sufficient to describe the complexity of the spiking or oscillations.

pLFP avalanches

Next, we investigated the avalanche dynamics of positive LFP peaks, which, as we have seen above, is not statistically related to firing activity (**Figure 6**). Similar to nLFP peaks, the pLFP avalanches defined for human wakefulness did not display power-law scaling (**Figure 10**). Both nLFP and pLFP had similar CDF of avalanche size across different species and cortices. The example shown in **Figure 10** (awake human) shows that across different thresholds, both nLFP and pLFP had variable lower bounds and high scaling

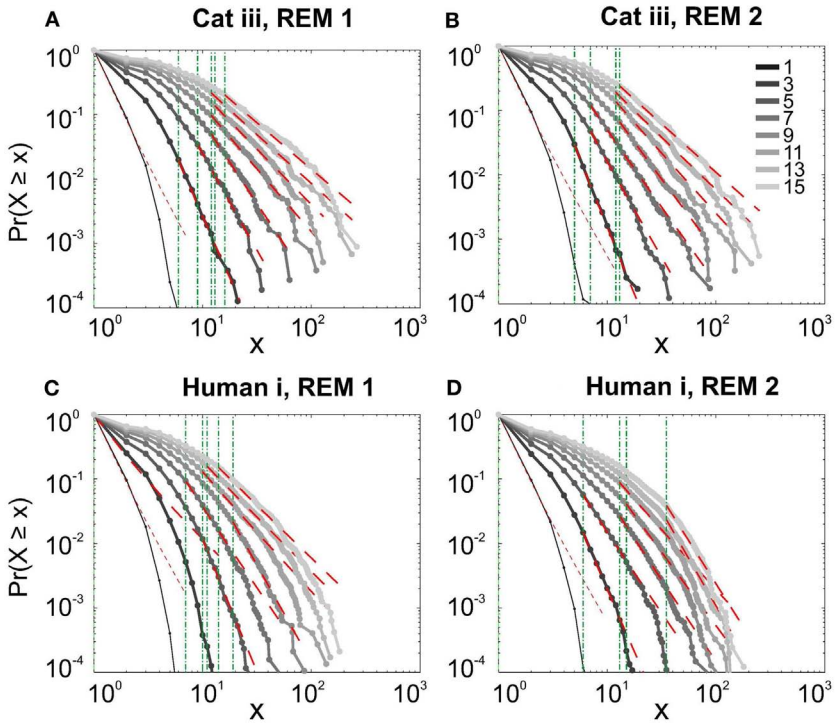

FIGURE 5 | Avalanche analysis of spiking activity during REM sleep. **(A)** Cat iii REM episode 1, **(B)** cat iii REM episode 2, **(C)** human i REM episode 1, **(D)** human i REM episode 2. Different line colors refer to different bin sizes as shown in the legend. Similar to awake and SWS, the lack of criticality, variability through different coarse graining thresholds, and lower bounds is the universal finding. For the mean/STD exponent values, see **Table 1**.

exponents for the region of the data that could statistically be considered for power-law properties. Moreover, the absence of any region with clear linear scaling in the logarithmic coordinates further confirms that there is no power-law scaling in this case. For details, see **Table 3**.

Avalanches in different cortical regions

In the cases that we had simultaneous, dual array multielectrode recordings from PMd and MI, the analyses showed that these two cortical areas do not show signs of criticality but have slight differences in their exponent values for MI and for PMd (**Tables 1** and **2**; **Figure 11**). Such findings show that the fact that these two cortices directly interact with each other, and one acts as input and one as the output of motor processing unit, is reflected in their slightly different CDF features. Thus, two different cortical areas seem to display similar features, although no sign of power-law scaling.

STATISTICAL ANALYSIS OF THE AVALANCHE DISTRIBUTIONS

Goodness of fit

Given data x and given lower cutoff for the power-law behavior X_{min}, we computed the corresponding p-value for the Kolmogorov-Smirnov test, according to the method described in Clauset et al. (2009). See methods for details. The results are given in **Tables 1**, **2**, and **3** ("gof" columns).

Avalanche size boundaries

Imposing lower or upper bounds when fitting avalanche distributions can greatly affect the outcome of the fit (Clauset et al., 2009). In many cases, the analyses have been limited to the lower boundary of avalanche size = 1 and X_{max} of N, where N is the number of channels. Using such bounds improves the fitting of the data by power-law compared to other distributions, as confirmed by KS-statistics (Klaus et al., 2011). The pitfalls of such an approach are two-fold: (a) the lower boundary is set to 1, therefore the avalanches that are below the acceptable lower bound of X_{min} are erroneously fitted with the power-law, thus reducing the reliability of the fit while producing mis-estimated scaling exponents (see Clauset et al., 2009 for details of lower bound selection). (b) X_{max} is set to the maximum active channels, and any return to a given channel is counted in the avalanche, but the maximum allowed avalanche size is limited to N, based on the argument that the large avalanches are infrequent and their inclusion implies misfit. This type of approach, limits the number of avalanches to an extreme degree and introduces a bias. Below we investigate this bias.

Avalanche size distribution and upper boundary limits

Figure 12 tests the effect of enforcing an upper boundary to the avalanche analysis. The red color shows the excluded (saturated) avalanches enforced by limiting the X_{max} to N (number of independent measures), while cyan represents the acceptable avalanches below this upper threshold. This figure shows that setting the X_{max} to a cutoff value of N, produces variable biases based on the bin size. Importantly, in simultaneously recorded regions, the majority of avalanches will be included in one case (like in PMd as shown in **Figure 12A**) but not in the other (like MI, as

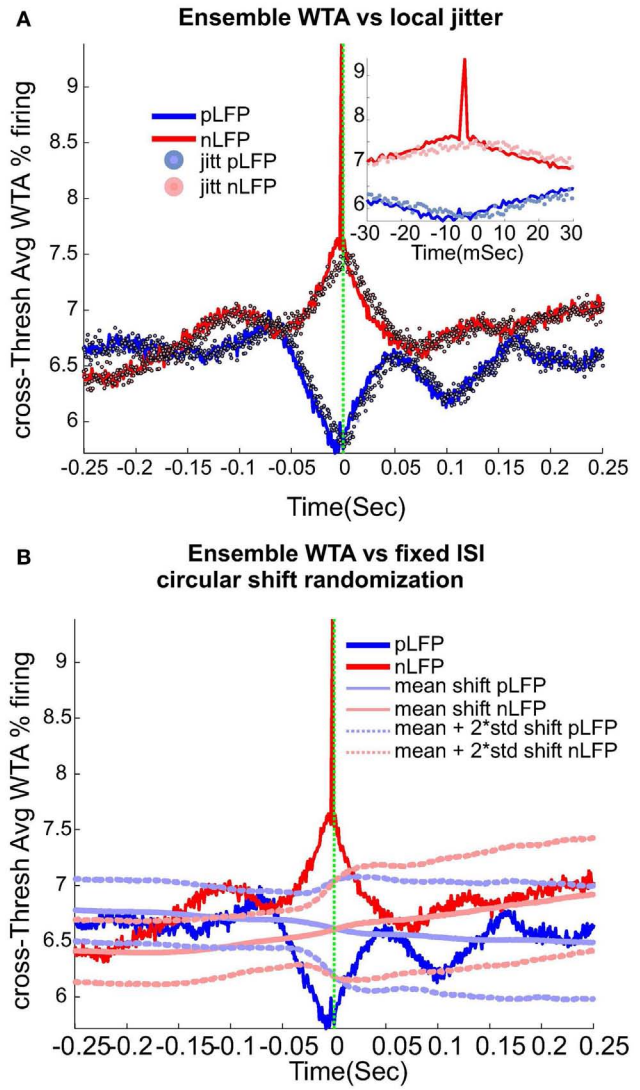

FIGURE 6 | Relation between unit firing and LFP peaks in wakefulness. nLFP (red) and pLFP(blue)-based wave-triggered-average (WTA) of percentage unit activity, showing that the negative peaks have closer association with an increase of neuronal firing. **(A)** Tightly regulated local jitter of nLFP peaks destroys the large nLFP peak. Inset shows the zoom around 0. **(B)** Preserving the internal structure of aggregate spike train and ensemble LFP peaks, but destroying the relation between the two leads to the disappearance of the nLFP peak. See text for details of randomization and controls. The WTA traces in this figure are from Human i, (based on 183127, 98520, and 47451 nLFP and 158737, 79225, and 36020 pLFP peaks for low, medium, and high threshold respectively.)

depicted in **Figure 12B**). Such discrepancy emphasizes that setting a cutoff will necessarily introduce a bias and causes variable results from region to region and from bin size to bin size.

Comparison of exponential and power-law fit: Model Mis-specification and lower boundary problem

It has been argued whether neuronal avalanches are better fitted by an exponential or power-law distribution. Here we tested two aspects, exponential vs. power-law comparison, as well as the effect of setting a lower boundary to the fit. It has been shown that defining a proper lower boundary improves the maximum likelihood that the distribution could be fit by a power-law (Clauset et al., 2009). In agreement with this, Klaus et al. (2011) used a lower boundary of 1 and showed that using KS-statistics, the power-law indeed provides a better fit to the data in comparison to exponential distribution. Here, we systematically tested whether such practice would return erroneous results in avalanche analysis. The results shown in **Figures 13A,B**, are from cat spikes data. For each bin size, we first defined the optimal lower boundary after Clauset et al., 2009; see Methods), called X_{min}. We started with a lower boundary set to 1, and reduced the distribution of avalanche data gradually up to X_{min}. For each newly produced set, we calculated the empirical CDF (ECDF) as well as the provisional fitted probability's CDF (based on direct maximum likelihood) for both exponential as well as power-law. The results for a sample bin size are shown in **Figure 13A**. Power-law at the lower boundary of 1 provides a bad fit. However, overall, power-law outperforms the exponential fit, specially after limiting the range of the data by increasing the lower boundary. The best power-law fit is obtained when the lower boundary approaches X_{min}.

This finding matches the results of the KS test (based on Clauset et al., 2009) as we report in this manuscript. However, from our analyses, we know that when we reach the best power-law fit, the estimated scaling exponents are too high for any known natural system to follow a self-organized criticality regime. Therefore, we have a situation where either one gets unreliable but desired scaling exponent by setting the lower boundary to 1, or one obtains reliable but undesired scaling exponent by setting the lower boundary to $X_{min} > 1$.

Next, we quantified the goodness of fit with a more rigorous approach than the simple KS test. If the parametric CDF is close to the probabilities from the ECDF, then the depicted line should approach the diagonal (1:1) line with minimal drift from it. For quantifying this, we measured the integral of the distance of each point on the p-p curves from the 1:1 diagonal line. This value should be zero in a perfect fit; its non-zero value shows departure from a perfect fit. **Figure 13B** shows the results for all bin sizes. Similar to Klaus et al. (2011), the power-law provides a better fit in comparison to exponential. However, there are two aspects that can not be ignored for this condition to be true: (a) the distance improves only as we tighten the lower bound criteria to be close to X_{min}, but it does not mean that this is a proper fit; (b) there is no rule of thumb for such an improvement; in almost all of the cases, a linear relationship in the normal probability plot distribution of the distance was not found. This shows that power-law provides a better fit than the exponential distribution, but that both fits are not satisfactory. We consider alternative distributions below.

Alternative distributions for avalanche dynamics

Although previously, at the microcircuit scale, some studies have asserted the existence of criticality as a universal characteristic of neural dynamics in both spike and LFP avalanches (Beggs and Plenz, 2003; Ribeiro et al., 2010), other evidence suggest that same behavior can also be observed through stochastic processes (Bedard et al., 2006; Touboul and Destexhe, 2010). In this study,

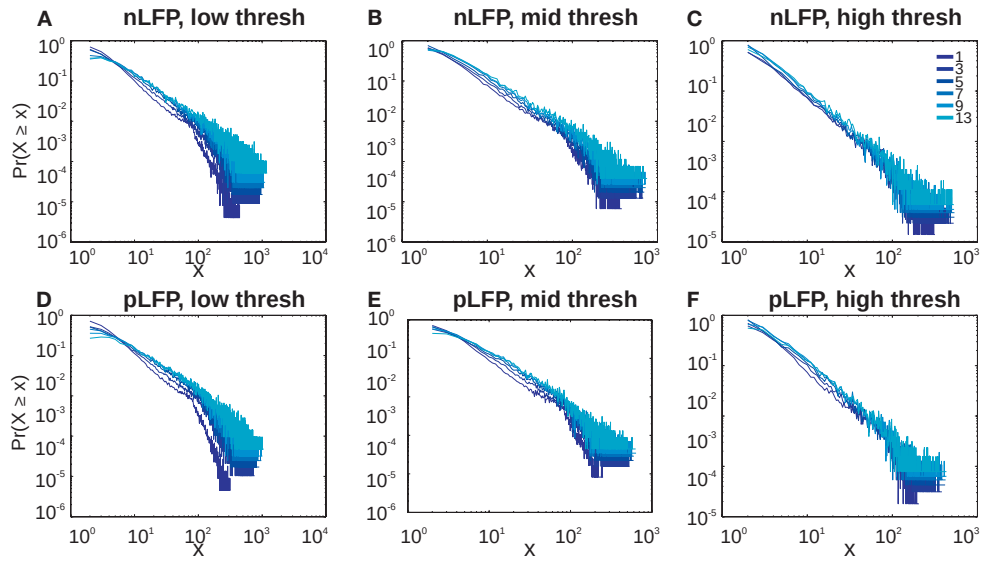

FIGURE 7 | Avalanche analysis in awake monkey LFPs in logarithmic representation. A power-law process has a linear trend in log-log scale. LFP (negative or positive) maxima avalanches for all coarse graining levels, as well as all thresholds, showed a linear trend. Upper row **(A–C)**, shows the nLFP for low, mid, and high thresholds respectively. Lower row **(D–F)**, shows the same for pLFP. Please notice that bin sizes 11 and 15 are not shown because for the clarity in the line plot; however, they too, also showed a very clear linear trend in this scale. Such trend is necessary but not sufficient for a process to be power-law. See text and **Figure 9**.

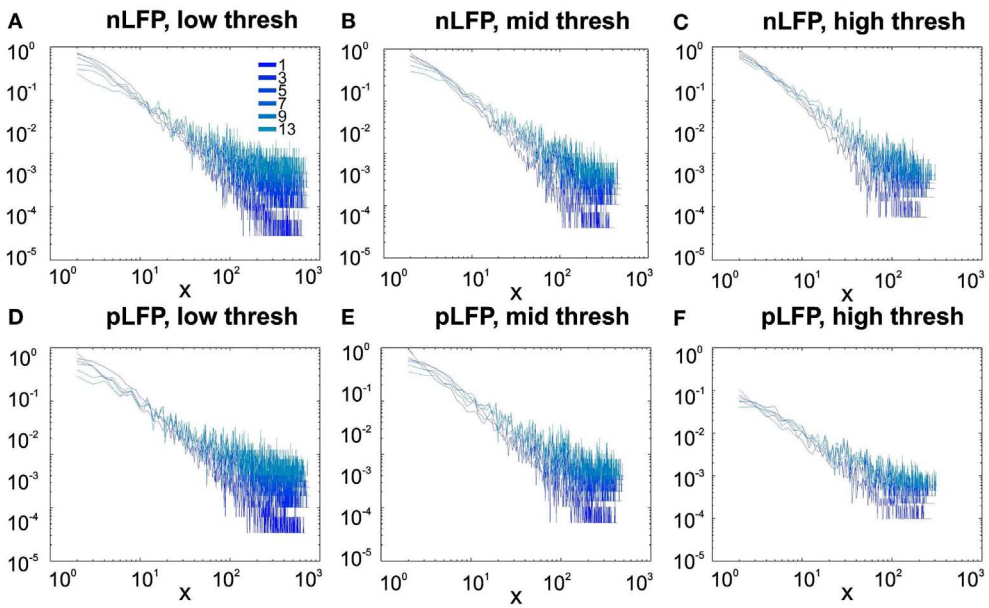

FIGURE 8 | Avalanche analysis in awake human LFP in logarithmic representation. A power-law process has a linear trend in log-log scale. LFP (negative or positive) maxima avalanches for all coarse graining levels, as well as all thresholds, showed a linear trend. Upper row **(A–C)**, shows the nLFP for low, mid, and high thresholds respectively. Lower row **(D–F)**, shows the same for pLFP. Please notice that bin sizes 11 and 15 are not shown because for the clarity in the line plot; however, they too, also showed a very clear linear trend in this scale. Such trend is necessary but not sufficient for a process to be power-law. See text and **Figure 9**.

after rigorous testing, we showed that the avalanches do not follow power-law as a universal feature. Thus we also tested whether an alternative probability distribution could provide a better estimate for the experimental observations.

We first tested a simple exponential fitting of the spike avalanches, by fitting straight lines in a log-linear plot. As seen from **Figure 13C**, a linear fit ("exp1") can only fit part of the data, as the initial points (for small size) do not scale linearly. In

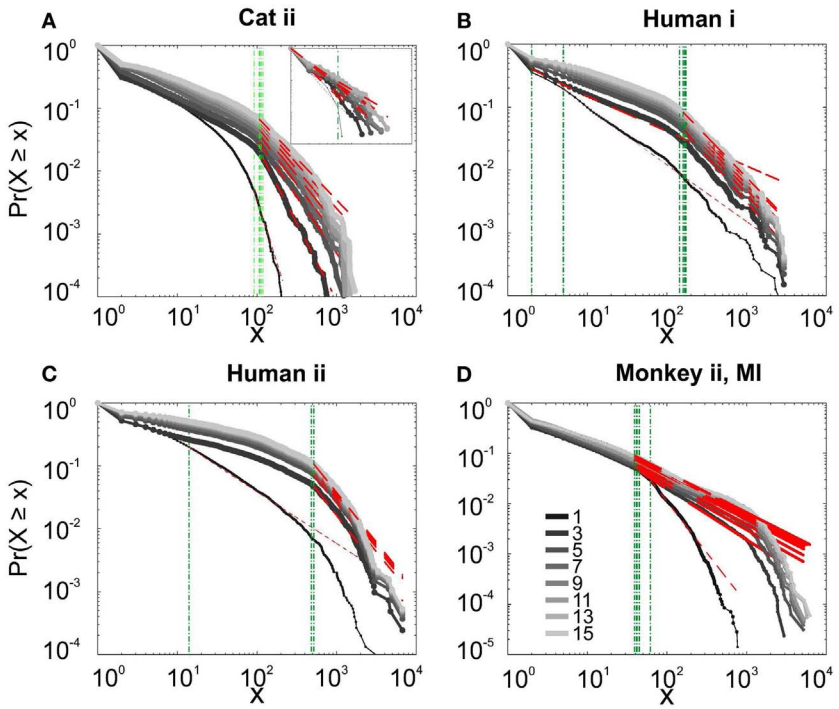

FIGURE 9 | Avalanche analysis based on LFP negative peaks in wakefulness. (A) Cat ii (96 electrode array) and Cat iii (inset, 8 electrode array), **(B)** Human i, **(C)** Human ii, **(D)** Monkey ii MI. In all cases, different binnings lead to variable lower bound and scaling exponents. Lack of linear trend in CDF shows that the observed linear trend in log-log scale, as shown in **Figures 7** and **8**, are not sufficient for showing that avalanche dynamics are power-law processes. For the mean/STD exponent values, see **Table 3**.

detection of the lower bound of linearity, i.e. (X_{min}), the robust bi-square method is more stringent than simple least square fits and leaves behind more data points for exponential fitting (see different lines in **Figure 13C**; errors based on bi-square are plotted in **Figure 13D**; see Methods for details on linearity optimization).

Next, we tested a multiple exponential fitting of the data. The rationale is that two exponential processes may represent differences in two populations of cells, for example excitatory and inhibitory cells. The fit resulting from a "sum of exponential processes" was extremely good in minimum residual and reliable prediction bounds for the data (**Figure 13E**). This "sum of exponential" model ("exp2") gave a very good performance in both full length (dark blue) and reduced above "X_{min}" (red). The "simple exponential" model (exp1) reaches a very good fit only for the reduced set (cyan) but not for the full length of the avalanches (light brown). For comparison of "exp1" and "exp2" on different spike avalanches, with and without "linearity improvement," see **Figure 13F**. Overall, it seems that both exp1 and exp2 exhibit comparably high values of goodness of fit for the reduced sets. However, only the double exponential fit was able to fit the entire dataset.

DISCUSSION

In the present paper, we have analyzed and compared the avalanche dynamics obtained from multielectrode recordings of spikes and LFPs, for three species, cat, monkey, and human. In each case, we used recordings exclusively made in non-anesthetized brain states, including quiet and active wakefulness, SWS (slow-wave sleep), and REM (Rapid eye movement). The primary result of our analysis is that there is no power-law scaling of neuronal firing, in any of the examined recordings, including "desynchronized" EEG states (wakefulness), SWS, and REM sleep. All species consistently showed distributions which approached exponential distributions. This confirms previous findings of the absence of power-law distributions from spikes in cats (Bedard et al., 2006), and extends these findings to monkeys and humans. An obvious criticism to that prior study is that a set of 8 electrodes is too low to properly cover the system, and the absence of power-law may be due to this subsampling. We show here that the same results are obtained when a significantly higher density of recording is used, confirming the absence of power-law.

In contrast, avalanche dynamics built from nLFPs displayed more nuanced results. In some cases, the avalanche size distributions appear to draw a straight line in log-log representations, but the more reliable CDF based tests did not show clear evidence for power-law scaling. Indeed, statistical tests such as the KS test did not give convincing evidence that these data are universally distributed according to a power-law. More importantly, while nLFP are related to firing activity, we showed that a similar behavior was also observed for pLFP peaks. The avalanche analysis from positive peaks displayed similar results as for negative peaks, although positive peaks displayed a weaker statistical relation to firing activity. Using 4 types of control/randomization we provide very robust evidence that the fundamental differences between nLFP and pLFP are not attributable to random behavior of spikes or LFP peaks. Yet still, the discretized thresholded LFPs,

Table 3 | Detailed awake LFP avalanche.

Bin size (ms)	Polarity	Threshold	CDF exponent	Pval	gof
1	Neg	Low	1.71	0	0.019
3	Neg	Low	2.99	0.056	0.051
5	Neg	Low	2.55	0	0.052
7	Neg	Low	2.84	0.074	0.052
9	Neg	Low	2.42	0	0.053
11	Neg	Low	2.37	0	0.059
13	Neg	Low	2.43	0	0.054
15	Neg	Low	2.36	0	0.052
1	Neg	Mid	1.83	0.002	0.015
3	Neg	Mid	2.79	0.425	0.040
5	Neg	Mid	2.84	0.55	0.042
7	Neg	Mid	2.81	0.376	0.048
9	Neg	Mid	2.84	0.345	0.050
11	Neg	Mid	2.84	0.435	0.048
13	Neg	Mid	2.71	0.098	0.058
15	Neg	Mid	2.74	0.204	0.056
1	Neg	High	1.9	0	0.018
3	Neg	High	1.55	0	0.029
5	Neg	High	2.44	0.645	0.036
7	Neg	High	2.43	0.201	0.046
9	Neg	High	2.41	0.672	0.036
11	Neg	High	2.39	0.67	0.035
13	Neg	High	2.3	0.496	0.036
15	Neg	High	2.3	0.36	0.040
1	Pos	Low	1.68	0	0.020
3	Pos	Low	1.37	0	0.073
5	Pos	Low	3.03	0	0.066
7	Pos	Low	4.21	0.762	0.051
9	Pos	Low	3.59	0.585	0.048
11	Pos	Low	3.39	0.43	0.047
13	Pos	Low	2.98	0.079	0.046
15	Pos	Low	2.9	0.032	0.052
1	Pos	Mid	1.74	0	0.018
3	Pos	Mid	3.67	0.128	0.062
5	Pos	Mid	3.79	0.047	0.069
7	Pos	Mid	5	0.827	0.061
9	Pos	Mid	3.78	0.797	0.041
11	Pos	Mid	3.68	0.926	0.036
13	Pos	Mid	3.87	0.797	0.049
15	Pos	Mid	3.51	0.553	0.046
1	Pos	High	1.76	0.009	0.020
3	Pos	High	1.47	0	0.061
5	Pos	High	3.19	0.169	0.067
7	Pos	High	3.17	0.063	0.066
9	Pos	High	3.07	0.251	0.061
11	Pos	High	3.09	0.325	0.059
13	Pos	High	3.18	0.286	0.062
15	Pos	High	2.74	0.033	0.061

Human i detailed Table.

show strikingly similar behavior in their avalanche statistics. These findings render any conclusions about self-organized criticality based on simple power-laws of PDFs as phenomenological.

Together, these results suggest that the power-law behavior observed previously in awake monkey (Petermann et al., 2009; Ribeiro et al., 2010) cannot be reproduced in awake humans' temporal cortex or cat and monkey motor cortex. This conclusion also extends to slow-wave sleep and REM sleep, which we found did not display power-law distributed avalanches, as defined from either spikes or LFPs. In searching for the linear domains in CDF based on the KS test, one can force the scaling exponent to fall within the range of the plausible values (comparable to those observed in known physical phenomena). Doing so, of course, yields more conservative values of scaling, but means that such scaling would be applicable to only a limited range of data. In fact, unless the system has universal scaling, there is always a tradeoff between the range to which a scaling exponent can be extended (i.e., the linear regime in the data) and the proximity of the scaling exponent value to those of a narrow range (in this case, values of the SOC systems are of interest). Our tests, did not force the scaling exponent to be limited to values between 1 and 2, therefore it had a more stringent emphasis on the linearity of more decades of the avalanche sizes. In some cases where the data showed statistically significant linearity, the obtained scaling exponents were an order of magnitude higher than what falls in the range of the critical regime of known physical phenomena. Conversely, these observations imply that, a single scaling exponent is not sufficient to explain the complex dynamics of ensemble activity.

A possibility worth exploring is that some form of power-law in LFPs is the result of volume conduction associated with LFPs recorded in high density arrays. When a peak is detected, it is often also present in many different channels. A possibility worth to explore is whether the same event could be volume-conducted across many channels in the array, which may lead to an artificial increase the large-size avalanches. This possibility should be examined by mathematical models of the volume conduction effect.

It must be noted that the evidence for self-organized criticality in neuronal cultures or in slices (Beggs and Plenz, 2003), as well as in anesthetized states (Hahn et al., 2010) is not contradictory with the present findings. The wiring of *in vitro* preparations, as well as the network dynamics in anesthesia, are evidently different than in the intact brain (Steriade, 2001). We find here that there is no evidence for SOC in wakefulness and natural sleep states, and for 3 different species. On the other hand, the report of power-law scaling of nLFPs avalanches in awake monkey (Petermann et al., 2009) seems in contradiction with the present findings. Many possibilities exist to reconcile these observations, such as differences between brain region, recording method, cortical layer, or volume conduction effects. These possibilities should be investigated in future studies. Moreover, in a recent report (Friedman et al., 2012), it has been shown that data from high density recordings (up to 512 electrodes) from from neural culture show elements of universality and that avalanches can be collapsed into a universal scaling function (Papanikolaou et al., 2011). Such findings confirm that brain circuits *in vitro* operate near criticality. Further studies should examine how to reconcile such evidence with the present *in vivo* findings.

Due to the high dimensionality of neural data, it is crucial to separate the features of the inferred models that are induced solely

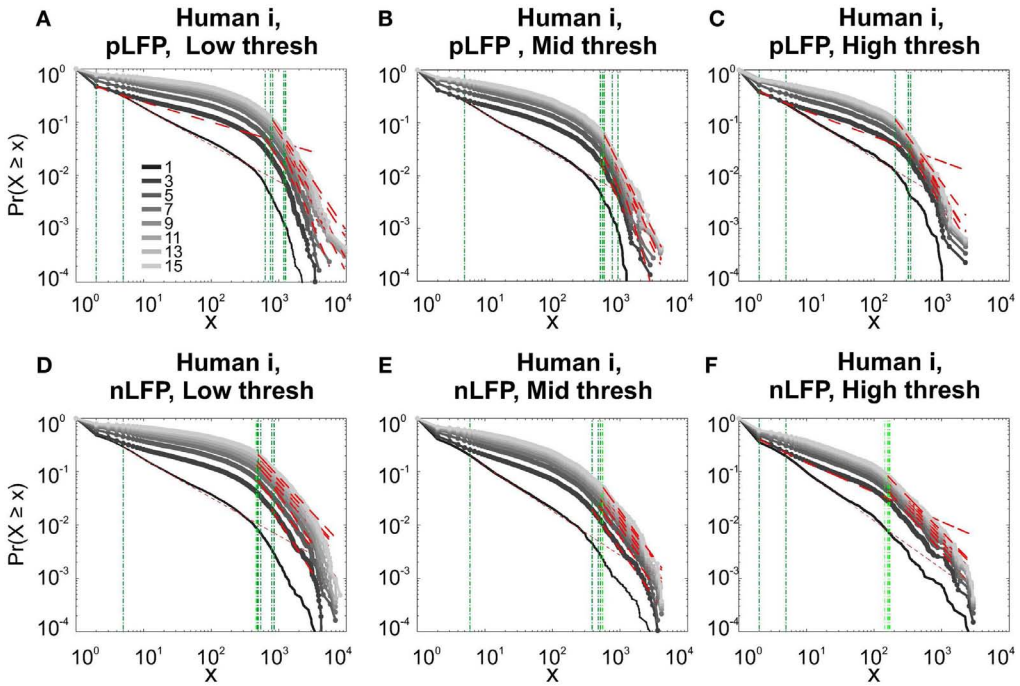

FIGURE 10 | Comparison of Avalanche analysis based on negative and positive peaks. (A–C) Show the CDF for different thresholds of pLFP and **(D–F)** are related to nLFP. LFP (negative or positive) maxima avalanches for all coarse graining levels, as well as all thresholds did not show linear trend in CDF, therefore negate power-law as the generating process. These curves show while nLFP has a closer relation with spiking, the avalanche dynamics of nLFP and pLFP are strikingly similar in their lack of robust criticality when tested with rigorous statistical tests.

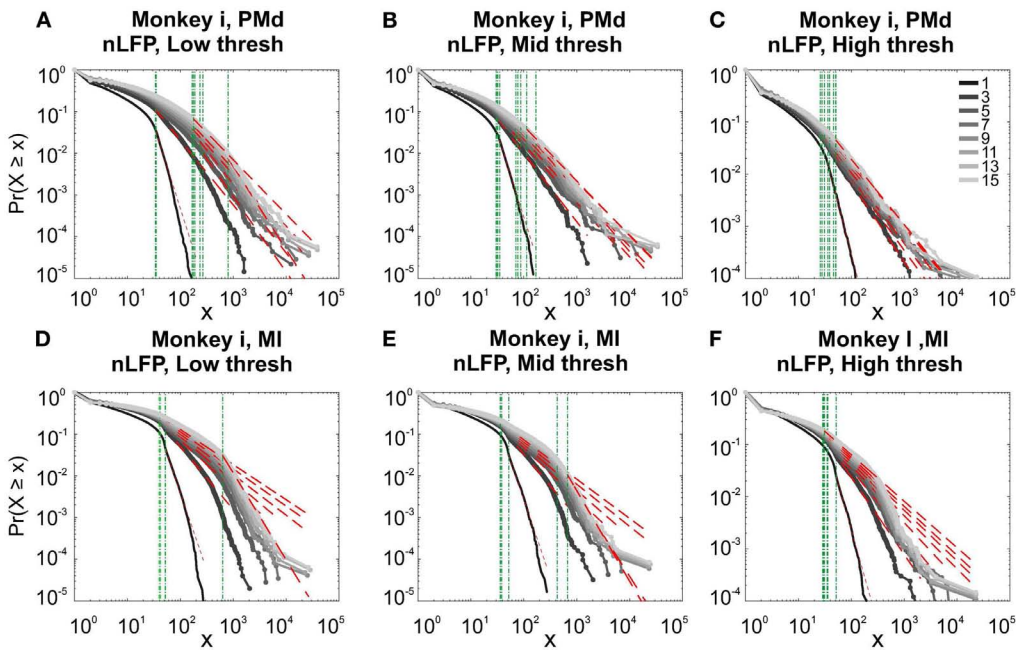

FIGURE 11 | Avalanche analysis in different cortical areas recorded simultaneously. Avalanche dynamics in nLFP shows that the CDF of the input and output units of two interacting cortices have slightly different characteristics but neither follow criticality regime. **(A)** Monkey i, MI, low threshold **(B)** Monkey i, MI, medium threshold, **(C)** Monkey i, MI, high threshold, **(D)** Monkey i, PMd, low threshold **(E)** Monkey i, PMd, medium threshold, **(F)** Monkey i, PMd, high threshold.

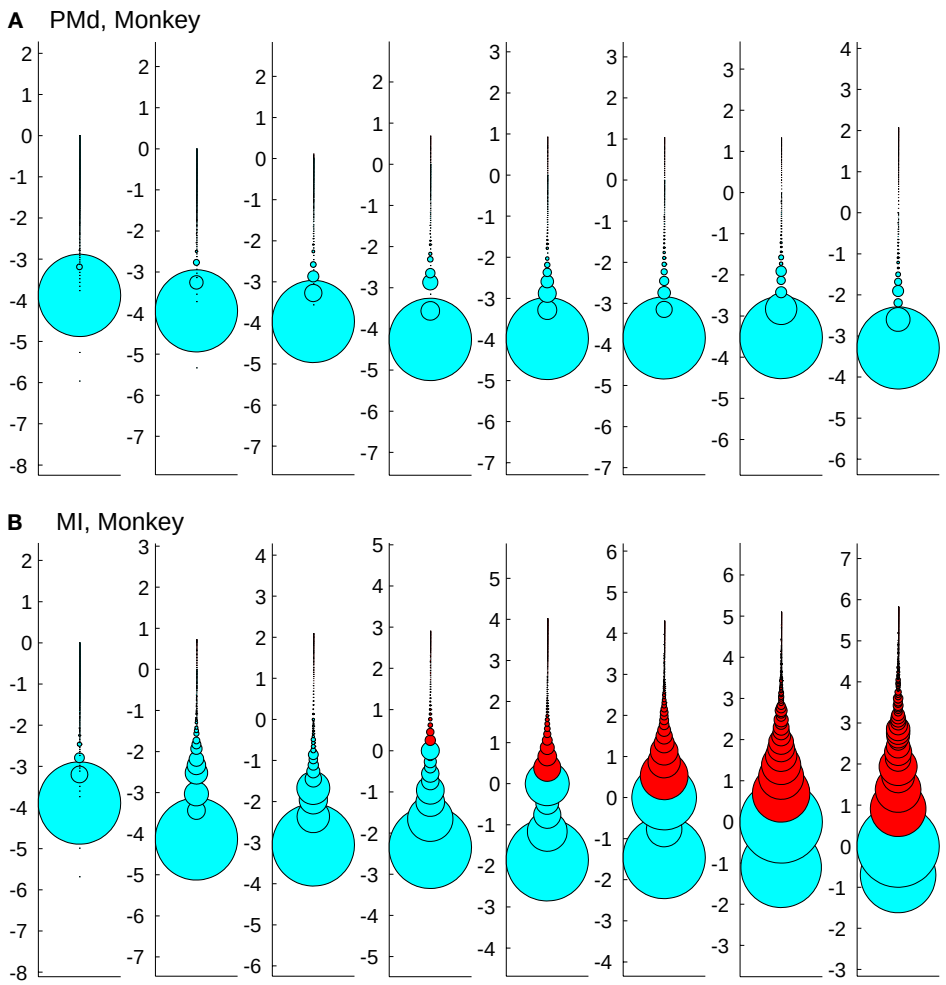

FIGURE 12 | Effects of setting upper boundaries on avalanche size distribution. Each column shows avalanches of a different bin size (increasing from left to right). **(A,B)** Show the results of spike avalanche size distribution of the PMd and MI (respectively). For each bin size, the distributions of different avalanche sizes are shown in circles; the avalanche size increases from the bottom to the top, while the size of each circle represents the ratio to the overall number of avalanches. Red color shows the excluded (saturated) avalanches enforced by limiting the X_{max} to N (number of independent measures; i.e., units in the case of spike avalanches and electrodes in the case of LFP avalanches). Cyan color shows the included avalanches. Y axis is in logarithmic scale for better visualization and the values of Y represent the orders of magnitude of N for proper comparison between different bin sizes (i.e., a given circle at $y = 2$, represents the avalanches that their size $= 2\log(N)$, its diameter shows the number of avalanches that had that size and its color shows whether it is included or excluded according to the $X_{max} = N$ rule).

by the inference scheme from those that reflect natural tendencies of the studied system (Mastromatteo and Marsili, 2011). In some cases, one could fit the data with different lines by limiting the range of the decades within which a fit is analyzed. While it is indeed possible, and highly likely, that neural data at this level follow a multi-scale regime, albeit such a property would push the system away from cohesively operating at self-organized criticality because the relation between microscopic interaction of the (neural) elements and collective behavior (of the cortical network) no longer manifests in single valued features, like a single scaling exponent.

Finally, it is important to emphasize that the present results were obtained using statistical tests similar to previous statistical analyses (Newman, 2005; Clauset et al., 2009). In particular, the use of the CDF distribution rather than simple log-log representations of the size distribution is a particularly severe test to identify if a system scales as a power-law. The use of statistical measures such as the Kolmogorov-Smirnov test (**Tables 1**, **2**, and **3**) also constitutes a good quantification of which distribution fits the data, and is largely superior to the least square fit in double logarithmic scale (Clauset et al., 2009). The uncertainty and goodness of fit were estimated by 1000 repetitions of each fitted distribution. We also showed that setting bounds to the fit can introduce biases in favor of power-law fits, as analyzed previously (Clauset et al., 2009). In agreement with this, it was found with bounded fits that power-law provides a better match to data compared to exponential distributions (Klaus et al., 2011). Our analysis shows that neither power-law nor exponential distributions provide acceptable

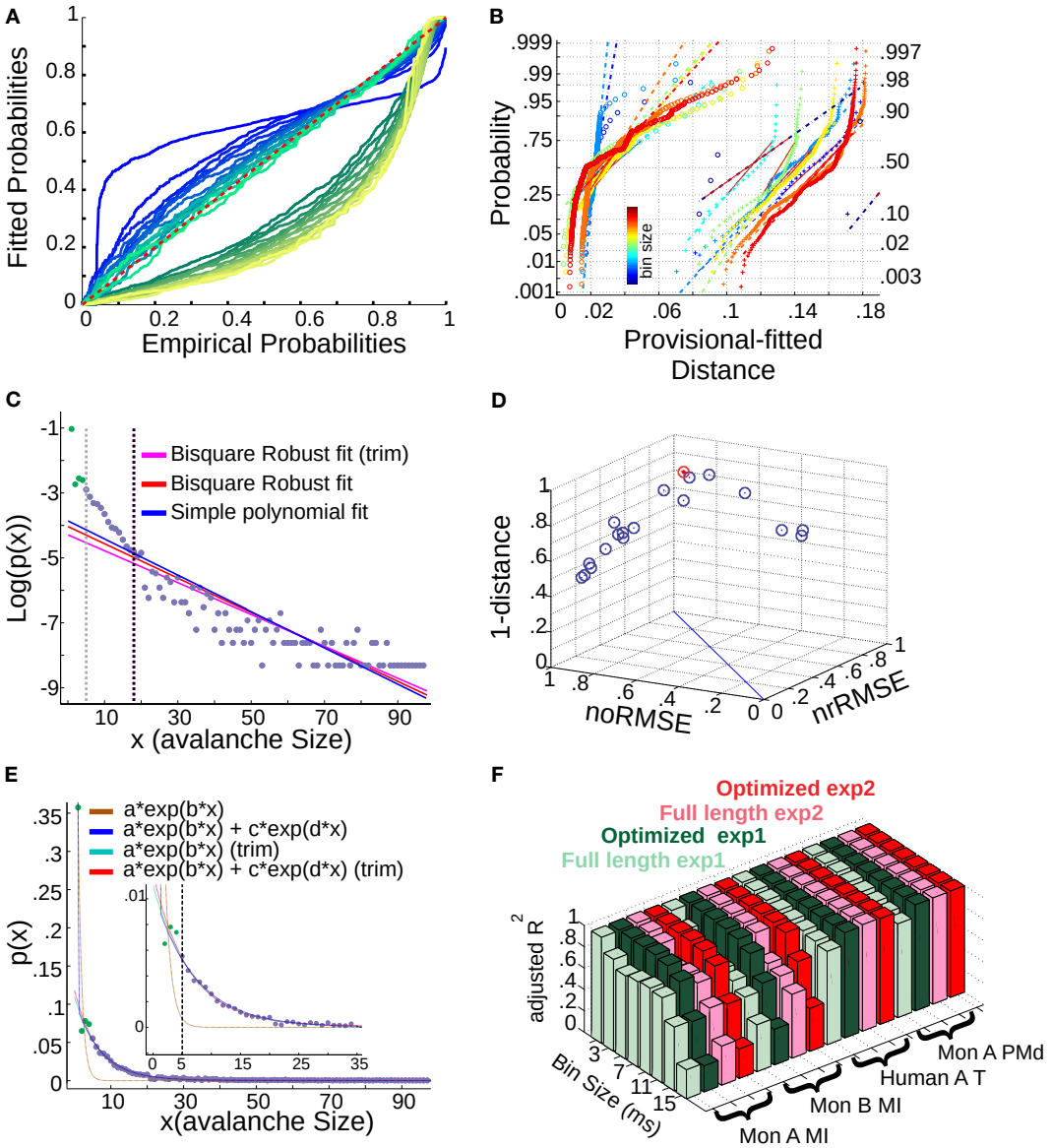

FIGURE 13 | (A,B) Fits comparison and lower boundary. **(C–F)** Alternative fits for avalanche size distributions. **(A)** Probability-Probability plot (ECDF vs. provisional CDF) for a sample bin size (cat i spike avalanche). Green colors are p-p plot for ECDF vs. exponential, and blue colors are for p-p plot for ECDF vs. power-law. In each color family, as the lower boundary is increased (from 1 to X_{min}), the color saturation fades; i.e., darkest color shows lower boundary of 1 and the lightest shows lower boundary of X_{min} (where X_{min} is based on the Clauset method for fitting power-law to empirical data). **(B)** Integral of p-p distance to the 1:1 diagonal (perfect match of the parametric CDF to ECDF). The colors (blue to red) are related to bin sizes (from smallest to biggest). Cross signs represents exponential distance and circles represents power-law distance to the ECDF. **(C)** Simple exponential fitting of spike avalanche data. The data points (purple and green) are plotted in a log-linear representation, together with a simple polynomial fit (blue), a robust fit calculated on the full length data (red) and a robust fit on the reduced data (magenta). The two vertical lines indicate the lower bound of the region of linearity, i.e., "X_{min}," calculated based on the simple polynomial fit (black) and the bi-square method (gray). **(D)** Comparison of the goodness of fit of different exponential fits to different reductions of the same dataset. The 3 coordinates are "normalized overall improvement of RMSE" (noRMSE), "normalized relative improvement of RMSE" (nrRMSE) and distance of a point from the diagonal in (noRMSE,nrRMSE) plane. Each point in this 3D space, is the result of a bi-square robust fit after elimination of the first i elements of the data (best fit in red). **(E)** Bi-exponential fitting of the same data. The "sum of exponential" model (exp2) gave a very good performance in both full length (dark blue) and reduced above "X_{min}" (red). The "simple exponential" model (exp1) reaches a very good fit only for the reduced set (cyan) but not for the full length of the avalanches (light brown). **(F)** Effects of linearity improvement on exponential fits. Each set of four colors refer to the spike avalanche of Monkey i (MI), Monkey ii (MI), Human A(Temporal), and Monkey i (PMd). In each set, green colors refer to the simple exponential family (exp1) and the red colors depict the sum of exponentials (exp2). Light green and light red, refer to the calculated $\bar{R}^2$ on full length avalanche sizes, while dark green and red show the average $\bar{R}^2$ for the dataset ranging from $N-1$ to $N-X_{min}$ where the optimized length X_{min} was 5 [see **(C,D)**]. **(C–E)** Were obtained from 15 ms bin avalanches from human i awake spikes.

fits to the datasets analyzed here. Multi-exponential fits suggest that bi-exponential processes provide a particularly good fit to the distributions, which suggests that the underlying neuronal dynamics is most compatible with two exponential processes, which could be for example excitation and inhibition, both scaling as exponential distributions. Such a possibility should be tested by further studies, and seem in agreement with the complementary excitatory and inhibitory dynamics found in the awake and sleeping brain (Peyrache et al., 2012).

ACKNOWLEDGMENTS

Research supported by Centre National de la Recherche Scientifique (CNRS, France), Agence Nationale de la Recherche (ANR, France), European Community Future and Emerging Technologies program (BRAINSCALES grant FP7-269921), the National Institutes of Health (NIH grants 5R01NS062092, R01 EB009282), and DARPA (BAA05-26, Revolutionizing Prosthetics). Nima Dehghani is supported by a fellowship from Ecole de Neurosciences de Paris (ENP).

REFERENCES

Bak, P. (1996). *How Nature Works.* New York: Springer-Verlag.

Bak, P., and Paczuski, M. (1995). Complexity, contingency, and criticality. *Proc. Natl. Acad. Sci. U.S.A.* 92, 6689–6696.

Bak, P., Tang, C., and Wiesenfeld, K. (1987). Self-organized criticality: an explanation of the 1/f noise. *Phys. Rev. Lett.* 59, 381–384.

Bauke, H. (2007). Parameter estimation for power-law tail distributions by maximum likelihood methods. *Eur. Phys. J. B* 58, 167–173.

Bedard, C., Kroger, H., and Destexhe, A. (2006). Does the 1/f frequency-scaling of brain signals reflect self-organized critical states? *Phys. Rev. Lett.* 97, 118102.

Beggs, J. M., and Plenz, D. (2003). Neuronal avalanches in neocortical circuits. *J. Neurosci.* 23, 11167–11177.

Chialvo, D. R. (2010). Emergent complex neural dynamics. *Nat. Phys.* 6, 744–750.

Clauset, A., Shalizi, C. R., and Newman, M. E. J. (2009). Power-law distributions in empirical data. *SIAM Rev.* 51, 661–703.

Destexhe, A., Contreras, D., and Steriade, M. (1999). Spatiotemporal analysis of local field potentials and unit discharges in cat cerebral cortex during natural wake and sleep states. *J. Neurosci.* 19, 4595–4608.

Frette, V., Christensen, K., Malthe-Sørenssen, A., Feder, J., Jøssang, T., and Meakin, P. (1996). Avalanche dynamics in a pile of rice. *Nature* 379, 49–52.

Friedman, N., Ito, S., Brinkman, B., Shimono, M., Lee DeVille, R., Dahmen, K., Beggs, J., and Butler, T. (2012). Universal critical dynamics in high resolution neuronal avalanche data. *Phys. Rev. Lett.* 108, 208102.

Giesinger, T. (2001). Scale invariance in biology: coincidence or footprint of a universal mechanism? *Biol. Rev. Camb. Philos. Soc.* 76, 161–209.

Goldstein, M. L., Morris, S. A., and Yen, G. G. (2004). Problems with fitting to the power-law distribution. *Eur. Phys. J. B* 41, 255–258.

Hahn, G., Monier, C., and Frégnac, Y. (2011). Revisiting power law in vivo as a function of the global brain state, using multiple recordings in anesthetized cat V1. *Abstr. Soc. Neurosci.* 451.10.

Hahn, G., Petermann, T., Havenith, M. N., Yu, S., Singer, W., Plenz, D., and Nikolic, D. (2010). Neuronal avalanches in spontaneous activity in vivo. *J. Neurophysiol.* 104, 3312–3322.

Jensen, H. J. (1998). *Self-Organized Criticality: Emergent Complex Behavior in Physical and Biological Systems.* Cambridge: Cambridge University Press.

Klaus, A., Yu, S., and Plenz, D. (2011). Statistical analyses support power law distributions found in neuronal avalanches. *PLoS ONE* 6, e19779. doi:10.1371/journal.pone.0019779

Malamud, B. D., Morein, G., and Turcotte, D. L. (1998). Forest fires: an example of self-organized critical behaviour. *Science* 281, 1840–1842.

Mastromatteo, I., and Marsili, M. (2011). On the criticality of inferred models. *J. Stat. Mech.* 2011, P10012.

Matsumoto, M., and Nishimura, T. (1998). Mersenne twister: a 623-dimensionally equidistributed uniform pseudo-random number generator. *ACM Trans. Model. Comput. Simul.* 8, 3–30.

Newman, M. E. J. (2005). Power laws, Pareto distributions and Zipf's law. *Contemp. Phys.* 46, 323–351.

Papanikolaou, S., Bohn, P., Sommer, R. L., Durin, R., Zapperi, Z., and Sethna, J. A. (2011). Universality beyond power laws and the average avalanche shape. *Nat. Phys.* 7, 316–320.

Parker, R. A., Davis, T. S., House, P. A., Normann, R. A., and Greger, B. (2011). The functional consequences of chronic, physiologically effective intracortical microstimulation. *Prog. Brain Res.* 194, 145–165.

Petermann, T., Thiagarajan, T. C., Lebedev, M. A., Nicolelis, M. A., Chialvo, D. R., and Plenz, D. (2009). Spontaneous cortical activity in awake monkeys composed of neuronal avalanches. *Proc. Natl. Acad. Sci. U.S.A.* 106, 15921–15926.

Peters, O., and Neelin, D. (2006). Critical phenomena in atmospheric precipitation. *Nat. Phys.* 2, 393–396.

Peyrache, A., Dehghani, N., Eskandar, E. N., Madsen, J. R., Anderson, W. S., Donoghue, J. A., Hochberg, L. R., Halgren, E., Cash, S. S., and Destexhe, A. (2012). Spatiotemporal dynamics of neocortical excitation and inhibition during human sleep. *Proc. Natl. Acad. Sci. U.S.A.* 109, 1731–1736.

Press, W. H., Flannery, B. P., Teukolsky, S. A., and Vetterling, W. (2007a). "Nonlinear models," in *Numerical Recipes: The Art of Scientific Computing,* Chap. 15 (Cambridge: Cambridge University Press), 773–839.

Press, W. H., Flannery, B. P., Teukolsky, S. A., and Vetterling, W. (2007b). "Random Numbers," in *Numerical Recipes: The Art of Scientific Computing,* Chap. 7, 3rd Edn (Cambridge: Cambridge University Press), 340–418.

Reed, W., and Hughes, B. (2002). From gene families and genera to incomes and internet file sizes: why power laws are so common in nature. *Phys. Rev. E* 66, 1–4.

Ribeiro, T., Copelli, M., Caixeta, F., Belchior, H., Chialvo, D. R., Nicolelis, M., and Ribeiro, S. (2010). Spike avalanches exhibit universal dynamics across the sleep-wake cycle. *PLoS ONE* 5, e14129. doi:10.1371/journal.pone.0014129

Steriade, M. (2001). *The Intact and Sliced Brain.* Cambridge: MIT Press.

Touboul, J., and Destexhe, A. (2010). Can power-law scaling and neuronal avalanches arise from stochastic dynamics? *PLoS ONE* 5, e8982. doi:10.1371/journal.pone.0008982

Truccolo, W., Hochberg, L., and Donoghue, J. (2010). Collective dynamics in human and monkey sensorimotor cortex: predicting single neuron spikes. *Nat. Neurosci.* 13, 105–111.

Conflict of Interest Statement: The authors declare that the research was conducted in the absence of any commercial or financial relationships that could be construed as a potential conflict of interest.

Received: 04 February 2012; accepted: 10 July 2012; published online: 03 August 2012.

Citation: Dehghani N, Hatsopoulos NG, Haga ZD, Parker RA, Greger B, Halgren E, Cash SS and Destexhe A (2012) Avalanche analysis from multielectrode ensemble recordings in cat, monkey, and human cerebral cortex during wakefulness and sleep. Front. Physio. ***3****:302. doi: 10.3389/fphys.2012.00302*

This article was submitted to Frontiers in Fractal Physiology, a specialty of Frontiers in Physiology.

frontiers in
PHYSIOLOGY

ORIGINAL RESEARCH ARTICLE
published: 26 September 2012
doi: 10.3389/fphys.2012.00384

Nested synchrony—a novel cross-scale interaction among neuronal oscillations

Simo Monto*

Department of Biomedical Engineering and Computational Science, School of Science, Aalto University, Espoo, Finland

Edited by:
Biyu J. He, NIH, NINDS, USA

Reviewed by:
Manfred G. Kitzbichler, Harvard Medical School, USA
Vadim Nikulin, Charite University Hospital, Germany

****Correspondence:***
Simo Monto, Department of Biomedical Engineering and Computational Science, School of Science, Aalto University, PO Box 12200, FI-00076 AALTO, Espoo, Finland.
e-mail: simo.monto@gmail.com

Neuronal interactions form the basis for our brain function, and oscillations and synchrony are the principal candidates for mediating them in the cortical networks. Phase synchrony, where oscillatory neuronal ensembles directly synchronize their phases, enables precise integration between separated brain regions. However, it is unclear how neuronal interactions are dynamically coordinated in space and over time. Cross-scale effects have been proposed to be responsible for linking levels of processing hierarchy and to regulate neuronal dynamics. Most notably, nested oscillations, where the phase of a neuronal oscillation modulates the amplitude of a faster one, may locally integrate neuronal activities in distinct frequency bands. Yet, hierarchical control of inter-areal synchrony could provide a more comprehensive view to the dynamical structure of oscillatory interdependencies in the human brain. In this study, the notion of nested oscillations is extended to a cross-frequency and inter-areal model of oscillatory interactions. In this model, the phase of a slower oscillation modulates inter-areal synchrony in a higher frequency band. This would allow cross-scale integration of global interactions and, thus, offers a mechanism for binding distributed neuronal activities. We show that inter-areal phase synchrony can be modulated by the phase of a slower neuronal oscillation using magnetoencephalography (MEG). This effect is the most pronounced at frequencies below 35 Hz. Importantly, changes in oscillation amplitudes did not explain the findings. We expect that the novel cross-frequency interaction could offer new ways to understand the flexible but accurate dynamic organization of ongoing neuronal oscillations and synchrony.

Keywords: neuronal oscillations, magnetoencephalography, nested oscillations, oscillation synchrony

INTRODUCTION

Neurons are capable of synchronizing their activity to a collective rhythm. These neuronal oscillations vary in frequency, amplitude, and source topography (Buzsaki and Draguhn, 2004). Theoretical (Singer and Gray, 1995) and experimental (Womelsdorf et al., 2006) work converge on the idea that synchronous neuronal assemblies are central for neuronal communication. Distinct oscillatory assemblies are able to synchronize their activities, and it has been proposed that such coherent oscillations provide temporal windows for efficient communication between distinct brain regions (Fries, 2005). Indeed, cortical oscillations and synchrony have been found to regulate stimulus processing in the neuronal (Cardin et al., 2009) and behavioral (Hamidi et al., 2009) level. Furthermore, it has been shown that such oscillation synchrony is related to neuronal spiking activity (Canolty et al., 2010). Thus, oscillatory neuronal populations and their synchronization play a key role in integrating activities in single cells and in the system level.

In monkey recordings, neuronal rhythms have been shown to provide windows of increased excitability that enhance processing of rhythmic stimuli (Schroeder and Lakatos, 2009). Interestingly, several experiments have found that these oscillations are organized so that the amplitude of a higher frequency oscillation correlates with the phase of a slower rhythm (Lakatos et al., 2005). This cross-frequency model of an oscillatory interaction, phase-modulated amplitude, is called a nested oscillation. Such hierarchical organization of nested rhythmic activities has been observed in a wide frequency range in human intracranial recordings as well, and these data support the functional significance of nested oscillations by showing that experimental conditions modulate the nested relationships (Canolty et al., 2006; He et al., 2010). Also extracranially recorded magnetoencephalography (MEG) data from resting humans has previously revealed a nested interaction between alpha and gamma frequency bands (Osipova et al., 2008).

In theoretical accounts of nested oscillations, the low-frequency oscillation has often been associated with periodic excitability changes, which then affects the amplitude of oscillations in higher frequency bands (Jensen and Colgin, 2007; Lakatos et al., 2008). The increased oscillation amplitude, which is observed in the higher frequency band, is considered to reflect not only increased levels of synaptic or spiking activity, but also enhanced neuronal synchronization. Based on this interpretation, we suggest a novel model of a non-local cross-frequency interaction, where the phase of the slower oscillation regulates inter-areal synchrony in the higher frequency band (**Figure 1**). In the above context this is analogous to the model of nested oscillations, as they both are then related to phase-modulation of neuronal synchrony, albeit in different spatial scales. Our model, which we term nested synchrony, includes both a cross-frequency

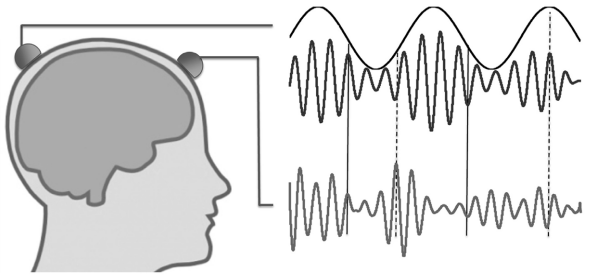

FIGURE 1 | Illustration of nested oscillations and nested synchrony. In nested oscillations, the phase of the slower oscillation modulates the higher-frequency amplitude measured at the same scalp location (two upper traces), but not that measured at a different location (lower trace). In contrast, nested synchrony means that the two faster oscillations become more tightly coupled in certain phases of the slow oscillation (around solid vertical lines) than in other phases (around dashed vertical lines).

interaction and an inter-areal interaction. Thus, it could be one candidate for mediating the complex dynamic relationships of neuronal oscillations across time scales and brain regions. Regulation of synchrony dynamics could be achieved through coordinating inter-areal synchrony in a higher frequency band by possibly meta-stable and scale-free dynamics provided by the lower frequencies. The aim of this study is to demonstrate the presence of nested synchrony in the human brain using MEG data recorded at rest.

METHODS

EXPERIMENT

We recorded MEG (Elekta Neuromag Oy, Finland) data from normal, consent subjects ($N = 4$; age 28–35 years, 1 female) in a silent, magnetically shielded room. The experiment was approved by the Ethical Committee of Hospital District of Helsinki and Uusimaa. The experiment consisted of one session of 20 min, during which the subjects were at rest, eyes closed. The sampling rate was 600 Hz, and the high-pass and low-pass acquisition filters were at 0.03 and 172 Hz. Data was recorded with 306 channels, of which the 204 planar gradiometer channels were used for this study.

PRE-PROCESSING

The data was first subjected to noise reduction by spatial Signal Space Separation (SSS) filtering and temporal projection of noise components by the temporal extension of SSS (Taulu and Simola, 2006) using the MaxFilter software (Elekta Neuromag Oy, Finland). Subsequent analyses were performed with custom-made software running in Matlab (MathWorks Inc, Natick, MA, U.S.A.).

Part of the cardiac artifact was not removed by SSS, and was therefore treated by applying ICA to the data. The component(s) corresponding to heart-related activity were recognized by hand based on their temporal dynamics, and projection in temporal domain was then applied to project them away. The data was then windowed to 4 s epochs, and bad epochs were discarded if peak-to-peak amplitude was larger than 10^{-10} T/m and by visual inspection.

After artifact rejection, data epochs were band-pass filtered to five distinct frequency bands using 6th-order elliptic filters. The pass-bands were 2–4 Hz, 4–8 Hz, 8–17 Hz, 17–34 Hz, and 35–70 Hz. After filtering, the data were downsampled to approximately six times the highest frequency component included in each filter. Each signal was first forward and then backward filtered to eliminate phase distortion.

NESTED SYNCHRONY ANALYSIS

To find out if the MEG data showed nested synchrony between two frequencies, $f_X < f_Y$, the phase locking value (Lachaux et al., 1999) between data from two gradiometer channels, x_i and x_j, at frequency f_Y was computed in 20 bins. The bins were determined by the phase of x_i at frequency f_X, ϕ^i_X, so that each bin included 5% of the samples—thus, the amount of data was uniform across the bins. The continuous phase of the signal x_i in frequency f_X, or x^i_X, was computed with its Hilbert transform ($\mathbf{H}$) as $\phi^i_X = \arg[\mathbf{H}(x^i_X)]$, where $\arg(x)$ is the argument, or phase, of a complex-valued x. Because estimation of PLV (phase-locking value) in short time windows suffers from high variance, we first computed the phase difference time series between channels x_i and x_j at frequency f_Y: $\Delta\phi^{i,j}_Y = \arg[\mathbf{H}(x^i_Y)\mathbf{H}(x^j_Y)^*]$, where * denotes complex conjugate. Then, each phase difference sample was sorted to one of the 20 bins according to the concurrent phase of x_i at frequency f_X, ϕ^i_X. After sorting the phase difference data to phase bins, PLV was computed within each bin as $\mathrm{PLV}^{i,j}_Y = \mathrm{abs}[\Sigma\ \exp(i\Delta\phi^{i,j}_Y)]/N$, where $i = (-1)^{1/2}$ and N is the number of samples in one bin. The result from this procedure is the higher-frequency PLV in the 20 consecutive bins of the lower oscillation phase range (**Figure 2B**). Then, a non-uniform PLV distribution would signify nested synchrony between channels x_i and x_j and between frequencies f_X and f_Y. We characterized the non-uniformity, or modulation, of the PLV distribution by fitting a sinusoidal period $a_{i,j} \times \sin[\{\phi^i_X\} + f_{i,j}] + b_{i,j}$ to the PLV data; here, $a_{i,j}$ is the magnitude of sinusoidal modulation of synchrony between x_i and x_j, $f_{i,j}$ is the phase shift of the sine function, $b_{i,j}$ is the constant term (roughly equal to the mean PLV across all bins), and $\{\phi^i_X\}$ are the centers of the 20 phase bins of ϕ^i_X. The sinusoidal fit was adopted to ensure that possible non-uniformity of the distribution was not due to stochastic fluctuations. In addition, the modulation was expected to be 2π-periodic, at most one peak or trough was expected in the distribution, and the model is simple (two non-trivial parameters, $a_{i,j}$ and $f_{i,j}$). The sine model was found to be acceptable by visual inspection of the data and the degree-of-freedom-adjusted R^2 goodness-of-fit values (see **Figure 2**). This nested synchrony analysis procedure was repeated for all pairs of channels (204 channels) and for frequency pairs that were not adjacent (six pairs). The sampling frequency in nested analysis was roughly six times of the highest frequency component in the higher frequency band data.

Nested amplitude modulation was analyzed in the same way as nested synchrony, except that the amplitude A of the single channel x_i in the higher frequency band f_Y, instead of the phase difference of two channels, was estimated using Hilbert transform, $A^i_Y = \mathrm{abs}[\mathbf{H}(x^i_Y)]$, and averaged in the bins determined by the phase of the lower-frequency oscillation, ϕ^i_X.

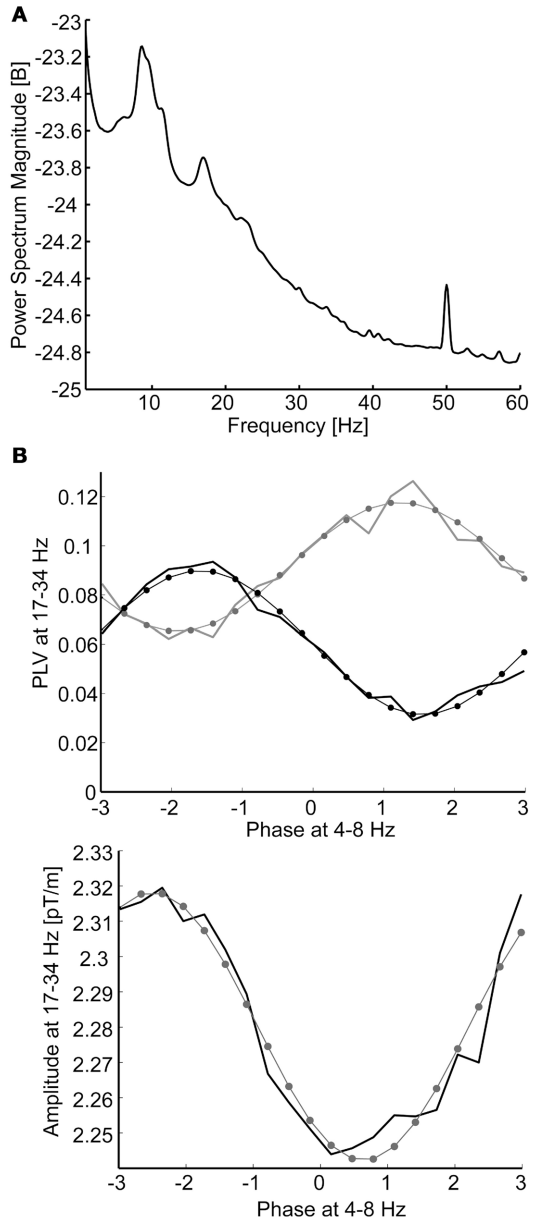

FIGURE 2 | (A) The grand average power spectrum pooled over all gradiometer channels and subjects. Only the 8–17 Hz frequency band coincides with peaks in the spectrum. **(B)** Modulation of beta-band (17–34 Hz) phase synchrony (above) and oscillation amplitude (below) as a function of theta-band (4–8 Hz) phase. Data are sorted to 20 phase bins and modeled with sinusoidal fits to the data (thin lines with dots at bin centers). Data are from a single subject: nested synchrony of MEG channel 190 with channels 16 (black line) and 35 (gray line), illustrating antagonist synchrony modulation, and nested oscillation in channel 190. The adjusted R^2 goodness-of-fits were 0.97 and 0.95 (above) and 0.95 (below).

To ensure that the possible findings of nested synchrony are not due to complicated data processing, similar pre-processing and data analyses were performed for noise data, which were recorded in a magnetically shielded room where no subject was present.

STATISTICAL EVALUATION

The significance of individual sinusoidal fits was checked by estimating the 95% confidence interval for the sinusoidal modulation amplitude, $a_{i,j}$, and inspecting that the confidence interval did not include 0. Significance of nested synchrony was then evaluated by generating 100 sets of surrogate data. These were created by permuting the order of epochs when choosing the phase bins from the lower-frequency data, while keeping the phase difference data itself intact. The real PLV data were then z-transformed (by subtracting the mean and dividing by standard deviation of the surrogate PLV values) to see if it differed significantly from the surrogate data. We used Bonferroni-corrected $\alpha = 0.05$ as the level of significance. The number of tests was $n = 204 \times 203 = 41{,}412$, so corrected level of significance was $\alpha_n = \alpha/n = 1.21 \times 10^{-6}$. The z-score required for a significant nested synchrony was then obtained from the cumulative standard normal distribution at the value 1-α_n, resulting in $z = 4.7$. In the case of nested oscillation, or amplitude modulation, the number of tests is $n = 204$, and the level of significance became $z = 3.5$.

SIMULATIONS OF CROSS-FREQUENCY COUPLING

We simulated two time series to represent recordings of neuronal activity at two distinct channels. The aim of these simulations was to inspect if nested oscillations and nested synchrony can be regulated independently, under varying levels of noise. The recorded signals were simulated with 10,000 samples of white noise, which was then filtered to two distinct frequency bands with a 5-fold frequency difference. The effects from nested interactions were then simulated by making the amplitude (in the case of nested oscillations) or the phase (in the case of nested synchrony) of the faster oscillations correlate with the phase of the slower oscillation. Separate parameters controlled the strength of nested oscillations, nested synchrony, and noise level. We then analyzed the resulting signals for nested oscillations and nested amplitude, like explained above (section "Nested Synchrony Analysis").

RESULTS

PRESENCE OF NESTED OSCILLATIONS IN RESTING-STATE MEG DATA

We first aimed at replicating earlier findings of nested oscillations. We evaluated the presence of cross-frequency amplitude modulations, or nested oscillations, in each gradiometer channel by computing the mean amplitude of a higher frequency oscillation in 20 bins determined by the phase of a lower frequency oscillation, by fitting a sinusoid to those data, and then comparing the amplitude modulation to that found in 100 sets of shuffled surrogate data and empty-room data (see Methods). The mean number of channels with significant nested oscillations ($z > 3.5$; Bonferroni correction with $n = 204$ and $p < 0.05$) per subject and frequency pair was 11 for the real data, whereas it was only 2 for the empty-room data (**Figure 3A**). Nested oscillations were the most prominent between frequency pairs 2–8 Hz, 2–17 Hz, and 4–17 Hz.

PRESENCE OF NESTED SYNCHRONY IN RESTING-STATE MEG DATA

We evaluated cross-frequency modulation of a higher-frequency phase synchrony as a function of the phase of a slower oscillation, or nested synchrony, between all MEG gradiometer channel

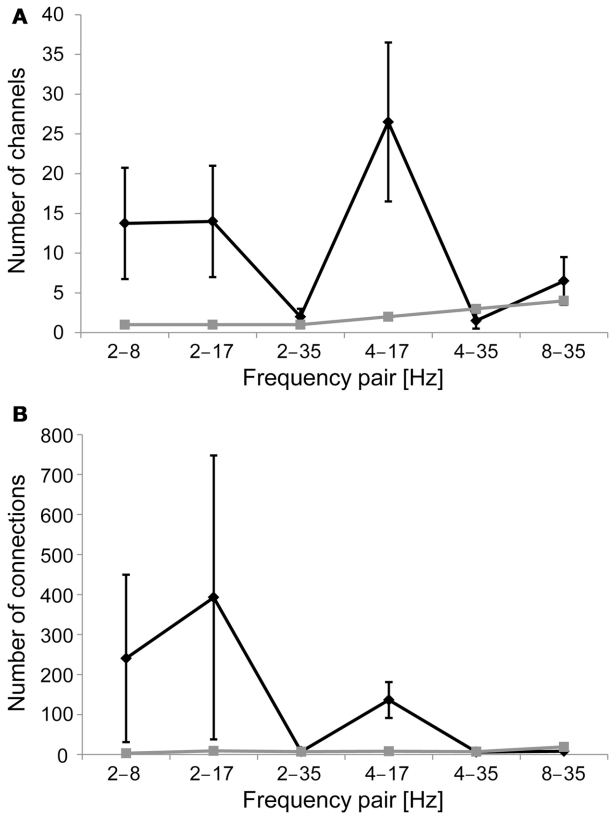

FIGURE 3 | (A) Number of channels that display significant nested oscillations (mean ± S.E.) in each frequency band pair. The black line is for the mean over subjects, and the gray line is for empty-room data. **(B)** As in **(A)**, but the number of channel pairs that display significant nested synchrony in each frequency band pair is indicated.

pairs. We computed PLV in 20 bins, which were determined by the phase of the slower oscillation, estimated the sinusoidal modulation over these bins, and confirmed the statistical significance of observed effects using a surrogate distribution from 100 sets of shuffled data, as well as empty-room data (see Methods). The mean number of channel pairs with significant nested synchrony ($z > 4.7$; Bonferroni correction with $n = 204 \times 203$ and $p < 0.05$) per subject and frequency pair was 132 for the real data, whereas it was only 9 for the empty-room data (**Figure 3B**). Nested synchrony was the strongest between frequency pairs 2–8 Hz, 2–17 Hz, and 4–17 Hz. Although statistically significant nested synchrony was found in the data, it was present only in a small fraction of channel pairs. There was, on average, less than one significant connection per gradiometer channel after correction for multiple comparisons. We then checked if the real data were better fitted with the sinusoidal function than the surrogate data by inspecting the number of significant sinusoidal fits. As expected, this number was generally higher for the real data than for the shuffled data (grand average z-score = 2.6), and individually significant ($z > 2.32$, corresponding to $p < 0.01$) in 9 out of 24 subject-frequency pairs. The sinusoidal fits of original empty-room data were not significantly better than those of shuffled empty-room data (mean z-score = 0.9). These findings provide evidence for nested synchrony in human brain activity.

NESTED SYNCHRONY AND CHANGES IN OSCILLATION AMPLITUDE

Phase synchrony among recording channels is known to be sensitive for artefacts due to volume conduction. Although we use planar gradiometer sensors with local sensitivity profiles to reduce this effect, there is still some artefactual contribution. However, the fact that we are inspecting modulation of synchrony reduces the vulnerability of our results to volume conduction. With fixed sources, the analyses are affected only when the amplitude of oscillations changes, which leads to changing patterns and magnitudes of artefactual synchrony. Furthermore, PLV estimates may be affected by two potential mechanisms of amplitude-caused bias: either higher oscillation amplitudes lead to enhanced SNR (signal-to-noise ratio) for oscillations, which then causes higher PLV estimates for the same underlying neuronal synchrony, or signals with low amplitude can become buried under common-form noise, which may then lead to higher noise-induced synchrony between those channels. Taken that nested oscillations, or amplitude modulation by low-frequency phase, has been established previously and was reproduced here, nested synchrony could potentially be related to such amplitude effects. However, there are several findings that point to a different direction. First, the relative modulation of amplitude is smaller than the relative modulation of phase synchrony ($p < 10^{-10}$, t-test across all significant connections in each subject and frequency pair), and it is not conceivable that small amplitude changes would cause relatively larger changes in phase synchrony. Furthermore, the preferred phases of amplitude and synchrony modulation are not the same: although linear regression between the preferred phases of amplitude and synchrony suggest significant correlation ($p < 0.001$ for all significant connections in each subject and frequency pair), the dependency is very weak (mean slope = 0.06). This means that amplitude and synchrony are enhanced at distinct times of the oscillatory cycle, thus the changes in oscillation amplitude via nested oscillations could not cause the nested synchrony observed here. Finally, it is established that artefactual synchrony due to volume conduction and measurement geometry is concentrated to the shortest inter-sensor distances. We found that the modulation of synchrony by lower-frequency phase often decreases as a function of inter-sensor distance, but the effect is very small (**Figure 4A**): it explains at most 1% of variability in the data (mean slope = −0.003). Furthermore, connectivity patterns typical for synchrony generated by volume conduction are not apparent in the spatial reconstructions (**Figure 4B**). Together, these analyses suggest that nested synchrony observed in this study is not an artifact due to volume conduction.

NESTED OSCILLATIONS AND NESTED SYNCHRONY ARE INDEPENDENT

To confirm that nested oscillations in two channels can be regulated independently of their nested synchrony, we performed simulations of two time series that were coupled via these cross-frequency relationships with different signal-to-noise levels (see section "Simulations of Cross-Frequency Coupling"). These simulations showed that it is possible to vary each of the three interactions simultaneously without affecting the others (**Table 1**).

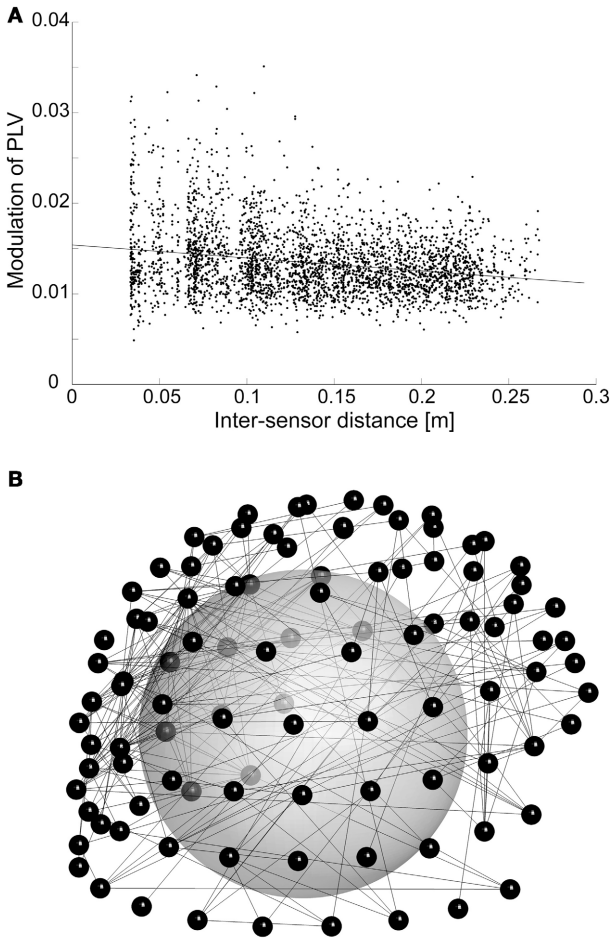

FIGURE 4 | (A) The modulation of PLV among higher-frequency (17 Hz) oscillations by the phase of an oscillation at lower frequency (4 Hz) is plotted against inter-sensor distance. This subject and frequency pair was selected, because it had the strongest correlation between distance and nested synchrony strength. For clarity, we visualize only those nested synchrony data that are significant and have adjusted R^2 goodness-of-fit higher than 0.75 (3418 data points). **(B)** Spatial visualization of the data in **(A)**, but with R^2-criterion of 0.9 (308 connections). The connections (lines) are depicted between sensors (small spheres) that are visualized in their 3D positions. The large sphere demonstrates the head inside the MEG helmet; the occipital pole is in the lower left corner, nose pointing to the right.

DISCUSSION

We have introduced and tested a novel cross-frequency interaction model of nested synchrony. In this model the neuronal inter-areal oscillatory interactions are modulated by a lower-frequency oscillation, in an analogous fashion to nested oscillations discovered previously (Lakatos et al., 2005; Canolty et al., 2006; Monto et al., 2008; Osipova et al., 2008; He et al., 2010). Our data indicate that nested synchrony is robustly, although sparsely, present in extracranial recordings of human brain activity. Nested synchrony was present in several frequency pairs, but it turned out that there was practically no nested synchrony or nested amplitude modulation in the gamma-band. This is probably because of poor SNR of gamma-band oscillations (**Figure 3A**).

Table 1 | Simulations of two coupled time series show that nested oscillations and nested synchrony can be controlled independently.

amp1	amp2	sync1	nestAmp1	nestAmp2	nestSync1	SNR
0	0	0	0,002	0,003	0,013	∞
1	0	0	0,623	0,005	0,017	∞
0	0	1	0,002	0,005	0,279	∞
1	1	1	0,628	0,612	0,287	∞
0	0	0	0,003	0,006	0,011	5
1	0	0	0,610	0,006	0,021	5
0	0	1	0,004	0,007	0,277	5
1	1	1	0,610	0,588	0,275	5
0	0	0	0,010	0,013	0,013	1
1	0	0	0,440	0,015	0,024	1
0	0	1	0,010	0,012	0,156	1
1	1	1	0,439	0,420	0,220	1

Changing the parameters controlling coupling within each signal (nested oscillations, amp1 and amp2) or coupling between the signals (nested synchrony, sync1) only affects the interaction (nestAmp1, nestAmp2, and nestSync1) that parameter is controlling. Changing the level of noise (SNR) does not affect the results remarkably.

Another explanation could be that inter-areal gamma-band synchrony is difficult to observe consistently with scalp recordings, as high-frequency synchronization is often attributed to short-range neuronal communication.

There are some potential caveats in our analyses of nested synchrony. PLV as a measure of oscillatory phase synchrony is sensitive not only to genuine phase correlations but also to artefacts from volume conduction and/or field spread. There are, however, grounds to believe that volume conduction does not play a significant role here. Our analysis has internal control for such artifacts, because we are not characterizing patterns of synchrony directly but the modulation of synchrony by the phase of a slower oscillation. Thus, artefactual synchrony could only play a role if the faster oscillatory amplitudes were modulated by the slower oscillation in the same fashion. However, we found that the relative modulation of synchrony was larger than the relative modulation of amplitude, and that the preferred phases of synchrony and amplitude were not identical (see section "Nested Synchrony and Changes in Oscillation Amplitude"). In addition, the lengths of nested synchrony connections (**Figure 4A**) and their spatial patterns (**Figure 4B**) support the view that volume conduction is not causing the nested synchrony found in this study, although its effect cannot be entirely neglected. Another possible caveat is the rather complicated data analysis methodology, which could produce some unintended effects. To rule out the possibility that nested synchrony would arise as an artifact of data processing, we recorded empty-room data, where no neuronal activity is present, and subjected these data to the same analyses than the subject data. We found no evidence of nested synchrony in the empty-room data (**Figure 3B**). This absence of nested synchrony in the absence of a subject suggests that recorded neuronal activity underlies the observed nested synchrony. Finally, it can be suspected if nested modulation of amplitude and phase can take place simultaneously in two signals. We addressed this issue

by performing simulations of two time series, and modulated these cross-frequency interactions parametrically. Our simulations indicate that it is possible to independently control the modulation of amplitude within two signals and the modulation of phase synchrony between them, although underlying physiological mechanisms are not reached with these simulations (**Table 1**).

Nested oscillations have been investigated in many studies previously. Perhaps the most popular subject in this field has been short-term memory, where the idea of temporal segmentation of memory contents by nested oscillations has been proposed (Lisman and Idiart, 1995). In a more recent line of research, the functional significance of nested oscillations in perception and attention has been elucidated, and the nested relationships are proposed to mediate a coupled hierarchy of oscillation frequencies (Lakatos et al., 2005, 2008). Furthermore, robust and widespread nested temporal relationships were discovered in arrhythmic (non-oscillatory) data as well (He et al., 2010), which might indicate the presence of fractal organization in brain background activity. Yet, complementary to studies above, modulation of spatial patterns of nested oscillations according to experimental tasks has been described, suggesting that these patterns may play a role in cognitive operations (Canolty et al., 2006).

Our results support the idea that phase synchrony dynamics are not regulated in isolation for each brain region and frequency band, but are intimately linked to neuronal oscillations in other brain regions and frequency bands. The findings also suggest that oscillatory inter-areal synchronization may be coordinated in varying time scales. If there are, indeed, oscillations in several frequency bands that contribute to changes in oscillation synchrony via the mechanism of nested synchrony, they may together play a significant role in dynamically coordinating the strength of interactions between oscillatory neuronal ensembles. This idea would consolidate the view of brain function being composed of hierarchically coupled scales (Lakatos et al., 2005; Palva and Palva, 2011). However, nested relations have been found even between non-oscillatory, or arrhythmic, activities (He et al., 2010). If the same holds true for nested synchrony as well, there arises a possibility for scale-free modulation of neuronal synchrony through the entire continuum of temporal and spatial scales. It must be noted here that the frequency ratio is not a limiting factor in the formulation of nested synchrony. In the current study, only a limited selection of frequency pairs was inspected. More detailed analysis would be required to determine if nested synchrony exists specifically between a set of narrow frequency bands or if it generalizes over several frequencies, including those where no peak in the amplitude spectrum can be seen.

While studies of nested oscillations have been successful in elucidating cross-frequency relationships in neuronal oscillations, the notion of nested synchrony proposed here could extend and corroborate these findings by combining cross-frequency interactions to inter-areal synchrony. Of particular interest here are the studies on the cross-frequency model of working memory, where slow (theta) oscillations phase controls faster (gamma) oscillations to store memories in their temporal patterns (Lisman and Idiart, 1995; Jensen and Lisman, 2005). As it is known that both theta and gamma oscillations participate in mediating information between hippocampal regions as well as between hippocampus and neocortex (Sirota et al., 2008; Colgin et al., 2009; Colgin, 2011), it would be interesting to see if nested modulations could be the mechanism for keeping the complex dynamics of multi-frequency oscillations and interactions in the hippocampo-neocortical system organized. Intriguingly, tight synchronization between hippocampal and cortical neuronal spikes has been linked to the theta oscillation generated in the hippocampus in rats (Siapas et al., 2005). Along similar lines, cortical gamma-band coherence was found to be correlated with hippocampal theta oscillations (Sirota et al., 2008). These data offer a putative example of rhythmically occurring inter-areal synchrony that is mediated by a slower oscillation, partially validating the idea of nested synchrony in a more detailed scale. The synchronization of intrinsic rhythmical activities in the brain to rhythmic external stimuli and related enhancement in stimulus processing (Schroeder and Lakatos, 2009) also point toward nested synchrony, because attention and processing of stimulus features are often promoted by synchronization of high-frequency oscillations. Another interesting and related example can be found in processing of speech: there, a coordinated hierarchy of feature processing levels and timescales is needed to execute and integrate the multitude of sub-tasks that are required to comprehend all aspects of speech (Hickok and Poeppel, 2007). Indeed, there exist interesting data on theta-entrained phase coding and spatio-temporally distributed processing of speech stimuli (Luo and Poeppel, 2007; Giraud et al., 2007). It remains to be seen if processing of speech is organized by nested relationships within and between specialized processing streams.

Local excitability changes are thought to underlie nested oscillation amplitude modulations, due to mechanisms related to either neuronal network properties or local environmental conditions (Jensen and Colgin, 2007; Lakatos et al., 2008). However, nested synchrony does not follow straightforwardly from local excitability changes, which have been related to slow oscillations, because it specifically requires coordination of phases among the higher-frequency activities. Even tight correlation between the slow oscillations is not an adequate condition for nested synchrony in the higher frequency band, unless there is direct $n : m$ phase locking. On the mechanistic side, nested oscillations and nested synchrony need not be entirely separate phenomena, because they both are related to changes in neuronal synchrony: whereas enhanced inter-areal synchrony can often be deciphered with scalp recordings, enhanced local synchrony is effectively seen as increased oscillation amplitude. The neuronal basis of phase-accurate synchronization over a distance is currently under investigation, and it might rely on different cellular mechanisms than synchronization over short distances (Kopell et al., 2000). The generation mechanisms of nested synchrony depend on the neuronal mechanisms that establish and sustain oscillation synchrony in the first place. Interneuron networks have been credited a central role in neuronal synchronization, and their properties might change depending on the phase of the slower oscillation. However, interneuron projections are mostly local, so this modulation would be expected to affect the local oscillations instead of long-distance synchrony. A more plausible mechanism could thus be related to long-range pyramidal cell projections, where

changes would allow local oscillations to continue as driven by the interneuron network but would affect long-distance synchronization (Kopell et al., 2000). Here, pyramidal cell membrane conductances would be the favored target for modulations by the slow oscillation.

We have so far investigated solely how slow oscillations in one area modulate phase synchrony between that area and another one. Yet, even more complex patterns may emerge from nested interactions. First, the individual pair-wise inter-areal synchronies are probably a part of at least one larger network. Second, sub-networks may in turn be regulated by different phases of distinct slower oscillations. Third, synchronization among the slower oscillations could provide another means to integrate different networks, all of which may carry different functionalities for information processing. These possibilities demonstrate the potential versatility of nested effects in mediating relationships between oscillatory activities in the brain, as well as the high number of possible combinations of cross- and within-frequency oscillatory interactions in brain dynamics.

In this article, we have described the model of nested synchrony, validated its existence in human neuronal activity, and proposed that it could be a viable candidate for mediating interactions between oscillatory networks at different frequencies and separated neuronal populations. In particular, it offers the possibility for a local neuronal network to participate in distinct neuronal interactions through simultaneously active mechanisms using phase-based coding only. In future, intracranial recordings will be needed to shed light on the extent and more detailed features of nested synchrony. Furthermore, this model could be applied to further investigate the interrelations between very slow brain activities, as observed with fMRI or full-band EEG, and faster neuronal oscillations (Monto et al., 2008). In addition, the subject's state could be manipulated experimentally to assess the functional significance of nested synchrony.

REFERENCES

Buzsaki, G., and Draguhn, A. (2004). Neuronal oscillations in cortical networks. *Science* 304, 1926–1929.

Canolty, R. T., Edwards, E., Dalal, S. S., Soltani, M., Nagarajan, S. S., Kirsch, H. E., Berger, M. S., Barbaro, N. M., and Knight, R. T. (2006). High gamma power is phase-locked to theta oscillations in human neocortex. *Science* 313, 1626–1628.

Canolty, R. T., Ganguly, K., Kennerley, S. W., Cadieu, C. F., Koepsell, K., Wallis, J. D., and Carmena, J. M. (2010). Oscillatory phase coupling coordinates anatomically dispersed functional cell assemblies. *Proc. Natl. Acad. Sci. U.S.A.* 107, 17356–17361.

Cardin, J. A., Carlen, M., Meletis, K., Knoblich, U., Zhang, F., Deisseroth, K., Tsai, L. H., and Moore, C. I. (2009). Driving fast-spiking cells induces gamma rhythm and controls sensory responses. *Nature* 459, 663–667.

Colgin, L. L. (2011). Oscillations and hippocampal-prefrontal synchrony. *Curr. Opin. Neurobiol.* 21, 467–474.

Colgin, L. L., Denninger, T., Fyhn, M., Hafting, T., Bonnevie, T., Jensen, O., Moser, M. B., and Moser, E. I. (2009). Frequency of gamma oscillations routes flow of information in the hippocampus. *Nature* 462, 353–357.

Fries, P. (2005). A mechanism for cognitive dynamics: neuronal communication through neuronal coherence. *Trends Cogn. Sci.* 9, 474–480.

Giraud, A. L., Kleinschmidt, A., Poeppel, D., Lund, T. E., Frackowiak, R. S., and Laufs, H. (2007). Endogenous cortical rhythms determine cerebral specialization for speech perception and production. *Neuron* 56, 1127–1134.

Hamidi, M., Slagter, H. A., Tononi, G., and Postle, B. R. (2009). Repetitive transcranial magnetic stimulation affects behavior by biasing endogenous cortical oscillations. *Front. Integr. Neurosci.* 3:14. doi: 10.3389/neuro.07.014.2009

He, B. J., Zempel, J. M., Snyder, A. Z., and Raichle, M. E. (2010). The temporal structures and functional significance of scale-free brain activity. *Neuron* 66, 353–369.

Hickok, G., and Poeppel, D. (2007). The cortical organization of speech processing. *Nat. Rev. Neurosci.* 8, 393–402.

Jensen, O., and Colgin, L. L. (2007). Cross-frequency coupling between neuronal oscillations. *Trends Cogn. Sci.* 11, 267–269.

Jensen, O., and Lisman, J. E. (2005). Hippocampal sequence-encoding driven by a cortical multi-item working memory buffer. *Trends Neurosci.* 28, 67–72.

Kopell, N., Ermentrout, G. B., Whittington, M. A., and Traub, R. D. (2000). Gamma rhythms and beta rhythms have different synchronization properties. *Proc. Natl. Acad. Sci. U.S.A.* 97, 1867–1872.

Lachaux, J. P., Rodriguez, E., Martinerie, J., and Varela, F. J. (1999). Measuring phase synchrony in brain signals. *Hum. Brain Mapp.* 8, 194–208.

Lakatos, P., Karmos, G., Mehta, A. D., Ulbert, I., and Schroeder, C. E. (2008). Entrainment of neuronal oscillations as a mechanism of attentional selection. *Science* 320, 110–113.

Lakatos, P., Shah, A. S., Knuth, K. H., Ulbert, I., Karmos, G., and Schroeder, C. E. (2005). An oscillatory hierarchy controlling neuronal excitability and stimulus processing in the auditory cortex. *J. Neurophysiol.* 94, 1904–1911.

Lisman, J. E., and Idiart, M. A. (1995). Storage of 7 +/- 2 short-term memories in oscillatory subcycles. *Science* 267, 1512–1515.

Luo, H., and Poeppel, D. (2007). Phase patterns of neuronal responses reliably discriminate speech in human auditory cortex. *Neuron* 54, 1001–1010.

Monto, S., Palva, S., Voipio, J., and Palva, J. M. (2008). Very slow EEG fluctuations predict the dynamics of stimulus detection and oscillation amplitudes in humans. *J. Neurosci.* 28, 8268–8272.

Osipova, D., Hermes, D., and Jensen, O. (2008). Gamma power is phase-locked to posterior alpha activity. *PLoS ONE* 3:e3990. doi: 10.1371/journal.pone.0003990

Palva, J. M., and Palva, S. (2011). Roles of multiscale brain activity fluctuations in shaping the variability and dynamics of psychophysical performance. *Prog. Brain Res.* 193, 335–350.

Schroeder, C. E., and Lakatos, P. (2009). Low-frequency neuronal oscillations as instruments of sensory selection. *Trends Neurosci.* 32, 9–18.

Siapas, A. G., Lubenov, E. V., and Wilson, M. A. (2005). Prefrontal phase-locking to hippocampal theta oscillations. *Neuron* 46, 141–151.

Singer, W., and Gray, C. M. (1995). Visual feature integration and the temporal correlation hypothesis. *Annu. Rev. Neurosci.* 18, 555–586.

Sirota, A., Montgomery, S., Fujisawa, S., Isomura, Y., Zugaro, M., and Buzsaki, G. (2008). Entrainment of neocortical neurons and gamma oscillations by the hippocampal theta rhythm. *Neuron* 60, 683–697.

Taulu, S., and Simola, J. (2006). Spatiotemporal signal space separation method for rejecting nearby interference in MEG measurements. *Phys. Med. Biol.* 51, 1759–1768.

Womelsdorf, T., Fries, P., Mitra, P. P., and Desimone, R. (2006). Gamma-band synchronization in visual cortex predicts speed of change detection. *Nature* 439, 733–736.

Conflict of Interest Statement: The author declares that the research was conducted in the absence of any commercial or financial relationships that could be construed as a potential conflict of interest.

Received: 30 January 2012; accepted: 09 September 2012; published online: 26 September 2012.

*Citation: Monto S (2012) Nested synchrony—a novel cross-scale interaction among neuronal oscillations. Front. Physio. **3**:384. doi: 10.3389/fphys.2012.00384*

This article was submitted to Frontiers in Fractal Physiology, a specialty of Frontiers in Physiology.

frontiers in
PHYSIOLOGY

ORIGINAL RESEARCH ARTICLE
published: 15 June 2012
doi: 10.3389/fphys.2012.00186

Scale-free and multifractal time dynamics of fMRI signals during rest and task

***P. Ciuciu*[1]*, *G. Varoquaux*[1,2,3], *P. Abry*[4], *S. Sadaghiani*[5] and *A. Kleinschmidt*[3]**

[1] *Life Science Division, Biomedical Imaging Department, NeuroSpin Center, Commissariat à l'Energie Atomique et aux Energies Alternatives, Gif-sur-Yvette, France*
[2] *Parietal Project-Team, INRIA Saclay-île de France, Gif-sur-Yvette, France*
[3] *INSERM U992, NeuroSpin Center, Gif-sur-Yvette, France*
[4] *Physics Department, CNRS, UMR 5672, École Normale Supérieure de Lyon, Lyon, France*
[5] *D'Esposito Lab, University of California, Berkeley, CA, USA*

Edited by:
Biyu J. He, National Institute of Neurological Disorders and Stroke, USA

Reviewed by:
John G. Holden, University of Cincinnati, USA
Dimitri Van De Ville, Ecole Polytechnique Fédérale de Lausanne, Switzerland

****Correspondence:***
P. Ciuciu, Life Science Division, Biomedical Imaging Department, NeuroSpin Center, Commissariat à l'Energie Atomique et aux Energies Alternatives, Bât 145 – Point Courier 156, F-91191 Gif-sur-Yvette, France.
e-mail: philippe.ciuciu@cea.fr

Scaling temporal dynamics in functional MRI (fMRI) signals have been evidenced for a decade as intrinsic characteristics of ongoing brain activity (Zarahn et al., 1997). Recently, scaling properties were shown to fluctuate across brain networks and to be modulated between rest and task (He, 2011): notably, Hurst exponent, quantifying long memory, decreases under task in activating and deactivating brain regions. In most cases, such results were obtained: First, from univariate (voxelwise or regionwise) analysis, hence focusing on specific cognitive systems such as Resting-State Networks (RSNs) and raising the issue of the specificity of this scale-free dynamics modulation in RSNs. Second, using analysis tools designed to measure a single scaling exponent related to the second order statistics of the data, thus relying on models that either implicitly or explicitly assume Gaussianity and (asymptotic) self-similarity, while fMRI signals may significantly depart from those either of those two assumptions (Ciuciu et al., 2008; Wink et al., 2008). To address these issues, the present contribution elaborates on the analysis of the scaling properties of fMRI temporal dynamics by proposing two significant variations. First, scaling properties are technically investigated using the recently introduced Wavelet Leader-based Multifractal formalism (WLMF; Wendt et al., 2007). This measures a collection of scaling exponents, thus enables a richer and more versatile description of scale invariance (beyond correlation and Gaussianity), referred to as multifractality. Also, it benefits from improved estimation performance compared to tools previously used in the literature. Second, scaling properties are investigated in both RSN and non-RSN structures (e.g., artifacts), at a broader spatial scale than the voxel one, using a multivariate approach, namely the Multi-Subject Dictionary Learning (MSDL) algorithm (Varoquaux et al., 2011) that produces a set of spatial components that appear more sparse than their Independent Component Analysis (ICA) counterpart. These tools are combined and applied to a fMRI dataset comprising 12 subjects with resting-state and activation runs (Sadaghiani et al., 2009). Results stemming from those analysis confirm the already reported task-related decrease of long memory in functional networks, but also show that it occurs in artifacts, thus making this feature not specific to functional networks. Further, results indicate that most fMRI signals appear multifractal at rest except in non-cortical regions. Task-related modulation of multifractality appears only significant in functional networks and thus can be considered as the key property disentangling functional networks from artifacts. These finding are discussed in the light of the recent literature reporting scaling dynamics of EEG microstate sequences at rest and addressing non-stationarity issues in temporally independent fMRI modes.

Keywords: scale invariance, self-similarity, multifractality, wavelet Leader, fMRI, brain dynamics, rest, task

1. INTRODUCTION

Much of what is known about brain function stems from studies in which a task or a stimulus is administered and the resulting changes in neuronal activity and behavior are measured. From the advent of human electroencephalography (EEG) to cognitive activation paradigms in functional Magnetic Resonance Imaging (fMRI), this approach proved very successful to study brain function, and more precisely functional specialization in human brain. It has relied, on one hand, on contrasting signal magnitude between different experimental conditions (Rosen et al., 1998) or task-specific hemodynamic response (HRF) shape (Dale, 1999) and, on other-hand, on statistical methods often framed within linear

or bilinear modeling strategies (Friston et al., 1995; Makni et al., 2005, 2008).

Spontaneous modulations of neural activity in Blood Oxygenation Level Dependent (BOLD) fMRI signals however arise without external input or stimulus and thus depict intrinsic brain activity (Damoiseaux et al., 2006). This ongoing activity constitutes a major part of fMRI recordings and is responsible for most of brain energy consumption. It has hence been intensively studied over the last decade using various methods ranging from *univariate*, i.e., Seed-based linear Correlation Analysis (SCA; Biswal et al., 1995; Greicius et al., 2003), to *multivariate* methods such as Independent Component Analysis (ICA; Calhoun et al., 2001; Beckmann and Smith, 2004), group-level ICA (Cole et al., 2010; Varoquaux et al., 2010b), or more recent dictionary learning techniques (Varoquaux et al., 2011). All these methods have revealed that interactions between brain regions, also referred to as *functional connectivity*, occur through these spontaneous modulations and consistently vary between rest and task (Damoiseaux et al., 2006; Fox et al., 2007). Resting-State Network (RSN) extraction from resting-state fMRI time series is thus achieved either by thresholding the correlation matrix computed between voxels or regions (seed-based or univariate approach) or by identifying spatial maps in ICA-based algorithms that closely match RSNs such as somato-sensory systems (visual, motor, auditory), the default mode, and attentional networks (ventral and dorsal; Fox et al., 2007; Smith et al., 2009). For a recent review about the pros and cons of the SCA and ICA approaches to RSN extraction, the reader can refer to Cole et al. (2010). Once RSNs are extracted, their topological properties can be analyzed with respect to *small-world* or *scale-free* models (Chialvo, 2004; Eguiluz et al., 2005; Zemanová et al., 2006; Bullmore and Sporns, 2009).

In parallel and alternatively to brain topology, the temporal dynamics of brain activity have also been extensively studied. It is now well accepted that brain activity, irrespective of the imaging technique involved in observation, is always arrhythmic and shows a scaling, or scale invariant or scale-free, time dynamics, which implies that no time scale plays a predominant or specific role. Often, scale invariance or *scale-free dynamics* is associated with *long-range correlation* in *time* (Linkenkaer-Hansen et al., 2001; Stam and de Bruin, 2004; Van de Ville et al., 2010), and accordingly, in the frequency domain, related to a *power-law* decrease of the power spectrum ($\Gamma(f) \propto 1/f^{\beta}$ with $\beta > 0$) in the limit of small frequencies ($f \to 0$). Interestingly, it is generally admitted that only low frequencies (<0.1 Hz) convey information related to neural connectivity in fMRI signals (Cordes et al., 2001; Leopold et al., 2003; Achard et al., 2006). Evidence of fractal or *scale-free* behavior in fMRI signals has been demonstrated for a long while (Zarahn et al., 1997; Bullmore et al., 2001; Bullock et al., 2003) though it was initially regarded as noise. Deeper investigations of the temporal *scale-free* property in fMRI have demonstrated that this constitutes an intrinsic feature of ongoing brain activity (c.f., e.g., Thurner et al., 2003; Shimizu et al., 2004; Maxim et al., 2005; Ciuciu et al., 2008; Wink et al., 2008; He et al., 2010; He, 2011). First attempts to identify stimulus-induced signal changes from scaling parameters were proposed in Thurner et al. (2003), Shimizu et al. (2004), where a voxel-based fluctuation analysis was applied to high temporal resolution fMRI data. Interestingly, fractal features of voxel time series have enabled to discriminate white matter, cerebrospinal fluid, and active from inactive brain regions during a block paradigm (Shimizu et al., 2004). Further, it was shown that scaling properties can be modulated in neurological disorder (Maxim et al., 2005) or between rest and task (Thurner et al., 2003; Shimizu et al., 2004; Ciuciu et al., 2008; Wink et al., 2008; He, 2011): It was shown that long memory, as quantified by the Hurst exponent, decreases during task in activating and deactivating brain regions. Analyzing scale invariance in temporal dynamics may thus provide new insights into how the brain works by mapping quantitative estimations of parameters with good specificities to cognitive states, task performance (Shimizu et al., 2004; Wink et al., 2008; He et al., 2010; He, 2011).

Small-world and scale-free topology led to model brain as a complex critical system, that is as a large conglomerate of interacting components, with possibly non-linear interactions (Bak and Paczuski, 1995; Chialvo, 2010). Further, these complex systems were then regarded as potential origins for long-range correlation spatio-temporal patterns, as critical systems, i.e., complex systems driven close to their phase transitions, constitute known mechanism yielding scaling time dynamics and generic $1/f$ power spectral densities (see e.g., Chialvo, 2010). They however so far failed to account for the existence of possibly richer scaling properties (such as, e.g., multifractality). At a general level, scale invariance in time dynamics and scale-free property of brain topology are, in essence, totally independent properties that must not be confused one with the other. Whether or not and how these two scale-free instances are related one to the other in the fMRI context remains a difficult and largely unsolved issue, far beyond the scope of the present contribution, that concentrates instead on performing a thorough analysis of scale invariance temporal dynamics in fMRI signals.

In the existing literature, the analysis of scale invariance in fMRI signals suffers from two limitations: First, it has often been performed at the voxel or region level, thus consisting of a collection of univariate analyses, suffering from the classical bias of voxel selection or region definition. Moreover, although the fluctuation of scale-free dynamics with tissue type has been studied in Shimizu et al. (2004), Wink et al. (2008) to derive that stronger persistency occurs in gray matter and that this background activity might represent neuronal dynamics, no systematic analysis has been undertaken to disentangle the scale-free properties of RSN and non-RSN components, such as artifacts. This investigation can be better handled using multivariate or ICA-like approaches. Second, scale invariance in fMRI signals has mostly been based on spectral analysis and/or *Detrended Fluctuation Analysis* (c.f., e.g., Thurner et al., 2003; Stam and de Bruin, 2004; He, 2011). This amounts to considering that scaling is associated only with the correlation or the spectrum (hence with the second order statistics) of the data and thus, implicitly and sometimes even explicitly, to assuming Gaussianity and (asymptotic) self-similarity for the data (cf., e.g., Eke et al., 2002) for a survey in the fMRI context). Also, it is now well-known that such technics lack robustness to disentangle stationarity/non-stationarity versus true scaling property issues and do not allow simple extension to account for richer scaling properties such as those observed in multifractal models. It is well accepted that wavelet analysis based analysis of scaling (cf., e.g.,

Abry et al., 1995, 1998; Bullmore et al., 2001; Veitch and Abry, 2001; Fadili and Bullmore, 2002) yield not only better estimation performance, but also show significant practical robustness, notably to non-stationarity, while paving the way toward the analysis of scaling properties beyond the strict second order (hence beyond Gaussianity and asymptotic self-similarity).

In this context, the present contribution elaborates on earlier works dedicated to the analysis of scale invariance in fMRI temporal dynamics by proposing two significant variations.

First, scale invariance dynamics is not investigated at the voxel or region spatial scale level independently. Instead, group-level resting-state networks are segmented by an exploratory multivariate decomposition approach, namely the MSDL algorithm (Varoquaux et al., 2011), detailed in Section 3: It produces both a set of spatial components and a set of times series, for each component and each subject, that conveys ongoing dynamics in functional networks but also in artifacts. As shown in Varoquaux et al. (2011), the sparsity promoting regularization involved in the MSDL algorithm enables to recover less noisy spatial maps than group-level or canonical ICA (Varoquaux et al., 2010b). This makes their interpretation easier in the context of small group of individuals. This technique is detailed in Section 3.

Second, to enable an in-depth analysis of the scaling properties of the temporal dynamics in fMRI signals, we resort to multifractal analysis, that measures not a single but a collection of scaling exponents, thus enabling a richer and more versatile description of scale invariance (beyond correlation and Gaussianity), referred to as multifractality. It is thus likely to better account for the variety and complexity of potential scaling dynamics, as already suggested in the context of fMRI in, e.g., Ciuciu et al. (2008), Wink et al. (2008). However, in contrast to Wink et al. (2008), and following the track opened in Ciuciu et al. (2008), we use a recent statistical analysis tool, the Wavelet Leader-based Multifractal formalism (WLMF; Wendt et al., 2007). This formalism benefits from better mathematical grounding and shows improved estimation performance compared to tools previously used in the literature. This framework is introduced in Section 4, after a review of the intuition, models, and methodologies underlying the definition and analysis of scaling temporal dynamics, thus, to some extend, continuing, and renewing the surveys provided in (Eke et al., 2002; Ciuciu et al., 2008).

These tools are combined together and applied to two datasets, corresponding to resting-state and activation runs. They are described in Section 2 (see also Sadaghiani et al., 2009). Modulations of scale-free and multifractal properties in space, i.e., between functional and artifactual components but also between rest and task, are statistically assessed at the group-level in Section 5.

In agreement with findings in He (2011), the results reported here confirm that fMRI signals can be modeled as stationary processes, as well as the decrease of the estimated long memory parameter under task. However, this is found to occur everywhere in the brain and not specifically in functional networks. Moreover, evidence for multifractality in resting-state fMRI signals is demonstrated except for non-cortical regions. Task-related modulations of multifractality appear only significant in functional networks and thus become the key property to disentangle functional networks from artifacts. However, in contrast to what happens for the long memory parameter, this modulation is not monotonous across the brain and varies between cortical and non-cortical regions. These results are further discussed in Section 6 in the light of recent findings related to scale-free dynamics of EEG microstate sequences and non-stationarity of functional modes. Conclusions are drawn in Section 7.

2. DATA ACQUISITION AND ANALYSIS

2.1. DATA ACQUISITION

Twelve right-handed normal-hearing subjects (two female; ages, 19–30) gave written informed consent before participation in an imaging study on a 3-T MRI whole-body scanner (Tim-Trio; Siemens). The study received ethics committee approval by the authorities responsible for our institution. Anatomical imaging used a T1-weighted magnetization-prepared rapid acquisition gradient-echo sequence [176 slices, repetition time (TR) 2300 ms, echo time (TE) 4.18 ms, field of view (FOV) 256, voxel size 1 mm × 1 mm × 1 mm]. Functional imaging used a T2*-weighted gradient-echo, echo-planar-imaging sequence (25 slices, TR = 1500 ms, TE = 30 ms, FOV 192, voxel size 3 mm × 3 mm × 3 mm). Stimulus presentation and response recording used the Cogent Toolbox (John Romaya, Vision Lab, UCL[1]) for Matlab and sound delivery a commercially available MR-compatible system (MR Confon).

The rs-fMRI dataset we consider in this study has already been published in Sadaghiani et al. (2009). Eight hundred-twenty volumes of task-free "resting-state" data (with closed, blind-folded eyes) were acquired before getting experimental runs of 820 volumes each. These experimental runs, which have not been analyzed in Sadaghiani et al. (2009), involve an auditory detection task (run 2, motor response), and make use of a sparse *supra*-threshold auditory stimulus detection.

The auditory stimulus was a 500-ms noise burst with its frequency band modulated at 2 Hz (from white noise to a narrower band of 0–5 kHz and back to white noise). Inter-stimulus intervals ranged unpredictably from 20 to 40 s, with each specific interval used only once. Subjects were instructed to report as quickly and accurately as possible by a right-hand key press whenever they heard the target sound despite scanner's background noise. Details about the definition of each subject's auditory threshold are available in Sadaghiani et al. (2009).

2.2. DATA ANALYSIS

We used here statistical parametric mapping (SPM5, Wellcome Department of Imaging Neuroscience, UK[2]. For image preprocessing (realignment, coregistration, normalization to MNI stereotactic space, spatial smoothing with a 5-mm full-width at half-maximum isotropic Gaussian kernel for single-subject and group analyses) and our own software developments for subsequent analyses. More precisely, the MSDL algorithm relies on the `scikit-learn` Python toolbox[3] and the multifractal analysis on the `WLBMF` Matlab toolbox[4].

[1] www.vislab.ucl.ac.uk
[2] www.fil.ion.ucl.ac.uk
[3] http://scikit-learn.org/stable/
[4] http://perso.ens-lyon.fr/herwig.wendt/

3. MULTIVARIATE DECOMPOSITION OF RESTING-STATE NETWORKS

3.1. MULTI-SUBJECT SPATIAL DECOMPOSITION TECHNIQUES

The fMRI signal observed in a voxel reflects many different processes, such as cardiac or respiratory noise, movement effects, scanner artifacts, or the BOLD effect that reveals the underlying neural activity of interest. We separate these different contributions making use of a recently introduced multivariate analysis technique that estimates jointly spatial maps and time series characteristic of these different processes (Varoquaux et al., 2011). Formally, this estimation procedure amounts to finding K spatial maps $\boldsymbol{V}_s \in \mathbb{R}^{p\times K}$ and the corresponding time series $\boldsymbol{U}_s \in \mathbb{R}^{n\times K}$, whose linear combination fits well the observed brain signals, $\boldsymbol{Y}_s \in \mathbb{R}^{n\times p}$, of length n, measured over p voxels, for subject s:

$$\boldsymbol{Y}_s = \boldsymbol{U}_s \boldsymbol{V}_s^{\mathrm{t}} + \boldsymbol{E}_s, \tag{1}$$

with $\boldsymbol{E}_s \in \mathbb{R}^{n\times p}$ the subject-level noise, or residuals not explained by the model. Finding $\boldsymbol{V}_s^{\mathrm{t}}$ enables the separation of the contributions of the different process that are mixed at the voxel level, but implies to work on spatial maps rather than on specific voxels. The number of spatial maps, K, is not chosen *a priori*, but selected by the procedure.

This problem can be seen as a blind source separation task in the presence of noise, and has often been tackled in fMRI using ICA, combined with principal component analysis (PCA) to reject noise (McKeown et al., 1998; Kiviniemi et al., 2003; Beckmann and Smith, 2004). In the multi-subject configuration, estimating the spatial maps on all subjects simultaneously makes it easy to relate the factors estimated across the different subjects. This can be done by concatenating the data across subject, modeling a common distribution (Calhoun et al., 2001), or by extending the data-reduction step performed in the PCA by a second level capturing inter-subject variability (Varoquaux et al., 2010b). More recently, it was proposed that the key to the success of ICA on fMRI data, is to recover sparse spatial maps (Daubechies et al., 2009; Varoquaux et al., 2010a). This hypothesis can be formulated as a sparse prior in model (1), which can then be estimated using sparse PCA or sparse dictionary learning procedures. With regards to our goal in this study, extracting time series specific to the various processes observed, a strong benefit of such procedures is that they can perform data-reduction, i.e., estimation of the residuals not explained by the model, and extraction of the relevant signals in a single step informed by our prior. On the opposite, with ICA-based procedures, the residuals are selected by the PCA step, and not the ICA step.

3.2. MULTI-SUBJECT DICTIONARY LEARNING ALGORITHM

In addition, Varoquaux et al. (2011) have adapted the dictionary learning procedures to a multi-subject setting, in a so-called *multi-subject dictionary learning* (MSDL) framework. On fMRI datasets, the procedure extracts a group-level atlas of spatial signatures of the processes observed, as well as corresponding subject-level maps, accounting for the individual specificities. They show that, with a small spatial smoothness prior added to the sparsity prior on the maps, the extracted patterns correspond to the segmentation of various structures in the signal: functional regions, blood vessels, interstitial spaces, sub-cortical structures... In these settings, the subject-level maps $\boldsymbol{V}_s$ are modeled as generated by group-level maps $\boldsymbol{V} \in \mathbb{R}^{p\times K}$ with additional inter-subject variability that appears as residual terms, $\boldsymbol{F}_s \in \mathbb{R}^{p\times K}$, at the group-level:

$$\forall s \in \{1, \ldots, S\}, \ \boldsymbol{V}_s = \boldsymbol{V} + \boldsymbol{F}_s.$$

The model is estimated by finding the group-level and subject-level maps that maximize the probability of observing the data at hand with the given prior. This procedure is known as a Maximum *A Posteriori* (MAP) estimate, and boils down to minimizing the negated log-likelihood of the model with an additional penalizing term. If the two sources of unexplained signal, i.e., subject-level residuals $\boldsymbol{E}_s$ and inter-subject variability $\boldsymbol{F}_s$ are modeled as Gaussian random variates, the log-likelihood term is the sum of squares of these errors. The prior term appears as the sum of the sparsity-inducing ℓ_1 norm of $\boldsymbol{V}$, and the ℓ_2-norm of the gradient of the map, enforcing the smoothness. This prior has been used previously in regression settings under the name of smooth-Lasso (Hebiri and van de Geer, 2011). Estimating the model from the data thus consists of minimizing the following criterion:

$$\mathcal{J}(\boldsymbol{U}_s, \boldsymbol{V}_s, \boldsymbol{V}) = \sum_{s=1}^{S} \left(\left\| \boldsymbol{Y}_s - \boldsymbol{U}_s \boldsymbol{V}_s^{\mathrm{t}} \right\|^2 + \mu \left\| \boldsymbol{V}_s - \boldsymbol{V} \right\|^2 \right) + \lambda \left(\|\boldsymbol{V}\|_1 + \boldsymbol{V}^{\mathrm{t}} \boldsymbol{L} \boldsymbol{V}/2 \right)$$

where, $\|\boldsymbol{V}\|_1$ is the ℓ_1 norm of $\boldsymbol{V}$, i.e., the sum the absolute values, $\boldsymbol{L}$ is the image Laplacian $-\boldsymbol{V}^{\mathrm{t}}\,\boldsymbol{L}\boldsymbol{V}$ is the norm of the gradient. λ is a parameter controlling the amount of prior set on the maps, and thus the amount of sparsity, that is set by Cross-Validation (CV). μ is a parameter controlling the amount of inter-subject validation, that is set by comparing intra-subject variance in the observations with inter-subject variance. For more details about the estimation procedure or the parameter setting, we refer the reader to Varoquaux et al. (2011).

3.3. RESTING-STATE MSDL MAPS

rs-fMRI runs were analyzed for $S = 12$ subjects, consisting of $n = 820$ volumes (time points) with a 3-mm isotropic resolution, corresponding to approximately $p = 50000$ voxels within the brain. The automatic determination rule of the number of maps exposed in Varoquaux et al. (2010a) converges to $K = 42$. Also, the CV procedure gives us the best CV criterion for $\lambda = 2$. The group-level maps $\boldsymbol{V}$ are shown in **Figure 1**. They have been manually classified in three groups: *Functional* (F), *Artifactual* (A), and *Undefined* (U) maps that appear color-coded in red, blue, and green, respectively. The undefined class appeared necessary to introduce some confidence measure in our classification and disambiguate well-established networks (e.g., dorsal attentional network) from inhomogeneous components mixing artifacts with neuronal regions (e.g., like in v_9). The anatomo-functional description of these group-level maps and their class assignment is given in **Table 1**. The same rules applied for individual maps V_s. In what follows, we will denote by $\mathcal{F}$, $\mathcal{A}$ and $\mathcal{U}$ the index sets of F/A/U-maps, respectively and by Card $(\mathcal{F}) = 25$, Card $(\mathcal{A}) = 13$, and Card $(\mathcal{U}) = 4$ their respective size.

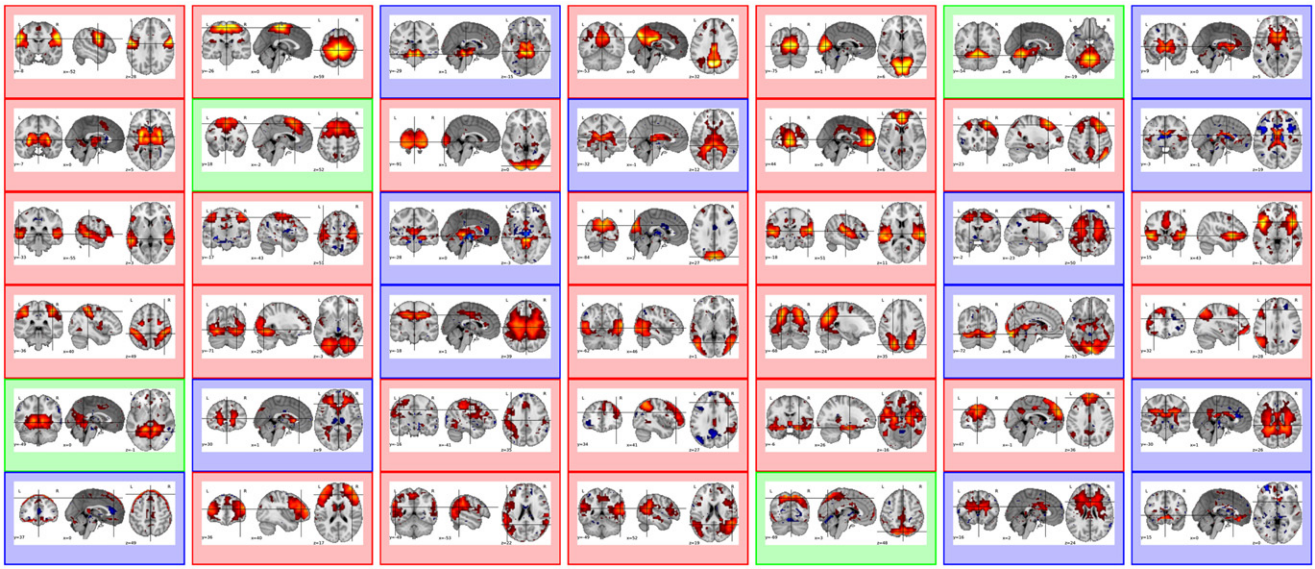

FIGURE 1 | From left to right and top to bottom, group-level MSDL maps $V=[v_1|\ldots|v_{42}]$ inferred from the multi-subject ($S=12$) resting-state fMRI dataset (Neurological convention: left is left). Functional (F), Artifactual (A), and Undefined (U) maps appear color-coded boxes in red, blue, and green, respectively. Let us denote $\mathcal{F}$, $\mathcal{A}$, and $\mathcal{U}$ the index sets of F/A/U-maps, respectively and Card ($\mathcal{F}$) = 25, Card ($\mathcal{A}$) = 13, and Card ($\mathcal{U}$) = 4 their respective size. Each map v_k consists of loading parameters within the (−1, 1) range where positive and negative values are depicted by the hot and cold parts of the color bar.

To compare spontaneous and evoked activity, the same spatial decomposition was used on resting-state (run 1, Rest) and task-related data, which were acquired during an auditory detection task (run 2, Task). In practice, this consists of projecting the task-related fMRI data $\widetilde{\boldsymbol{Y}}_s$ onto the inferred spatial maps $\boldsymbol{V}_s$ by minimizing the following least square criterion, $\left\|\widetilde{\boldsymbol{Y}}_s - \boldsymbol{W}_s \boldsymbol{V}_s^{\mathrm{t}}\right\|^2$, with respect to $\boldsymbol{W}_s$. The time series solution admits a closed-form expression: $\widetilde{\boldsymbol{U}}_s = \widetilde{\boldsymbol{Y}}_s \boldsymbol{V}_s \left(\boldsymbol{V}_s^{\mathrm{t}} \boldsymbol{V}_s\right)^{-1}$. The subsequent scale-free analysis is applied to the two sets of $n \times K$ map-level fMRI time series $\boldsymbol{U}_S = [\boldsymbol{u}_{s,1}|\ldots|\boldsymbol{u}_{s,K}]^{\mathrm{t}}$ and $\widetilde{\boldsymbol{U}}_s = \left[\widetilde{\boldsymbol{u}}_{s,1}|\ldots|\widetilde{\boldsymbol{u}}_{s,K}\right]^{\mathrm{t}}$ in a univariate manner, that is to each time series $\boldsymbol{u}_{s,k}$ and $\widetilde{\boldsymbol{u}}_{s,k}$ for Rest and Task, respectively.

4. SCALE-FREE: INTUITION, MODELS, AND ANALYSES

4.1. INTUITION

In the analysis of evoked brain activity, it is common to seek correlations of BOLD signals with any *a priori* shape of the hemodynamic response convolved with the experimental paradigm. In the frequency domain, this amounts to seeking response energy concentration in pre-defined spectral bands, as induced for instance by periodic stimulation (e.g., flashing checkerboards). In resting-state fMRI, it is now well admitted that intrinsic brain activity is characterized by scale-free properties (Zarahn et al., 1997; He, 2011). This constitutes a major change in paradigm as it implies that brain activity is not to be analyzed via the amounts of energy it shows within specific and *a priori* chosen frequency bands, but instead via the fact that all frequencies are jointly contributing in an equivalent manner to its dynamics. *Scale-free* dynamics are usually described in the spectral domain by a power-law decrease: Let $Y(t)$ denote the signal quantifying brain activity and $\Gamma_Y(f)$ its Power Spectral Density (PSD). Scale-free property is classically envisaged as:

$$\mathcal{M}_0 : \Gamma_Y(f) \simeq C|f|^{-\beta}, \quad \beta \geq 0, \tag{2}$$

with $f_m \leq |f| \leq f_M$, $f_M/f_m \gg 1$. Such a power-law behavior over a broad range of frequencies implies that no frequency in that range plays a specific role, or equivalently, that they are all equally important. To analyze brain activity, this power-law relation thus becomes a more important feature than the energy measured at some specific frequencies. For instance, it implies that energy at frequency f_1 can be deduced from energy at frequency f_2 according to He (2011):

$$\Gamma_Y(f_2) = \Gamma_Y(f_1)\left(|f_2|/|f_1|\right)^{-\beta}. \tag{3}$$

In the scale-free framework, one therefore tries to quantify brain activity by considering the scaling exponent β (or variants) as the key descriptor. Let us moreover note that the terminology *scale-free* is equivalent to *scale invariance* or simply *scaling*, encountered in other scientific fields, where this property has also been found to play a central role (c.f., Abry et al., 2002; Ciuciu et al., 2008).

4.2. SCALE-FREE MODELS

4.2.1. From spectrum to increments

Though appealing, equations (2) and (3) do not provide practitioners with a versatile enough definition of *scale-free* with respect to real-world data analysis. Indeed, they concentrate only on the second order statistics and hence account neither for the marginal distribution (first order statistics) of the signal Y, nor for its higher

Table 1 | Classification of group-level $V = |v_1| \ldots |v_{42}|$ maps according to the F/A/U labeling.

Index	Anatomo-functional description	Label	Network
v_1	Ventral primary sensorimotor cortex	F (f_1)	Mot.
v_2	Dorsal primary motor cortex or edge of recorded volume	U (u_1)	
v_3	Midbrain	A (a_1)	Oth.
v_4	Precuneus, posterior cingulate cortex	F (f_2)	DMN
v_5	Calcarine cortex (V1)	F (f_3)	Vis.
v_6	Anterior cerebellar lobe	F (f_4)	N-c
v_7	Ventricles	A (a_2)	Ven.
v_8	Caudate, thalamus, and putamen	F (f_5)	N-c
v_9	Pre- and supplementary motor cortex	U (u_2)	
v_{10}	Occipital cortex	F (f_6)	Vis.
v_{11}	Ventricles	A (a_3)	Ven.
v_{12}	Median prefrontal cortex	F (f_7)	DMN
v_{13}	Right lateralized fronto-parietal cortex	F (f_8)	Fr.-par.
v_{14}	Ventricles	A (a_4)	Ven.
v_{15}	Superior temporal and inferior frontal gyrus	F (f_9)	Lang.
v_{16}	Primary sensorimotor cortex	F (f_{10})	Mot.
v_{15}	Artifact	A (a_5)	Oth.
v_{18}	Dorsal occipital cortex	F (f_{11})	Vis.
v_{19}	Supratemporal cortex	F (f_{12})	Aud.
v_{20}	Semioval center (white matter)	A (a_6)	WhM.
v_{21}	Anterior insula and cingulate cortex	F (f_{13})	
v_{22}	Frontal Eye Fields (FEF), intra-parietal cortex	F (f_{14})	Att.
v_{23}	Ventral occipital cortex	F (f_{15})	Vis.
$v24$	Semioval center (white matter)	A (a_7)	WhM.
v_{25}	Lateral occipital cortex	F (f_{16})	Vis.
v_{26}	Parieto-occipital cortex	F (f_{17})	Vis.
v_{27}	Extracerebral space	A (a_8)	Oth.
v_{28}	Left lateralized ventral fronto-parietal cortex	F (f_{18})	Fr.-par.
v_{29}	Retrosplenial and anterior occipital cortex	U (u_3)	
v_{30}	White matter	A (a_9)	WhM.
v_{30}	Left lateralized fronto-parietal system	F (f_{19})	Fr.-par.
v_{32}	Right lateralized ventral fronto-parietal system	F (f_{20})	Att.
v_{23}	Mesial temporal system	F (f_{21})	
v_{34}	Dorsomedian frontal cortex	F (f_{22})	DMN
v_{35}	White matter	A (a_{10})	WhM.
v_{36}	Motion-related artifact	A (a_{11})	Mov.
$v37$	Bilateral prefrontal cortex and anterior Caudate	F (f_{23})	
v_{38}	Left lateralized temporo-parietal junction and inferior frontal gyrus	F (f_{24})	Att.
v_{39}	Right lateralized temporo-parietal junction and inferior frontal gyrus	F (f_{25})	Att.
v_{40}	Bilateral superior parietal lobe	U (u_4)	
v_{41}	White matter	A (a_{12})	WhM.
v_{42}	Artifact	A (a_{13})	Oth.

The F-maps have been subdivided in different functional networks: Attentional, Default Mode Network, Motor, Visual. Basal Ganglia (Thalamus, Caudate, and Putamen) and cerebellum have been put together under the Non-cortical label. They will be considered together in the following set: $\mathcal{N}$ = {Att, DMN, Mot, N-c, Vis}. The artifacts have been distinguished in four types: Ventricles, White Matter, Movement, and Other. The corresponding set will be denoted $\mathcal{T}$ = {Ven, WhM, Mov, Oth}.

order dynamics (or dependence structure). For instance, it does not indicate whether data are jointly Gaussian or depart, weakly, or strongly, from Gaussianity.

To investigate how to enrich Model $\mathcal{M}_0$, let us assume for now that Y consists of a stationary jointly Gaussian process, with PSD as in equation (2). Equivalently, this implies that the covariance function behaves as $C_Y(\tau) \sim \sigma_Y^2(1 + C'|\tau|^{-\alpha})$, for $\tau_m \leq \tau \leq \tau_M$, with $\alpha = 1 - \beta$. A simple calculation hence shows that $\mathbb{E}(Y(t+\tau) - Y(t))^2 = \mathbb{E}Y(t+\tau)^2 + \mathbb{E}Y(t)^2 - 2\mathbb{E}Y(t+\tau)Y(t) = c_2|\tau|^{-\alpha}$. The Gaussianity of Y further implies that $\forall q > -1$:

$$\mathbb{E}|Y(t+\tau) - Y(t)|^q = c_q|\tau|^{-\frac{q\beta}{2}}, \ \tau_m \leq \tau \leq \tau_M. \tag{4}$$

Defining $X(t) = \int^t Y(s)ds$, equation (4) straightforwardly implies that, as long as $\tau_m \leq \tau_1, \tau_2 \leq \tau_M$:

$$\left\{ \frac{X(t+\tau_1) - X(t)}{\tau_1^H} \right\}_{t\in\mathbb{R}} \overset{fdd}{=} \left\{ \frac{X(t+\tau_2) - X(t)}{\tau_2^H} \right\}_{t\in\mathbb{R}}, \tag{5}$$

with $H = (-\alpha/2) = (\beta+1)/2$, and where $f\underline{d}d$ means equality of all joint finite dimensional distributions: i.e., $(X(t+\tau_1) - X(t))/\tau_1^H$ and $(X(t+\tau_2) - X(t))/\tau_2^H$ have the same joint distributions. In turn, this implies that $\forall q > -1$, such that $\mathbb{E}|X(t)|^q < \infty$:

$$\mathbb{E}|X(t+\tau) - X(t)|^q = c_q|\tau|^{qH}, \ \tau_m \leq \tau \leq \tau_M, \ or \tag{6}$$

$$\mathbb{E}|X(t+\tau_2) - X(t)|^q = \mathbb{E}|X(t+\tau_1) - X(t)|^q \left(\frac{|\tau_2|}{|\tau_1|} \right)^{qH}, \tag{7}$$

with $\tau_m \leq \tau_1, \tau_2 \leq \tau_M$, which are reminiscent of equations (2) and (3).

4.2.2. Self-Similar processes with stationary increments

Equations (6) and (7) turn out to hold not only for jointly Gaussian 1/*f*-processes but for a much wider and better defined class, that of self-similar processes with stationary increments, referred to as H-sssi processes, and defined as, c.f., Samorodnitsky and Taqqu (1994):

$$\mathcal{M}_1: \quad \{X(t)\}_{t\in\mathbb{R}} \overset{fdd}{=} \left\{ a^H X(t/a) \right\}_{t\in\mathbb{R}}, \tag{8}$$

$\forall a > 0$, $H \in (0, 1)$. Essentially, it means that X cannot be distinguished (statistically) from any copy, dilated by scale factor $a > 0$,

(Continued)

on condition that the amplitude axis is scaled by a^H. Parameter H is referred to as the self-similarity exponent. A major practical consequence of this definition consists of the fact that equations (6) and (7) hold for all τ (resp., τ_1,τ_2).

The central benefit of such a definition is that it does not require the data to be Gaussian but provides both theoreticians and practitioners with a well-defined model. For analysis, fMRI data can hence be envisaged as the increment process $Y(t)=X(t+\tau_0)-X(t)$ of an H-sssi process X (where τ_0 is an arbitrary constant chosen to make sense with respect to physiology and data acquisition set up, e.g., $\tau_0=\mathrm{TR}$). This constitutes a second model to account for scale-free properties in data, that encompasses the *simpler* $1/f$-spectrum first model.

Further, if joint Gaussianity is assumed, the model becomes even more precise as the only Gaussian H-sssi process X is the so-called fractional Brownian motion (fBm), c.f., e.g., Mandelbrot and van Ness (1968), hereafter labeled $X(t)\equiv B_H(t)$. The corresponding increment process $Y(t)=G_H(t)=B_H(t+1)-B_H(t)$ is termed fractional Gaussian noise (fGn). Additionally, note that it may sometimes constitute a practical and relevant challenging issue to decide whether brain activity is better modeled by the H-sssi process X (hence a non-stationary process) or by its increment process Y (hence a stationary process; c.f., e.g., Ciuciu et al., 2008; He et al., 2010; He, 2011).

4.2.3. Multifractal processes

In a number of situations, it has been actually observed on a variety of real-world data of very different nature (c.f., e.g., Abry et al., 2002 for reviews) that equation (6) holds over a wide range of τs, however, with scaling exponents that depart significantly from the theoretical linear behavior qH:

$$\mathbb{E}|X(t+\tau)-X(t)|^q = c_q|\tau|^{\zeta(q)},\ \tau_m\le\tau\le\tau_M. \tag{9}$$

The generic behaviors modeled by equation (9) can be considered as a practical or operational, definition of scale-free property. Let us note that, by nature, $\zeta(q)$ is necessarily a concave function of q (c.f., e.g., Wendt et al., 2007).

Scaling exponents $\zeta(q)$ that are strictly concave rule out the use of H-sssi process as models. Instead, a broader class should be used, referred to as that of *multifractal processes*. This is however a large and not-well-defined class of processes. For the purposes of this contribution, let us use a particular subclass of multifractal processes defined as fBm subordinated to a *multiplicative Compound Poisson cascade*:

$$\mathcal{M}_2 : X(t) := B_H(A(t)),\ \text{where } A(t)=\int^t W(s)ds, \tag{10}$$

with $W(s)$ a multiplicative Compound Poisson cascade (or martingale), such as those defined in Barral and Mandelbrot (2002). The complete definition of these cascades has been given and studied with details elsewhere and is hence not recalled here (c.f., Bacry et al., 2001; Barral and Mandelbrot, 2002; Chainais et al., 2005). It is enough to emphasize that they rely on the choice of positive random variables whose moments of order q define the $\zeta(q)$. The process X thus defined satisfies equation (9) with strictly convex tunable scaling exponents $\zeta(q)$, has stationary increments Y, and has distributions that depart from strict jointly Gaussian laws. Such departures, that may however turn subtle and hard to detect in practice, are precisely quantified by the departure of $\zeta(q)$ from a linear behavior in q. The $\zeta(q)$ therefore convey a rich information about data X, and hence about Y, as they account for the entire dependence structure of the data, hence both to the time dynamic and distributions of data. Their accurate estimation from real-world data therefore naturally constitutes an important practical challenge discussed below.

4.3. SCALE-FREE ANALYSIS

4.3.1. From spectrum to wavelet analysis

Assuming that data Y have a power-law spectrum behavior as in equation (2), it is natural to rely on spectral estimation to measure β. A classical tool in spectrum analysis is the Welch estimator that consists in splitting data Y into blocks and in averaging the squared Fourier transforms computed independently over each block. For scale-free data, it is hence expected that:

$$\hat{\Gamma}_Y(f)=\sum_k \left|\langle Y, g_{f,k}\rangle\right|^2 \simeq C|f|^{-\beta}, \tag{11}$$

where the $g_{f,k}=g_0(t-k)e^{\imath 2\pi ft}$ are translated into time and into frequency templates of a reference pattern $g_0(t)$. This relation can be further used to estimate β.

It has been shown that wavelet transforms can achieve better performance both in the analysis of scale-free properties in real-world data, and in the estimation of the corresponding scaling parameters (c.f., Abry et al., 1995, 1998; Veitch and Abry, 2001). The discrete wavelet transform (DWT) coefficients of Y are defined as:

$$d_Y(j,k)=\int_{\mathbb{R}} Y(t)\ 2^{-j}\psi_0\left(2^{-j}t-k\right)\ dt \equiv \langle Y,\psi_{j,k}\rangle, \tag{12}$$

where the $\psi_{j,k}=2^{-j}\psi_0(2^{-j}t-k)$ consists of templates of a reference pattern ψ_0 translated in time and dilated (by a factor $a=2^j$). It is referred to as the *mother-wavelet*: an elementary function, characterized by fast exponential decays in both the time and frequency domains, as well as by a strictly positive integer $N_\psi\ge 1$, the *number of vanishing moments*, defined as $\forall k=0,1,\ldots,N_\psi-1$, $\int_{\mathbb{R}} t^k\psi_0(t)dt\equiv 0$, and $\int_{\mathbb{R}} t^N\psi_0(t)dt\neq 0$. Note the choice of the L^1-norm (as opposed to the more common L^2-norm choice) that better matches scaling analysis. For further introduction to wavelet transforms, the reader is referred to, e.g., Mallat (2009).

Defining $S_Y^d(j,2)=\frac{1}{n_j}\sum_{k=1}^{n_j}\left|d_Y(j,k)\right|^2$ (with n_j the number of $d_X(j,k)$ available at scale 2^j), one obtains (c.f. Abry et al., 1995):

$$\mathbb{E}S_Y^d(j,2)=\int_{\mathbb{R}}\Gamma_Y(f)\left|\Psi_0\left(2^jf\right)\right|^2 df \tag{13}$$

where Ψ_0 denotes the Fourier transform of ψ_0. This indicates that $S_Y^d(j,2)$ can be read as a wavelet based estimate of the PSD and is hence referred to as the *wavelet spectrum*. It measures the amount of energy of Y around the frequency $f_j=f_0/2^j$ where f_0 is a constant that depends on the explicit choice of ψ_0 (for the

Daubechies wavelet used here, $f_0 \simeq 3f_s/4$ with f_s the sampling frequency). This correspondence between the Fourier and wavelet spectra is illustrated on fMRI signals in **Figure 2**. For scale-free processes satisfying equation (2), it implies:

$$S_Y^d(j,2) \equiv \frac{1}{n_j}\sum_{k=1}^{n_j}\left|\langle Y,\psi_{j,k}\rangle\right|^2 \simeq C_2 2^{j(\beta-1)},\ a_m \le 2^j \le a_M.$$

While this formally looks like equation (11), it has been shown in detail how and why the wavelet spectrum yields better estimates of the scaling exponents β than Welch based-ones, both in terms of estimation performance and robustness to various forms of non-stationarity in data that may be confused with scale-free behaviors (Abry et al., 1995, 1998; Veitch and Abry, 2001). Notably, it was shown how wavelet analysis enables to disentangle non-stationarity, stemming from fMRI environment, from true long memory in brain activity. Also, the wavelet spectrum avoids the potentially difficult issue that consists of deciding *a priori* whether empirical data are better modeled by Y or X, needed by classical spectrum estimation, that can only be applied to stationary data. In a nutshell, these benefits stem from the use of the change of scale operator to design the analysis tool, that intuitively matches scale-free behavior more naturally than a frequency shift operator.

4.3.2. From 2nd to other statistical orders: Wavelet leaders

As discussed in Section 4.2, analyzing in-depth scale-free properties implies investigating not only the spectrum (i.e., the second order statistics of data) but rather the entire dependence structure, i.e., the whole range of available statistical orders q. It had initially been thought that this would amount to extending the definition of $S_Y^d(j,2)$ to other orders q, $S_Y^d(j,q) \equiv \frac{1}{n_j}\sum_{k=1}^{n_j}\left|\langle Y,\psi_{j,k}\rangle\right|^q$. It has however recently been shown that this approach, though intuitive and appealingly *simple*, fails to yield satisfactory estimation of the $\zeta(q)$. Notably, wavelet coefficients show little power in enabling practitioners to decide whether $\zeta(q)$ is a linear or strictly concave function of q. Instead, it is now well documented that the estimation of the $\zeta(q)$ should be based on Wavelet Leaders (Wendt et al., 2007).

Let us now assume that ψ_0 has a compact time support and introduce the global regularity of Y, h_m, defined as: $h_m = \liminf_{2^j\to 0}\log(\sup_k|d_Y(j,k)|)/\log(2^j)$. Therefore, h_m can be estimated by a linear regression of the log of the magnitude of the largest wavelet coefficient at scales 2^j versus the log of the scales 2^j (Wendt et al., 2007). Let $\gamma \ge 0$ be defined as, with $\epsilon > 0$: $\gamma = 0$ if $h_m > 0$, and $\gamma = -h_m + \epsilon$ otherwise. Further, let $\lambda_{j,k}$ denote the dyadic interval $\lambda_{j,k} = [k2^j,\ (K+1)2^j)$, and denote by $3\lambda_{j,k}$ the union of $\lambda_{j,k}$ and its 2 closest neighbors, $3\lambda_{j,k} = [(k-1)2^j,\ (k+2)2^j)$. The wavelet leaders $L_Y^{(\gamma)}$ are defined as $L_Y^{(\gamma)}(j,k) = \sup_{\lambda'\subset 3\lambda_{j,k}} 2^{\gamma j}\left|d_Y(\lambda')\right|$. In practice, $L_Y^{(\gamma)}(j,k)$ simply consists of any of the largest coefficients $2^{\gamma j}|d_Y(\lambda')|$ located at scales finer or equal to 2^j and within a small time neighborhood. It is then necessary to form the so-called wavelet Leader structure functions that reproduce the scale-free properties in Y according to:

$$S_Y^L(j,q,\gamma) \equiv \frac{1}{n_j}\sum_{k=1}^{n_j}\left(L_Y^{(\gamma)}(j,k)\right)^q \simeq c_q 2^{j\zeta(q,\gamma)}, \tag{14}$$

Moreover, for a large class of processes, one has: $\zeta(q,\gamma) = \zeta(q) + \gamma q$. For all real-world data analyzed so far with WLMF, this relation is found to hold, by varying γ (c.f. Wendt et al., 2007 for a thorough discussion). This has also been verified empirically for fMRI data. Further, because it can take any concave shape, the function $\zeta(q,\gamma)$ is often written as a polynomial expansion (Arneodo et al., 2002): $\zeta(q,\gamma) = \Sigma_{p\ge 1}\, c_p^{(\gamma)} q^p/p!$. Notably, the second order truncation $\zeta(q,\gamma) \simeq c_1^{(\gamma)} q + c_2^{(\gamma)} q^2/2$ (with $c_2^{(\gamma)} \le 0$ by concavity) can be regarded as a potentially interesting approximation that captures the crucial information regarding whether the $\zeta(q,\gamma)$ are linear in q (hence indicating H-sssi models) or strictly concave (hence suggesting multiplicative cascade models). Interestingly, the coefficients $c_p^{(\gamma)}$ entering the polynomial expansion of $\zeta(q,\gamma)$ are not abstract figures but rather turn out to be quantities deeply tied to the scale-free properties of Y, as they are related to the scale dependence of the cumulants of order $p \ge 1$, $C_Y^{(\gamma)}(j,p)$, of the random variable $\ln L_Y^{(\gamma)}(j,k)$:

$$\forall p \ge 1,\ C^{(\gamma)}(j,p)_Y = c_{0,p}^{(\gamma)} + c_p^{(\gamma)} \ln 2^j. \tag{15}$$

Equations (14) and (15) suggest that the $\zeta(q,\gamma)$ or $c_p^{(\gamma)}$ can be efficiently estimated from linear regressions: $\hat{\zeta}(q,\gamma) = \Sigma_{j=j_1}^{j_2} w_j \log_2 S_Y^L(j,q,\gamma)$ and $\hat{c}_p^{(\gamma)} = \log_2 e \Sigma_{j=j_1}^{j_2} w_j \hat{C}_Y^L(j,p,\gamma)$. The weights w_j are chosen to perform ordinary (or non-weighted) least squares estimation (c.f. Veitch and Abry, 2001 for discussion). Further, $\zeta(q,\gamma) = \zeta(q) + \gamma q$ obviously implies that $c_1 = c_1^{(\gamma)} - \gamma$ and $\forall p \ge 2$, $c_p = c_p^{(\gamma)}$.

This wavelet Leader-based analysis of scale-free properties is intimately and ultimately related to *multifractal analysis*, the detailed introduction of which is beyond the scope of the present contribution. We restate here only its essence. Multifractal analyses describe globally the fluctuations along time of the local regularity of a signal $Y(t)$. This local regularity is measured by the so-called Hölder exponent $h(t)$, that essentially compares Y around time t_0 against a local power-law behavior: $|Y(t) - Y(t_0)| \le |t - t_0|^h$, $|t - t_0| \to 0$. The variations of h along time are then described globally via the multifractal spectrum, consisting of the collection

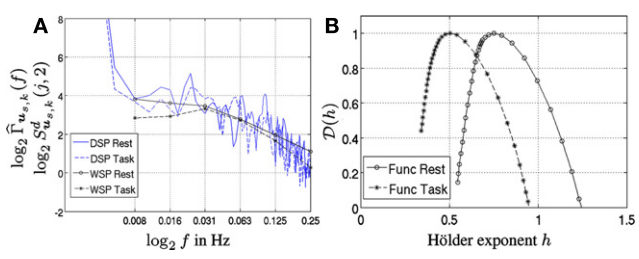

FIGURE 2 | (A) Welch (blue curves) vs. Wavelet (**black** curves) spectra associated with a F-map (f_{18}). Solid and dashed lines correspond to rest and task, respectively. **(B)** Corresponding multifractal spectra $\mathcal{D}(h)$.

of Hausdorff dimensions, $\mathcal{D}(h)$, of the sets of points $\{t,h(t)=h\}$. In practice, the multifractal spectrum is estimated indirectly via (a Legendre transform of) the function $\zeta(q)$. The approximation $\zeta(q)\simeq c_1 q + c_1 q^2/2$ translates into $\mathcal{D}(h)\simeq 1-(h-c_1)^2/(2|c_2|)$. For thorough and detailed introductions to multifractal analysis, the reader is referred to, e.g., Wendt et al. (2007). Examples of such multifractal spectra estimated using the WLMF from real fMRI signals are illustrated in **Figure 2B**. An outcome of the mathematical theory underlying multifractal analysis, of key practical importance and impact, is the following: the function $\mathcal{D}(h)$ theoretically constitutes a rich characterization of the scale-free properties of a signal Y and its complete and entire estimation requires the use, in equation (14), of both positive and negative order qs, concentrated left and right around 0 (Wendt et al., 2007).

5. MULTIFRACTAL ANALYSIS OF MSDL MAPS

5.1. SINGLE-SUBJECT ANALYSIS

5.1.1. Scaling range

For analysis, orthonormal minimal-length time support Daubechies's wavelets were used with $N_\psi = 3$. Scale-free properties are systematically found to hold within a 4-octave range ($(j_1,j_2)=(3,6)$), corresponding to a frequency range of [0.008, 0.063] Hz[5], which is hence consistent with the upper limit 0.1 Hz classically associated with the hemodynamics boundary and scaling in fMRI data (Cordes et al., 2001).

5.1.2. Fourier vs. wavelet spectra

For illustrative purposes, two time series corresponding to a functional map ($k=28$, $\boldsymbol{f}_{18}$ in **Table 1**), were selected in the rest and task runs from the first subject. In **Figure 2A**, the Fourier spectrum estimate ($\log_2 \hat{\Gamma}_{\boldsymbol{u}_{s,k}}(f)$) based on Welch's averaged periodogram and its wavelet spectrum counterpart ($\log_2 S^d_{\boldsymbol{u}_{s,k}}(j,2)$) are found to closely match, as predicted by equation (13). Interestingly, **Figure 2A** shows that the β exponent, measured within frequency range [0.008, 0.063] Hz, in equation (2) (i.e., the neg-slope of the log-spectra $\log_2 \widehat{\Gamma}_{\boldsymbol{u}_{s,k}}(f)$) decreases with task-related activity in $\boldsymbol{f}_{18}$. This amounts to observing lower Hurst exponent $H=(\beta-1)/2$ in the task-related dataset: $\widehat{H}^{\mathrm{R}}_{f_{18}} \simeq 0.66$ and $\widehat{H}^{\mathrm{T}}_{f_{18}} \simeq 0.5$. As shown in the following, this decrease of self-similarity is not specific to functional maps and will be observed in artifactual and undefined maps. Following He (2011), the stationarity of fMRI signals is confirmed since we systematically observed $\widehat{H}^{\mathrm{R,T}}_k < 1$.

5.1.3. Multifractal spectrum

For the same time series, MF spectra $\mathcal{D}(h)$, estimated using the WLMF tool described above, are depicted in **Figure 2B**. The decrease of self-similarity between rest and task is captured by a shift to the left of the position $\widehat{c}_1$ of the maximum of $\mathbb{D}(h)$: $((\widehat{c}_1)^{\mathrm{R}}_{f_{18}}, (\widehat{c}_1)^{T}_{f_{18}}) = (0.75, 0.5)$ It should also be noted that parameter $\widehat{c}_1$ systematically takes values that are close to those of the Hurst exponent. This is consistent with the theoretical modeling of scale-free property that establishes a clear connection between c_1 and H and predicts $c_1 \simeq H$ (c.f. Wendt et al., 2007). Therefore, in the following, c_1 will be referred to as the self-similarity parameter although this is a slight misnomer. Further, **Figure 2B** confirms the presence of multifractality in fMRI data as strictly negative $c_2<0$ are almost always observed. Indeed, parameter c_2 quantifies the width of $\mathcal{D}(h$; as a curvature radius of $\mathcal{D}(h)$ around $(\widehat{c}_1)$: $\widehat{c}_2 < 0$. Multifractality is however not specific to a given brain state since we measured $((\widehat{c}_2)^{\mathrm{R}}_{f_{18}}, (\widehat{c}_2)^{\mathrm{T}}_{f_{18}}) = (-0.07, -0.06)$. In this example, multifractality, as measured by the width of the multifractal spectra, is decreased from rest to task. However, opposite fluctuations will be also observed amongst F-maps.

The sole two self-similarity and multifractality parameters c_1 and c_2 are therefore used from now on as sufficient and relevant descriptors of the scale-free properties of fMRI signals (superscript γ is dropped for the sake of conciseness, while γ has been systematically set to $\gamma=2$).

5.2. GROUP-LEVEL ANALYSIS

5.2.1. Group-level scale-free properties

Let $c^{j,s}_{i,k}$ denote the $\hat{c}_1$ and $\hat{c}_2$ estimates (index $i=1{:}2$) for differents maps (index $k=1{:}K$), runs (index $j=$ R,T for Rest and Task, respectively) and for different subjects (index s). The map-dependent group-level values have been computed as $\mu^j_{i,k} = \Sigma_{s=1}^S \hat{c}^{j,s}_{i,k}/S$ and sorted according to their labeling (F/A/U-maps) given in **Table 1**. Then, global spatial averaging of the means $\mu^j_{i,k}$ has been performed so as to derive global F/A/U-average parameter estimates: $\bar{\mu}^j_{i,F} = \Sigma_{k\subset\mathcal{F}} \mu^j_{i,k}/\mathrm{Card}(\mathcal{F})$, $\bar{\mu}^j_{i,A}$, and $\bar{\mu}^j_{i,U}$ are defined equivalently. In the same spirit, group-level multifractal attributes $\bar{\mu}^j_{i,\nu_\ell}$ are derived for each functional network $\nu_\ell \in \mathcal{N} = \{\mathrm{Att, DMN, Mot, N\text{-}c, Vis}\}$ such that $\bar{\mu}^j_{i,n_\ell} = \Sigma_{k\in n_\ell} \mu^j_{i,k}/\mathrm{Card}(\boldsymbol{n}_\ell)$, $\forall \ell = 1{:}5$, and $j=$ (R,T). We proceed in the same way for analyzing artifact types $t_r \in \mathcal{T} = \{\mathrm{Ven, WhM, Mov, Oth}\}$, and computing $\bar{\mu}^j_{i,\boldsymbol{t}_r}$ for $r=1{:}4$.

As shown in **Figure 3**[top], the group-averaged values of self-similarity $\mu^j_{1,k}$ lie approximately in the same range [0.55, 1], indicating long memory, for all components (F/A/U-maps). An almost systematic decrease of self-similarity is observed in the task-related dataset ($\delta_{1,k} = \mu^{\mathrm{T}}_{1,k} - \mu^{\mathrm{R}}_{1,k} < 0$), for $k\in\mathcal{F}\cup\mathcal{A}\cup\mathcal{U}$. This trend is therefore not specific to F-maps. Moreover, the average decrease computed over F-maps is about the same as the one estimated for A and U-maps ($\bar{\delta}_{1,F} = -0.125$, $\bar{\delta}_{1,A} = -0.11$ and $\bar{\delta}_{1,U} = -0.13$). Also, the averaged standard deviations ($\bar{\sigma}^{\mathrm{R}}_{1,F}$, $\bar{\sigma}^{\mathrm{R}}_{1,A}$, and $\bar{\sigma}^{\mathrm{R}}_{1,U}$) computed over the F/A/U-maps, are close to each other ($\bar{\sigma}^{\mathrm{R}}_{1,F/A/U} \approx 0.18$) and systematically increase with the task-related activity($\bar{\sigma}^{\mathrm{T}}_{1,F/A/U} > \bar{\sigma}^{\mathrm{R}}_{1,F/A/U}$).

Figure 3[bottom] illustrates that the group-averaged values of $\mu^{\mathrm{R,T}}_{2,k}$ are almost all negative in the F/A/U-maps indicating multifractality in fMRI time series irrespective of the map type or brain state. Between rest to task-related situation minor changes in the A and U-maps are also observed since $|\delta_{2,k}|<0.03$ for $k\in\mathcal{U}\cup\mathcal{A}$) while we measured $|\delta_{2,k}|<0.08$ for $k\in\mathcal{F}$ ($\delta_{2,k} = \mu^{\mathrm{T}}_{2,k} - \mu^{\mathrm{R}}_{2,k}$).

[5]The scale and band-specific central frequency are related according to $f_j = 3f_e/(42^j)$.

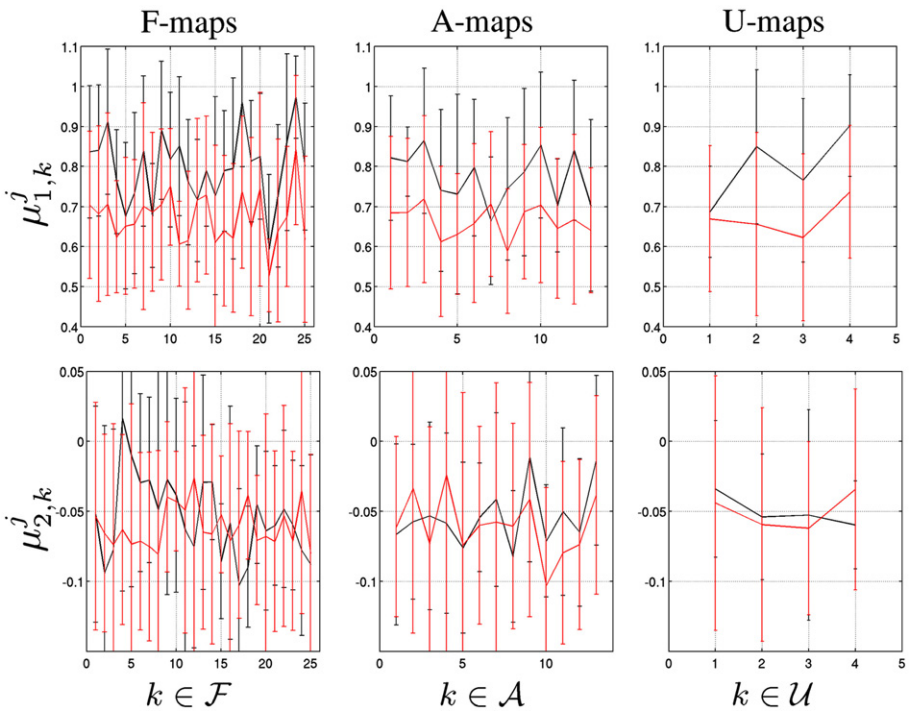

FIGURE 3 | From left to right: Group-averaged map-dependent MF parameters $\mu^j_{1,k}$ (top), $\mu^j_{2,k}$ (bottom) specific to F/A/U-maps defined in Table 1. Black and red curves code for $j=$R (Rest) and $j=$T (Task).

Hence, the level of multifractality does not change much between rest and task in irrelevant maps. In contrast, large changes in the multifractal parameters are observed in F-maps, while not systematically in the same direction. For instance, in cerebellum (f_4), basal ganglia (f_5), DMN (f_7) and fronto-parietal network (f_8) evoked activity induces a large increase of multifractality ($\delta_{2,k} < 0$) while in the auditory and attentional systems (e.g., f_{12} and f_{24}, respectively), which are supposed to be involved in the auditory detection task, the converse observation holds, i.e. ($\delta_{2,k} > 0$. Also, it is worth noticing that the averaged standard deviations computed over the A/U-maps increase when switching from rest to task ($\bar{\sigma}^{\mathrm{R}}_{2,A} = 0.06 < \bar{\sigma}^{\mathrm{T}}_{2,A} = 0.09$ and $\bar{\sigma}^{\mathrm{R}}_{2,U} = 0.05 < \bar{\sigma}^{\mathrm{T}}_{2,U} = 0.085$) while they remain at the same level in the F-maps: $\bar{\sigma}^{\mathrm{R}}_{2,F} \approx \bar{\sigma}^{\mathrm{T}}_{2,F} \approx 0.08$.

We computed the grand means of the self-similarity parameters $\bar{\mu}^{\mathrm{R,T}}_{1,F/A/U}$ over the F/A/U-maps, respectively, and draw the same conclusion at this macroscopic level, as demonstrated in **Figures 4A–C**: the decrease of self-similarity from rest to task is not specific to functional components and only slightly fluctuates between networks and artifact types. Moreover, we did not observe any significant modification of the grand means of multifractal parameter estimates $\bar{\mu}^{\mathrm{R,T}}_{2,F/A/U}$ between rest and task, as illustrated in **Figure 4D**. This motivated deeper investigations at the network and artifact levels, especially concerning the fluctuation of multifractality induced by task. **Figure 4E** reveals that a major increase of multifractality ($\bar{\mu}^{\mathrm{T}}_{2,\boldsymbol{n}_4} < \bar{\mu}^{\mathrm{R}}_{2,\boldsymbol{n}_4}$) occurred only in the non-cortical regions while no major change appeared in the artifacts ($\bar{\mu}^{\mathrm{T}}_{2,\boldsymbol{t}_r} \simeq \bar{\mu}^{\mathrm{R}}_{2,\boldsymbol{t}_r}, \forall r \in \mathcal{T}$) as shown in **Figure 4F**.

5.2.2. One-sample statistical tests

To assess the statistical significance of the multifractal parameters for the rest and task-related datasets at the group-level, we used *one-sided* tests associated with the following null hypotheses $\forall k \in \mathcal{F} \cup \mathcal{A} \cup \mathcal{U}$:

$$\left.\begin{array}{lll} H_{0,j}^{(1,k)} : \mu^j_{1,k} & \leq 0.5, & \text{(White noise or SRD)} \\ H_{0,j}^{(2,k)} : \mu^j_{2,k} & = 0., & \text{(H} - \text{sssi process).} \end{array}\right\} \quad (16)$$

We also conducted similar tests at the macroscopic level ($k \in \mathcal{N} \cup \mathcal{T}$) by replacing $\mu^j_{i,k}$ with $\bar{\mu}^j_{i,k}$ in the null hypotheses (16). Because there is no definite proof nor evidence that MF parameter estimates $\hat{c}^{j,s}_{i,k}$ should be normally distributed across subjects, we investigated different statistics (Student-t, Wilcoxon's signed rank (WSR) statistic). Indeed, other statistics may provide more sensitive results in presence of outliers. To account for multiple comparisons (K tests performed simultaneously) and to ensure correct specificity control (control of false positives), the Bonferroni correction was applied.

Rejecting $H_{0,j}^{(1,k)}$ clearly amounts to localizing brain areas or components eliciting significant long memory or self-similarity. Rejecting $H_{0,j}^{(2,k)}$ enables to discriminate multifractality from self-similarity. Similar tests involving $\bar{\mu}^j_{i,F/A/U}$, $\bar{\mu}^j_{i,\boldsymbol{n}_\ell}$, and $\bar{\mu}^j_{i,\boldsymbol{t}_r}$ in the definition of null hypotheses(16) for ($i=1, 2$) were also performed.

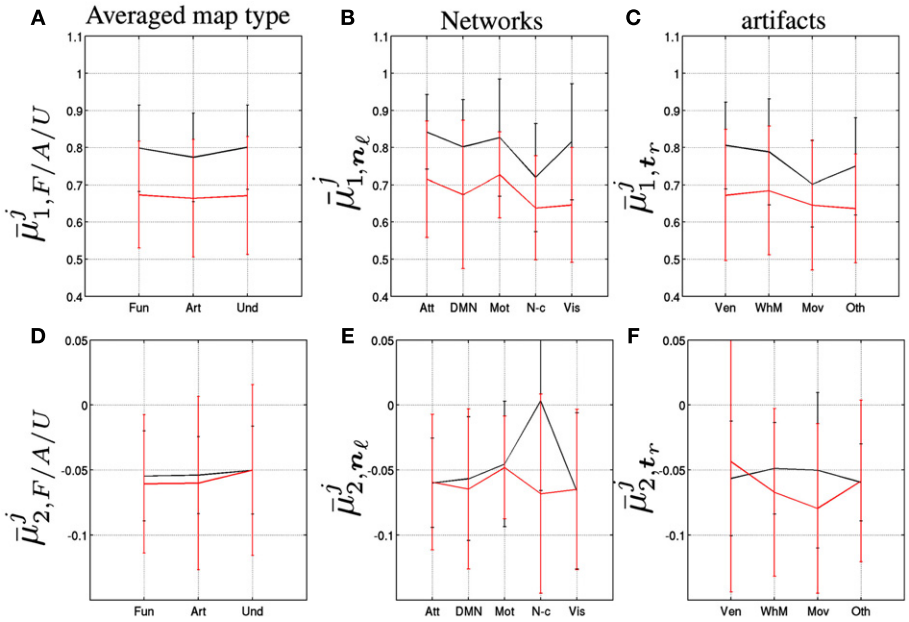

FIGURE 4 | Top: Group-level grand-mean self-similarity parameter $\bar{\mu}^{j}_{1,k}$ averaged over the F/A/U-maps, i.e., $k \in \mathcal{F}/\mathcal{A}/\mathcal{U}$ (A), the functional networks, $k \in \mathcal{N}$ (B) and the artifact types, $k \in \mathcal{T}$, (C). Bottom: Group-level grand-mean multifractality parameter $\bar{\mu}^{j}_{2,k}$ averaged over the F/A/U-maps, i.e., $k \in \mathcal{F}/\mathcal{A}/\mathcal{U}$ **(D)**, the functional networks, $k \in \mathcal{N}$ **(E)** and the artifact types, $k \in \mathcal{T}$, **(F)**. **Black** and red curves code for j = R (Rest) and j = T (Task).

Analysis of statistical significance of F-maps regarding $H^{(1),k}_{0,R}$ showed that most components (22/25) rejected this null hypothesis at rest using T-test and thus were significantly self-similar (see blue curves in **Figure 5A**). The task effect then induced a loss of significance in the vast majority of components as shown in **Figure 5B**: only four maps ($\boldsymbol{f}_{10}, \boldsymbol{f}_{14}, \boldsymbol{f}_{18}$, and $\boldsymbol{f}_{24}$) demonstrated a significant level of self-similarity using T-test in the task-related dataset. These maps are related to the motor, fronto-parietal, and attentional (parieto-temporal junction and IPS/FEF) networks. Two out of them are lateralized in the left hemisphere. Statistical analysis of F-maps regarding $H^{(2),k}_{0,R}$ demonstrated that only six components ($\boldsymbol{f}_{15}, \boldsymbol{f}_{17}, \boldsymbol{f}_{18}, \boldsymbol{f}_{21}, \boldsymbol{f}_{23}, \boldsymbol{f}_{24}$) rejected this null hypothesis at rest: see red curves in **Figure 5A**. The task-related modulation tends to reduce the number of significant F-maps: As depicted in **Figure 5B**, only 3 components survived the T-test ($\boldsymbol{f}_{10}$, $\boldsymbol{f}_{15}$, and $\boldsymbol{f}_{19}$) in the task-related dataset. Interestingly, $\boldsymbol{f}_{10}$ and $\boldsymbol{f}_{19}$ are likely to be involved in the auditory detection task and the motor response since they belong to the Motor and Attentional networks. Hence, a significant level of multifractality is observed during task in components that were monofractal at rest. Besides, the level of multifractality remains significant in the ventral occipital cortex ($\boldsymbol{f}_{15}$) irrespective of the brain state and that a few components in the visual ($\boldsymbol{f}_{17}$), fronto-parietal ($\boldsymbol{f}_{18}$), temporal ($\boldsymbol{f}_{21}$), prefrontal ($\boldsymbol{f}_{23}$), and attentional ($\boldsymbol{f}_{24}$) networks became monofractal under the task effect.

Statistical analysis of A and U-maps regarding $H^{(1),k}_{0,j}$ showed the same behavior when switching from rest to task, namely a strong decrease of the number of significant self-similar components (from 10 to 4 and 4 to 2 for A/U-maps, respectively): see blue curves in **Figures 5C–F**, respectively. Statistical analysis of A and U-maps regarding $H^{(2),k}_{0,j}$ also demonstrated a reduction of the number of multifractal components in A/U-maps. Two artifactual components ($\boldsymbol{a}_{10}$ and $\boldsymbol{a}_{12}$) located in the white matter remained consistently multifractal in both datasets and one undefined component ($\boldsymbol{u}_3$) became significantly multifractal when switching from rest to task. In all cases, a loss of significance is observed using WSR tests (dash dotted curves) instead of T-tests (solid curves) indicating that there is no outlier in this group and thus that the Gaussian distribution hypothesis is tenable.

Then, we focused on the statistical analysis at different macroscopic scales, first by averaging all F/A and U-maps respectively so as to derive a mean behavior for F/A/U-maps. Finally, we looked at functional networks and artifact types in more details. Blue curves in **Figures 6A,B** report such results for the rest and task-related datasets, respectively. We still observed a significant level of self-similarity in all averaged groups (blue curves) irrespective of the brain state: $\bar{H}^{(1,F/A/U)}_{0,j}$ is systematically rejected for $j =$ (R, T). However, we still noticed a reduction of statistical significance induced by task irrespective of the map type. More interestingly, we found at this macroscopic level that all averaged maps were multifractal at rest whereas only the functional one remained multifractal during task: see red curves in **Figures 6A,B**. Further, statistical analysis of functional networks defined in **Table 1** was conducted to understand which network drives this effect. When comparing p-values in **Figures 6C,D** on functional networks, we observed that all remained significantly self-similar in both states, while the DMN is close to the significance level $\alpha = 0.05$ during task (blue curves). Regarding multifractality, only the non-cortical regions appeared monofractal at rest and all networks kept a significant amount of multifractality during task. In

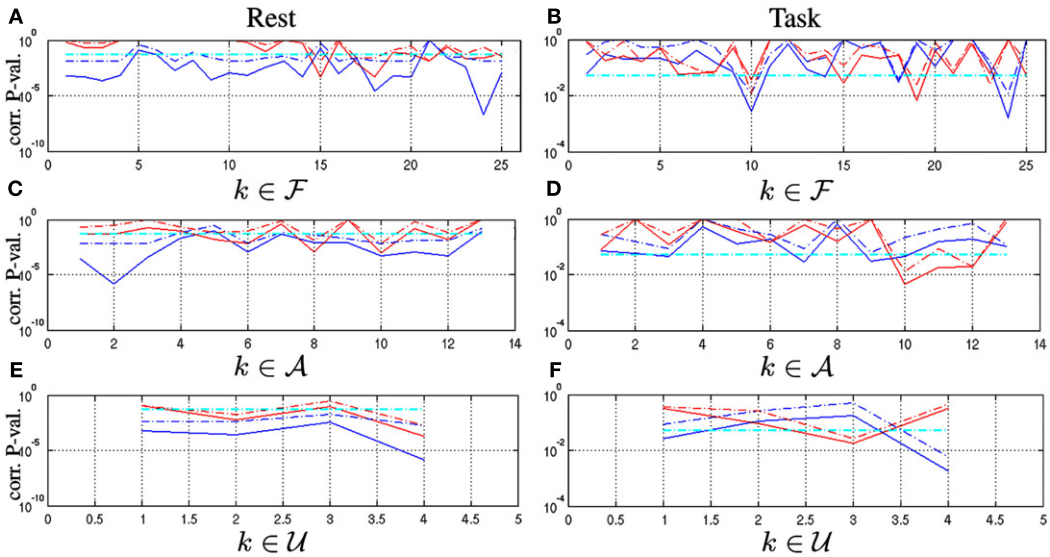

FIGURE 5 | Corrected p-values associated with one-sample Student-t (–,–) and WSR (-.,-.) tests performed on resting-state ([A,C,E]) and task-related multifractal parameters ([B,D,F]) for assessing $H_{0,j}^{(1,\cdot)}$ (blue curves) and $H_{0,j}^{(2,\cdot)}$ (red curves) on the functional ([A-B]), artifactual ([C-D]) and undefined maps ([E-F]), respectively. Significance level ($\alpha = 0.05$) is shown in - -.

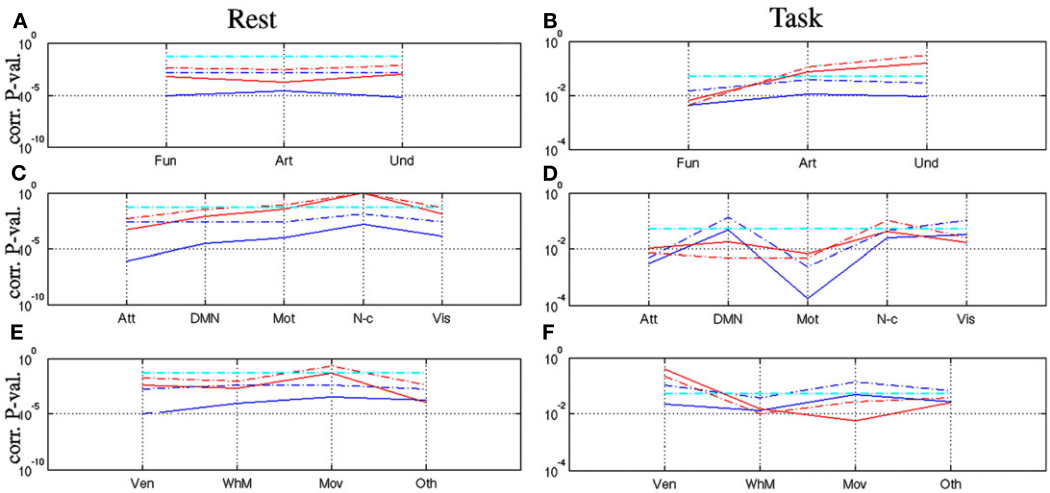

FIGURE 6 | Corrected p-values associated with one-sample Student-t (–,–) and WSR (-.,-.) tests performed on resting-state ([A,C,E]) and task-related multifractal parameters ([B,D,F]) for assessing $H_{0,j}^{(1,\cdot)}$ (blue curves) and $H_{0,j}^{(2,\cdot)}$ (red curves) on the averaged map types ([A-B]), networks $\mathcal{N}$ ([C-D]) and artifact types $\mathcal{T}$ ([E-F]), respectively. Significance level ($\alpha = 0.05$) is shown in - -.

contrast, this observation did not hold for artifacts: when looking at **Figures 6E,F** in detail, the signal related to ventricles became monofractal during task.

5.2.3. 2-way repeated measures ANOVA

In order to assess any significant change of self-similarity or multifractality between rest and task, we entered the subject-dependent parameter estimates ($\hat{c}_{i,k}^{j,s}$) in several 2-way repeated measures ANOVAs involving two factors: brain state (two values: $j = \mathrm{R}, \mathrm{T}$) and map type (with varying number of values). These ANOVAs were conducted separately for assessing self-similarity ($i = 1$) and multifractality ($i = 2$) changes. First six ANOVAs (three for each parameter) were carried out by considering the F/A/U-maps as the second factor, respectively. This second factor thus took a number of values that depends on the set under study: $\mathcal{F}$, $\mathcal{A}$, or $\mathcal{U}$. Results are summarized in **Table 2**. Regarding the analysis of self-similarity ($\hat{c}_{1,k}^{j,s}$ parameters), a significant brain state effect appeared in all F/A/U-maps, and a significant map effect in the F and A-sets. Significant interactions were found for the F and U-maps. This confirms that the level of self-similarity is not sufficient to disentangle functional networks from artifactual or undefined maps.

Table 2 | 2-way repeated measures ANOVA results based on the $\hat{c}_{i,k}^{j,s}$ parameters for $i=\{1,2\}$, $j=$(R,T), $s=1{:}S$, and $k\in\mathcal{F}$ (top), $k\in\mathcal{A}$ (middle), $k\in\mathcal{U}$ (bottom).

Level	Param.	Source	F score	*p*-val.
F-maps	$\hat{c}_{1,k}^{j,s}$	State	9.54	**0.01**
		Map	4.31	**1e-09**
		State × Map	1.76	**0.02**
F-maps	$\hat{c}_{2,k}^{j,s}$	State	0.13	0.73
		Map	1.19	0.25
		State × Map	1.56	**0.04**
A-maps	$\hat{c}_{1,k}^{j,s}$	State	5.73	**0.03**
		Map	2.4	**0.008**
		State × Map	1.32	0.21
A-maps	$\hat{c}_{2,k}^{j,s}$	State	0.09	0.77
		Map	2.4	**0.007**
		State × Map	0.71	0.74
U-maps	$\hat{c}_{1,k}^{j,s}$	State	5.39	**0.04**
		Map	2.91	0.06
		State × Map	3.16	**0.04**
U-maps	$\hat{c}_{2,k}^{j,s}$	State	2.43e-05	0.99
		Map	0.68	0.57
		State × Map	0.63	0.6

Bold font indicates statistically significant results i.e., p-value < 0.05.

Table 3 | 2-way repeated measures ANOVA results based on the $\hat{c}_{i,k}^{j,s}$ parameters for $i=\{1,2\}$, $j=$(R,T), $s=1{:}S$, and $k\in\mathcal{N}$ (top) and $k\in\mathcal{T}$ (bottom).

Level	Param.	Source	F score	p-val.
Networks	$\hat{c}_{1,k}^{j,s}$	State	9.78	**0.01**
		Network	4.18	**0.006**
		State × Network	1.09	0.37
Networks	$\hat{c}_{2,k}^{j,s}$	State	1.013	0.34
		Network	3.18	**0.02**
		State × Network	2.97	**0.03**
Artifacts	$\hat{c}_{1,k}^{j,s}$	State	4.85	**0.05**
		Artifact	2.33	0.09
		State × Artifact	1.16	0.34
Artifacts	$\hat{c}_{2,k}^{j,s}$	State	0.31	0.59
		Artifact	1.03	0.39
		State × Artifact	1.085	0.37

Bold font indicates statistically significant results i.e., p-value < 0.05.

As regards ANOVAs based on $\hat{c}_{2,k}^{j,s}$ parameters, a significant interaction for F-maps is found, thus indicating that the averaged change in multifractality between rest and task is significant for functional maps only. In summary, only F-maps exhibited significant interactions for both multifractal attributes.

Akin to the one-sample analyses above, we looked at a larger spatial scale, the functional network, and artifact type levels and performed similar ANOVAs, corresponding results are reported in **Table 3**. While both functional networks and artifacts demonstrate a significant change in the self-similarity parameter between rest and task, only functional networks made the map type effect significant. More importantly, the key feature for discriminating functional networks from artifacts relied on ANOVAs based on $\hat{c}_{2,k}^{j,s}$ parameters. Indeed, a significant network effect and more importantly a significant interaction between rest and task are observed in functional networks.

5.2.4. Two-sample statistical tests

To localize which maps are responsible for statistically significant ANOVA results, we finally performed two-sample T-tests in which we tested the following null hypotheses:

$$\begin{cases} \widetilde{H}_0^{(1,k)} : \mu_{1,k}^{\mathrm{R}} = \mu_{1,k}^{\mathrm{T}},\ \forall k \in \mathcal{F}\cup\mathcal{A}\cup\mathcal{U} \\ \widetilde{H}_0^{(2,k)} : \mu_{2,k}^{\mathrm{R}} = \mu_{2,k}^{\mathrm{T}},\ \forall k \in \mathcal{F}\cup\mathcal{A}\cup\mathcal{U}. \end{cases} \tag{17}$$

We also conducted similar tests at the macroscopic level ($k\in\mathcal{N}\cup\mathcal{T}$) by replacing $\mu_{i,k}^{j}$ with $\bar{\mu}_{i,k}^{j}$ in the null hypotheses (17). The fluctuations in self-similarity being systematically in the same direction between rest and task, we performed one-sided tests as regards the $\mu_{1,k}^{j}$'s while two-sided tests were considered for the $\mu_{2,k}^{j}$'s: task-related positive and negative fluctuations of $\mu_{2,k}^{j}$ were actually observed in Subsection 5.2.1. **Figures 7A,B** shows the uncorrected p-values for the F-maps and networks, respectively. We rejected $\widetilde{H}_0^{(1,k)}$ for ($\boldsymbol{f}_3$, $\boldsymbol{f}_4$, $\boldsymbol{f}_{11}$, $\boldsymbol{f}_{18}$, $\boldsymbol{f}_{25}$) at a significance level set to $\alpha_1=0.01$ and $\widetilde{H}_0^{(2,k)}$ for ($\boldsymbol{f}_4$, $\boldsymbol{f}_7$, $\boldsymbol{f}_{18}$) at $\alpha_2=0.05$. These components clearly explain significant results reported in **Table 2** about the changes in self-similarity and multifractality that occurred in F-maps. Interestingly, among the latter, the null hypothesis was rejected because of a large increase of multifractality in ($\boldsymbol{f}_4$, $\boldsymbol{f}_7$). In contrast, a decrease of multifractality was responsible for the rejection of $\widetilde{H}_0^{(2,k)}$ in $\boldsymbol{f}_{18}$. When setting $\alpha_2=\alpha_1=0.01$, only $\boldsymbol{f}_{18}$ survived this threshold and thus remained the single functional component for which a significant difference of self-similarity and multifractality was found between rest and task. This component clearly drove the significant interaction reported in **Table 2** for the change in multifractality in F-maps. **Figure 7B** also showed that the state effect reported in **Table 3** on ($\hat{c}_{1,k}^{j,s}$) at the network level was driven by the attentional, motor, and visual systems. Last, the significant interaction reported in **Table 3** on ($\hat{c}_{2,k}^{j,s}$) is explained by the non-cortical regions as shown in **Figure 7B**.

Figures 7C,D shows the localization of the state effects reported in **Tables 2** and **3** for the changes in self-similarity that occurred in artifacts at the local and global levels. No A-map enabled to reject $\widetilde{H}_0^{(1,k)}$ at the α_1 significance level but a majority of A-maps ($\boldsymbol{a}_{1:4}$, $\boldsymbol{a}_6$, $\boldsymbol{a}_8$, $\boldsymbol{a}_{10}$, $\boldsymbol{a}_{12}$) contributed to the significant state effect observed in **Table 2**. At the global artifact level, the ventricles appear as the main source of the significant state effect reported in **Table 3** for the change in self-similarity. Also, no significant difference in multifractality was reported for artifacts whatever the observation level (A-maps or averaged artifacts). Similarly, **Figure 7E** enables us to show that $\boldsymbol{u}_2$ and $\boldsymbol{u}_4$ were the main sources of the significant state effect and interactions reported in **Table 2** for the change in self-similarity. At the macroscopic level, we finally observed in **Figure 7F** that only the grand mean of functional maps leads to a

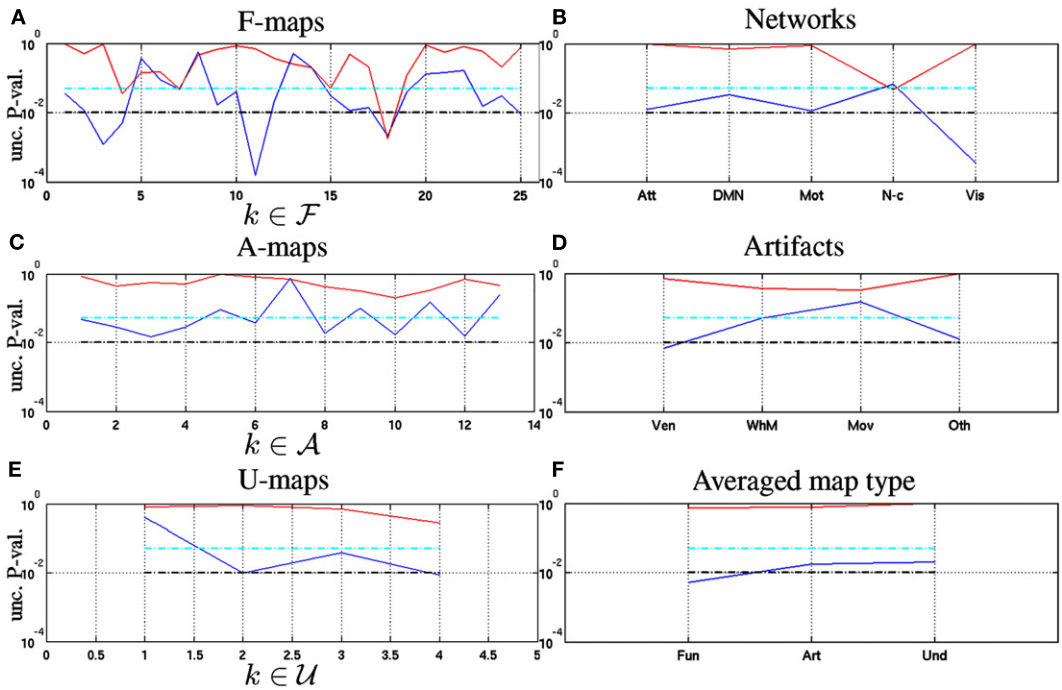

FIGURE 7 | Uncorrected p-values associated with two-samples Student-t test performed between resting-state and task-related multifractal parameters for assessing $\widetilde{H}_0^{(1,\cdot)}$ (blue curves) and $\widetilde{H}_0^{(2,\cdot)}$ (red curves) on the functional (A), artifactual (C) and undefined maps (E), respectively. Similar tests were computed at a broader spatial scale on the functional networks **(B)**, the artifacts **(D)** and the averaged map types **(F)**, respectively. Significance levels ($\alpha_1 = 0.01$ and $\alpha_2 = 0.05$) are shown in - - and - -, respectively.

significant modulation of self-similarity between rest and task at level α_1.

6. DISCUSSION

6.1. RESULTS INTERPRETATION

This study analyzed in-depth the scale-free properties of fMRI signals, using multifractal methodologies, and their modulations during rest and task both in functional networks and artifactual regions. The underlying goal was to finely characterize which properties are specific to functional networks and which modulation can be expected for these networks from task-related activity. Previous attempts in the literature (Cordes et al., 2001; Leopold et al., 2003; He, 2011) focused on functional networks without comparing results with the behavior of artifacts. The main reason comes from the fact that seed region analyses were only conducted in such studies. Hence, no comparison with vascular or ventricles-related signals was undertaken.

Our results confirmed that fMRI signals are stationary and self-similar but not specifically in functional networks. Also we showed that the amount of self-similarity significantly varies between rest and task not only in functional networks involved in our auditory detection task with a motor response (Attentional, Motor) but also quite surprisingly in the visual system and in some artifacts (ventricles) and undefined maps. This observation led us to investigate the scale-free structure of fMRI signals using richer models, namely multifractal processes, to which the WLMF toolbox is dedicated. Our statistical results demonstrate first that fMRI signals are multifractal, second that interactions between brain state and maps only occurred in F-maps and functional networks and third, that specific F-maps such as in non-cortical regions demonstrated a statistically significant fluctuation between rest and task. This result shows that the concept of multifractality permits to disentangle functional components from artifactual ones, in a robust and significant manner.

However, in contrast to self-similarity that systematically decreases with evoked activity, multifractality decreases in cortical (f_{18}) but increases in non-cortical (f_4, f_7). Thus, task-related activity has no systematic impact with respect to increase/decrease of multifractality. Interestingly, we found a statistically non-significant trend toward a decrease of multifractality in regions primarily involved in the task (f_{12}, f_{24}, f_{25}). However, the group size of this study remains small (12 subjects only) to achieve significant results, mainly because of the between-subject variability and of the difficulty in estimating $\hat{c}_{2,k}^{j,s}$ parameters on short time series.

Further investigations beyond the scope of this paper are necessary to find out any general trend on the direction change of multifractality with evoked activity by cross-correlating multifractal parameters with task-related activity (e.g., group-level Z-scores) and task performance. However, to derive reliable results for multifractality, a larger group of individuals will be considered and a larger number of scans will be acquired while maintaining the same scanning time: To this end, accelerated SENSE imaging will be used together with recent reconstruction algorithms so as to improve temporal resolution (Chaari et al., 2011b).

6.2. MONOFRACTAL SCALE-FREE EEG MICROSTATE SEQUENCES VS. MULTIFRACTAL DYNAMICS FOR RSN

The results obtained in this contribution shows multifractal temporal dynamics in fMRI signals and thus naturally lead to question the potential origins and generative mechanisms for this departure from the more traditional long-range correlation modeling of scale invariance. A natural track to inspect consists of that of the relations between hemodynamic (fMRI) and electrical (EEG) signatures for brain activity at rest. This question has been intensively studied over the last decade (Laufs et al., 2003; Mantini et al., 2007; Britz et al., 2010; Musso et al., 2010; Van de Ville et al., 2010; Yuan et al., 2012), first by measuring cross correlations between fMRI data at rest and EEG-informed regressors derived from the convolution of the EEG power signal in five well-identified frequency bands ($\delta \in (1,4)$ Hz, $\theta \in (4,7)$ Hz, $\alpha \in (8,12)$ Hz, $\beta \in (13,30)$ Hz, and $\gamma > 30$ Hz) with the canonical HRF. This approach revealed the negative correlation of α-band activity with the attentional network and the positive correlation with β_2-band with the default mode network (precuneus and posterior cingulate cortex; Laufs et al., 2003). Also, Mantini et al. (2007) showed that functional resting-state networks have different EEG signatures which are not specific to a given frequency band but are rather spread over several oscillations regimes (e.g., correlation between α and β power in specific RSN), a consequence of the so-called oscillation hierarchy (Buzsáki, 2006) and the of phase-amplitude cross-frequency coupling (He et al., 2010). However, none of these works enable to explain the low frequency fluctuations ($<$0.1 Hz) or scale-free dynamics of the fMRI signal at rest, because this phenomenon is much more widespread than oscillations.

Scale-free dynamics of brain electrical activity at rest has recently been studied (Van de Ville et al., 2010) but not directly on raw data. Instead, EEG microscates that correspond to short periods (100 ms) during which the EEG scalp topography remains quasi-stable, have been first segmented. Remarkably, it has been shown that only four different EEG microstate patterns are necessary to describe the ongoing electrical brain activity at rest (Britz et al., 2010) and that these four microscates correlate with well-known RSNs, which were classically identified from fMRI dataset alone using group-level ICA. This demonstrated that the EEG microstate with rapid fluctuations might be considered as the electrophysiological signature of intrinsic functional connectivity patterns. The investigation of scale-free dynamics was thus performed on the EEG microstate sequence to understand how fast the microscates are changing and what kind of correlation structure (short or long-range) they bring (Van de Ville et al., 2010).

The recent finding that EEG microscate sequences reveal purely monofractal dynamics (Van de Ville et al., 2010), irrespective of the data filtering, may lead to conclude that the same monofractal behavior in the fMRI signature of RSN (strongly correlate with these microstates) should be expected, if one assumes a linear and time invariant HRF model for the neurovascular coupling. However, the results obtained in the present contribution can be considered not only as evidence in favor of multifractality in fMRI data, but also as evidence that this multifractal effect is discriminant of cortical versus non-cortical regions and characteristic of functional network with respect to modulation under task.

Several factors may explain this apparent discrepancy. First, an accurate comparison of both sets of result would require a precise match of the range of scales (or frequencies) within which scale invariance is analyzed and corresponding parameters measured. Here, the selected range of frequencies corresponds to ([0.008,0.063]Hz), while the monofractal behavior of EEG microstate sequences was exhibited on a distinct frequency range, i.e. ([0.063, 3.9]Hz) in Van de Ville et al. (2010). Comparison of scaling properties requires that the same frequency range is selected but this constraint is clearly not tenable across modalities like EEG and fMRI given the fMRI sampling rate.

Second, it is indeed very unlikely that a linear and time invariant filtering may create multifractality in fMRI starting from a monofractal electrophysiological signal in EEG. The general issue of the relations between (linear and non-linear) filtering and multifractality were barely studied theoretically so far but interestingly, Abry et al. has shown that simple non-linear filter can turn mono- into multifractality. Hence, another putative origin for the apparent contradiction between our findings and those in Van de Ville et al. (2010) lies in refined descriptions of HRF model by non-linear dynamical systems (e.g., Balloon model; Buxton et al., 1998, 2004). Of course, linear and stationary approximations like the canonical HRF model (Glover, 1999) or non-parametric alternatives (Vincent et al., 2010; Chaari et al., 2011a) have been validated but only on evoked activity and considering inter-stimulus intervals larger than 3 s. For shorter ISIs, non-linear hemodynamics has turned out to be a valid property (Liu and Gao, 2000). In this context, habituation, or repetition suppression effects may occur and induce a sublinear hemodynamic response, which would modify scaling properties (Dehaene-Lambertz et al., 2006; Ciuciu et al., 2009). Hence, by modeling the sequence of EEG transient brain states as a series of short *time epochs*, this could induce non-linearities in the hemodynamic system that could explain the switch from purely fractal EEG microstates to multifractal signatures in the corresponding RSNs.

Third, instead of segregating EEG microstates in multiple groups based upon the maximal spatial dissimilarity between groups (Britz et al., 2010; Musso et al., 2010), a more recent analysis of joint EEG/fMRI resting-state data has revealed a larger number (thirteen) of EEG microstates that show temporal independence from each other (Yuan et al., 2012). In this latter work, all resting-state networks including visual, motor, auditory, attention, saliency and default mode networks were characterized by a specific electrophysiological signature involving several EEG microstates. This clearly indicates that the original analysis of scale-free dynamics for EEG microscates done in Van de Ville et al. (2010) should be revisited on this larger number of metastable states to disentangle whether multifractality in this larger set of microstates has been discarded due to averaging effects. It is actually clear that the sequence mixing thirteen different microstates may generate richer *singularities* (abrupt changes between microstates) than the ones relying on four microstates only. Fourth, the temporal signatures of EEG microstates found in Musso et al. (2010), Van de Ville et al. (2010) are correlated in time since the spatial similarity was the key factor to identify

them. As a consequence, the microstate sequences is correlated too and might loose some singularities that could be found out in the microstate sequences generated by Yuan et al. (2012). Finally, the presence of multifractality in resting-state (and task-related) MEG data has been evidenced in the sensor space in Zilber et al. (2012). These findings open new research avenues: For instance, it is natural to explore whether the observed multifractal properties can be related multiplicative cascade processes, that is to one of the only practical mechanism known to generate multifractal dynamics, or to investigate whether this cascade takes place at meso or macroscopic scales, as well as to figure out how brain networks could implement such cascade mechanisms. This topic is beyond the scope of the present contribution, however the log-normal statistics of neuronal firing rate could provide us with a first clue to uncover any generative process underlying multifractal dynamics.

6.3. STATIONARITY VS. NON-STATIONARITY OF THE RSN DYNAMICS

Recent results in resting-state fMRI reveal temporally independent functional modes of spontaneous brain activity (Smith et al., 2012) and postulate the presence of temporally non-stationary modes in part of the default mode network by resorting to high temporal resolution fMRI. While stationarity receives a unique and clear definition, non-stationarity can correspond to a bunch of different situations; for example, non-stationarity might (i) refer to an apparent change over time in the correlation between two regions or (ii) refer to changes in the mean and/or variance in the time course of a functional network.

The wavelet based analysis of scaling proposed here already addresses a number of such situations. The fact that the estimated Hurst coefficient of fMRI time series remains consistently below 1 indicates that fMRI signals at hand here are better modeled as a stationary step process Y rather than as a non-stationary random walk X. Further, wavelet analysis are known to bring robustness against various forms of non-stationarities, such as smooth trends superimposed to data, to mean or variance modulation (c.f. *(ii)*). The multifractal analysis performed here is thus not impaired by such form of non-stationarities. This leaves open issues such as the presence of oscillations superimposed to scaling. Given that time series are very short, the use of formal stationarity test will lack power and are not likely to reject stationarity. Further, in all the analysis conducted in the present work, no evidence of non-stationarity in the fMRI time series at hand were evidenced. This is in agreement with what has been reported in He (2011) in an fMRI ROI-based analysis. Finally, previous attempts to scale-free analysis of densely sampled fMRI datasets in time (using the EVI sequence; Rabrait et al., 2008) already confirmed the validity of a the stationarity assumption; see Ciuciu et al. (2008).

7. CONCLUSION

We uncovered multifractal scale-free dynamics of fMRI time series over four octaves (15–125 s) both in functional networks and in artifacts. We then disentangled functional components from artifactual ones in a robust and significant manner by demonstrating that only the former gave rise to significant modulations of the multifractal attributes between rest and task-related activity. Variability in human performance scores also generally exhibits power-law distributions, whose strength (or exponent) is often modulated across conditions and tasks (Holden et al., 2011). This paves the way toward future works devoted to investigating the extent to which behavioral properties are correlated with the change of scale-free dynamics in neuroimaging time series (MEG, fMRI) acquired during multisensory learning (Seitz et al., 2007).

ACKNOWLEDGMENTS

The authors thank the French National Research Agency (ANR) for its financial support to the SCHUBERT (ANR-09-JCJC-0071) young researcher project (2009-13). The authors are also grateful to the anonymous reviewers and the associate editor, Dr. BJ He, for their remarks and criticisms that helped us to improve the manuscript and enlarge the readership. Finally, we would like to warmly thank Dr. V. van Wassenhove for her careful rereading and constructive comments.

REFERENCES

Abry, P., Baraniuk, R., Flandrin, P., Riedi, R., and Veitch, D. (2002). Multiscale network traffic analysis, modeling, and inference using wavelets, multifractals, and cascades. *IEEE Signal Process. Mag.* 3, 28–46.

Abry, P., Gonçalvès, P., and Flandrin, P. (1995). *Wavelets, Spectrum Estimation and 1/f Processes,* Chap. 103. Springer-Verlag, NY: Wavelets and Statistics, Lecture Notes in Statistics.

Abry, P., Veitch, D., and Flandrin, P. (1998). Long-range dependence: revisiting aggregation with wavelets. *J. Time Ser. Anal.* 19, 253–266.

Achard, S., Salvador, R., Whitcher, B., Suckling, J., and Bullmore, E. (2006). A resilient, low-frequency, small-world human brain functional network with highly connected association cortical hubs. *J. Neurosci.* 26, 63–72.

Arneodo, A., Audit, B., Decoster, N., Muzy, J.-F., and Vaillant, C. (2002). "Wavelet-based multifractal formalism: applications to dna sequences, satellite images of the cloud structure and stock market data," in *The Science of Disasters*, eds A. Bunde, J. Kropp, and H. J. Schellnhuber (Springer), 27–102.

Bacry, E., Delour, J., and Muzy, J. (2001). Multifractal random walk. *Phys. Rev. E Stat. Nonlin. Soft Matter Phys.* 64, 026103.

Bak, P., and Paczuski, M. (1995). Complexity, contingency, and criticality. *Proc. Natl. Acad. Sci. U.S.A.* 92, 6689–6696.

Barral, J., and Mandelbrot, B. (2002). Multifractal products of cylindrical pulses. *Probab. Theor. Relat. Fields* 124, 409–430.

Beckmann, C., and Smith, S. (2004). Probabilistic independent component analysis for functional magnetic resonance imaging. *IEEE Trans. Med. Imaging* 23, 137–152.

Biswal, B., Zerrin Yetkin, F., Haughton, V., and Hyde, J. (1995). Functional connectivity in the motor cortex of resting human brain using echo-planar MRI. *Magn. Reson. Med.* 34, 537–541.

Britz, J., Van De Ville, D., and Michel, C. M. (2010). BOLD correlates of EEG topography reveal rapid resting-state network dynamics. *Neuroimage* 52, 1162–1170.

Bullmore, E., Long, C., Suckling, J., Fadili, J., Calvert, G., Zelaya, F., Carpenter, T., and Brammer, M. (2001). Colored noise and computational inference in neurophysiological (fMRI) time series analysis: resampling methods in time and wavelet domains. *Hum. Brain Mapp.* 12, 61–78.

Bullmore, E., and Sporns, O. (2009). Complex brain networks: graph theoretical analysis of structural and functional systems. *Nat. Rev. Neurosci.* 10, 186–198.

Bullock, T., Mcclune, M., and Enright, J. (2003). Are the electroencephalograms mainly rhythmic? Assessment of periodicity in wide-band time series. *Neuroscience* 121, 233–252.

Buxton, R. B., Uludag, K., Dubowitz, D. J., and Liu, T. T. (2004). Modeling the hemodynamic response to brain activation. 23(Suppl. 1), S220–S233.

Buxton, R. B., Wong, E. C., and Frank, L. R. (1998). Dynamics of blood flow and oxygenation changes during brain activation: the balloon model. *Magn. Reson. Med.* 39, 855–864.

Buzsáki, G. (2006). *Rhythms of the Brain.* New York: Oxford university Press.

Calhoun, V. D., Adali, T., Pearlson, G. D., and Pekar, J. J. (2001). A method for making group inferences from functional MRI data using independent component analysis. *Hum. Brain Mapp.* 14, 140–151.

Chaari, L., Forbes, F., Vincent, T., Dojat, M., and Ciuciu, P. (2011a). "Variational solution to the joint detection estimation of brain activity in fMRI," in *14th MICCAI'11, LNCS 6892 (Part II)* (Toronto: Springer Verlag), 260–268.

Chaari, L., Pesquet, J.-C., Benazza-Benyahia, A., and Ciuciu, P. (2011b). A wavelet-based regularized reconstruction algorithm for SENSE parallel MRI with applications to neuroimaging. *Med. Image Anal.* 15, 185–201.

Chainais, P., Riedi, R., and Abry, P. (2005). On non scale invariant infinitely divisible cascades. *IEEE Trans. Inform. Theor.* 51, 1063–1083.

Chialvo, D. R. (2004). Critical brain networks. *Physica A* 340, 756–765.

Chialvo, D. R. (2010). Emergent complex neural dynamics. *Nat. Phys.* 6, 744–750.

Ciuciu, P., Abry, P., Rabrait, C., and Wendt, H. (2008). Log Wavelet Leaders Cumulant Based Multifractal Analysis of EVI fMRI Time Series: Evidence of Scaling in Ongoing and Evoked Brain Activity. *IEEE J. Sel. Top. Signal Process.* 2, 929–943.

Ciuciu, P., Sockeel, S., Vincent, T., and Idier, J. (2009). "Modelling the neurovascular habituation effect on fMRI time series," in *Proceedings of the 34th IEEE International Conference on Acoustic, Speech and Signal Processing,* (Taipei: IEEE Conference Publications), 433–436.

Cole, D. M., Smith, S. M., and Beckmann, C. F. (2010). Advances and pitfalls in the analysis and interpretation of resting-state FMRI data. *Front. Syst. Neurosci.* 4:8. doi:10.3389/fnsys.2010.00008

Cordes, D., Haughton, V., Arfanakis, K., Carew, J., Turski, P., Moritz, C., Quigley, M., and Meyerand, M. (2001). Frequencies contributing to functional connectivity in the cerebral cortex in "resting-state" data. *AJNR Am. J. Neuroradiol.* 22, 1326–1333.

Dale, A. M. (1999). Optimal experimental design for event-related fMRI. *Hum. Brain Mapp.* 8, 109–114.

Damoiseaux, J. S., Rombouts, S. A., Barkhof, F., Scheltens, P., Stam, C. J., Smith, S. M., and Beckmann, C. F. (2006). Consistent resting-state networks across healthy subjects. *Proc. Natl. Acad. Sci. U.S.A.* 103, 13848–13853.

Daubechies, I., Roussos, E., Takerkart, S., Benharrosh, M., Golden, C., D'Ardenne, K., Richter, W., Cohen, J. D., and Haxby, J. (2009). Independent component analysis for brain fmri does not select for independence. *Proc. Natl. Acad. Sci. U.S.A.* 106, 10415–10422.

Dehaene-Lambertz, G., Dehaene, S., Anton, J.-L., Campagne, A., Ciuciu, P., Dehaene, G. P., Denghien, I., Jobert, A., Le Bihan, D., Sigman, M., Pallier, C., and Poline, J.-B. (2006). Functional segregation of cortical language areas by sentence repetition. *Hum. Brain Mapp.* 27, 360–371.

Eguiluz, V. M., Chialvo, D. R., Cecchi, G. A., Baliki, M., and Apkarian, A. V. (2005). Scale-free brain functional networks. *Phys. Rev. Lett.* 94, 1–4.

Eke, A., Herman, P., Kocsis, L., and Kozak, L. R. (2002). Fractal characterization of complexity in temporal physiological signals. *Physiol. Meas.* 23, R1–R38.

Fadili, J., and Bullmore, E. (2002). Wavelet-generalized least squares: a new BLU estimator of linear regression models with 1/f errors. *Neuroimage* 15, 217–232.

Fox, M. D., Snyder, A. Z., Vincent, J. L., and Raichle, M. E. (2007). Intrinsic fluctuations within cortical systems account for intertrial variability in human evoked brain responses. *Proc. Natl. Acad. Sci. U.S.A.* 56, 171–184.

Friston, K., Holmes, A. P., Worlsey, K., Poline, J.-B., Frith, C., and Frackowiak, R. (1995). Statistical parametric maps in functional neuroimaging: a general linear approach. *Hum. Brain Mapp.* 2, 189–210.

Glover, G. H. (1999). Deconvolution of impulse response in event-related BOLD fMRI. *Neuroimage* 9, 416–429.

Greicius, M., Krasnow, B., Reiss, A., and Menon, V. (2003). Functional connectivity in the resting brain: a network analysis of the default mode hypothesis. *Proc. Natl. Acad. Sci. U.S.A.* 100, 253–258.

He, B. (2011). Scale-free properties of the functional magnetic resonance imaging signal during rest and task. *J. Neurosci.* 31, 13786–13795.

He, B., Zempel, J., Snyder, A., and Raichle, M. (2010). The temporal structures and functional significance of scale-free brain activity. *Neuron* 66, 353–369.

Hebiri, M., and van de Geer, S. (2011). The smooth-lasso and other $1+2$-penalized methods. *Electron. J. Stat.* 5, 1184–1226.

Holden, J. G., Choi, I., Amazeen, P. G., and Van Orden, G. (2011). Fractal $1/f$ dynamics suggest entanglement of measurement and human performance. *J. Exp. Psychol. Hum. Percept. Perform.* 37, 935–948.

Kiviniemi, V., Kantola, J., Jauhiainen, J., Hyvärinen, A., and Tervonen, O. (2003). Independent component analysis of nondeterministic fMRI signal sources. *Neuroimage* 19, 253–260.

Laufs, H., Krakow, K., Sterzer, P., Eger, E., Beyerle, A., Salek-Haddadi, A., and Kleinschmidt, A. (2003). Electroencephalographic signatures of attentional and cognitive default modes in spontaneous brain activity fluctuations at rest. *Proc. Natl. Acad. Sci. U.S.A.* 100, 11053–11058.

Leopold, D., Murayama, Y., and Logothetis, N. (2003). Very slow activity fluctuations in monkey visual cortex: implications for functional brain imaging. *Cereb. Cortex* 13, 422–433.

Linkenkaer-Hansen, K., Nikouline, V., Palva, J., and Ilmoniemi, R. (2001). Long-range temporal correlations and scaling behavior in human brain oscillations. *J. Neurosci.* 21, 1370–1377.

Liu, H.-L., and Gao, J.-H. (2000). An investigation of the impulse functions for the nonlinear BOLD response in functional MRI. *Magn. Reson. Imaging* 18, 11053–11058.

Makni, S., Ciuciu, P., Idier, J., and Poline, J.-B. (2005). Joint detection-estimation of brain activity in functional MRI: a multichannel deconvolution solution. *IEEE Trans. Signal Process.* 53, 3488–3502.

Makni, S., Idier, J., Vincent, T., Thirion, B., Dehaene-Lambertz, G., and Ciuciu, P. (2008). A fully Bayesian approach to the parcel-based detection-estimation of brain activity in fMRI. *Neuroimage* 41, 941–969.

Mallat, S. (2009). *A Wavelet Tour of Signal Processing: The Sparse Way.* Burlington, MA: Academic Press.

Mandelbrot, B., and van Ness, J. (1968). Fractional Brownian motion, fractional noises and applications. *SIAM Rev. Soc. Ind. Appl. Math.* 10, 422–437.

Mantini, D., Perrucci, M. G., del Gratta, C., Romani, G. L., and Corbetta, M. (2007). Electrophysiological signatures of resting state networks in the human brain. *Proc. Natl. Acad. Sci. U.S.A.* 104, 13170–13175.

Maxim, V., Sendur, L., Fadili, J., Suckling, J., Gould, R., Howard, R., and Bullmore, E. (2005). Fractional Gaussian noise, functional MRI and Alzheimer's disease. *Neuroimage* 25, 141–158.

McKeown, M., Makeig, S., Brown, G., Jung, T., Kindermann, S., Bell, A., and Sejnowski, T. (1998). Analysis of fMRI data by blind separation into independent spatial components. *Hum. Brain Mapp.* 6, 160–188.

Musso, F., Brinkmeyer, J., Mobascher, A., Warbrick, T., and Winterer, G. (2010). Spontaneous brain activity and EEG microstates. A novel EEG/fMRI analysis approach to explore resting-state networks. *Neuroimage* 52, 1149–1161.

Rabrait, C., Ciuciu, P., Ribès, A., Poupon, C., Leroux, P., Lebon, V., Dehaene-Lambertz, G., Le Bihan, D., and Lethimonnier, F. (2008). High temporal resolution functional MRI using parallel echo volume imaging. *J. Magn. Reson. Imaging* 27, 744–753.

Rosen, B. R., Buckner, R. L., and Dale, A. M. (1998). Event-related functional MRI: past, present and future. *Proc. Natl. Acad. Sci. U.S.A.* 95, 773–780.

Sadaghiani, S., Hesselmann, G., and Kleinschmidt, A. (2009). Distributed and antagonistic contributions of ongoing activity fluctuations to auditory stimulus detection. *J. Neurosci.* 29, 13410–13417.

Samorodnitsky, G., and Taqqu, M. (1994). *Stable Non-Gaussian Random Processes.* New York: Chapman and Hall.

Seitz, A., Kim, R., van Wassenhove, V., and Shams, L. (2007). Simultaneous and independent acquisition of multisensory and unisensory associations. *Perception* 36, 1445–1453.

Shimizu, Y., Barth, M., Windischberger, C., Moser, E., and Thurner, S. (2004). Wavelet-based multifractal analysis of fMRI time series. *Neuroimage* 22, 1195–1202.

Smith, S. M., Fox, P. T., Miller, K. L., Glahn, D. C., Fox, P. M., Mackay, C. E., Filippini, N., Watkins, K. E., Toro, R., Laird, A. R., and Beckmann, C. F. (2009). Correspondence of the brain's functional architecture during activation and rest. *Proc. Natl. Acad. Sci. U.S.A.* 106, 13040.

Smith, S. M., Miller, K. L., Moeller, S., Xu, J., Auerbach, E. J., Woolrich, M. W., Beckmann, C. F., Jenkinson, M., Andersson, J., Glasser, M. F., Van Essen, D. C., Feinberg, D. A., Yacoub, E. S., and Ugurbil, K. (2012).

Temporally-independent functional modes of spontaneous brain activity. *Proc. Natl. Acad. Sci. U.S.A.* 109, 3131–3136.

Stam, C. J., and de Bruin, E. A. (2004). Scale-free dynamics of global functional connectivity in the human brain. *Hum. Brain Mapp.* 22, 97–109.

Thurner, S., Windischberger, C. Moser, E., Walla, P., and Barth, M. (2003). Scaling laws and persistence in human brain activity. *Physica A* 326, 511–521.

Van de Ville, D., Britz, J., and Michel, C. M. (2010). EEG microstate sequences in healthy humans at rest reveal scale-free dynamics. *Proc. Natl. Acad. Sci. U.S.A.* 107, 18179–18184.

Varoquaux, G., Gramfort, A., Pedregosa, F., Michel, V., and Thirion, B. (2011). Multi-subject dictionary learning to segment an atlas of brain spontaneous activity. *Inf. Process. Med. Imaging* 22, 562–573.

Varoquaux, G., Keller, M., Poline, J., Ciuciu, P., and Thirion, B. (2010a). "ICA-based sparse features recovery from fMRI datasets," in *Proceedings of the 7th IEEE International Symposium on Biomedical Imaging*, Rotterdam, 1177–1180.

Varoquaux, G., Sadaghiani, S., Pinel, P., Kleinschmidt, A., Poline, J.-B., and Thirion, B. (2010b). A group model for stable multi-subject ICA on fMRI datasets. *Neuroimage* 51, 288–299.

Veitch, D., and Abry, P. (2001). A statistical test for the time constancy of scaling exponents. *IEEE Trans. Signal Process.* 49, 2325–2334.

Vincent, T., Risser, L., and Ciuciu, P. (2010). Spatially adaptive mixture modeling for analysis of within-subject fMRI time series. *IEEE Trans. Med. Imaging* 29, 1059–1074.

Wendt, H., Abry, P., and Jaffard, S. (2007). Bootstrap for empirical multifractal analysis. *IEEE Signal Process. Mag.* 24, 38–48.

Wink, A.-M., Bullmore, E., Barnes, A., Bernard, F., and Suckling, J. (2008). Monofractal and multifractal dynamics of low frequency endogenous brain oscillations in functional MRI. *Hum. Brain Mapp.* 29, 791–801.

Yuan, H., Zotev, V., Phillips, R., Drevets, W. C., and Bodurka, J. (2012). Spatiotemporal dynamics of the brain at rest – exploring EEG microstates as electrophysiological signatures of BOLD resting state networks. *Neuroimage* 60, 2062–2072.

Zarahn, E., Aguirre, G. K., and D'Esposito, M. (1997). Empirical analysis of BOLD fMRI statistics. I. Spatially unsmoothed data collected under null-hypothesis conditions. *Neuroimage* 5, 179–197.

Zemanová, L., Zhou, C., and Kurths, J. (2006). Structural and functional clusters of complex brain networks. *Physica D* 224, 202–212.

Zilber, N., Ciuciu, P., Abry, P., and van Wassenhove, V. (2012). "Modulation of scale-free properties of brain activity in MEG," in *Proceedings of the 9th IEEE International Symposium on Biomedical Imaging*, Barcelona, 1531–1534.

Conflict of Interest Statement: The authors declare that there search was conducted in the absence of any commercial or financial relationships that could be construed as a potential conflict of interest.

Received: 10 February 2012; accepted: 19 May 2012; published online: 15 June 2012.

Citation: Ciuciu P, Varoquaux G, Abry P, Sadaghiani S and Kleinschmidt A (2012) Scale-free and multifractal time dynamics of fMRI signals during rest and task. Front. Physio. ***3****:186. doi: 10.3389/fphys.2012.00186*

This article was submitted to Frontiers in Fractal Physiology, a specialty of Frontiers in Physiology.

frontiers in
PHYSIOLOGY

ORIGINAL RESEARCH ARTICLE
published: 30 July 2012
doi: 10.3389/fphys.2012.00307

What kind of noise is brain noise: anomalous scaling behavior of the resting brain activity fluctuations

Daniel Fraiman [1,2] ***and Dante R. Chialvo*** [1,3,4]*

[1] *Consejo Nacional de Investigaciones Científicas y Tecnológicas, Rosario, Argentina*
[2] *Departamento de Matemática y Ciencias, Universidad de San Andrés, Buenos Aires, Argentina*
[3] *Facultad de Ciencias Médicas, Universidad Nacional de Rosario, Rosario, Argentina*
[4] *David Geffen School of Medicine, University of California, Los Angeles, CA, USA*

Edited by:
Tjeerd W. Boonstra, University of New South Wales, Australia

Reviewed by:
Bruce West, US Army Research Office, USA
Michael Breakspear, The University of New South Wales, Australia

***Correspondence:**
Dante R. Chialvo, Consejo Nacional de Investigaciones Científicas y Tecnológicas, Santa Fe 3100, Rosario (2000), Argentina.
e-mail: dchialvo@ucla.edu

The study of spontaneous fluctuations of brain activity, often referred as brain noise, is getting increasing attention in functional magnetic resonance imaging (fMRI) studies. Despite important efforts, much of the statistical properties of such fluctuations remain largely unknown. This work scrutinizes these fluctuations looking at specific statistical properties which are relevant to clarify its dynamical origins. Here, three statistical features which clearly differentiate brain data from naive expectations for random processes are uncovered: First, the variance of the fMRI mean signal as a function of the number of averaged voxels remains constant across a wide range of observed clusters sizes. Second, the anomalous behavior of the variance is originated by bursts of synchronized activity across regions, regardless of their widely different sizes. Finally, the correlation length (i.e., the length at which the correlation strength between two regions vanishes) as well as mutual information diverges with the cluster's size considered, such that arbitrarily large clusters exhibit the same collective dynamics than smaller ones. These three properties are known to be exclusive of complex systems exhibiting critical dynamics, where the spatio-temporal dynamics show these peculiar type of fluctuations. Thus, these findings are fully consistent with previous reports of brain critical dynamics, and are relevant for the interpretation of the role of fluctuations and variability in brain function in health and disease.

Keywords: brain noise, correlations length, criticality, fMRI, scaling

1. INTRODUCTION

It is now recognized that important information can be extracted from the brain spontaneous activity, as exposed by recent analysis (Biswal et al., 1995; Fox and Raichle, 2007; Smith et al., 2009). For instance, the structure and location of large-scale brain networks can be derived from the interaction of cortical regions during rest which closely match the same regions responding to a wide variety of different activation conditions (Fox and Raichle, 2007; Smith et al., 2009). These so-called resting state networks (RSNs) can be reliably computed from the fluctuations of the blood oxygenated level dependent signal (BOLD) signals of the resting brain, with great consistency across subjects (Xiong et al., 1999; Cordes et al., 2000; Beckmann et al., 2005) even during sleep (Fukunaga et al., 2006) or anesthesia (Vincent et al., 2007).

In the same direction, the information content of the brain BOLD signal's variability *per se* is receiving increasing interest. Recently (Garret et al., 2010) it was shown in a group of subjects of different age, that the BOLD signal variability (standard deviation) is a better predictor of the subject age than the average. Furthermore, additional work focused on the relation between the fMRI signal variability and a task performance, concluded that faster and more consistent performers exhibit significantly higher brain variability across tasks than the poorer performing subjects (Garrett et al., 2011). Overall, these results suggest that the understanding of the brain resting dynamics can benefit from a detailed study of the BOLD variability *per se*.

In this work we characterize the statistical properties of the spontaneous BOLD fluctuations and discuss its possible dynamical mechanisms. The paper is organized as follow: in the next section the origin of the data is described as well the pre-processing of the signal. The definitions of regions of interest is described as well as how to construct subsets of different sizes, needed to compute fluctuations. The results section starts with the analysis of the average spontaneous fluctuations for each RSN, which identify anomalous scaling of the variance as a function of the number of elements. Next, this anomaly is explored to determine its origins by studying in detail the temporal correlations in clusters of different sizes. Finally the analysis of the correlation length is described, revealing a distinctive divergence with the size of the cluster considered. The paper close with a discussion of the relevance of the uncovered anomalous scaling for the current views of large scale brain dynamics. For clarity of presentation, the calculations that are not central to the main message of the paper, are presented separately in an Appendix.

2. METHODS

2.1. DATA ACQUISITION

fMRI data was obtained from five healthy right-handed subjects (21–60 years old, mean = 40.2) using a 3T Siemens Trio

whole-body scanner with echo-planar imaging capability and the standard radio-frequency head coil. Subjects were scanned following a typical brain resting state protocol (Fox and Raichle, 2007) lying in the scanner and asked to keep their mind blank, eyes closed, and avoid falling asleep. All participants gave written informed consent to procedures approved by the IRB Committee of the University of Islas Baleares (Mallorca, Spain) who approved the study.

2.2. IMAGE PRE-PROCESSING AND ANALYSIS

In each subject, 240 BOLD images, spaced by 2.5 s, were obtained from $64 \times 64 \times 49$ voxels of dimension 3.4375 mm $\times$ 3.4375 mm $\times$ 3 mm. Pre-processing was performed using FMRIB Expert Analysis Tool [FEAT, Jezzard et al., 2001, http://www.fmrib.ox.ac.uk/fsl], involving motion correction using MCFLIRT; slice-timing correction using Fourier-space time-series phase-shifting; non-brain removal using BET; spatial smoothing using a Gaussian kernel of full-width-half-maximum 5 mm. Brain Images were normalized to standard space with the MNI 152 (average brain image at Montreal Neurological Institute) template using FLIRT (http://www.fmrib.ox.ac.uk/analysis/research/flirt) and resampled to $2 \times 2 \times 2$ mm resolution. Data was band pass filtered (0.01 Hz–0.1 Hz) using a zero lag filter to avoid scanner drift and high frequency artifacts.

2.3. CHOICE OF REGIONS OF INTEREST

It is known that the brain activity fluctuations at rest exhibit large-scale spatial correlations. The presence of these robust correlations is reflected on the coherent activity which determine the spatial domains of the RSN. Therefore, our analysis is focussed on the statistical analysis of the RSN fluctuations. At least since Beckmann et al. (2005). Probabilistic Principal Component Analysis (PICA) is used to identify the eight most relevant RSN. Each component corresponds to a characteristic time series, and its respective spatial Z-score map. Under a Gaussian/Gamma mixture model these Z-maps were thresholded in order to find the locations of the voxels which significantly contribute to each of the eight time-courses [see **Figure 6** in Beckmann et al. (2005)] and used to define the clusters here. This is illustrated in **Figure 1A**, where the depicted regions correspond to the territory covered by each of the RSN extracted in Beckmann et al. (2005) using ICA techniques. For each independent component Z-map we arbitrarily set a threshold that segment the map into isolated regions of different sizes (see **Figure 1B**). The criteria to select regions is arbitrary, but the present results are independent of the selection criteria, as long as the regions belong to the same RSN. Alternatively, functional areas (such as Brodmann areas) can be used to define clusters of different sizes (as for a portion of the results in **Figure 3**). We proceed by using a spatial mask for each of the eight networks to extract the time series of the BOLD fMRI time series. The masks, in **Figure 1**, correspond to the eight most important RSN, namely the visual medial (box a) and lateral (b) cortical areas, the auditory (c), sensory motor (d), default mode (e), executive control (f), and the fronto-parietal right (g) and left (h) regions. Each network is comprised by a variable number of spatial clusters, each cluster composed by a variable number of voxels. For instance the visual RSN (VIS) includes just three relatively large clusters, each one composed by thousand of voxels, contrasting with the Fronto-Parietal Left (FPL) network which involves seven clusters with sizes ranging from a few up to thousands of voxels. **Table 1** shows the thresholds used in each independent component and how many regions have been defined. The results presented in this paper are independent of the particular value of threshold used.

3. RESULTS

To analyze the noise properties, we look at the behavior of the variance and correlations under various manipulations of the size of the ensemble of voxels where these fluctuations occurs. This is a common strategy in other statistical physics problems where very distinctive scaling behavior can be observed depending of the type of fluctuations the system is able to exhibit (Stanley, 1987).

3.1. ANOMALOUS SCALING OF THE VARIANCE

We start by studying the fluctuations of the BOLD signal around its mean. The signal of interest, for the 35 RSN clusters, is defined as

$$B_h(\vec{x}_i, t) = B(\vec{x}_i, t) - \frac{1}{N_H}\sum_{i=1}^{N_H} B(\vec{x}_i, t), \tag{1}$$

where $\vec{x}_i$ represents the position of the voxel i that belongs to the cluster H of size N_H. These signals will be used to study the correlation properties of the activity in each cluster.

The mean activity of each h cluster is defined as

$$\overline{B}(t) = \frac{1}{N_H}\sum_{i=1}^{N_H} B(\vec{x}_i, t), \tag{2}$$

and its variance is defined as

$$\sigma^2_{\overline{B}(t)} = \frac{1}{T}\sum_{t=1}^{T}(\overline{B}(t) - \overline{\overline{B}})^2, \tag{3}$$

where $\overline{\overline{B}} = \frac{1}{T}\sum_{t=1}^{T}\overline{B}(t)$ and T the number of temporal points. Please notice that the average subtracted in Equation 1 is the mean at time t (computed over N voxels) of the BOLD signals, not to be confused with the BOLD signal averaged over T temporal points.

Since the BOLD signal fluctuate widely and the number N of voxels in the clusters can be very large, one might expect that the aggregate of Equation 1 obeys the law of the large numbers. If this was true, the variance of the mean field $\sigma^2_{\overline{B}(t)}$ in Equation 3 would decrease with N as N^{-1}. In other words one would expect a smaller amplitude fluctuation for the average BOLD signal recorded in clusters [i.e., $\overline{B}(t)$] comprised by large number of voxels compared with smaller clusters. However, the data in **Figure 2** shows otherwise, the variance of the average activity remains approximately constant over a change of four orders of magnitude in cluster' sizes. The strong departure from the N^{-1} decay is enough to disregard further statistical testing. Nevertheless, we test a null hypothesis recomputing the variance for artificially constructed clusters having similar number of voxels but

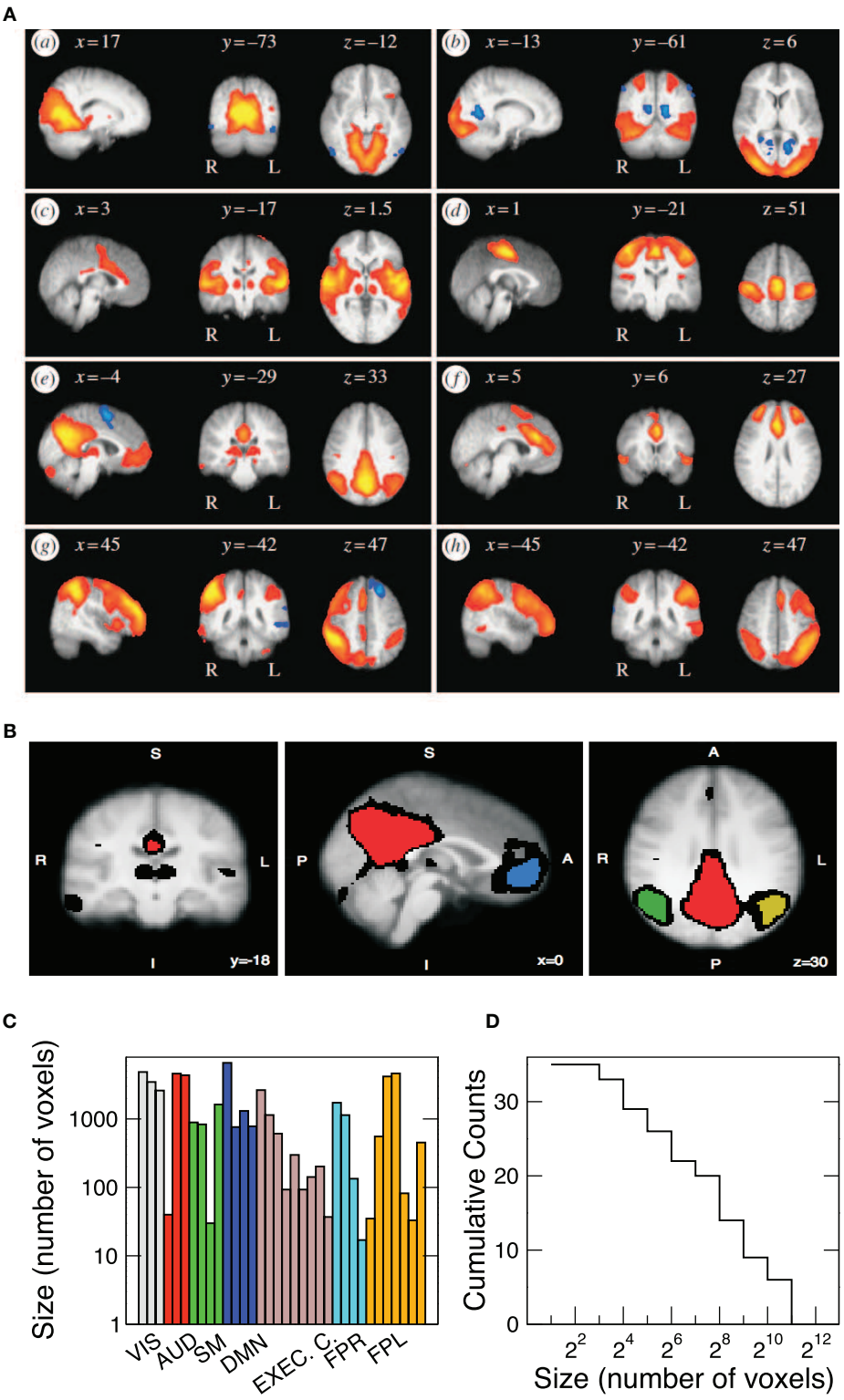

FIGURE 1 | (A) Spatial maps of the eight most relevant brain resting networks as described by Beckmann et al. (2005). Each map shows the locations of each RSN (shown in sagittal, coronal, and axial views) where the coordinates refer to mm distances from the anterior commissure. Label VIS corresponds to visual; AUD to auditory; SM to sensory motor; DMN to default model network; EXEC. C. to executive control; FPR and FPL to fronto-parietal right and left, respectively. **(B)** Example (coronal, sagital, and axial views) of the four regions of interest extracted from the DMN. The red region is composed of 6611 voxels, the blue region of 761, the green one of 1308, and the yellow region contains 780 voxels. Black voxels correspond to the ones in the original thresholded *Z*-map. Bottom panels depict the sizes of the 35 clusters **(C)** studied here as well as its cumulative size distribution **(D)**.

Table 1 | *Z*-threshold used in each independent component for defining the regions.

RSN	Vis. 1	Vis. 2	Aud.	Sens. M.	D.M.	E.C.	F. P. R	F. P. L
Threshold	4	3.3	2.4	3.4	2.2	2.7	3.2	2.2
# regions	1	2	3	4	4	9	4	8

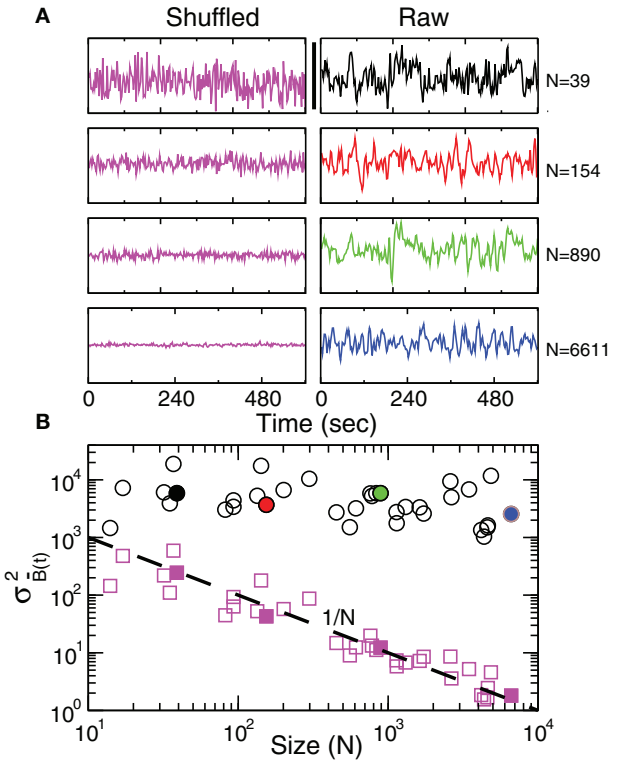

FIGURE 2 | Anomalous scaling of brain BOLD temporal fluctuations. Panel **A** show four examples of average BOLD time series (i.e., $\overline{B}(t)$ in Equation 2) computed from clusters of different sizes N. Note that while the amplitude of the raw BOLD signals (right panels) remains approximately constant, in the case of the shuffled data sets (left panels) the amplitude decreases drastically for increasing cluster sizes. Panel **B** shows the calculations for the 35 clusters (circles) plotted as a function of the cluster size demonstrating that variance is independent of the RSN's cluster size. The squares symbols show similar computations for a surrogate time series constructed by randomly reordering the original BOLD time series, which exhibit the expected $1/N$ scaling (dashed line). Filled symbols in Panel **B** are used to denote the values for the time series used as examples in Panel **A**.

composed of the randomly reordered $B_k(t)$ BOLD raw time series (panels in **Figure 2A** denoted "Shuffled"). As expected, in this case the variance (plotted using squares symbols in **Figure 2B**) obeys the N^{-1} law (dashed line in **Figure 2B**). The variance of the average BOLD signal is directly proportional to the coordination between the voxels involved. In particular, under the hypothesis that the BOLD signal of voxel k, $B_k(t)$, is a stationary stochastic process (indexed by time t) with $\mathbb{E}(B_k(t)) = \mu_k$, and $\mathbb{V}ar(B_k(t)) = \sigma_k^2$, the variance of the average signal is maximum in the case where there exist perfect coordination (i.e., all BOLD signals are perfectly synchronized). In this last case, the value of

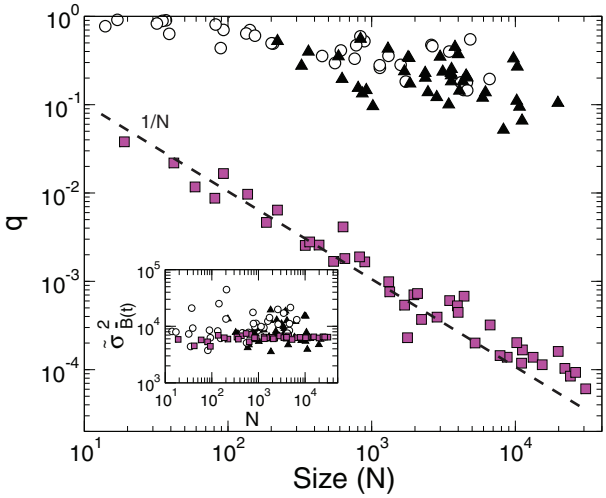

FIGURE 3 | The value of the quotient *q*, expressing the measured variance relative to its maximum possible value, as a function of cluster size *N*. Empty circles correspond to the 35 regions derived from the RSN (same as in **Figure 2**) and filled triangles to the 41 Brodmann areas. The filled squares, obeying the $1/N$ scaling (dashed line), correspond to clusters of different sizes constructed from a random selection of voxels. The inset shows the average maximum of the BOLD signal variance of a cluster ($\tilde{\sigma}^2_{\overline{B}(t)}$) as a function of N.

$\sigma^2_{\overline{B}(t)}$ is equal to the mean value of the individual time variances defined as

$$\tilde{\sigma}^2_{\overline{B}(t)} := \frac{1}{N}\sum_{k=1}^{N}\sigma_k^2. \tag{4}$$

The inset of **Figure 3** (circles) shows that this maximum value does not depend on N, i.e., the mean value of the variance of the BOLD signal from a region does not depend on its size. Now we ask how far from its maximum value is the observed variance of the BOLD average signal. In particular, we compute the quotient

$$q := \frac{\sigma^2_{\overline{B}(t)}}{\tilde{\sigma}^2_{\overline{B}(t)}} \tag{5}$$

for this purpose. As it is shown in **Figure 3** (empty circles) the value of q decreases rather slowly with the size of the cluster.

In order to distinguish how much of the constancy of the variance demonstrated up until now is related with the fact that the time series belong to clusters that are independent components (Beckmann et al., 2005) we repeated the scaling analysis using clusters defined by the Brodmann areas. The results in **Figure 3** confirm the same anomalous scaling behavior demonstrated for the regions selected from the RSN networks, as shown by the values of $\tilde{\sigma}^2_{\overline{B}(t)}$ and q for the Brodmann areas (filled triangles). As before, we control the expected $1/N$ scaling for independent time series by computing the quotient q for clusters of various sizes constructed from a random selection of voxels. This is shown by the filled square points in **Figure 3**.

3.2. TEMPORAL FLUCTUATIONS AND SPATIAL CORRELATIONS

For spatio-temporal signals the relationship between the temporal fluctuations of the average signal and its space correlation function is well defined (Ross, 1996). In our case, for the normalized (see Appendix) BOLD signals, $Z_i(t)$ ($\mathbb{V}ar(Z_k(t)) = 1$ and $\mathbb{E}(Z_k(t)) = 0$), the relationship is:

$$\sigma^2_{\overline{Z}(t)} = \frac{1}{N}(1 + (N-1)\cdot\langle C\rangle). \tag{6}$$

Where $\langle C\rangle$ is the mean spatial correlation,

$$\langle C\rangle = \frac{2}{N(N-1)}\sum_{i=1}^{N-1}\sum_{j=i+1}^{N}\rho_{i,j}, \tag{7}$$

$\rho_{i,j}$ the correlation between voxels i and j, and $\sigma^2_{\overline{Z}(t)}$ is the variance of the average signal (defined in Equation 3). Equation 6 shows that the variance of the mean activity depends on the size of the region, and on $\langle C\rangle$, which is determined by the shape of the correlation function, $C(r)$ (see Appendix for a formal discussion).

Equation 6 suggest that it can be productive to investigate the correlations properties of the BOLD data. The point to clarify is whether the average spatial correlation $\langle C\rangle$ is constant throughout the entire recordings or, alternatively, its average value is the product of a combination of some instances of high spatial coordination intermixed with moments of dis-coordination. The relevance of this distinction, which will be further discussed latter, is to establish up to which point correlations are dictated by the structural (i.e., fixed) connectivity or by the dynamics. In order to answer this question we study the mean correlation ($\langle C\rangle$) as a function of time for regions of interest of various sizes. In particular, we compute this value using Equation 7 but estimating $\rho_{i,j}$ for non-overlapping periods of 10 temporal points.

Figure 4 shows the behavior of $\langle C\rangle$ over time for four different cluster's sizes. Notice that, in all cases, there instances of large correlation followed by moments of week coordination, as those indicated by the arrows in the uppermost panel. We have verified that this behavior is not sensitive to the choice of the length of the window in which $\langle C\rangle$ is computed (see the Appendix). These bursts keep the variance of the correlations almost constant (i.e., in this example, there is a minor decrease in variance (by a factor of 0.4) for a huge increase in size (by a factor of 170). This peculiar behavior of the correlation is observed for any of the cluster sizes as shown in the bottom panel of **Figure 4** where the variance of $\langle C\rangle$ is approximately constant, despite the four order of magnitude increase in sizes.

The results of these calculations implies that independently of how large the size of the cluster considered, there is always an instance in which a large percentage of voxels are highly coherent and another instance in which each voxels activity is relatively independent.

A very metaphorical way to visualize the behavior of the correlations is to think of the patterns of spontaneous activity as "clouds" of relatively higher activity moving slowly throughout the brain's cortex. Thus, the moments of large coordination shown in **Figure 4** correspond to the passage of a "cloud" throughout the entire region, regardless of how large the region is.

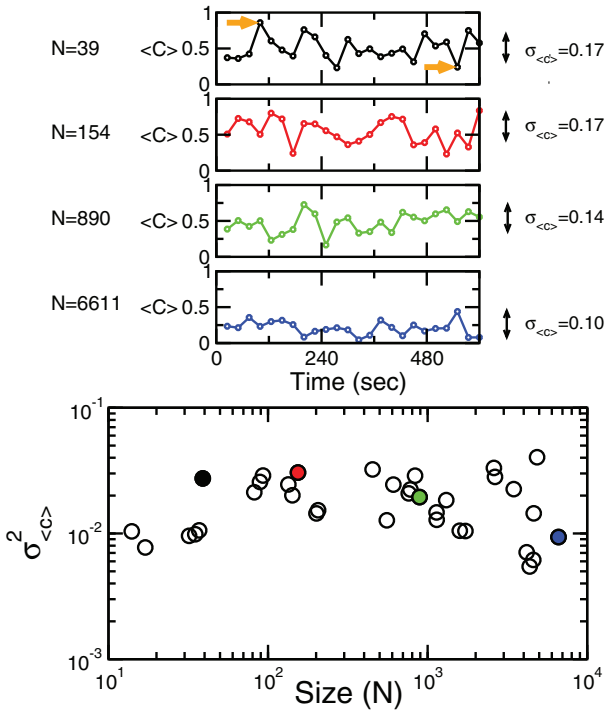

FIGURE 4 | Bursts of high correlations are observed at all cluster sizes, resulting in approximately the same variance, despite the four orders of magnitude change in the cluster size. The top panels illustrate representative examples of short-term mean correlation $\langle C\rangle$ of the BOLD signals as a function of time for four sizes spanning four orders of magnitude. The arrows show examples of two instances of highly correlated and weakly correlated activity, respectively. Bottom panel shows the variance of $\langle C\rangle$ as a function of cluster sizes. The four examples on the top traces are denoted with filled circles in the bottom plot.

3.3. DIVERGENCE OF THE CORRELATION LENGTH

The results in the previous paragraphs indicate that the anomalous scaling of the variance can be related to dynamical changes in the correlations. A straightforward approach to understand the correlation behavior commonly used in large collective systems (Cavagna et al., 2010) is to determine the correlation length at various system's sizes. The correlation length is the average distance at which the correlations of the fluctuations around the mean crosses zero. It describes how far one has to move to observe any two points in a system behaving independently of each other. Notice that, by definition, the computation of the correlation length is done over the fluctuations around the mean, and not over the raw BOLD signals, otherwise global correlations may produce a single spurious correlation length value commensurate with the brain size.

Thus, we start by computing for each voxel BOLD time series their fluctuations around the mean of the cluster that they belong. Recall the expression in Equation 1:

$$B_h(\vec{x}_i, t) = B(\vec{x}_i, t) - \frac{1}{N_H}\sum_{i=1}^{N_H} B(\vec{x}_i, t), \tag{8}$$

where B is the BOLD time series at a given voxel and $\vec{x}_i$ represents the position of the voxel i that belongs to the cluster H of size N_H. By definition the mean of the BOLD fluctuations of each cluster vanishes,

$$\sum_{i=1}^{N_k} \overline{B_h}(\vec{x}_i, t) = 0 \qquad \forall t. \tag{9}$$

Next we compute the average correlation function of the BOLD fluctuations between all pairs of voxels in the cluster considered, which are separated by a distance r:

$$\langle C_H(r)\rangle = < \frac{\begin{array}{l}(B_H(\overrightarrow{x}, t) - < B_h(\overrightarrow{x}, t) >_t)(B_H(\overrightarrow{x} \\ + r\overrightarrow{u}, t) - < B_h(\overrightarrow{x} + r\overrightarrow{u}, t) >_t)\end{array}}{\begin{array}{l}(< B_H(\overrightarrow{x}, t)^2 >_t - < B_H(\overrightarrow{x}, t) >_t^2)^{1/2} \\ (< B_H(\overrightarrow{x} + r\overrightarrow{u}, t)^2 >_t \\ - < B_H(\overrightarrow{x} + r\overrightarrow{u}, t) >_t^2)^{1/2}\end{array}} >_{t, \overrightarrow{x}, \overrightarrow{u}} \tag{10}$$

where $\vec{u}$ is a unitary vector, and $\langle . \rangle_w$ represent averages over w. The typical form we observe for $C(r)$ is shown in the top panel of **Figure 5**. The first striking feature to note is the absence of a unique $C(r)$ for all clusters. Nevertheless, they are qualitatively similar, being at short distances close to unity, to decay as r increases, and then becoming negative for longer voxel-to-voxel distances. Such behavior indicates that within each and any cluster, on the average, the fluctuations around the mean are strongly positive at short distance and strongly anti-correlated at larger distances, whereas there is no range of distance for which the correlation vanishes.

The most notorious result is the fact that correlations decay with distance slower in larger clusters than in relatively smaller clusters, giving rise to the family of curves shown in **Figure 5** (top panel). This is condensed in the calculation of the correlation length ξ, which is the zero of the correlation function, $C(r = \xi) = 0$ (as in the example shown by the arrow in **Figure 5**, top). The correlation length diverges with the size of the cluster, as demonstrated in the middle panel of **Figure 5**. This divergence extends up to the size of the brain, as shown by the ξ values (red squares in middle panel of **Figure 5**) computed for the eight unpartitioned RSN. Note that while the existence of a zero crossing in C is warranted by the subtraction of the mean cluster activity (in Equation 8), its divergence with cluster size is not.

3.4. MUTUAL INFORMATION

Although the present observations can be appropriately described solely in terms of correlations, the same concept can be also casted in terms of information measures, which are often used to estimate the degree of coherence between regions or neural structures. The mutual information between any two X and Y time series from different brain voxels is defined as:

$$MI(X; Y) = H(X) - H(X|Y) \tag{11}$$

where $H(X)$ is the entropy of X and $H(X|Y)$ is the entropy of X given Y computed as usual (Press et al., 1988). In principle, given the behavior observed for the correlations, these

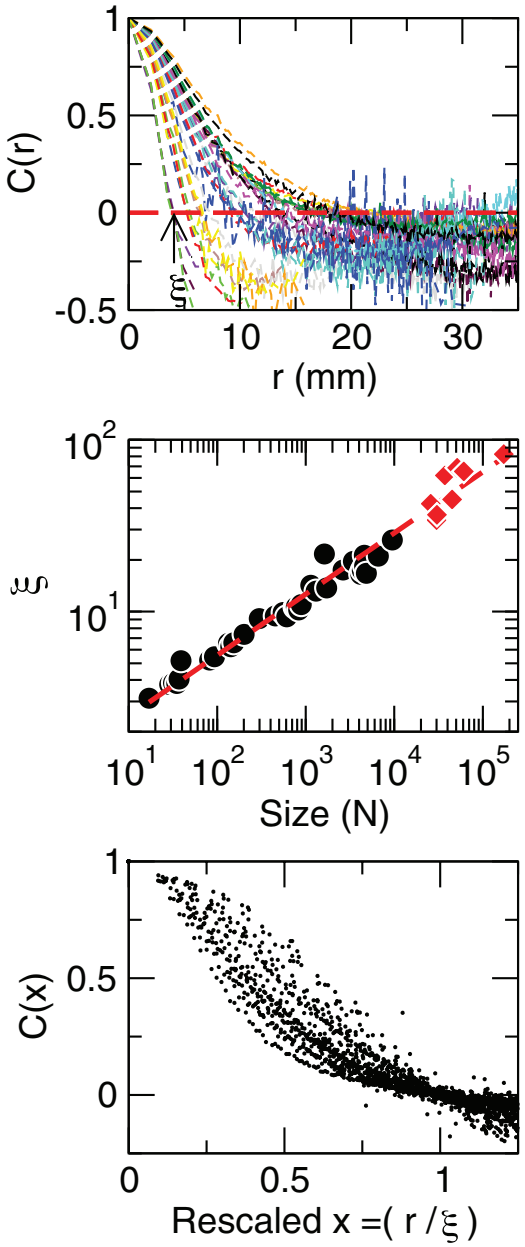

FIGURE 5 | Contrary to naive expectations, large clusters are as correlated as relatively smaller ones: the correlation length increases with cluster size. Each line in the top panel shows the mean cross-correlation $C(r)$ of BOLD activity fluctuations as a function of distance r averaged over all time series of each of the 35 clusters shown in **Figure 1**. The correlation length ξ, denoted by the zero crossing of $C(r)$ is not a constant. The middle panel shows, in double log plot, the functional dependence $\xi \sim dN^{1/3}$, i.e., ξ grows linearly with the average cluster' diameter d for all the 35 clusters (filled circles). The rightmost points (diamonds) corresponding to the ξ values computed for each of the eight RSN without any partitioning shows that the correlation length keep increasing up to the size of the brain (the dotted line is a guide to the eye with slope 1/3). The scale invariance is graphically illustrated by the bottom panel, where all $C(r)$ data are replotted after rescaling the horizontal axis as $x = r/\xi$, showing a good overlap. Note that a perfect collapse of these curves can not be expected because of the severe anisotropy, imposed by the brain anatomy, affecting the estimation of the distance r.

information measures should exhibit scale-invariant scaling as well. This is confirmed by the results in **Figure 6**, which demonstrate that the average mutual information is not affected by the size of the cluster considered, since information decays slower in larger clusters. This analysis shows that, as was shown for the correlation, the information length (determined here for an arbitrary threshold value of 0.4 bits) diverges with the size of the of the clusters.

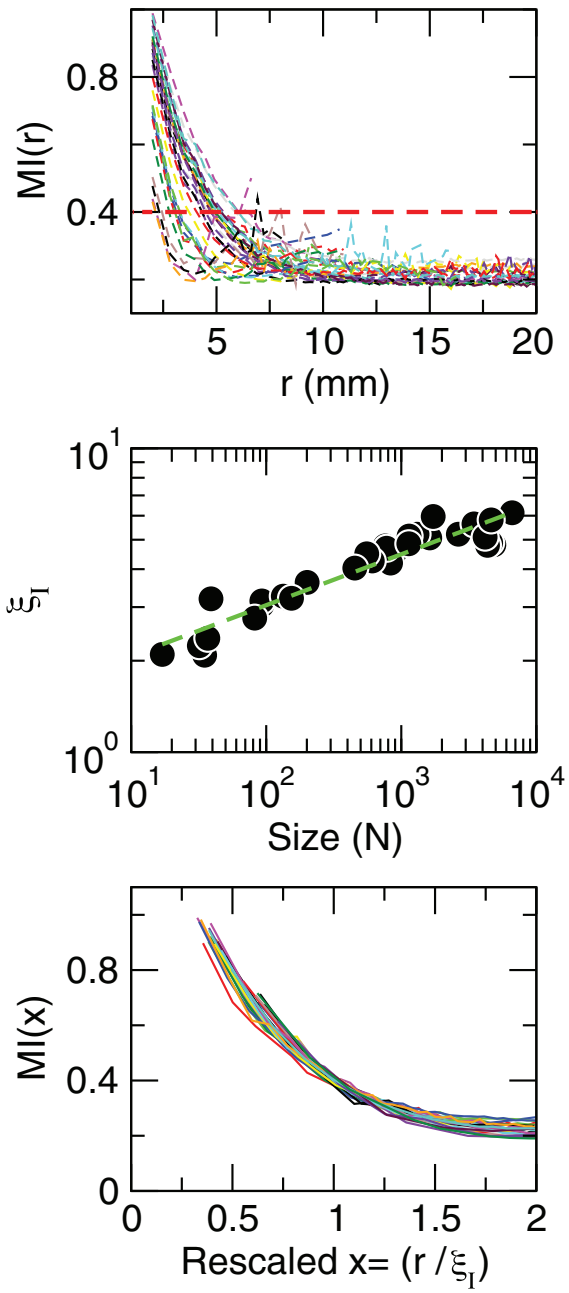

FIGURE 6 | Mutual information increases with cluster size. Each line in the top panel shows the mutual information $MI(r)$ as a function of distance r averaged over all time series of each of the 35 clusters shown in **Figure 1**. The length at which $MI(r)$ decreased to a given value (red line in the top panel) denoted as ξ_I, is an increasing function of the size of the cluster (middle panel). The bottom panel illustrates the good data collapse after rescaling the horizontal axis as $x = r/\xi_I$.

4. DISCUSSION

In this work, key statistical properties of the brain BOLD signal variability were investigated. The results are relevant to the understanding of the brain spontaneous activity fluctuations in health and disease. The three most relevant findings that we may discuss are:

- the variance of the average BOLD fluctuations computed from ensembles of widely different sizes remains constant, (i.e., anomalous scaling);
- the analysis of short-term correlations reveals bursts of high coherence between arbitrarily far apart voxels indicating that the variance' anomalous scaling has a dynamical (and not structural) origin;
- the correlation length measured at different regions increases with region's size, as well as its mutual information.

Concerning the constant variance of the BOLD activity, the present results imply that the usual framework in which the BOLD signal and noise are discussed need to be reconsidered. For instance, it is commonplace to consider that the non-coherent part of the activity (i.e., the noise) can be averaged out by enlarging the spatial (i.e., more voxels) or temporal (i.e., more samples) scale. The presence of anomalous scaling implies that signal and noise in the brain are at least ill defined and that filtering by averaging (to improve its quality) signals with anomalous variance, by definition, can be anomalous as well. The anomalous scaling also has implication for the monitoring of the RSNs activity, a topic that has received wide attention recently for its potential to track healthy or pathological conditions. The results here imply that, under these anomalous conditions, the signal of a few voxels can be, asymptotically, as representative and informative as the average of the entire RSN. It need to be noted, that the anomalous scaling discussed here due to the emergence of collective dynamics is not new, Kaneko (1990) demonstrated the breach of law of large numbers in numerical models more than two decades ago.

The second finding, showing that the observed dynamical short-term changes in the correlations drives up the variance, is relevant for the interpretation of the brain functional connectivity. The evaluation of functional connectivity between regions often uses the average correlation, and the results in **Figure 4** show that, despite the relatively weak average functional connectivity values, it can be instances in which the correlation reaches high levels. In other words, under the demonstrated anomalous scaling conditions, the usual pairwise measures has inherent limitations for the proper interpretation of these collective states. In passing, it need to be noted that these instances of high coherence were recently confirmed using a different method, which demonstrate avalanches of activity encompassing relatively large regions of each RSN (Tagliazucchi et al., 2012). Of course, the role of these epochs of transient synchronous states in driving perception, awareness, and consciousness are consistent with the views

championed by Varela and coworkers more than a decade ago (Varela et al., 2001) as discussed recently (Werner, 2010).

The third result concerning the divergence of the correlation length with increasing cluster size is perhaps the most telling one, because is in contrast with the prevailing viewpoints about brain functional connectivity. Indeed it is implicit in the interpretation of functional connectivity studies the notion that brain activity *propagates* between and across brain regions. However, for such propagating waves a constant correlation length (i.e., its wavelength) is always expected, which is not what it is consistently found in the present data. The divergence of correlations with size (and its associated anomalous scaling) suggests, in addition, that our current mathematical approaches to model cortical dynamics could be ill-fated. The issue is that most of the large scale models [for superb reviews see Rolls and Deco, 2010; Sporns, 2010] are defined by an adjacency matrix specifying the "structural connectivity" between a large number of regions and some kind of neural dynamics assigned to each node (i.e., cortical region). Lets imagine that such model is scaled up by increasing the number of regions an order of magnitude, while the correlation length of the activity fluctuations is measured as in the experiments here. A reasonable conjecture is that current large-scale brain models would have problems to replicate the present findings, since anomalous scaling only appears at criticality (discussed below) while current models are purposely tuned to the ordered regime.

Finally, an important question is concerned with the origin of the statistical properties unveiled in this work. We suggest that a candidate explanation which is able to unify all the observations presented here can be found in the context of critical phenomena (Stanley, 1987; Bak, 1996; Christensen and Moloney, 2005). It is well known that dynamical systems composed of very large number of interacting non-linear elements, under some conditions, exhibit emergent collective behavior with ubiquitous properties (Anderson, 1972). Examples of emergent phenomena sharing common features are the collective dynamics of birds in a flock (Cavagna et al., 2010), spins of a magnet (Stanley, 1987), water molecules in the atmosphere (Peters and Neelin, 2006), peoples financial decisions (Lux and Marchesi, 1999), or ants traffic in a foraging swarm (Rauch et al., 1995; Beekman et al., 2001). In all these cases, each agent in isolation may have its own stereotypical behavior, but when placed to interact in very large numbers, and under certain conditions, the entire system will drift toward a type of collective dynamics which lies in between complete order and complete disorder. At this point [known as an order-disorder phase transition (Stanley, 1987; Chialvo, 2010)] the collective dynamics of the system exhibit distinctive universal properties. Amongst them, the most significant common features include the divergence of correlations, the anomalous scaling, and the presence of moments of high coordination seen here for the RSN fluctuations. Since the emergence of these properties require conditions near an order-disorder phase transition, its observation it is often considered a *distinctive signature* of critical dynamics, as reported recently by Cavagna et al. for sterling flock dynamics (Cavagna et al., 2010). In particular, it is known that only near a critical point ξ can grow with system size, where the collective global effects overcomes the individuals dynamics, resulting in the emergence of correlated domains of arbitrary size, where information propagates equally well up to the size of the entire system.

In summary, the analysis of the BOLD' fluctuations of the resting brain shows anomalous statistical properties, bursts of highly correlated states and divergence of correlation length, which are dynamical properties known to be found only near a critical point of a phase transition. These findings are fully consistent with previous reports of large-scale brain critical dynamics (Fraiman et al., 2009; Kitzbichler et al., 2009; Chialvo, 2010; Expert et al., 2011; Tagliazucchi et al., 2012) and may be one answer to the question in the title in the sense that brain noise corresponds, rigorously speaking, to the type of (spatial and temporal) fluctuations only observed in systems near criticality. This view may be relevant for the interpretation of the role of fluctuations and variability in brain function in health and disease.

ACKNOWLEDGMENTS

Work supported by NIH NINDS (USA), grant NS58661, by Consejo Nacional de Investigaciones Científicas y Tecnológicas (CONICET) (Argentina), by the Spanish Ministerio de Economia y Productividad (previously Ministerio de Ciencia y Tecnologia) (Spain) and by European Funds—FEDER, grant SEJ2007-62312. We thank Prof. Pedro Montoya and M. Muñoz (UIB, Mallorca, Spain) for discussions and help in data acquisition, and E. Tagliazucchi, P. Balenzuela, A. Haimovici (UBA, Argentina) and L. Hess, A. Tardivo, A. Yodice (UNR, Argentina) for continuous discussions.

REFERENCES

Anderson, P. (1972). More is different. *Science* 177, 393–396.

Bak, P. (1996). *How Nature Works. The Science of Self-Organized Criticality*. New York, NY: Copernicus Press.

Beckmann, C. F., De Luca, M., Devlin, J. T., and Smith, S. M. (2005). Investigations into resting-state connectivity using independent component analysis. *Philos. Trans. R. Soc. Lond. B Biol. Sci.* 360, 1001–1013.

Beekman, M., Sumpter, D. J. T., and Ratnieks, F. L. W. (2001). Phase transition between disordered and ordered foraging in pharaohs ants. *Proc. Natl. Acad. Sci. U.S.A.* 98, 9703–9706.

Biswal, B., Zerrin Yetkin, F., Haughton, V., and Hyde, J. (1995). Functional connectivity in the motor cortex of resting human brain using echo-planar MRI. *Magn. Reson. Med.* 34, 537–541.

Cavagna, A., Cimarelli, A., Giardina, I., Parisi, G., Santagati, R., Stefanini, F., and Viale, M. (2010). Scale-free correlations in starling *flocks*. *Proc. Natl. Acad. Sci. U.S.A.* 107, 11865–11870.

Chialvo, D. R. (2010). Complex emergent neural dynamics. *Nat. Phys.* 6, 744–750.

Christensen, K., and Moloney, N. R. (2005). *Complexity and Criticality*. London, UK: Imperial College Press.

Cordes, D., Haughton, V. M., Arfanakis, K., Wendt, G. J., Turski, P. A., Moritz, C. H., Quigley, M. A., and Meyerand, M. E. (2000). Mapping functionally related regions of brain with functional connectivity MR imaging. *Am. J. Neuroradiol.* 21, 1636–1644.

Expert, P., Lambiotte, R., Chialvo, D. R., Christensen, K., Jensen, H. J., Sharp, D. J., and Turkheimer, F. (2011). Self-similar correlation function in brain resting-state fMRI. *J. R. Soc. Interface* 8, 472–479.

Fox, M. D., and Raichle, M. E. (2007). Spontaneous fluctuations in brain activity observed with functional magnetic resonance imaging. *Nat. Rev. Neurosci.* 8, 700–711.

Fraiman, D., Balenzuela, P., Foss, J., and Chialvo, D. R. (2009). Ising-like dynamics in large-scale functional brain networks. *Phys. Rev. E* 79, 061922.

Fukunaga, M., Horovitz, S. G., van Gelderen, P., de Zwart, J. A., Jansma, J. M., Ikonomidou, V. N., Chu, R., Deckers, R. H., Leopold, D. A., and Duyn, J. H. (2006). Large-amplitude, spatially correlated fluctuations in BOLD fMRI signals during extended rest and early sleep stages. *Magn. Reson. Imaging* 24, 979–992.

Garret, D., Kovacevic, N., McIntosh, A., and Grady, C. (2010). Blood oxygen level-dependent signal variability is more than just noise. *J. Neurosci.* 30, 4914–4921.

Garrett, D., Kovacevic, N., McIntosh, A. R., and Grady, C. L. (2011). The importance of being variable. *J. Neurosci.* 31, 4496–4503.

Jezzard, P., Mathews, P., and Smith, S. M. (2001). *Functional MRI: An Introduction to Methods*. Oxford, UK: Oxford University Press.

Kaneko, K. (1990). Globally coupled chaos violates the law of large numbers but not the central limit theorem. *Phys. Rev. Lett.* 65, 1391–1294.

Kitzbichler, M. G., Smith, M. L., Christensen, S. R., and Bullmore, E. (2009). Broadband criticality of human brain network synchronization. *PLoS Comput. Biol.* 5:e1000314. doi: 10.1371/journal.pcbi.1000314

Lux, T., and Marchesi, M. (1999). Scaling and criticality in a stochastic multi-agent model of a financial market. *Nature* 397, 498–500.

Peters, O., and Neelin, D. (2006). Critical phenomena in atmospheric precipitation. *Nat. Phys.* 2, 393–396.

Press, W. H., Flannery, B. P., Teukolsky, S. A., and Vetterling, W. T. (1988). *Numerical Recipes in C: The Art of Scientific Computing*. Cambridge, MA: Cambridge University Press.

Rauch, E., Millonas, M. M., and Chialvo, D. R. (1995). Pattern formation and functionality in swarm models. *Phys. Lett. A* 207, 185–193.

Rolls, E. T., and Deco, G. (2010). *The Noisy Brain*. London: Oxford University Press.

Ross, S. M. (1996). *Stochastic Processes*. New York, NY: John Wiley and Sons Inc.

Smith, S. M., Fox, P. T., Miller, K. L., Glahn, D. C., Fox, P. M., Mackay, C. E., Filippini, N., Watkins, K. E., Toro, R., Laird, A. R., and Beckmann, C. F. (2009). Correspondence of the brain's functional architecture during activation and rest. *Proc. Natl. Acad. Sci. U.S.A.* 106, 13040–1345.

Sporns, O. (2010). *Networks of the Brain*. London: MIT Press.

Stanley, H. E. (1987). *Introduction to Phase Transitions and Critical Phenomena*. Oxford: Oxford University Press.

Tagliazucchi, E., Balenzuela, P., Fraiman, D., and Chialvo, D. R. (2012). Criticality in large-scale brain fMRI dynamics unveiled by a novel point process analysis. *Front. Physiol.* 3:15. doi: 10.3389/fphys.2012.00015

Varela, F., Lachaux, J.-P., Rodriguez, E., and Martinerie, J. (2001). The Brainweb: phase synchronization and large scale integration. *Nat. Rev. Neurosci.* 2, 229–239.

Vincent, J. L., Patel, G. H., Fox, M. D., Snyder, A. Z., Baker, J. T., Van Essen, D. C., Zempel, J. M., Snyder, L. H., Corbetta, M., and Raichle, M. E. (2007). Intrinsic functional architecture in the anesthetized monkey brain. *Nature* 447, 83–87.

Werner, G. (2010). Fractals in the nervous system: conceptual implications for theoretical neuroscience. *Front. Physiol.* 1:15. doi: 10.3389/fphys.2010.00015

Xiong, J., Parsons, L., Gao, J., and Fox, P. (1999). Interregional connectivity to primary motor cortex revealed using MRI resting state images. *Hum. Brain Mapp.* 8, 151–156.

Conflict of Interest Statement: The authors declare that the research was conducted in the absence of any commercial or financial relationships that could be construed as a potential conflict of interest.

*Received: 05 February 2012; accepted: 12 July 2012; published online: 30 July 2012. Citation: Fraiman D and Chialvo DR (2012) What kind of noise is brain noise: anomalous scaling behavior of the resting brain activity fluctuations. Front. Physio. **3**:307. doi: 10.3389/fphys.2012.00307*

This article was submitted to Frontiers in Fractal Physiology, a specialty of Frontiers in Physiology.

APPENDIX

Additional information is provided here to supplement the main results. The first item is concerned with the robustness of the short-term correlations presented in **Figure 4**. The second point deals with the generality of the divergence of correlations and the last one discuss formally the presence of long-range correlations in the fMRI data.

SHORT-TERM CORRELATIONS

As discussed in **Figure 4**, the presence of bursts of high and low correlations observed throughout clusters of very different size is the dynamical base for the violation of the law of the large numbers. It is then important to demonstrate that the estimation of the short-term correlations' variance is robust. For that, we recomputed the results in **Figure 4** for various window lengths. This is presented in **Figure A1** which shows that the variance of $\langle C\rangle$ is independent of N regardless of the window length at which it is estimated.

ξ SCALING

The divergence of correlation length discussed in **Figure 5** predicts a functional dependence $\xi \sim dN^{1/3}$, i.e., ξ grows linearly with the average cluster' diameter d. The results in **Figure A2**, obtained from the analysis of fMRI data from four different subjects, confirm such scaling relation.

LONG-RANGE CORRELATIONS

In spatio-temporal data it is well known the relationship between the temporal fluctuations of a mean magnitude and the space correlation function. Let suppose we want to study a brain region (our clusters in the main text) of N voxels. Denote a voxel of the region as i which is characterized by its position in space ($\vec{r}_i$), and by its dynamics represented in the BOLD signal $[B_i(t)]$. In addition, to simplify the notation we are going to work here with normalized BOLD signals,

$$Z_i(t) \equiv \frac{B_i(t) - \overline{B_i}}{\sigma_i}, \tag{12}$$

where $\overline{B_i} = \frac{1}{T}\sum_{h=1,\ldots,T} B_i(t)$ and $\sigma_i^2 = \frac{1}{T}\sum_{h=1,\ldots,T}(B_i(t) - \overline{B_i})^2$. Each voxel signal $[Z_i(t)]$ has now zero mean and variance one. The average signal over the region, which is:

$$\overline{Z}(t) = \frac{1}{N}\sum_{i=1}^{N} Z_i(t), \tag{13}$$

fluctuates in time. Our interest here are the fluctuations of $\overline{Z}(t)$. It can be shown, using the definition of the variance of a sum of random variables, that the variance of the average signal of the cluster is:

$$Var(\overline{Z}) = \frac{1}{N}(1 + (N-1)\langle C\rangle), \tag{14}$$

where $\langle C\rangle$ is the mean spatial correlation, $Var(\overline{Z}) = \frac{1}{T}\sum_{t=1}^{T}(\overline{Z}(t) - \overline{\overline{Z}})^2$ and $\overline{\overline{Z}} = \frac{1}{T}\sum_{t=1}^{T}\overline{Z}(t)$.

Since we are interested also on how correlations affect variance, let consider some cases. If there exist null variability between all the voxels in the region, that is all voxels of the region do exactly the same in time, the left term of Equation 14 remains equal to one no matter the size (N) of the region is. In any other case $Var(\overline{Z})$ will be less than one. The variance of the mean activity depends on the size of the region, and on $\langle C\rangle$, which is determined by the shape of the correlation function, $C(r)$. Therefore, in order to understand the asymptotic behavior of $Var(\overline{Z})$ with N we need to make some hypothesis over $C(r)$.

First, the mean correlation,

$$\langle C\rangle = \frac{2}{N(N-1)}\sum_{i<j} cor(Z_i, Z_j), \tag{15}$$

is approximated by its continuous version

$$\langle C\rangle \approx \frac{2\pi}{V}\int_{0.5}^{r^*} C(r) r^2 dr, \tag{16}$$

where r^* is the radius of the spherical region under study, and V its volume. Now, we discuss some hypothesis about the *asymptotic* behavior of $C(r)$. For example, if there exist an exponential decay,

$$C(r) \sim e^{-\lambda r}, \tag{17}$$

then the mean correlation satisfies:

$$\langle C\rangle \sim N^{-1}. \tag{18}$$

In the case where long-range correlations are present,

$$C(r) \sim \frac{1}{r^{\alpha}}, \tag{19}$$

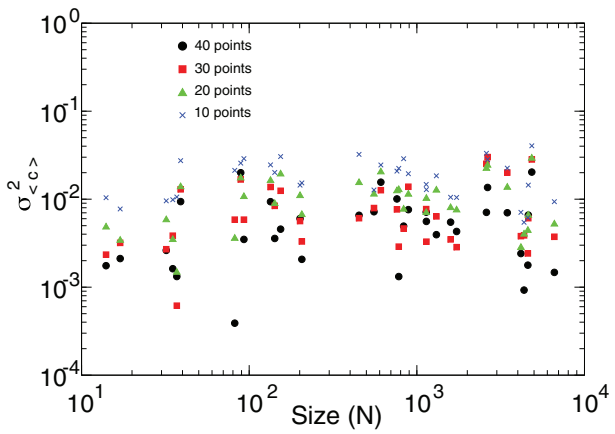

FIGURE A1 | The variance of the mean short-term spatial correlation $\langle C\rangle$ (already shown in Figure 4) is independent of the cluster' sizes N regardless of the window length (10–40 time steps) at which it is estimated.

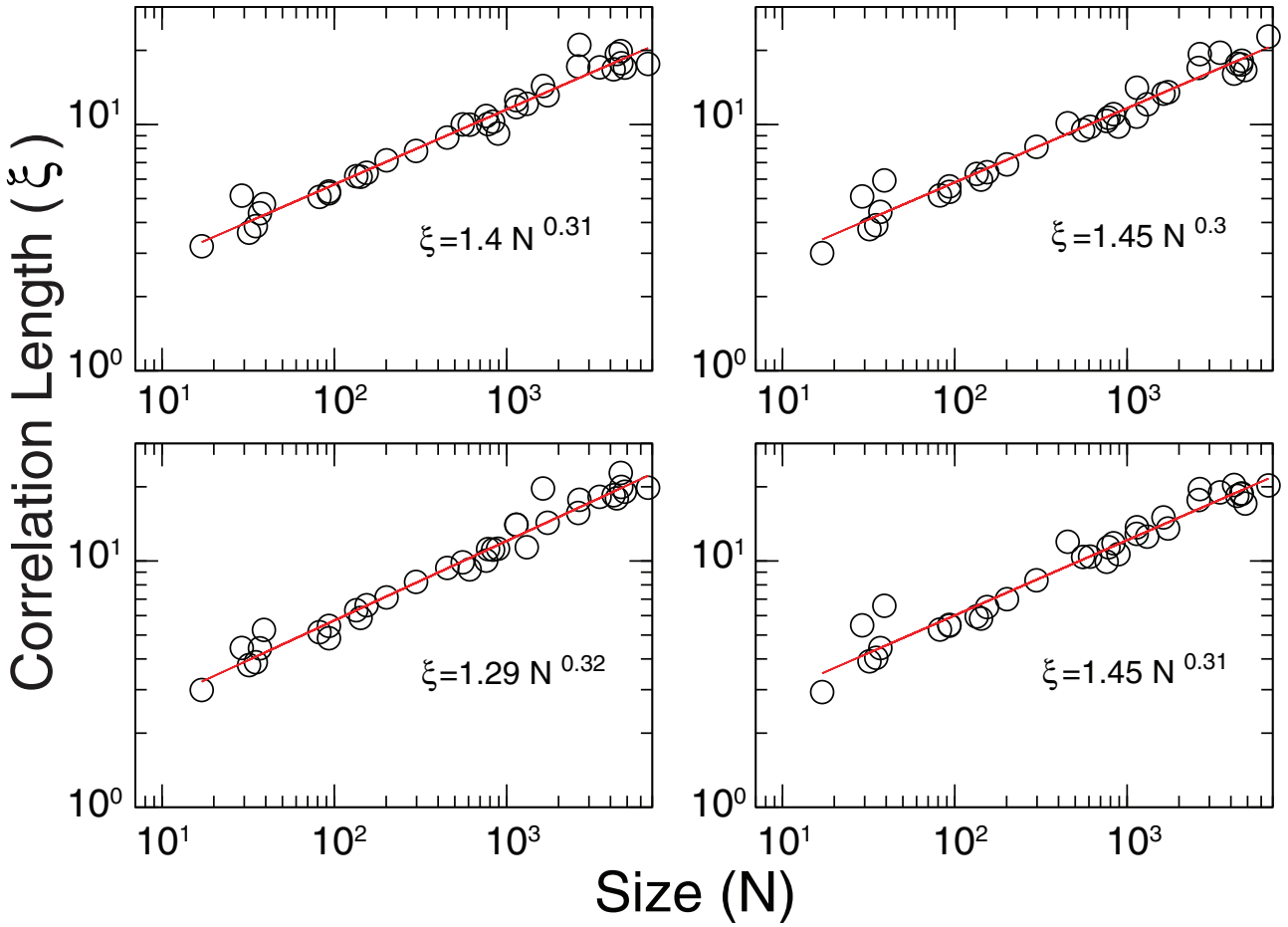

FIGURE A2 | Estimation of the correlation length ξ divergence. In all cases the results are very close to the scaling found in **Figure 5**; $\xi \sim dN^{1/3}$.

the mean correlation satisfies:

$$\langle C \rangle \sim N^{-\alpha/3}. \tag{20}$$

Putting all together in Equation 21, the spatial decay of the fMRI data correlations will be given by the product of N by $Var(\overline{Z})$ as a function of N, leading to two very different asymptotic statistical behavior:

$$\begin{cases} \text{For long-range correlations} & NVar(\overline{Z}) \sim N^{1-\alpha/3} \\ \text{For short-range correlations} & NVar(\overline{Z}) \sim k. \end{cases} \tag{21}$$

Figure A3 shows $N.Var(\overline{Z})$ as a function of N for brain data. The straight line in the log-log plot confirm that in the brain data there exist long range correlations. In particular, we obtain a exponent $\alpha = 0.9$ (for $C(r) \sim \frac{1}{r^{\alpha}}$) which agrees very well with the result recently obtained by Expert et al. (2011). For completeness we plot also the results of numerical calculations using an exponential correlation function which clearly depart from the brain data.

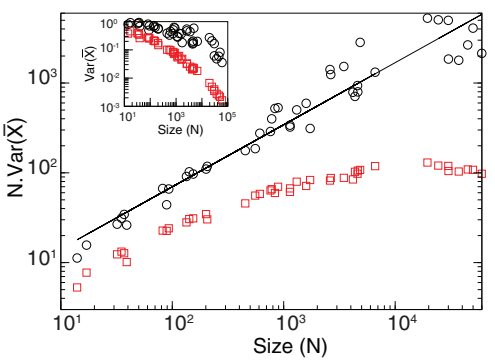

FIGURE A3 | Long-range correlations. Black circles correspond to brain data and red squares to the results from an exponential interaction model with the same geometry for each cluster. In the exponential case as N grows the average correlation converges, meanwhile for the brain data it continues growing demonstrating the presence of long-range correlations in the data. The black line corresponds to a power law fit $y = kx^{-0.7}$. From Equation 21 we obtain an exponent $\alpha = 0.9$. The inset corresponds to the variance of the mean activity as a function of N.

frontiers in
PHYSIOLOGY

METHODS ARTICLE
published: 30 November 2012
doi: 10.3389/fphys.2012.00450

Detrended fluctuation analysis: a scale-free view on neuronal oscillations

Richard Hardstone[1], Simon-Shlomo Poil[1], Giuseppina Schiavone[1], Rick Jansen[1,2], Vadim V. Nikulin[3], Huibert D. Mansvelder[1] and Klaus Linkenkaer-Hansen[1]*

[1] Department of Integrative Neurophysiology, Center for Neurogenomics and Cognitive Research, Neuroscience Campus Amsterdam, VU University Amsterdam, Amsterdam, Netherlands
[2] Department of Psychiatry, VU University Medical Center, Neuroscience Campus Amsterdam, Amsterdam, Netherlands
[3] Neurophysics Group, Department of Neurology, Charité – Universitätsmedizin, Berlin, Germany

Edited by:
Biyu J. He, NIH, NINDS, USA

Reviewed by:
Andras Eke, Semmelweis University, Hungary
Simon Farmer, National Hospital for Neurology & Neurosurgery and Institute of Neurology, UK

***Correspondence:**
Klaus Linkenkaer-Hansen, Department of Integrative Neurophysiology, Center for Neurogenomics and Cognitive Research, Neuroscience Campus Amsterdam, VU University Amsterdam, De Boelelaan 1085, 1081 HV Amsterdam, Netherlands.
e-mail: klaus.linkenkaer@cncr.vu.nl

Recent years of research have shown that the complex temporal structure of ongoing oscillations is scale-free and characterized by long-range temporal correlations. Detrended fluctuation analysis (DFA) has proven particularly useful, revealing that genetic variation, normal development, or disease can lead to differences in the scale-free amplitude modulation of oscillations. Furthermore, amplitude dynamics is remarkably independent of the time-averaged oscillation power, indicating that the DFA provides unique insights into the functional organization of neuronal systems. To facilitate understanding and encourage wider use of scaling analysis of neuronal oscillations, we provide a pedagogical explanation of the DFA algorithm and its underlying theory. Practical advice on applying DFA to oscillations is supported by MATLAB scripts from the Neurophysiological Biomarker Toolbox (NBT) and links to the NBT tutorial website http://www.nbtwiki.net/. Finally, we provide a brief overview of insights derived from the application of DFA to ongoing oscillations in health and disease, and discuss the putative relevance of criticality for understanding the mechanism underlying scale-free modulation of oscillations.

Keywords: long-range temporal correlations, criticality, ongoing oscillations, detrended fluctuation analysis, scale-free dynamics

INTRODUCTION

When investigating nature we often discard the observed variation and describe its properties in terms of an average, such as the mean or median (Gilden, 2001). For some objects or processes, however, the average value is a poor description, because they do not have a typical or "characteristic" scale. Such systems are broadly referred to as "scale-free" (Bassingthwaighte et al., 1994). There is growing evidence that physiological processes can exhibit fluctuations without characteristic scales and that this scale-free dynamics is important for their function (Bassingthwaighte et al., 1994; Bak, 1996; Goldberger et al., 2002; Stam, 2005; Ghosh et al., 2008; He et al., 2010; West, 2010). Detrended fluctuation analysis (DFA; Peng et al., 1994), a method for analyzing scaling behavior in time series, has played a critical role in this success. We believe, however, that DFA could prove valuable to a wider community of neuroscientists than its current users. Thus, the aim of this paper is to promote and facilitate investigations of the scale-free amplitude modulation of ongoing neuronal oscillations with the use of DFA (Linkenkaer-Hansen et al., 2001).

Our paper is structured as follows. First, we provide a beginner's introduction to the Section "Fundamental Concepts Required to Understand DFA." This is followed by the presentation of "The DFA" and the special requirements regarding "DFA applied to neuronal oscillations." With the theory covered, the reader is referred to MATLAB code and tutorials in the Section "Try it Yourself Using the Neurophysiological Biomarker Toolbox (NBT)." Finally, we illustrate the value of DFA in "Insights from the application of DFA to neuronal oscillations."

FUNDAMENTAL CONCEPTS REQUIRED TO UNDERSTAND DFA

To understand how the DFA algorithm quantifies some of the properties of scale-free fluctuations, we introduce the concepts of self-affinity and stationarity and show how they apply to scale-free signals.

SELF-AFFINITY

Self-affinity is a property of fractal time series (Mandelbrot, 1967; Turcotte, 1997). It is a special case of self-similarity, according to which a small part of a fractal structure is similar to the whole structure. When this small part is an exact replica of the whole then the fractal is exact, which is the case for purely mathematical and geometrical fractals (e.g., the van Koch curve and the Mandelbrot tree; Peitgen et al., 1992). When the self-similarity is expressed in terms of statistical properties (e.g., the mean and standard deviation for a portion of a fractal are scaled versions of the mean and standard deviation of the whole) then the fractal is a statistical fractal. Whilst the self-similarity property is isotropic and applies along all the dimensions of a fractal object, self-affinity describes anisotropic scaling where statistical properties of the fractal scale differently along different dimensions. In the case of a time series, the time dimension is rescaled.

Nature hosts some intriguing examples of self-similar structures, such as the Roman cauliflower (*Romanesco broccoli*), in

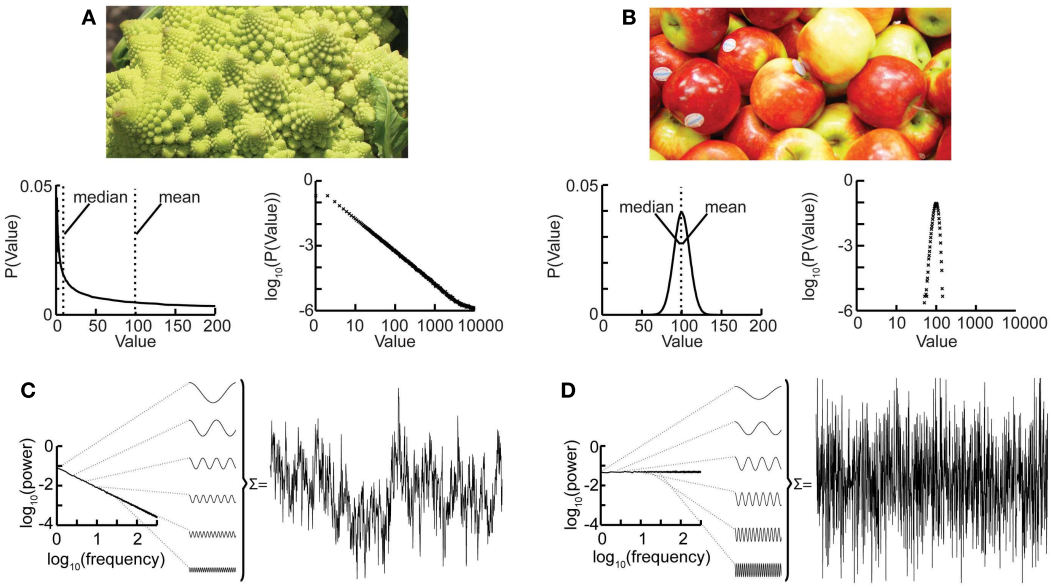

FIGURE 1 | The Roman cauliflower is a striking example of self-similarity in nature. (A) The cauliflower is composed of flowers that are similar to the entire cauliflower. These smaller flowers, in turn, are composed of flowers that are similar to the smaller flowers. The self-similarity is apparent on at least four levels of magnification, thereby illustrating the scale-free property that is a consequence of self-similarity (*bottom left*). A hypothetical distribution of the likelihood of flowers on a cauliflower having a certain size. This property is captured by the power-law function. The mean or median of a power-law, however, provide a poor representation of the scale-free distribution (and in a mathematical sense is not defined) (*bottom right*). The power-law function makes a straight line in double-logarithmic coordinates. The slope of this line is the exponent of the power-law, which captures an important property of scale-free systems, namely the relationship between the size of objects or fluctuations on different scales. **(B)** As the size of apples shows smaller variation they are well described by taking an average value such as the mean or median. (*bottom left*) Hypothetical distribution showing the likelihood of apples having a certain size. Both the mean and median are good statistics to convey the size of the apples. (*bottom right*) Plotting the normal distribution on double-logarithmic coordinates has little effect on the appearance of the distribution, which still shows a characteristic scale. **(C)** Time-signals can also be viewed as self-affine as they can be transformed into a set of sine-waves of different frequencies. In a $1/f$ signal the lower frequency objects have larger amplitude than the higher frequency objects which we can compare with there being fewer large cauliflowers than there are small cauliflowers. **(D)** A white-noise signal is also self-affine, but now the lower frequency objects have the same amplitude as the higher frequency objects meaning that only the high-frequency fluctuations are visible in the signal.

which almost exact copies of the entire flower may be recognized on multiple smaller scales (**Figure 1A**). Physiological time series may exhibit statistical self-affine properties (Eke et al., 2000, 2002). Self-affine processes and self-similar structures have in common that the statistical distribution of the measured quantity follows a power-law function, which is the only mathematical function without a characteristic scale. Self-affine and self-similar phenomena are therefore called "scale-free."

Considering again the example of the *Romanesco broccoli*, we can say that it is a "scale-free" structure, because there is no typical size of flower on the cauliflower, with the frequency of a certain size of flower being inversely proportional to its size. A scale-free time series will in a similar fashion be composed of sine-waves with amplitudes inversely proportional to their frequency (**Figure 1C**), seen as a straight line when the power spectrum is plotted on double-logarithmic axis. This is in contrast to the wide variety of objects that have a typical scale, e.g., the size of the apples on a tree. None of them will be very small or very large; rather, they will form a Gaussian distribution centered on some characteristic size, which is well represented by the mean of the distribution. Qualitatively, the characteristic scale is present at the expense of rich variability. Similarly, a time series in which all frequencies are represented with the same amplitude will lack the rich variability of the scale-free time series and is referred to as "*white-noise*" (**Figure 1D**). Whereas phenomena with characteristic scales are well defined by their mean and standard deviation (**Figures 1B,D**), scale-free phenomena are better described by the exponent of a power-law function, because it captures the relationship between objects or fluctuations on different scales (**Figures 1A,C**).

Let us now introduce the mathematical definitions:

A non-stationary stochastic process is said to be *self-affine* in a statistical sense, if a rescaled version of a small part of its time series has the same statistical distribution as the larger part. For practical purposes, it is sufficient to assess the standard deviation. Thus, the process, Y, is self-affine if for all windows of length t:

$$Y(Lt) \equiv L^H Y(t) \tag{1}$$

where:

- "$Y(Lt)$" and "$Y(t)$" are values of a process at time windows of length Lt and t, respectively.
- "L": window length factor
- "H": Hurst parameter, dimensionless estimator of self-affinity
- "$\equiv$": the standard deviation on both sides of the equation are identical (Beran, 1994).

To illustrate the implications of this definition for the property of a self-affine process, we consider a self-affinity parameter of

0.75 and derive the standard deviation for two and three times the length of the time-scale. To double the time-scale, we set $L = 2$;

$$Y(2t) \equiv 2^{0.75} Y(t)$$
$$Y(2t) \equiv 1.68 Y(t)$$

Therefore, the standard deviation of a signal twice the length of $y(t)$ is 1.68 times larger than that of the original signal $y(t)$.

Tripling the window size with $L = 3$ gives;

$$Y(3t) \equiv 3^{0.75} Y(t)$$
$$Y(3t) \equiv 2.28 Y(t)$$

The standard deviation increases by a factor of 2.28. In other words, with a self-affinity parameter $H = 0.75$, the standard deviation grows with increasing window size according to the power-law, L^H. This mathematical formulation shows another property of self-affine processes which is scale-invariance: the scaling of the standard deviation is not dependent on the absolute scale. A signal exhibiting the described behavior is also said to exhibit "scale-free" fluctuations with a "power-law scaling exponent" *H*. *H* is the Hurst-coefficient (Mandelbrot and Wallis, 1969) and ranges between 0 and 1. *H* approaching 1 describes a signal of smooth appearance, typically meaning that high values are followed by high values (i.e., there are dependencies over time), while H close to 0 is a signal with rough, "hairy" appearance, which typically means faster switching between high and low values.

The estimation of the scaling exponent is particularly interesting for neuronal oscillation dynamics, because it can reveal the presence of long-range temporal correlations (LRTC) in neuronal network oscillations (Linkenkaer-Hansen et al., 2001). In the following sections we will show you how.

STATIONARY AND NON-STATIONARY PROCESSES

Definition: a process $X(t)$ is stationary if the distribution of $X(t)$ is independent of t, the joint distribution of $X(t_1 + \tau)$ and $X(t_2 + \tau)$ is independent of τ and similarly – for all k – for the joint distributions of $X(t_1 + \tau) \ldots X(t_k + \tau)$ (Mandelbrot, 1982).

When performing scale-free analysis of a time series, it is essential to have a model of whether the underlying process is stationary. This is because many of the methods used on a time series to estimate *H* make assumptions about whether the process is stationary or not. For example, self-affinity as described above only applies to non-stationary processes, because by definition the variance of a stationary process does not alter with the amount of time looked at (Beran, 1994).

Scale-free processes which are stationary are usually modeled as fractional Gaussian noise (fGn), and non-stationary processes are modeled as fractional Brownian motion (fBm). Nevertheless, there is a strong relationship between these two types of processes in that, by definition, the increments of a fBm process are modeled as a fGn process with the same Hurst parameter, for more details on these models (see Mandelbrot, 1982; Eke et al., 2000). This relationship allows us to apply the definition of self-affinity given above to a stationary fGn process, by first converting it into its non-stationary fBm equivalent as follows. Given the time series $y(t)$, we define the *signal profile* as the cumulative sum of the signal:

$$x(t) = \sum_{k=1}^{t} y(k) - \langle y \rangle \tag{2}$$

where $\langle y \rangle$ is the mean of the time series. The subtraction of the mean eliminates the global trend of the signal. The advantage of applying scaling analysis to the signal profile instead of the signal, is that it makes no *a priori* assumptions about the stationarity of the signal. When computing the scaling of the signal profile, the resulting scaling exponent, α, is an estimation of *H*. If α is between 0 and 1, then *x* was produced by a stationary process which can be modeled as a fGn process with $H = \alpha$. If α is between 1 and 2 then *x* was produced by a non-stationary process, and $H = \alpha - 1$ (Eke et al., 2000).

SCALING OF AN UNCORRELATED STATIONARY PROCESS

We now show that the scaling of a so-called random walk process can be used to infer whether a time series is uncorrelated. A random walk is a non-stationary probabilistic process derived from the cumulative sum of independent random variables, where each variable has equal probability to take a value of 1 or −1. Imagine a walker that at each time step can either take one step left (−1) or right (+1) with equal probabilities (**Figure 2A**). The sequence of the steps representing independent random variables forms a stationary time series as it can only take two values which do not depend on time (**Figures 2B,D**). If we calculate the standard deviation of this time series for differently sized time windows we will not see a scaling effect as there will always on average be an equal number of 1's and −1's. As the probability of taking either action does not depend on any previous actions, the process is said to be "*memory-less.*"

Now, if we compute the cumulative sum of this time series, using Eq. 2 for obtaining the random walk, we can calculate the distance that the walker deviates from the zero line where it started (following a given number of steps; **Figures 2A,C,E**). This distance changes with the number of steps that the walker has taken. Therefore, it is possible to calculate how the standard deviation of distance from the origin (referred to as random walk fluctuations) changes depending on the number of steps that the walker has taken.

We can calculate this by working out the relationship between the displacement, *x*, at time *t* and time $t + 1$. If at time *t* the walker is at position x_t then at time $t + 1$ the walker will be at position $x_t - 1$ or $x_t + 1$ with equal likelihood. Therefore, we can calculate the mean square displacement at time $t + 1$:

$$\begin{aligned} \left\langle x_{t+1}^2 \right\rangle &= \frac{\left\langle (x_t + 1)^2 + (x_t - 1)^2 \right\rangle}{2} \\ &= \frac{\left\langle x_t^2 + 2x_t + 1 + x_t^2 - 2x_t + 1 \right\rangle}{2} \\ \left\langle x_{t+1}^2 \right\rangle &= \frac{2\left\langle x_t^2 \right\rangle + 2}{2} = \left\langle x_t^2 \right\rangle + 1 \end{aligned} \tag{3}$$

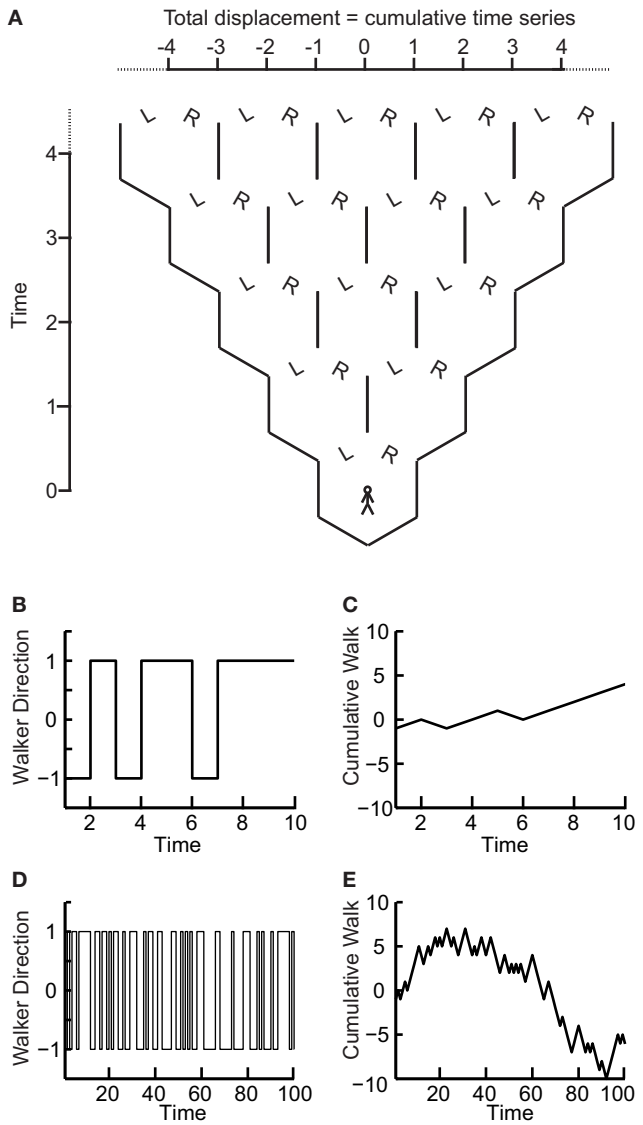

FIGURE 2 | The "random walk": the signal profile of a stationary time series may reveal self-affinity. (A) At each time step a walker moves randomly to the left (−1) or right (+1) with equal probability. At any time step the probability of being at a certain displacement from the origin depends on the number of different paths that could take the walker there. **(B)** The walker's steps form a time series that is stationary as its value does not depend on time. **(C)** The signal profile can take arbitrarily large values as the time increases. **(D)** Looking at the walker time series on a longer time-scale the standard deviation does not change as the signal cannot take larger values. **(E)** The cumulative sum, or random walk process, on a longer time-scale shows larger variance than on the shorter time-scale **(C)** therefore the walker may exhibit self-affinity or scale-free behavior.

Let us define the starting position to be 0, i.e., the mean square displacement at time 0 is:

$$\langle x_0^2 \rangle = 0$$

Now, we can calculate the mean square displacement after an arbitrary number of steps by applying Eq. 3 iteratively:

$$\langle x_1^2 \rangle = \langle x_0^2 \rangle + 1 = 0 + 1 = 1$$
$$\langle x_2^2 \rangle = \langle x_1^2 \rangle + 1 = 1 + 1 = 2$$
$$\langle x_3^2 \rangle = \langle x_2^2 \rangle + 1 = 2 + 1 = 3$$
$$\ldots$$
$$\left(x_L^2\right) = L$$

Thus, the mean square displacement after a walk of length L steps, or equivalently, the root-mean-square displacement after L steps is the square root of L:

$$\left(\langle x_L^2 \rangle\right)^{0.5} = L^{0.5} \tag{4}$$

For a zero mean signal, x, the root-mean-square displacement is the standard deviation. Thus, the cumulative sum of a randomly fluctuating zero mean signal will have the standard deviation growing with window length, L, according to a power-law with the exponent of 0.5. Now, recall from Eq. 1 that if the standard deviation of a signal scales by a factor L^H according to the length of the signal, L, then the process exhibits self-affinity with Hurst exponent H. Thus, we have derived that a stationary randomly fluctuating process has a signal profile, which is self-affine with a scaling exponent $\alpha = 0.5$.

SCALING OF CORRELATED AND ANTI-CORRELATED SIGNALS

What happens to the self-affinity of a process when we add memory in the sense that the probability of an action depends on the previous actions that the walker has made? Different classes of processes with memory exist. Let us focus on those with positive correlations and those with anti-correlations. Anti-correlations can be seen as a stabilizing mechanism: any action the walker makes means that when taking future actions the walker will be more likely to take the opposite action (**Figure 3A**). This leads to smaller fluctuations on longer time-scales than seen by chance (**Figure 3B**). Positive correlations have the opposite effect: any action the walker takes makes it more likely to take that action in the future (**Figure 3A**). This leads to large fluctuations in the integrated signal (**Figure 3B**). We define a fluctuation function as the standard deviation of the signal profile:

$$f(L) = \left(\langle x_L^2 \rangle\right)^{0.5} = L^{\alpha} \tag{5}$$

We note from Eq. (4) that this function grows as a power-law with self-affinity parameter $\alpha = 0.5$ for a stationary random signal. Using Eq. (5) – and as shown in **Figure 3C** – it follows that if the fluctuations scale according to time with:

- $0 < \alpha < 0.5$ then the process has a memory, and it exhibits anti-correlations. (can be modeled by a fGn with $H = \alpha$)
- $0.5 < \alpha < 1$ then the process has a memory, and it exhibits positive correlations. (can be modeled by a fGn with $H = \alpha$)
- $\alpha = 0.5$ then the process is indistinguishable from a random process with no memory. (can be modeled by a fGn with $H = \alpha$)
- $1 < \alpha < 2$ then the process is non-stationary. (can be modeled as a fBm with $H = \alpha - 1$).

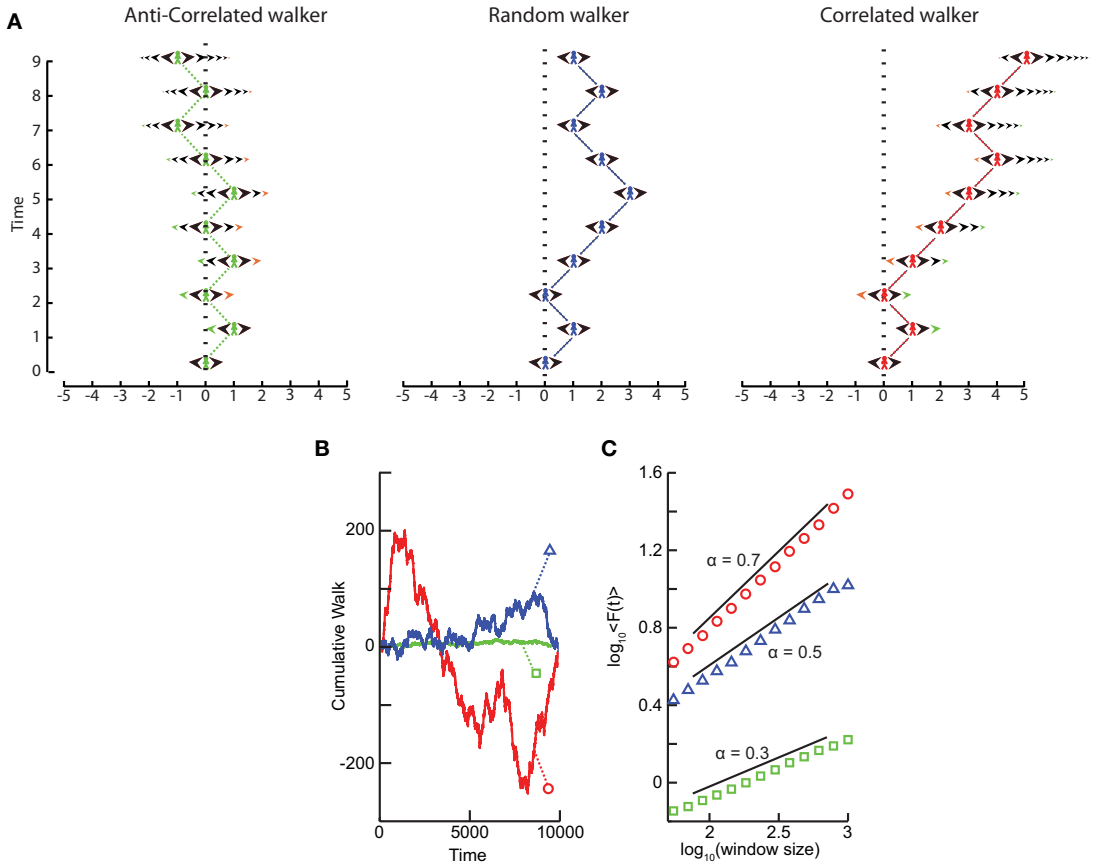

FIGURE 3 | Processes with a memory produce qualitatively, and quantitatively, different fluctuations compared to a random walk process. (A) Correlations occur when the "walker's" decision to follow a certain direction is influenced by its past actions. (Left) Path of an anti-correlated walker shown over time. At each time step the walker makes a decision based on a weighted choice between left and right. The weighted choice can be seen by the sum of the areas of the arrows pointing left and right. Each action the walker takes continues to influence future actions, with the walker being more likely to take the opposite action. This is illustrated as a gradual accumulation of arrows that refer to past actions, but also decrease in size over time, because the bias contributions of those actions decay over time. The green arrows show how the first action the walker takes (going Right) persists over time, with the influence getting smaller as time goes on seen by the green arrow size decreasing. (Center) Path of a random walker shown over time. The random walker is not influenced by previous actions and so always has equal probability of going left or right. (Right) Path of a correlated walker shown over time. Here each action the walker takes influences future actions by making the walker more likely to take that action. The green arrows show that by taking the action of going right at time 0, the walker is more likely to go right in future time steps with the influence getting smaller as time goes on. **(B)** Cumulative signal for a positively correlated process (*red, circle*) shows larger fluctuations over time than a random walker (*blue, triangle*). An anti-correlated signal (*green, square*) shows smaller fluctuations over time. **(C)** By looking at the average fluctuations for these different processes at different time-scales, we can quantify this difference. A random walker shows a scaling exponent of 0.5, with the positively correlated process having a larger exponent, and the anti-correlated process having a smaller exponent.

For short-range correlations the scaling exponent will deviate from 0.5 only for short window sizes, because the standard deviation of the integrated signal in long windows will be dominated by fluctuations that have no dependence on each other. Thus, it is important to report the range where the scaling is observed. We return to the practical issues of identifying the scaling range in the section on "Insights from the application of DFA to neuronal oscillations."

EFFECTS OF TRENDS ON SCALING

We have seen that calculating the fluctuation of signal profiles in windows of different sizes can be used to quantify the scale-free nature of time series. However calculating the fluctuations at a certain time-scale is strongly influenced by whether the signal has a steady trend on longer time-scales. This trend is unlikely to be part of a process on the time-scale of that window and may be removed by subtracting the linear trend in the window, and then calculating the standard deviation. This way we know that processes on scales larger than the given window size will only marginally influence the fluctuation function, Eq. (5).

To illustrate this, consider a white-noise signal with and without a slow trend (**Figure 4A**). The standard deviation of the integrated signal with a trend necessarily will be larger for any window size and, importantly, also grow faster with increasing window sizes compared to the signal without a trend (**Figure 4B**). Detrending the signal profile, however, efficiently reveals the true scaling

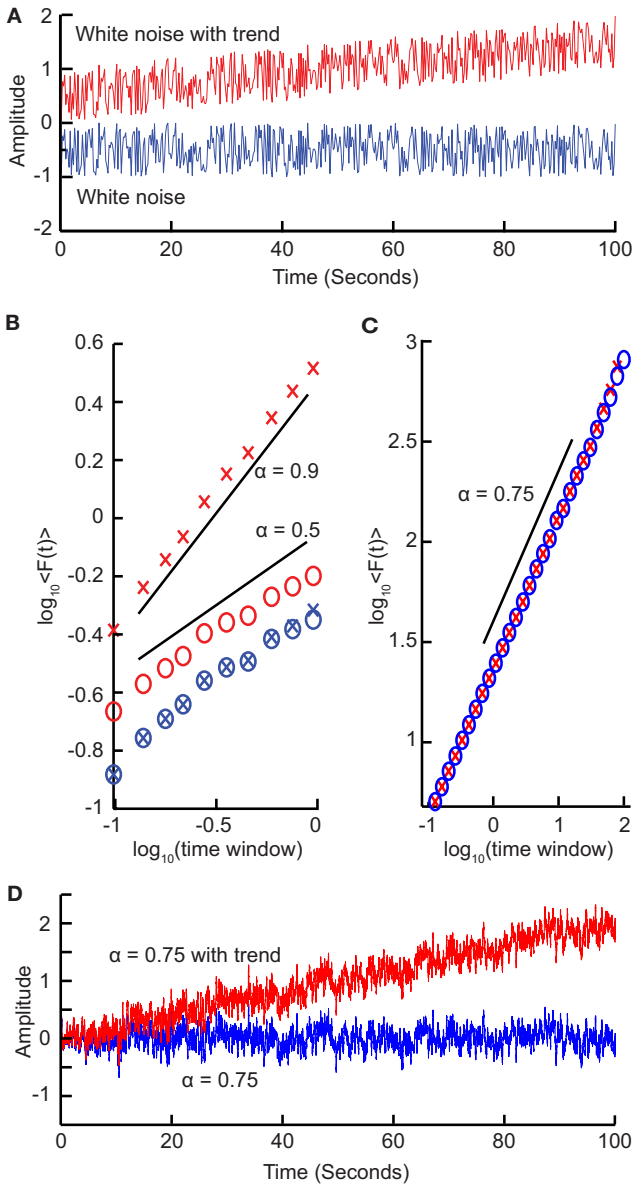

FIGURE 4 | Trends on longer time-scales can introduce false correlations into the signal. (A) For a signal with a trend, the standard deviation will be larger ($\sigma = 0.41$) than the same signal with no trend ($\sigma = 0.29$). **(B)** Average fluctuations for a window size shown for a white-noise signal (*blue crosses*) and the same signal with a trend added (*red crosses*) show different scaling. By removing the linear trend of the integrated signal from each window before calculating the standard deviation (*circles*), we recover the scaling seen without the long-time-scale trend. **(C)** Importantly, detrending self-similar signals with trends (*red crosses*) also recovers the scaling of the original signal (*blue circles*). **(D)** Self-similar signal ($\alpha = 0.75$) with trend (*red*) and without trend (*blue*) used in **(C)**.

of the signal with a superimposed trend both for uncorrelated (**Figure 4B**) and correlated (**Figures 4C,D**) signals. This is the basis for the robust performance of the DFA algorithm which we describe in the next section.

THE DETRENDED FLUCTUATION ANALYSIS

Detrended fluctuation analysis, was introduced by Peng et al. (1994) to quantify LRTC with less strict assumptions about the stationarity of the signal than the auto-correlation function. This was supported with a set of online tutorials and datasets[1] to allow researchers to investigate the method on real-life data (Goldberger et al., 2000). Since then, the algorithm has found widespread application as indicated by more than 1800 citations to (Peng et al., 1994; Google Scholar, September 2012), and it is one of the most commonly used methods to quantify the scale-free nature of physiological time series and their alteration in disease (Peng et al., 1995; Castiglioni et al., 2010; Frey et al., 2011). The DFA is based on the rationale described in the sections presented so far, and can be summarized as follows:

1. Compute the cumulative sum of the time series (**Figure 5A**) to create the signal profile (**Figure 5B**).
2. Define a set of window sizes, $\boldsymbol{T}$, which are equally spaced on a logarithmic scale between the lower bound of four samples (Peng et al., 1994) and the length of the signal.
   - a. For each window length $t \in \boldsymbol{T}$
   - a.i. Split the signal profile into a set ($\boldsymbol{W}$) of separate time series of length t, which have 50% overlap.
   - a.ii. For each window $w \in \boldsymbol{W}$
   - a.ii.1. Remove the linear trend (using a least-squares fit) from the time series to create w^{detrend} (**Figure 5C**)
   - a.ii.2. Calculate the standard deviation of the detrended signal, $\sigma(w^{\text{detrend}})$
   - a.iii. Compute fluctuation function as the mean standard deviation of all identically sized windows:

$$< F(t) >= \text{mean}(\sigma(\boldsymbol{W}))$$

3. Plot the fluctuation function for all window sizes, $\boldsymbol{T}$, on logarithmic axes (**Figure 5D**).
4. The DFA exponent, α, is the slope of the trend line in the range of time-scales of interest and can be estimated using linear regression (**Figure 5D**).

Here, we have chosen logarithmically spaced window sizes, because it gives equal weight to all time-scales when we fit a line in log-log coordinates using linear regression. The lower end of the fitting range is at least four samples, because linear detrending will perform poorly with less points (Peng et al., 1994). For the high end of the fitting range, DFA estimates for window sizes >10% of the signal length are more noisy due to a low number of windows available for averaging (i.e., less than 10 windows). Finally, the 50% overlap between windows is commonly used to increase the number of windows, which can provide a more accurate estimate of the fluctuation function especially for the long-time-scale windows.

The DFA exponent is interpreted as an estimation of the Hurst parameter, as explained with the random walker example, i.e., the

[1] http://www.physionet.org

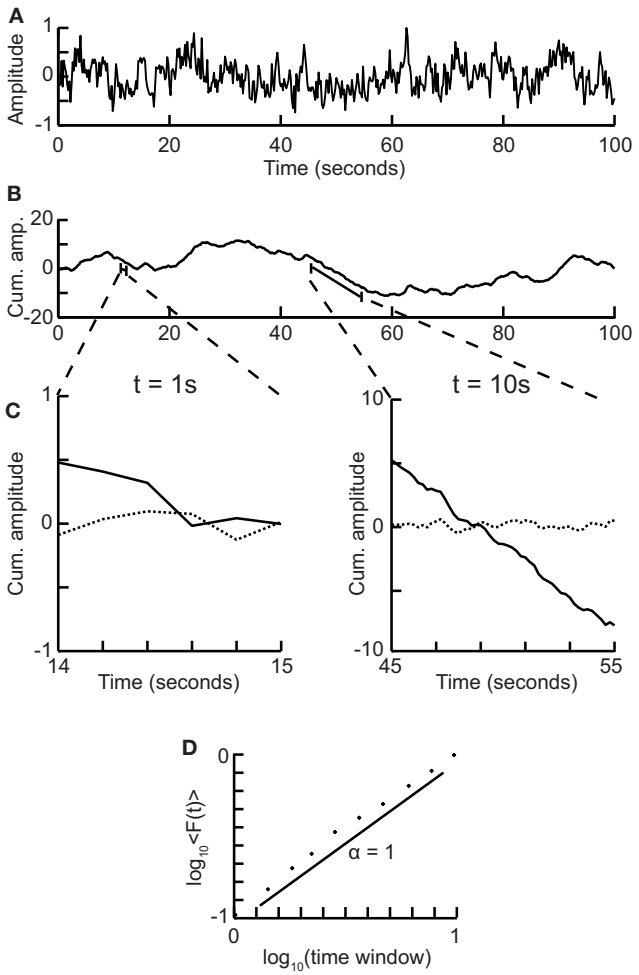

FIGURE 5 | Step-wise explanation of Detrended Fluctuation Analysis. **(A)** Original time series. Taken from a 1/*f* signal sampled at 5 Hz with a duration of 100 s. **(B)** Cumulative sum of original signal shows large fluctuations away from the mean. **(C)** For each window size looked at, remove the linear trend from the signal, and then calculate the fluctuation. Two example window sizes shown with signal shown as solid line, and detrended signal shown as dotted line. **(D)** Plot the mean fluctuation per window size against window size on logarithmic axes. The DFA exponent is the slope of the best-fit line ($\alpha = 1$).

time series is uncorrelated if $\alpha = 0.5$. If $0.5 < \alpha < 1$ then there are positive correlations present in the time series as you are getting larger fluctuations on longer time-scales than expected by chance. If $\alpha < 0.5$ then the time series is anti-correlated, which means that fluctuations are smaller in larger time windows than expected by chance.

Since DFA was first introduced several papers have tested the performance of DFA in relation to trends (Hu et al., 2001), non-stationarities (Chen et al., 2002), pre-processing such as artifact rejection (Chen et al., 2002), and coarse-graining (Xu et al., 2011). Other trend-removal techniques have been proposed, such as higher-order polynomial (Kantelhardt et al., 2001) or adaptive detrending (Riley et al., 2012); however, these have not yet been tested in the DFA analysis of neuronal oscillations.

DFA APPLIED TO NEURONAL OSCILLATIONS

Synchronized activity between groups of neurons occurs in a range of frequencies spanning at least four orders of magnitude from 0.01 to 100 Hz (Buzsáki, 2006). The power spectral density plotted on double-logarithmic axes roughly follows a power-law distribution, but there are also several "peaks" seen along it, corresponding to the classical frequency bands (e.g., theta, alpha, beta, etc.; **Figure 6B**). In this section, we describe how to apply DFA to the amplitude modulation in these frequency bands, and show how they have been utilized in quantifying healthy and pathological conditions. We cannot apply DFA directly to the band-pass filtered signal, because it will appear as a strongly anti-correlated signal because of the peaks and troughs averaging out when computing the cumulative sum. Instead, we focus on the amplitude envelope of oscillations.

Our method consists of four steps:

1. Pre-processing of signals.
2. Create band-pass filter for the frequency band of interest.
3. Extract the amplitude envelope and perform DFA.
4. Determine the temporal integration effect of the filter to choose the window sizes for calculating the DFA exponent.

PRE-PROCESSING OF SIGNALS

Sharp transient artifacts are common in EEG signals. These large jumps in the EEG signal on multiple channels are, e.g., caused by electrode movement. Leaving these in the signal is likely to affect the DFA estimates, whereas removing them has little effect on the estimated exponent (Chen et al., 2002). Other artifacts from, e.g., eye movement, respiration heartbeat, sweat are also likely to disturb the estimate, thus they should be removed.

Another factor that can influence the DFA estimate is the signal-to-noise ratio of the signal. The lower this ratio, the more biased the estimated scaling is toward an uncorrelated signal. Simulations indicated that a SNR >2 is sufficient to accurately determine LRTC (Linkenkaer-Hansen et al., 2007).

FILTER DESIGN

To filter the EEG/MEG data (**Figure 6A**) we use a band-pass finite-impulse-response filter (FIR). This is used instead of an infinite impulse response filter (IIR) to avoid introducing long-range correlations in the signal before calculating the fluctuation function. The filter order for the FIR filter is recommended to be set to two cycles of the lowest frequency in order to accurately detect the oscillations while also limiting the temporal integration caused by the filter. In (**Figure 6B**) we can see a clear peak in the alpha band frequency range (8–13 Hz) and therefore we would band-pass filter in this frequency range with a filter order set to two cycles of 8 Hz.

EXTRACT THE AMPLITUDE ENVELOPE AND PERFORM DFA

When applying DFA to neuronal oscillations, we are interested in how the amplitude of an oscillation changes over time. To calculate this we extract the amplitude envelope from the filtered signal by taking the absolute value of the Hilbert transform (**Figure 6C**; Nikulin and Brismar, 2005). The Hilbert transform is easily accessible in most programming languages (e.g., scipy.signal.Hilbert in

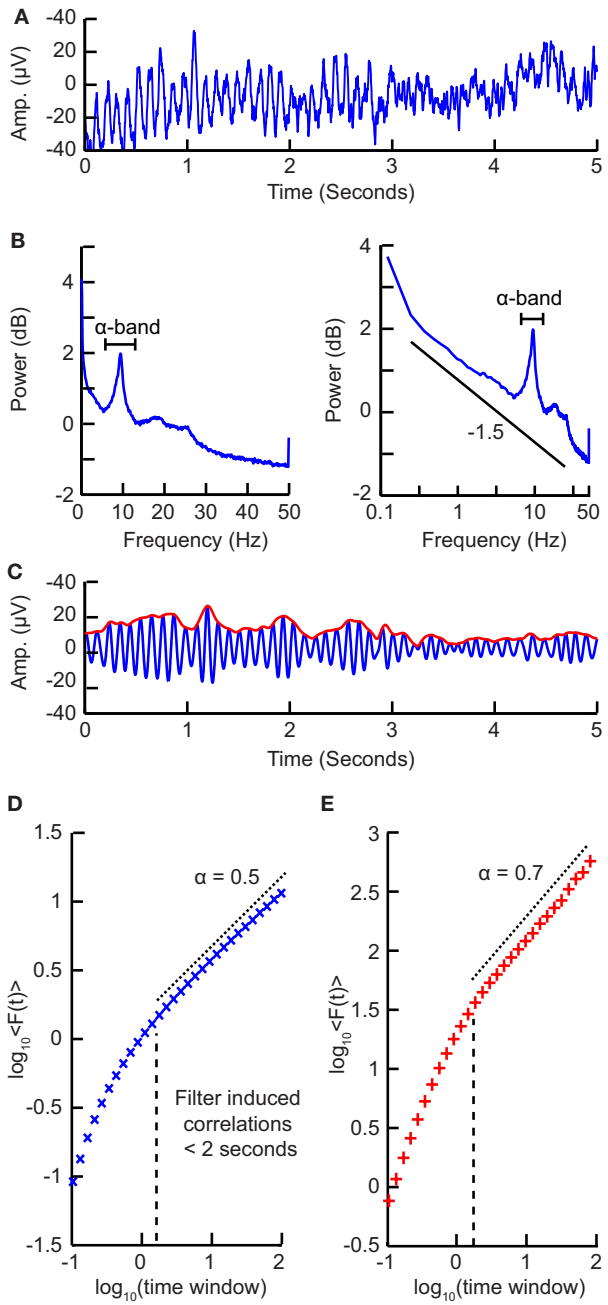

FIGURE 6 | Step-wise explanation of applying DFA to neuronal oscillations. (A) EEG recording from electrode Oz shows clear oscillations during a 15 min eyes-closed rest session. Data were recorded at 250 Hz and band-passed filtered between 0.1 and 200 Hz. **(B)** Power spectrum (Welch method, zero padded) shown in logarithmic (left) and double-logarithmic axes (right), shows clear peak in the alpha band. **(C)** Signal in **(B)** filtered in the alpha band (8–13 Hz) using a fir filter with an order corresponding to the length of two 8 Hz cycles (*blue*). Amplitude envelope (*red*) calculated using the Hilbert transform. **(D)** DFA applied to the amplitude envelope of white-noise signal filtered using the same filter as in **(C)**. At time windows <2 s, filter-induced correlations are visible through a bend away from the 0.5 slope. **(E)** DFA applied to the amplitude envelope of the alpha band filtered EEG signal shows long-range temporal correlations between 2 and 90 s with exponent $\alpha = 0.71$.

Python (Scipy), Hilbert in Matlab). Wavelet transforms, however, have also been used to extract the amplitude envelope (Linkenkaer-Hansen et al., 2001). Once you have the amplitude envelope you can perform DFA on it. However, to decide which window sizes to calculate the exponent from, you first need to follow step 4.

DETERMINING THE TEMPORAL INTEGRATION EFFECT OF THE FILTER

Filtering introduces correlation in the signal between the neighboring samples (e.g., due to the convolution in case of FIR filtering). Thus, including very small window sizes in the fitting range of the fluctuation function will lead to an overestimation of temporal correlations (**Figure 6D**). The effect of a specific filter on the DFA may be estimated using white-noise signals (where a DFA exponent of 0.5 is expected; Nikulin and Brismar, 2004):

a) Create 1000 white-noise signals each one corresponding to ∼1000 s.
b) Filter each signal using the filter designed in step 2.
c) Extract the amplitude envelopes of the filtered noise signals (step 3).
d) Perform DFA on each signal, and average all fluctuation functions.
e) Estimate the lowest fitting time window where the fluctuation function starts to curve away from an exponent of 0.5.

Now that you have the window sizes that have only negligible filter effect, you are finally able to calculate the DFA exponent (**Figure 6E**).

TRY IT YOURSELF USING THE NEUROPHYSIOLOGICAL BIOMARKER TOOLBOX

The NBT was created to facilitate integration of multiple biomarkers and to support large-scale biomarker research in the Matlab environment. DFA has been implemented as part of the NBT. You can download NBT from http://www.nbtwiki.net, where you can also find further tutorials on using this toolbox. NBT can import various data formats (e.g., raw, .dat, .mat, .txt) into the NBT format. The NBT format is defined by three main .mat files: the first contains the signal stored in a matrix, the second contains information about the signal, the third contains the biomarker objects and it is automatically created when you compute a biomarker. The three files are named according to the NBT convention:

- *projectID.subjectID.date.condition.mat* for the signal
- *projectID.subjectID.date.condition_info.mat* for the signal information
- *projectID.subjectID.date.condition_analysis.mat* for the biomarkers.

After you have imported your data into NBT format a variety of actions can be performed on the data, from viewing and preprocessing data to biomarker computation, statistical analysis, and visualization. In the following, we show how a single biomarker, the DFA exponent, can be calculated using the MATLAB command line or a script.

You can also find this tutorial (with more details) online: http://www.nbtwiki.net/doku.php?id=tutorial:detrended_fluctuation_analysis_dfa

REMOVING ARTIFACTS

Before performing any analysis you need to load the signal (already converted into NBT format) into the workspace. Type the following line in the command window to load the signal:

```
[Signal,SignalInfo,path]=nbt_load_file;
```

Signal and *SignalInfo* are the main variables on which NBT works, containing the signal and signal information respectively. Most of the NBT functions have these two variables as input and produce an updated version of them after specific internal processing.

Now you can proceed with artifacts removal. NBT provides several functions to help in this (e.g., an interface for visual inspection of bad channels and noisy epochs, Independent Component Analysis functions for removing periodic artifacts, and different semi-automatic algorithms for facilitating the data cleaning process), but we will not go into details here. However, we would like to emphasize that large-amplitude transient artifacts will influence the temporal structure of the signal and, therefore, it is better to remove them prior to DFA computation (Chen et al., 2002).

FILTER THE SIGNAL AND EXTRACT THE AMPLITUDE ENVELOPE

First, we use the function nbt_GetAmplitudeEnvelope to filter the signal using a FIR filter and get the amplitude envelope using the Hilbert transform, *[AmplitudeEnvelope, AmplitudeEnvelopeInfo] = nbt_GetAmplitudeEnvelope(Signal, SignalInfo, hp, lp, filter_order)*. Let us assume that we want to find the DFA in the alpha frequency band (8–13 Hz):

```
[AmplitudeEnvelope,AmplitudeEnvelopeInfo]
=nbt_GetAmplitudeEnvelope
  (Signal, SignalInfo, 8, 13, 2/8);
```

Note the last parameter 2/8. This is the filter order (in seconds), which we set such that at least two 8 Hz oscillations cycles are covered by the filter window.

PERFORM DFA

The DFA exponents can be then computed using the function nbt_doDFA defined as follow: *[DFAobject,DFA_exp]=nbt_doDFA (Signal, SignalInfo, FitInterval, CalcInterval, DFA_Overlap,DFA_Plot, ChannelToPlot, res_logbin)*.

The parameters, *FitInterval* and *Calcinterval*, determine the time windows in seconds over which we fit and calculate respectively. The *DFA_overlap* tells how much overlap we want between our windows (in this case 50%, see below). The plotting parameters *DFA_plot* assumes value 1 if you want to visualize the result, otherwise 0; in *ChannelToPlot* you can specify for which channel you want to plot the fluctuation function. The last parameter is the resolution of the logarithmic binning, which by default is 10 per decade.

Now find the DFA exponents and visualize the fluctuation function by typing:

```
[DFAobject,DFA_exp]=nbt_doDFA
   (AmplitudeEnvelope,AmplitudeEnvelopeInfo,
   [2 25], [0.8 30], 0.5, 1, 1, []);
```

This instruction will calculate the fluctuation function with 50% overlapping windows from 0.8 to 30 s, and find the DFA exponent by fitting in the interval from 2 to 25 s. The DFA exponent will be stored in *DFA_exp* and *DFA_object* is a structure that stores information such as the fluctuation for each time window and the parameters used to calculate the DFA.

INSIGHTS FROM THE APPLICATION OF DFA TO NEURONAL OSCILLATIONS

The discovery of LRTC in the amplitude envelope of ongoing oscillations, was based on 10 subjects recorded with EEG and MEG for 20 min during eyes-closed and eyes-open rest (Linkenkaer-Hansen et al., 2001). In both conditions, amplitude envelopes of alpha and beta oscillations exhibited power-law scaling behavior on time-scales of 5–300 s with DFA exponents significantly higher than for band-pass filtered white-noise (**Figure 7A**). These results were further validated by showing $1/f$ power spectra and a power-law decay in the auto-correlation function.

The robustness of LRTC in ongoing oscillations has been confirmed in several follow-up studies, albeit often based on shorter experiments and scaling analysis in the range of about 1–25 s (Linkenkaer-Hansen et al., 2007; Monto et al., 2007; Berthouze et al., 2010; Smit et al., 2011; **Figure 7B**). The power-law scaling behavior in the theta band is reported less often (Smit et al., 2011), and to our knowledge LRTC in the delta band have only been investigated in subdural EEG (Monto et al., 2007). LRTC have also not been reported often in the gamma band due to the low SNR obtained from EEG/MEG recordings in this band. Invasive recordings in non-human primates, however, have reported $1/f$ spectra for the amplitude modulation in both low and high gamma bands (Leopold et al., 2003). Recordings from the subthalamic nucleus in Parkinson patients even show prominent LRTC in the very high-frequency gamma range (>200 Hz), especially when treated with the dopamine-precursor drug Levodopa (Hohlefeld et al., 2012).

To gain validity for LRTC it has been shown that LRTC have a link to the underlying genetics of the subject. This link was provided in (Linkenkaer-Hansen et al., 2007) where the scaling of eyes-closed rest EEG from monozygotic and dizygotic twin subjects ($n = 368$) showed that ∼60% of the variance of DFA exponents in the alpha- and beta-frequency bands is attributable to genetic factors (**Figure 7C**). This was an important result as it clearly showed that the non-random patterns of fluctuations in the ongoing oscillations are governed by low-level biological factors as opposed to uncontrolled experimental variables during the recording sessions. The finding also provides an explanation of the significant test-retest reliability of DFA exponents (**Figure 7D**; Nikulin and Brismar, 2004).

Several studies have reported that DFA exponents of neuronal oscillations are independent of oscillation power for a given frequency band, both when the oscillations are recorded with subdural EEG (Monto et al., 2007) and scalp EEG (Linkenkaer-Hansen et al., 2007; Smit et al., 2011; **Figure 7E**). These results together indicate that the DFA can be used as a robust measure of oscillatory dynamics, which captures different features of brain activity than those seen in classical analysis such as power in a frequency band.

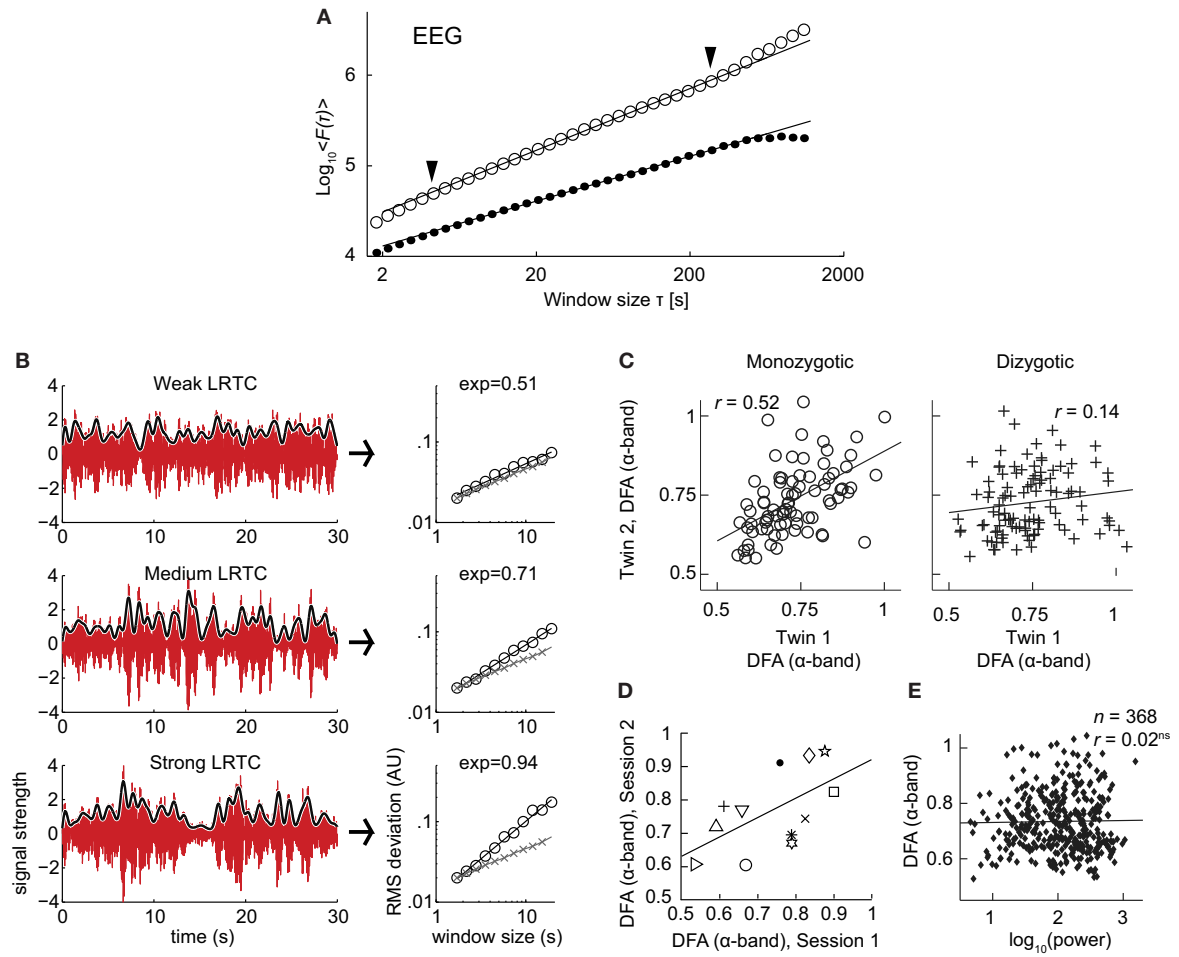

FIGURE 7 | Results of applying DFA to neuronal oscillations. (A) Robust long-range temporal correlations are observed in the amplitude envelope of human EEG alpha oscillations using the DFA. *Circles*, eyes-closed rest condition; *Dots*, surrogate data (Figure modified from Linkenkaer-Hansen et al., 2001). **(B)** Differences in the scale-free modulation of the amplitude envelope of neuronal oscillations are prominent among individuals and can be quantified using DFA. Here shown for three filtered EEG signals (6–13 Hz) with weak (*top*), medium (*middle*), and strong (*bottom)* LRTC (from channel O2). The gray lines represent the amplitude envelope (low-pass filtered, 1 Hz). DFA fluctuation functions are shown to the right, with signal (*circles)*, and white-noise (*crosses*). The DFA exponent is the slope of the fluctuation function. (Figure modified from Smit et al., 2011). **(C)** Individual differences in long-range temporal correlations in alpha oscillations are to a large extent accounted for by genetic variation, as seen by the difference in correlations of DFA exponents between monozygotic and dizygotic twins (Figure modified from Linkenkaer-Hansen et al., 2007). **(D)** DFA has high test-retest reliability. DFA exponents from the amplitude modulation of alpha oscillations, two sessions with an interval of 6–28 days, symbols indicates different subjects (Figure modified from Nikulin and Brismar, 2004). **(E)** The DFA exponent is independent of oscillation power. Data were recorded using EEG on 368 subjects during a 3 min eyes-closed rest session (Figure modified from Linkenkaer-Hansen et al., 2007).

DFA AS A BIOMARKER OF NEUROPHYSIOLOGICAL DISORDER

We have so far discussed the results of applying DFA to healthy subjects; however, some of the most exciting results have come from pre-clinical studies, which indicate possible functional roles for LRTC. For example, a breakdown of LRTC in the amplitude fluctuations of resting-state theta oscillations detected in the left sensorimotor region was reported for patients with major depressive disorder (Linkenkaer-Hansen et al., 2005). Interestingly, the severity of depression, as measured by the Hamilton depression rating scale, inversely correlated with the DFA exponent of the patients (**Figure 8A**). Reduction in the LRTC of oscillations has also been reported in the alpha band in the parietal region in patients with Alzheimer's disease (Montez et al., 2009; **Figure 8B**). Furthermore, reduction in the alpha and beta bands in the centro-parietal and fronto-central areas has also been reported for patients with schizophrenia (Nikulin et al., 2012).

Interestingly, it seems as though it is not only a loss of LRTC that correlates with disorders, but also elevated levels of LRTC. A study (Monto et al., 2007) looked at different scales of neuronal activity by using subdural EEG to record the areas surrounding an epileptic focus in five patients during ongoing seizure-free activity. They discovered that the LRTC are abnormally strong near the seizure onset zone (**Figure 8C**). Further, it was shown that administration of the benzodiazepine lorazepam to the patients, leads to decreased DFA exponents in the epileptic focus, suggesting that the pharmacological normalization of seizure activity brings with

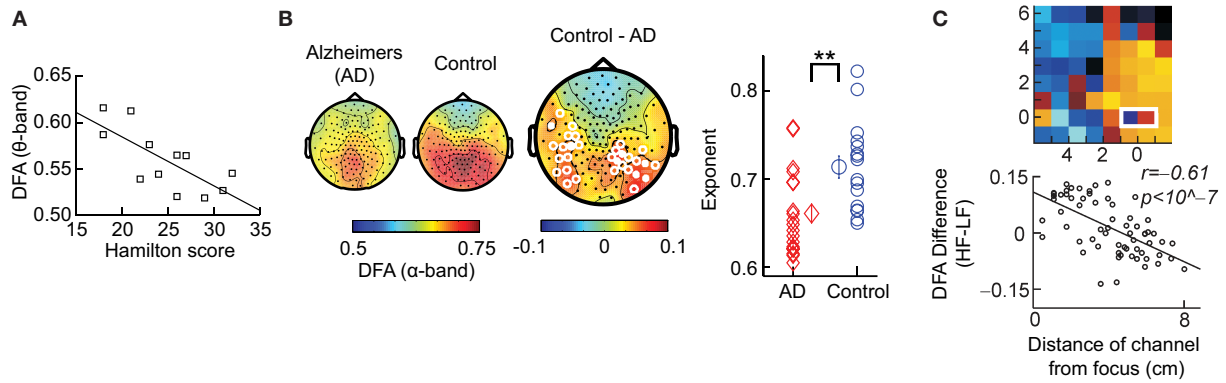

FIGURE 8 | DFA is a promising biomarker for pre-clinical studies. (A) DFA exponents of theta oscillations in left sensorimotor region correlate with the severity of depression based on the Hamilton score. Data recorded from 12 depressed patients with MEG, during an eyes-closed rest session of 16 min. (Figure modified from Linkenkaer-Hansen et al., 2005). **(B)** DFA of alpha oscillations shows a significant decrease in the parietal area in patients with Alzheimer's disease than in controls. MEG was recorded during 4 min of eyes-closed rest and the DFA exponent estimated in the time range of 1–25 s. (*Right*) Individual-subject DFA exponents averaged across significant channels are shown for the patients diagnosed with early stage Alzheimer's disease ($n = 19$) and the age-matched control subjects ($n = 16$; Figure modified from Montez et al., 2009). **(C)** Difference in the DFA exponent of high frequencies (beta band) and low frequencies (alpha band) indicates the location of the epileptic focus (*white box*). Data recorded from an epileptic subject using subdural EEG during seizure-free activity (modified from Monto et al., 2007 by permission of Oxford University Press).

it also a normalization of LRTC. Interestingly, however, DFA exponents were observed to increase in the seizure-free surrounding areas, which may correspond to the increase in LRTC observed *in vitro* after application of Zolpidem, which is also a GABAergic modulator (Poil et al., 2011).

Overall these studies seem to indicate that there is an optimal level of temporal structure of oscillations and any deviation from this can result in a significant loss of function (Poil et al., 2012). Importantly, whereas early studies have estimated the DFA exponent from the scaling of the fluctuation function across almost two orders of magnitude in time (Linkenkaer-Hansen et al., 2001, 2004; Parish et al., 2004; Monto et al., 2007), most reports have used one decade of fitting range and found the DFA a very useful biomarker to study neuronal dynamics in health and disease.

OUTLOOK

In the last 10 years there has been rapid progress in the field of LRTC analysis of neuronal signals (Linkenkaer-Hansen et al., 2001; Parish et al., 2004; Stead et al., 2005; Monto et al., 2007). However, there are still many fundamental issues that need to be addressed, thus presenting many exciting opportunities for applying LRTC methodology to studies of normal and pathologic brain functioning.

It has for a long time been recognized that the brain functions at different time-scales, ranging from a few tens of milliseconds required for the perception of stimuli, to tens of seconds spent on different cognitive operations (Axmacher et al., 2006; Buzsáki, 2006; Cassenaer and Laurent, 2007; Lisman, 2010). Yet, rarely were neuronal dynamics studied with approaches incorporating different time-scales in order to better understand integrative brain mechanisms. In this sense LRTC represent a unique approach describing in a succinct way how neuronal activity unfolds in time taking into account different time-scales. Given that neuronal signals are often non-stationary, DFA has been proven to be a reliable method for capturing LRTC. The DFA method can be successfully applied to both resting-state and task-dependent recordings. It can also be used for quantifying brain activity during different tasks, such as mental counting, visual and motor imagery, or even during presentation of different stimuli. Here the neuronal reactivity caused by the stimuli is usually transient in the order of hundreds of milliseconds and as such can easily be ruled out as the source for modulation of neuronal dynamics on the scale of tens of seconds (Linkenkaer-Hansen et al., 2004), the latter rather being related to the attentional or vigilance states. Recently DFA has been adapted to allow detection of time-varying scaling exponents (Berthouze and Farmer, 2012), which could prove useful in data where brain-state changes could be expected to produce different scaling, e.g., at the onset of sleep (Kim et al., 2009) or in acute response to drugs (Monto et al., 2007; Hohlefeld et al., 2012).

In (Monto et al., 2008) it was shown that there are infraslow oscillations with a frequency of 0.01–0.1 Hz that predict human behavioral performance and were correlated with the amplitude of the classical frequency bands (alpha, beta, gamma, etc.). However, it is yet to be determined whether the amplitude modulation of the classical frequency band oscillations are the cause of infraslow oscillations, which is theoretically plausible, because these oscillations often have non-zero mean (Nikulin et al., 2007). Alternatively, a mechanism that is not directly related to the neuronal oscillations could produce excitability changes in the cortex, which would be reflected in infraslow oscillations and modulate the amplitude of all the other oscillations.

One of the main explanations for the presence of LRTC in neuronal oscillations has been the hypothesis of a brain being in a critical-state (Bak, 1996; Linkenkaer-Hansen et al., 2001; Kello et al., 2010). Criticality in neuronal networks has been related to optimal information processing using computational models (Kinouchi and Copelli, 2006). At the level of neuronal populations, criticality is reflected in scale-free distributions of local field potential propagations, so-called neuronal avalanches, and these have been observed both *in vitro* (Beggs and Plenz,

2003) and *in vivo* (Petermann et al., 2009). Importantly, it was recently shown in computational models of neuronal oscillations that LRTC emerges only when networks produce critical neuronal avalanches and this occurs when excitatory and inhibitory connectivities are balanced (Poil et al., 2012). Thus, it is likely that LRTC reflect critical-state dynamics of neuronal networks, but more work is needed to explain how variation in DFA exponents in different frequency bands and anatomical regions relate to neuronal avalanches, criticality, and computation.

ACKNOWLEDGMENTS

This work was supported by Netherlands Organization for Scientific Research (NWO) Physical Sciences Grant 612.001.123 to Klaus Linkenkaer-Hansen, a talent grant to Klaus Linkenkaer-Hansen (CvB, VU University Amsterdam), a Young Talent grant to Richard Hardstone from Neuroscience Campus Amsterdam, and a Top Talent grant to Simon-Shlomo Poil (NWO). Rick Jansen was supported by a grant from the "Integrative Analysis and Modeling" program of the Neuroscience Campus Amsterdam.

REFERENCES

Axmacher, N., Mormann, F., Fernández, G., Elger, C. E., and Fell, J. (2006). Memory formation by neuronal synchronization. *Brain Res. Rev.* 52, 170–182.

Bak, P. (1996). *How Nature Works: The Science of Self-Organized Criticality*. Berlin: Springer.

Bassingthwaighte, J. B., Liebovitch, L. S., and West, B. J. (1994). *Fractal Physiology*. New York: Oxford University Press.

Beggs, J. M., and Plenz, D. (2003). Neuronal avalanches in neocortical circuits. *J. Neurosci.* 23, 11167–11177.

Beran, J. (1994). *Statistics for Long-Memory Processes*. New York: Chapman & Hall/CRC.

Berthouze, L., and Farmer, S. F. (2012). Adaptive time-varying detrended fluctuation analysis. *J. Neurosci. Methods* 209, 178–188.

Berthouze, L., James, L. M., and Farmer, S. F. (2010). Human EEG shows long-range temporal correlations of oscillation amplitude in Theta, Alpha and Beta bands across a wide age range. *Clin. Neurophysiol.* 121, 1187–1197.

Buzsáki, G. (2006). *Rhythms of the Brain*. Oxford: Oxford University Press.

Cassenaer, S., and Laurent, G. (2007). Hebbian STDP in mushroom bodies facilitates the synchronous flow of olfactory information in locusts. *Nature* 448, 709–713.

Castiglioni, P., Parati, G., Di Rienzo, M., Carabalona, R., Cividjan, A., and Quintin, L. (2010). Scale exponents of blood pressure and heart rate during autonomic blockade as assessed by detrended fluctuation analysis. *J. Physiol. (Lond.)* 589, 355–369.

Chen, Z., Ivanov, P. C., Hu, K., and Stanley, H. (2002). Effect of nonstationarities on detrended fluctuation analysis. *Phys. Rev. E Stat. Nonlin. Soft Matter Phys.* 65, 041107.

Eke, A., Hermán, P., Bassingthwaighte, J., Raymond, G., Percival, D., Cannon, M., et al. (2000). Physiological time series: distinguishing fractal noises from motions. *Pflugers Arch.* 439, 403.

Eke, A., Herman, P., Kocsis, L., and Kozak, L. (2002). Fractal characterization of complexity in temporal physiological signals. *Physiol. Meas.* 23, R1.

Frey, U., Maksym, G., and Suki, B. (2011). Temporal complexity in clinical manifestations of lung disease. *J. Appl. Physiol.* 110, 1723.

Ghosh, A., Rho, Y., McIntosh, A., Kötter, R., and Jirsa, V. (2008). Noise during rest enables the exploration of the brain's dynamic repertoire. *PLoS Comput. Biol.* 4, e1000196. doi:10.1371/journal.pcbi.1000196

Gilden, D. L. (2001). Cognitive emissions of 1/*f* noise. *Psychol. Rev.* 108, 33–56.

Goldberger, A. L., Amaral, L. A. N., Glass, L., Hausdorff, J. M., Ivanov, P. Ch., Mark, R. G., et al. (2000). PhysioBank, PhysioToolkit, and PhysioNet: components of a new research resource for complex physiologic signals. *Circulation* 101, E215–E220.

Goldberger, A. L., Amaral, L. A. N., Hausdorff, J. M., Ivanov, P. C., Peng, C. K., and Stanley, H. E. (2002). Fractal dynamics in physiology: alterations with disease and aging. *Proc. Natl. Acad. Sci. U S A.* 99, 1.

He, B. J., Zempel, J. M., Snyder, A. Z., and Raichle, M. E. (2010). The temporal structures and functional significance of scale-free brain activity. *Neuron* 66, 353–369.

Hohlefeld, F. U., Huebl, J., Huchzermeyer, C., Schneider, G. H., Schönecker, T., Kühn, A. A., et al. (2012). Long-range temporal correlations in the subthalamic nucleus of patients with Parkinson's disease. *Eur. J. Neurosci.*

Hu, K., Ivanov, P. C., Chen, Z., Carpena, P., and Stanley, H. E. (2001). Effect of trends on detrended fluctuation analysis. *Phys. Rev. E Stat. Nonlin. Soft Matter Phys.* 64, 011114.

Kantelhardt, J. W., Koscielny-Bunde, E., Rego, H. H. A., Havlin, S., and Bunde, A. (2001). Detecting long-range correlations with detrended fluctuation analysis. *Physica A* 295, 441–454.

Kello, C. T., Brown, G. D. A., Ferrer-I-Cancho, R., Holden, J. G., Linkenkaer-Hansen, K., Rhodes, T., et al. (2010). Scaling laws in cognitive sciences. *Trends Cogn. Sci. (Regul. Ed.)* 14, 223–232.

Kim, J. W., Shin, H. B., and Robinson, P. A. (2009). Quantitative study of the sleep onset period via detrended fluctuation analysis: normal vs. narcoleptic subjects. *Clin. Neurophysiol.* 120, 1245–1251.

Kinouchi, O., and Copelli, M. (2006). Optimal dynamical range of excitable networks at criticality. *Nat. Phys.* 2, 348–351.

Leopold, D. A., Murayama, Y., and Logothetis, N. K. (2003). Very slow activity fluctuations in monkey visual cortex: implications for functional brain imaging. *Cereb. Cortex* 13, 422.

Linkenkaer-Hansen, K., Monto, S., Rytsälä, H., Suominen, K., Isometsä, E., and Kähkönen, S. (2005). Breakdown of long-range temporal correlations in theta oscillations in patients with major depressive disorder. *J. Neurosci.* 25, 10131–10137.

Linkenkaer-Hansen, K., Nikouline, V. V., Palva, J. M., and Ilmoniemi, R. J. (2001). Long-Range temporal correlations and scaling behavior in human brain oscillations. *J. Neurosci.* 21, 1370–1377.

Linkenkaer-Hansen, K., Nikulin, V. V., Palva, J. M., Kaila, K., and Ilmoniemi, R. J. (2004). Stimulus-induced change in long-range temporal correlations and scaling behaviour of sensorimotor oscillations. *Eur. J. Neurosci.* 19, 203–218.

Linkenkaer-Hansen, K., Smit, D. J. A., Barkil, A., Van Beijsterveldt, T. E. M., Brussaard, A. B., Boomsma, D. I., et al. (2007). Genetic contributions to long-range temporal correlations in ongoing oscillations. *J. Neurosci.* 27, 13882–13889.

Lisman, J. (2010). Working memory: the importance of theta and gamma oscillations. *Curr. Biol.* 20, R490–R492.

Mandelbrot, B. (1967). How long is the coast of Britain? Statistical self-similarity and fractional dimension. *Science* 156, 636.

Mandelbrot, B. B. (1982). *The Fractal Geometry of Nature*. New York: Times Books.

Mandelbrot, B. B., and Wallis, J. R. (1969). Some long-run properties of geophysical records. *Water Resour. Res.* 5, 321–340.

Montez, T., Poil, S. S., Jones, B. F., Manshanden, I., Verbunt, J., Van Dijk, B. W., et al. (2009). Altered temporal correlations in parietal alpha and prefrontal theta oscillations in early-stage Alzheimer disease. *Proc. Natl. Acad. Sci. U.S.A.* 106, 1614.

Monto, S., Palva, S., Voipio, J., and Palva, J. M. (2008). Very slow EEG fluctuations predict the dynamics of stimulus detection and oscillation amplitudes in humans. *J. Neurosci.* 28, 8268–8272.

Monto, S., Vanhatalo, S., Holmes, M. D., and Palva, J. M. (2007). Epileptogenic neocortical networks are revealed by abnormal temporal dynamics in seizure-free subdural EEG. *Cereb. Cortex* 17, 1386.

Nikulin, V. V., and Brismar, T. (2004). Long-range temporal correlations in alpha and beta oscillations: effect of arousal level and test-retest reliability. *Clin. Neurophysiol.* 115, 1896–1908.

Nikulin, V. V., and Brismar, T. (2005). Long-range temporal correlations in electroencephalographic oscillations: relation to topography, frequency band, age and gender. *Neuroscience* 130, 549–558.

Nikulin, V. V., Jönsson, E. G., and Brismar, T. (2012). Attenuation of long range temporal correlations in the amplitude dynamics of alpha and beta neuronal oscillations in patients with schizophrenia. *Neuroimage* 61, 162–169.

Nikulin, V. V., Linkenkaer-Hansen, K., Nolte, G., Lemm, S., Müller, K. R., Ilmoniemi, R. J., et al. (2007). A novel mechanism for evoked responses in the human brain. *Eur. J. Neurosci.* 25, 3146–3154.

Parish, L., Worrell, G., Cranstoun, S., Stead, S., Pennell, P., and Litt, B. (2004). Long-range temporal correlations in epileptogenic and non-epileptogenic human hippocampus. *Neuroscience* 125, 1069–1076.

Peitgen, H. O., Jurgens, H., and Saupe, D. (1992). *Chaos and Fractals: New Frontiers of Science.* New York: Springer.

Peng, C., Havlin, S., Stanley, H., and Goldberger, A. (1995). Quantification of scaling exponents and crossover phenomena in nonstationary heartbeat time series. *Chaos* 5, 82–87.

Peng, C. K., Buldyrev, S. V., Havlin, S., Simons, M., Stanley, H. E., and Goldberger, A. L. (1994). Mosaic organization of DNA nucleotides. *Phys. Rev. E Stat. Phys. Plasmas Fluids Relat. Interdiscip. Topics* 49, 1685.

Petermann, T., Thiagarajan, T. C., Lebedev, M. A., Nicolelis, M. A. L., Chialvo, D. R., and Plenz, D. (2009). Spontaneous cortical activity in awake monkeys composed of neuronal avalanches. *Proc. Natl. Acad. Sci. U.S.A.* 106, 15921–15926.

Poil, S.-S., Hardstone, R., Mansvelder, H. D., and Linkenkaer-Hansen, K. (2012). Critical-state dynamics of avalanches and oscillations jointly emerge from balanced excitation/inhibition in neuronal networks. *J. Neurosci.* 32, 9817–9823.

Poil, S. S., Jansen, R., Van Aerde, K., Timmerman, J., Brussaard, A. B., Mansvelder, H. D., et al. (2011). Fast network oscillations in vitro exhibit a slow decay of temporal auto-correlations. *Eur. J. Neurosci.* 34, 394–403.

Riley, M., Bonnette, S., Kuznetsov, N., Wallot, S., and Gao, J. (2012). A tutorial introduction to adaptive fractal analysis. *Front. Physiol.* 3:371. doi:10.3389/fphys.2012.00371

Smit, D. J. A., De Geus, E. J. C., Van De Nieuwenhuijzen, M. E., Van Beijsterveldt, C. E. M., Van Baal, G. C. M., Mansvelder, H. D., et al. (2011). Scale-free modulation of resting-state neuronal oscillations reflects prolonged brain maturation in humans. *J. Neurosci.* 31, 13128–13136.

Stam, C. (2005). Nonlinear dynamical analysis of EEG and MEG: review of an emerging field. *Clin. Neurophysiol.* 116, 2266–2301.

Stead, M., Worrell, G., and Litt, B. (2005). Frequency and dependence of long range temporal correlations in human hippocampal energy fluctuations. *Complexity* 10, 35–44.

Turcotte, D. L. (1997). *Fractals and Chaos in Geology and Geophysics.* Cambridge: Cambridge University Press.

West, B. J. (2010). Frontiers: fractal physiology and the fractional calculus: a perspective. *Front. Physiol.* 1:12. doi:10.3389/fphys.2010.00012

Xu, Y., Ma, Q. D. Y., Schmitt, D. T., Bernaola-Galván, P., and Ivanov, P. C. (2011). Effects of coarse-graining on the scaling behavior of long-range correlated and anti-correlated signals. *Physica A* 390, 4057–4072.

Conflict of Interest Statement: The authors declare that the research was conducted in the absence of any commercial or financial relationships that could be construed as a potential conflict of interest.

Received: 30 January 2012; accepted: 10 November 2012; published online: 30 November 2012.

Citation: Hardstone R, Poil S-S, Schiavone G, Jansen R, Nikulin VV, Mansvelder HD and Linkenkaer-Hansen K (2012) Detrended fluctuation analysis: a scale-free view on neuronal oscillations. Front. Physio. ***3****:450. doi: 10.3389/fphys.2012.00450*

This article was submitted to Frontiers in Fractal Physiology, a specialty of Frontiers in Physiology.

frontiers in
PHYSIOLOGY

REVIEW ARTICLE
published: 28 March 2012
doi: 10.3389/fphys.2012.00062

Activity-dependent neuronal model on complex networks

***Lucilla de Arcangelis*[1]* and *Hans J. Herrmann*[2,3]**

[1] *Department of Information Engineering, Second University of Naples, Aversa, Italy*
[2] *Institute Computational Physics for Engineering Materials, Eidgenössische Technische Hochschule, Zürich, Switzerland*
[3] *Departamento de Física, Universidade Federal do Ceará, Fortaleza, Brazil*

Edited by:
Tjeerd W. Boonstra, University of New South Wales, Australia

Reviewed by:
John M. Beggs, Indiana University, USA
Michael Muskulus, Norwegian University of Science and Technology, Norway

***Correspondence:**
Lucilla de Arcangelis, Department of Information Engineering, Second University of Naples, via Roma 29, Aversa, 81031 Caserta, Italy.
e-mail: lucilla.dearcangelis@unina2.it

Neuronal avalanches are a novel mode of activity in neuronal networks, experimentally found *in vitro* and *in vivo*, and exhibit a robust critical behavior: these avalanches are characterized by a power law distribution for the size and duration, features found in other problems in the context of the physics of complex systems. We present a recent model inspired in self-organized criticality, which consists of an electrical network with threshold firing, refractory period, and activity-dependent synaptic plasticity. The model reproduces the critical behavior of the distribution of avalanche sizes and durations measured experimentally. Moreover, the power spectra of the electrical signal reproduce very robustly the power law behavior found in human electroencephalogram (EEG) spectra. We implement this model on a variety of complex networks, i.e., regular, small-world, and scale-free and verify the robustness of the critical behavior.

Keywords: neuronal model, complex networks, self-organized criticality

1. INTRODUCTION

The activity in neuronal networks consists in one or more action potentials in a single neuron or an ensemble of neurons. The first case is typical for small networks, as some experimental systems *in vitro*, where isolated spikes can be observed. The presence of a number of action potentials in an ensemble of neurons not always is a consequence of an external stimulus. Neuronal systems exhibit an intense spontaneous activity, known since a long time, whose relation with the response to stimulation is not fully understood yet. It is however well established that spontaneous activity cannot be simply reduced to a background noise uncorrelated to the system response. Indeed, experimental results for the cat visual cortex (Arieli et al., 1996) have shown that the intensity of the response to an external stimulus is roughly proportional to the intensity of the spontaneous activity state of the system when the stimulus is applied. The variability in the response provided to the repeated application of the same stimulus is therefore caused by the different levels of ongoing activity. A similar analysis has been performed at the intracellular level on the same system, confirming that the spatio-temporal structure of the spontaneous activity influences the response signal (Azouz and Gray, 1999).

The typical form of spontaneous activity consists in the almost synchronous emission of action potentials in a large number of neurons, followed by periods of substantial inactivity. These high activity events, named bursts, are observed both during development and in mature systems and can last from a few to several hundreds milliseconds. Conversely, the quiet periods can last seconds and have been attributed to a variety of mechanisms: The decrease in the available neurotransmitter (Stevens and Tsujimoto, 1995; Staley et al., 1998); the presence of an inhibitory factor leading to a disabilitation of the neurotransmitter release (Stevens and Tsujimoto, 1995; Staley et al., 1998); the inactivation, or remodulation of the response, of the glutamate receptors (Maeda et al., 1995). An alternative form of temporal organization is slow oscillations between high activity and low activity states with a typical frequency of 0.3–1 Hz. The temporal organization of this spontaneous activity has been characterized by the distribution of inter-times, i.e., the temporal intervals between successive bursts or successive spikes (Segev et al., 2002).

In 2003 Beggs and Plenz have identified a novel form of spontaneous activity, neuronal avalanches (Beggs and Plenz, 2003, 2004). Coronal slices of rat somatosensory cortex were placed onto a 8×8 multielectrode array (MEA) and spontaneous activity was induced by bath perfusion with the glutamate receptor agonist NMDA in combination with a dopamine receptor agonist. The intrinsic activity of the system was monitored by measuring the potential at each electrode. This local field potential (LFP) integrates the electrical activity of neurons placed in the region surrounding the electrode: negative peaks in the LFP measure the influx of positive ions and therefore the cumulative membrane potential variation of the neurons in the region. Experimental data show that before 6 days *in vitro* activity is mainly composed of sparse activations but during the second week simultaneous activations occur in several electrodes. The novel idea was to examine this electrophysiological signal on a finer temporal scale, which was able to evidence a complex spatio-temporal structure. Indeed, activity starting at one electrode may involve more, non-necessarily neighboring, electrodes. Binning time in cells of duration δt, allows to create a spatio-temporal grid reporting the active electrodes in each temporal cell. A neuronal avalanche is therefore defined as a sequence of successively active electrodes between two temporal bins with no activity. The total number of active electrodes, or alternatively the sum of all LFPs, is defined as the size s of an avalanche and the time interval with ongoing activity as its duration T.

The striking result is that both size and duration have no characteristic value, i.e., their distributions exhibit a power law behavior. The analysis at a finer temporal scale is then able to enlighten the non-synchronous character of the bursts. The exponents of these

power law distributions depend on the choice for the temporal bin δt. Indeed larger bins make active electrodes belonging to different avalanches to merge into the same larger event, leading to a smaller exponent. In order to identify the appropriate value of δt, Beggs and Plenz (2003) verified that if δt is equal to the average value of the time delay between two successive LFPs in the culture, the exponent does not depend any longer on the specific culture. They were then able to identify the universal scaling behavior.

$$\begin{aligned} P(s) &\propto s^{-\sigma} \quad \text{with} \quad \sigma = 1.5 \pm 0.1 \\ P(T) &\propto T^{-\tau} \quad \text{with} \quad \tau = 2.0 \pm 0.1. \end{aligned} \tag{1}$$

The power law behavior for the size distribution is followed by an exponential cut-off due to the finite size of the system, whereas for the duration distribution it extends over about one decade and the exponential cut-off sets in at about 10 ms.

The results *in vitro* have been confirmed by extended studies *in vivo* on anesthetized rats during development (Gireesh and Plenz, 2008) and awake rhesus monkeys (Petermann et al., 2009). Spontaneous neuronal activity recorded by MEA placed in the rat cortical layer 2/3 at the beginning and the end of the second week postnatal, shows higher frequency (up to 100 Hz) oscillations nested into lower frequency (4–15 Hz) oscillations. At the end of the first week postnatal, bursts start to organize into high frequency oscillations and become more synchronized during the second week. Synchronous activity in the bursts exhibits the same scaling behavior found for neuronal avalanches *in vitro* [equation (1)]. This similarity between *in vitro* and *in vivo* experiments supports the idea that the emergence of nested oscillations reflects the development of layer 2/3 in the cortex. Ongoing activity measured in the primary motor and premotor areas of two awake monkeys, sitting with no behavioral task, nor under particular stimulus, exhibits also neuronal avalanches. Their organization is independent of the detection threshold and exhibits scale invariance. Power laws for the size and duration distributions confirm the scaling behavior in equation (1) and suggest that in large neuronal networks a wide variety of avalanche sizes is possible, including clusters percolating throughout the system. This indicates that the largest cluster is solely controlled by the system size and not by the dynamics. This result also generalizes avalanche dynamics across species and different cortical areas. Criticality can be therefore considered as a generic property of spontaneous cortical activity, which may indicate that networks with a larger response repertoire were selected over others throughout evolution. A flexible spontaneous activity could then underlie and optimize important cortical functions as learning and memory.

The investigation on the spontaneous activity has been performed also for dissociated neurons from different networks as rat hippocampal neurons (Mazzoni et al., 2007), rat embryos (Pasquale et al., 2008), or leech ganglia (Mazzoni et al., 2007). Neurons are mechanically dissociated by trituration through fine-tipped pipettes and placed onto a MEA, pre-coated with adhesion promoting molecules, in a nutrient medium. Under fixed conditions of humidity and temperature, neurons start to develop a network of synaptic connections and, after a variable period *in vitro*, exhibit spontaneous electrical activity. The electrodes of the MEA in these experiments record the spikes, rather than the LFPs, due to individual neurons attached to them. As a consequence, the temporal scale for the data analysis has to take into account this difference in order to properly characterize the neuronal response. Choosing the average inter-spike time at a single electrode as the temporal scale for data binning, the spontaneous activity is monitored during the development and in mature cultures. Different behaviors are observed. Only those systems exhibiting a medium level of synchronization between random spikes and synchronized bursts exhibit critical behavior. For those cultures the scaling behavior is very robust and in agreement with equation (1). In particular, the emergence of a critical state has been found to be strongly related to the aging of the system, namely after the first few weeks *in vitro*, where the behavior of the system is subcritical, some cultures may self-organize, and reach the critical state as they mature (Pasquale et al., 2008).

In real brain neurons are known to be able to develop an extremely high number of connections with other neurons, that is a single cell body may receive inputs from even a hundred thousand pre-synaptic neurons. One of the most fascinating questions is how an ensemble of living neurons self-organizes, developing connections to give origin to a highly complex system. The dynamics underlying this process might be driven both by the aim of realizing a well connected network leading to efficient information transmission, and the energetic cost of establishing very long connections. The morphological characterization of a neuronal network grown *in vitro* has been studied (Shefi et al., 2002) by monitoring the development of neurites in an ensemble of few hundred neurons from the frontal ganglion of adult locusts. After few days the cultured neurons have developed an elaborated network with hundreds of connections, whose morphology and topology has been analyzed by mapping it onto a connected graph. The short path length and the high clustering coefficient measured indicate that the network belongs to the category of small-world networks (Watts and Strogatz, 1998), interpolating between regular and random networks. In classical small-world networks the majority of sites have a number of connections close to the average value in the network. Real neuronal networks behave quite differently, since neurons with quite diverse number of connections are observed. Indeed, the properties of the functionality network have been measured experimentally in human adults (Eguiluz et al., 2005). Functional magnetic resonance imaging has shown that this network has universal scale-free properties, namely it exhibits a distribution of out-going connection number, k_{out}, which follows a power law, i.e., $n(k_{out}) \propto k_{out}^{-2}$, independent of the different tasks performed by the patients. This behavior suggests that in the network few neurons are highly connected and act as hubs with respect to information transmission. Small-world features have been also measured for functionality networks in healthy humans, whereas they are not present in patients affected by neurological diseases: Alzheimer patients have longer path lengths (as in regular networks; Stam et al., 2007) whereas schizophrenic patients show a more random architecture of the underlying network (Rubinov et al., 2009). Epileptic patients exhibit a more ordered neuronal network during seizures (Ponten et al., 2007), whereas brain tumor patients a more random one (Bartolomei et al., 2006).

2. THE MODEL

2.1. CONNECTIVITY NETWORKS

The first step to develop a model simulating neuronal dynamics is the choice of the specific network of connections. The simplest choice is a regular lattice, i.e., a square lattice for a two-dimensional system. However, following recent experimental results, we allow neurons to develop long range connections: Starting from a regular lattice, a small fraction of bonds, from 0 to 10%, is rewired, namely one of the two connected neurons is chosen at random in the system. This procedure originates long range connections and gives rise to a small-world network (Watts and Strogatz, 1998; Shefi et al., 2002), which more realistically reproduces the connections in the real brain.

In a small-world networks the number of connections for different neurons is close to an average number. In order to reproduce the experimental data on the connectivity distribution in functionality networks, we implement also scale-free networks. More precisely, we set N neurons at random positions in two-dimensional space and to each neuron we assign an out-going connectivity degree, k_{out}, according to the distribution measured by fMRI measurements of ongoing activity in humans (Eguiluz et al., 2005). Each neuron has a degree equal to a random number between $k_{out}^{min} = 2$ and $k_{out}^{max} = 100$ according to the probability distribution $n(k_{out}) \propto k_{out}^{-2}$. The two neurons are chosen according to a distance dependent probability, $p(r) \propto e^{-r/5<r>}$, where r is their spatial distance (Roerig and Chen, 2002).

In order to consider a network with both features, small-world and scale-free, we also implement the Apollonian network. This has been recently introduced (Andrade et al., 2005) in a simple deterministic version starting from the problem of space-filling packing of spheres according to the ancient Greek mathematician Apollonius of Perga. In its classical version the network associated to the packing gives a triangulation that physically corresponds to the force network of the sphere packing. One starts with the zeroth order triangle of corners P_1, P_2, P_3, places a fourth site P_4 in the center of the triangle and connects it to the three corners ($n = 0$). This operation will divide the original triangle in three smaller ones, having in common the central site. The iteration $n = 1$ proceeds placing one more site in the center of each small triangle and connecting it to the corners (**Figure 1**). At each iteration n, going from 0 to N, the number of sites increases by a factor 3 and the coordination of each already existing site by a factor 2. More precisely, at generation N there are

$$m(k, N) = 3^N, 3^{N-1}, 3^{N-2}, \ldots, 3^2, 3, 1, 3$$

vertices, with connectivity degree

$$k(N) = 3, 3 \times 2, 3 \times 2^2, \ldots, 3 \times 2^{N-1}, 3 \times 2^N, 2^{N+1} + 1$$

respectively, where the two last values correspond to the site P_4 and the three corners P_1, P_2, P_3. The maximum connectivity value then is the one of the very central site P_4, $k_{max} = 3 \times 2^N$, whereas the sites inserted at the N-th iteration will have the lowest connectivity 3.

The important property of the Apollonian network is that it is scale-free. In fact, it has been shown (Andrade et al., 2005) that the discrete cumulative distribution of connectivity degrees $P(k) = \Sigma_{k' \geq k} m(k, N)/N_N$, where $N_N = 3 + (3^{(N+1)} - 1)/2$ is the total number of sites at generation N, can be fitted by a power law. More precisely, $P(k) \propto k^{1-\gamma}$, with $\gamma = \ln 3/\ln 2 \sim 1.585$. Moreover the network has small-world features. This implies (Watts and Strogatz, 1998) that the average length of the shortest path l behaves as in random networks and grows slower than any positive power of N, i.e., $l \propto (\ln N)^{3/4}$. Furthermore the clustering coefficient C is very high as in regular networks ($C = 1$) and contrary to random networks. For the Apollonian network C has been found to be equal to 0.828 in the limit of large N. On this basis, the Apollonian network appears to have all the new features that we would like to investigate: small-world property found experimentally (Shefi et al., 2002) and possibility of a very high connectivity degree (scale-free). Moreover it also presents sites connecting bonds of all lengths. Also this last feature can be found in real neuronal networks, where the length of an axon connecting the pre-synaptic with the post-synaptic neuron can vary over several orders of magnitude, from micrometers to centimeters. Finally, most studies in the literature consider the case of a fully connected network, where each neuron is connected to every other neuron. Even if not completely realistic, we consider also this last case.

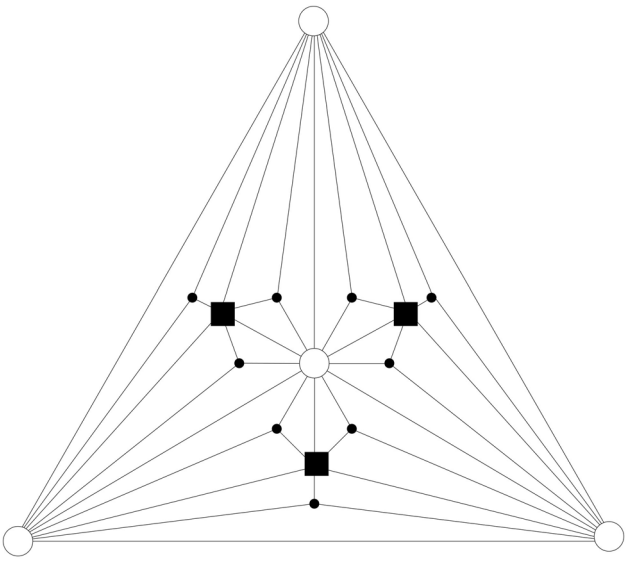

FIGURE 1 | Apollonian network for $N = 2$: iterations $n = 0, 1, 2$ are symbols ○, ■, ●, respectively.

2.2. NEURONAL DYNAMICS

We here discuss a neuronal network model based on self-organized criticality ideas (Bak, 1996). The model implements several physiological properties of real neurons: a continuous membrane potential, firing at threshold, synaptic plasticity, and pruning. In order to define the model we need to specify the behavior of the single neuron under different conditions, the dynamics then determines the system behavior (de Arcangelis et al., 2006a; Pellegrini et al., 2007; de Arcangelis and Herrmann, 2010). We consider N neurons at the nodes of the chosen network, characterized by their

potential v_i. The neuron positions will then be ordered in space for regular lattices and small-world networks, organized in a hierarchical manner for the Apollonian network and randomly chosen in two dimensions for the scale-free and fully connected networks. Once the network of output connections is established, we identify the resulting degree of in-connections, k_{in_j}, for each neuron j. To each synaptic connection we assign an initial random strength g_{ij}, where $g_{ij} \neq g_{ji}$, and to each neuron randomly either an excitatory or an inhibitory character, with a fraction p_{in} of inhibitory synapses. Whenever at time t the value of the potential at a site i is above a certain threshold $v_i \geq v_{\max}$, the neuron sends action potentials which arrive to each of the k_{out_i} pre-synaptic buttons and lead to a total production of neurotransmitter proportional to v_i. As a consequence, the total charge that could enter into connected neurons is proportional to $v_i k_{out_i}$. Each of them receives charge in proportion to the strength of the synapses g_{ij}

$$v_j\,(t+1) = v_j\,(t) \pm \frac{v_i\,(t)\,k_{out_i}}{k_{in_j}} \frac{g_{ij}\,(t)}{\sum_k g_{ik}\,(t)} \tag{2}$$

where the sum is extended to all out-going connections of i. In equation (2) the membrane potential variation is obtained by dividing the received charge by the surface of the soma of the post-synaptic neuron, proportional to the number of in-going terminals k_{in_j}. The plus or minus sign in equation (2) is for excitatory or inhibitory synapses, respectively. In regular networks neurons have about the same number of in-going and out-going connections, therefore equation (1) reduces to the simpler expression $v_j(t+1) = v_j(t) \pm v_i(t)\frac{g_{ij}(t)}{\sum_k g_{ik}(t)}$. The same consideration holds for small-world networks.

The firing rate of real neurons is limited by the refractory period, i.e., the brief period after the generation of an action potential during which a second action potential is difficult or impossible to elicit. The practical implication of refractory periods is that the action potential does not propagate back toward the initiation point and therefore is not allowed to reverberate between the cell body and the synapse. In our model, once a neuron fires, it remains quiescent for one time step and it is therefore unable to accept charge from firing neighbors. This ingredient indeed turns out to be crucial for a controlled functioning of our numerical model. In this way an avalanche of charges can propagate far from the input through the system. The initial values of the neuron potentials are uniformly distributed random numbers and the value of v_{max} is fixed equal to 6 in all simulations. Moreover, a small fraction (10%) of neurons is chosen to be output sites, i.e., an open boundary, with a zero fixed potential, playing the role of sinks for the charge. They model neurons connected to neurons not belonging to the slice and avoid that an excess to charge influx would lead to supercritical behavior. Each time neuronal activity stops in the network, an external stimulus is necessary to trigger further activity, which therefore mimics the nutrients from the bath needed to keep a real neuronal network alive. This stimulus consists in increasing the potential of a random neuron by a random quantity uniformly distributed between 0 and v_{max}.

During the propagation of an avalanche according to equation (2), we identify the bonds connecting two successively active neurons, namely neurons whose activity is correlated. The strength of their connections is increased proportionally to the activity of the synapse, namely the membrane potential variation of the post-synaptic neuron induced by the pre-synaptic neuron

$$g_{ij}\,(t+1) = g_{ij}\,(t) + \alpha\, i_{ij}\,(t) \tag{3}$$

where $i_{ij}(t)$ is the current through that synaptic connection and α a dimensionless parameter. Once an avalanche of firings comes to an end, the strength of all inactive synapses is reduced by the average strength increase per bond

$$\Delta g = \sum_{ij,t} \delta g_{ij}\,(t)\,/N_a \tag{4}$$

where N_a is the number of bonds active in the previous avalanche. Here α is the only parameter controlling both the strengthening and the weakening rule in the Hebbian plasticity and represents the ensemble of all possible physiological factors influencing synaptic plasticity. By implementing these rules, our neuronal network "memorizes" the most used paths of discharge by increasing their strength, whereas the less solicited synapses slowly atrophy. Indeed, once the strength of a bond is below an assigned small value $g_t = 10^{-4}$, we remove it, i.e., set its strength equal to zero, which corresponds to the so-called pruning.

We implement synaptic plasticity rules during a series of N_p stimuli in order to modify the synaptic strengths, initially set at random. In this way we do not impose a strength configuration but let the system activity tune their values. Once a percentage of bonds is pruned, we stop plastic adaptation and we perform our measurements, by applying a new sequence of stimuli without modifying the synaptic strengths. The extension of the plastic adaptation procedure then represents the level of experience, or *age*, of the system, whose response we monitor over a time-scale much shorter than the one needed for structural adaptation. All data presented in this manuscript are averaged over long temporal sequences in several initial network configurations. More precisely, for regular and small-world networks we average data on 10 different initial configurations with a sequence of 10000 avalanches per configuration. On the Apollonian network we average over 100 different initial configurations and a sequence of 30000 avalanches per configuration. For scale-free and fully connected networks we average over 60 different initial configurations and a sequence of 50000 stimulations per configuration.

3. PRUNING

The total number of pruned bonds at the end of each avalanche, N_{pb}, in general depends on the initial conductance g_0, therefore it is interesting to investigate the two cases of either all initial conductances equal to 0.25, or being uniformly distributed between 0 and 1. First the case of equal initial conductances is analyzed. The strength of the parameter α, controlling both the increase and decrease of synaptic strength, determines the plasticity dynamics in the network. This homeostatic mechanism implies that the more the system learns strengthening the used synapses, the more the unused connections will weaken. For large values of α the system strengthens more intensively the synapses carrying current but also very rapidly prunes the less used connections, reaching after

a short transient a plateau where it prunes very few bonds. On the contrary, for small values of α the system takes more time to initiate the pruning process and slowly reaches a plateau (**Figure 2**). The inset of the figure shows the asymptotic value of the fraction of surviving bonds, calculated as the total number of bonds in the unpruned network minus the asymptotic number of pruned bonds, as function of α. The number of unpruned bonds asymptotically reaches its largest value at the value $\alpha \simeq 0.03$ for different networks. This could be interpreted as an optimal value for the system with respect to plastic adaptation.

For the Apollonian network it is interesting to investigate if pruning acts in the same way on bonds created at different iterations n, $n = 0, \ldots, N$, or rather tends to eliminate bonds of some particular iteration. The probability to prune bonds of different n is evaluated, that is the number of pruned bonds over the total number of bonds for each iteration stage, as function of the number of applied stimuli. **Figure 3** shows that the plateau is reached at about the same value of N_p and the shape of the curve is similar for each n. However the probability to prune bonds with large n is higher: These are the bonds created in the last iterations and therefore embedded in the interior of the network. This suggests that the most active bonds are the long range ones (small n), which therefore support most of the information transport through the network. It is also interesting to notice that, since the total number of bonds depends exponentially on n, the gaps between the asymptotic values of the probability for successive generations depend exponentially on n. In the inset of **Figure 3** we show the asymptotic number of pruned bonds per generation on a semi-log scale, this quantity is well fitted by the exponential behavior $N_{pb} \simeq \exp n$.

The same analysis has been performed for random initial conductances between 0 and 1. The results are similar to the previous case. It can be noticed that pruning starts already at $N_p = 1$, since conductances close to zero are present, and the plateau is reached after about 1000 stimuli. The value of α which optimizes the number of active bonds is about 0.030 also for the Apollonian network. In this case, the pruning behavior for different iterations is similar to the previous case, with the pruning probability exponentially increasing with n, as $N_{pb} \simeq \exp n$.

The effect of pruning on the connectivity degree of the network is an interesting quantity to monitor on scale-free networks. On Apollonian networks we evaluate the number of sites with a number of out-going connections k_{out} as function of k_{out} in the initial network and after application of a given number of external stimuli (**Figure 4**). After the application of few external stimuli, i.e., for a short plastic adaptation, the distribution $n(k_{out})$ shows the same scaling behavior of the original Apollonian network. As the pruning process goes on, sites exhibit varying connectivity degree, and new values of k_{out} appear. The result is that the scaling behavior is progressively lost, as well as the scale-free character of the network, since there is a generalized decrease of the connectivity in the network.

4. AVALANCHE STATISTICS

After "aging" the system applying plasticity rules during N_p external stimuli, we submit the system to a new sequence of stimuli with no modification of synaptic strengths. The response of the system to this second sequence models the spontaneous activity of a trained neuronal network with a given level of experience. We analyze this activity by measuring the avalanche size distribution $n(s)$ and the time duration distribution $n(T)$.

The avalanche size distribution $n(s)$ consistently exhibits power law behavior for different values of model parameters. **Figure 5** shows the avalanche size distribution for different networks and values of N_p, including also the case $N_p = 0$ (no plasticity adaptation), for random initial conductances and the optimal value of

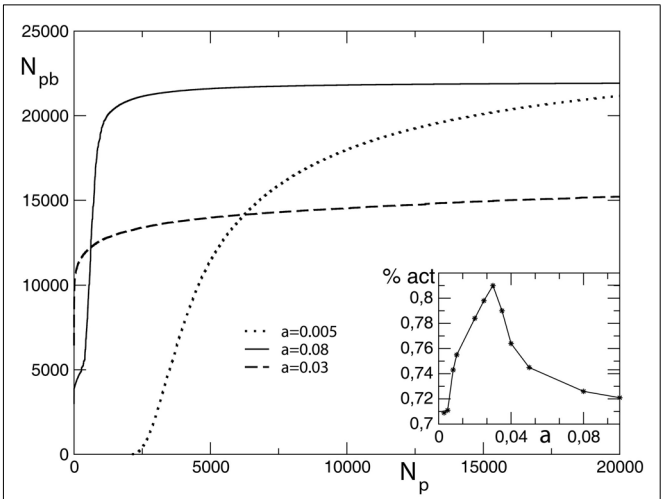

FIGURE 2 | Average number of pruned bonds N_{pb} as function of the number of external stimuli N_p for a square lattice of linear size $L = 100$, equal initial conductances, and different values of α. In the inset we show the asymptotic value of the percentage of surviving bonds as function of α.

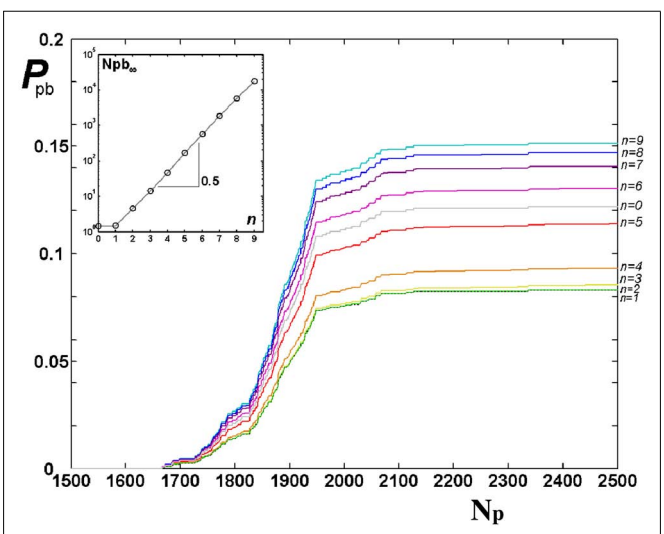

FIGURE 3 | Probability of pruning for bonds of different iterations n of Apollonian networks, from bottom $n = 0$ to top $n = 9$, as function of the number of external stimuli N_p for equal initial synaptic strengths. In the inset, the asymptotic N_{pb} (after 5000 stimuli) is shown as function of n with the exponential fit $N_{pb} \simeq \exp 0.5n$.

α. The value of the exponent is obtained by regression of the log-binned data and found to be $\sigma = 1.5 \pm 0.1$ for all networks, except the Apollonian network where $\tau = 1.8 \pm 0.2$. The exponent is stable with respect to variations of the parameters for both equal and random initial conductances. More accurate methods, as maximum likelihood fitting, should verify the stability of these values (Clauset et al., 2009).

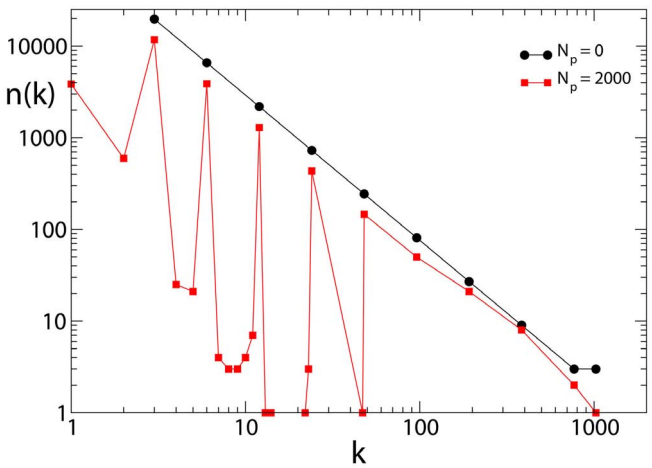

FIGURE 4 | Connectivity degree distribution $n(k_{out})$ at different pruning stages N_p for Apollonian networks with equal initial synaptic strengths and $\alpha = 0.020$. As soon as pruning starts to eliminate bonds, new connectivity degrees appear, not present in the original network. Conversely, two out of the three corner sites, which for the generation $N = 9$ have initially a connectivity degree 1025, may loose bonds because of pruning and, as a result, $n(1025) = 1$.

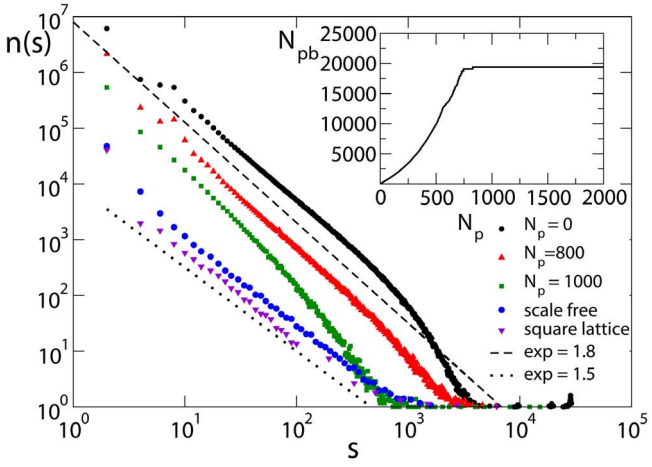

FIGURE 5 | Avalanche size distribution for different networks with $p_{in} = 0.05$: the square lattice ($N = 10^6$, $\alpha = 0.03$); the scale-free network ($N = 4000$); and the Apollonian network for different values of N_p (9th generation with $\alpha = 0.030$). Initial synaptic strengths are randomly distributed. Data are logarithmically binned. In the inset, the corresponding behavior of the number of pruned bonds for the Apollonian network is shown.

It is interesting to stress the importance of noise: Indeed, by applying the external stimulation not at random but at a fixed neuron, the scaling exponent becomes $\sigma = 1.2 \pm 0.1$ (de Arcangelis et al., 2006a). We notice that, for fixed size s, increasing N_p decreases the number of avalanches of that size, suggesting that strong plasticity remodeling decreases activity. The exponent appears to be independent of N_p, as long as the number of pruned bonds, N_{pb}, is far from the plateau (see inset in **Figure 5**). Similar results are found for equal initial conductances. The dependence of the critical behavior on synaptic strengths has been recently investigated in networks of integrate-and-fire neurons (Levina et al., 2007). The value of the exponent is compatible within error bars with the value found in the experiments of Beggs and Plenz (2003), 1.5 ± 0.4. However, one has to notice that experimental results for neuronal avalanches were obtained for local field potentials, i.e., the underlying events correspond to local population spikes, whereas the numerical events are single neuronal spikes. The slightly larger value of the exponent, found on the Apollonian network, suggests that the peculiar hierarchical structure of the network may reduce the probability of very large avalanches but does not change substantially the electrical activity. For larger N_p, the distribution exhibits an increase in the scaling exponent and finally looses the scaling behavior for very large N_p values, in the plateau regime for the number of pruned bonds.

In order to investigate the role of plastic modifications on the production of very large avalanches, simulations are performed for fully connected networks which undergo plastic adaptation routines of different length. All networks exhibit supercritical behavior, namely an excess of very large avalanches, due to the high level of connectivity in the system (**Figure 6**). Very large avalanches involve almost all neurons and their large number hinders pruning, namely there are only very few synapses in the system repeatedly inactive which progressively weaken and atrophy. This behavior is independent of the extension of the plastic adaptation. No pruning is observed even following the application of hundred thousand stimuli. Very large avalanches therefore seem to be sustained by the high connectivity in the system and apparently do

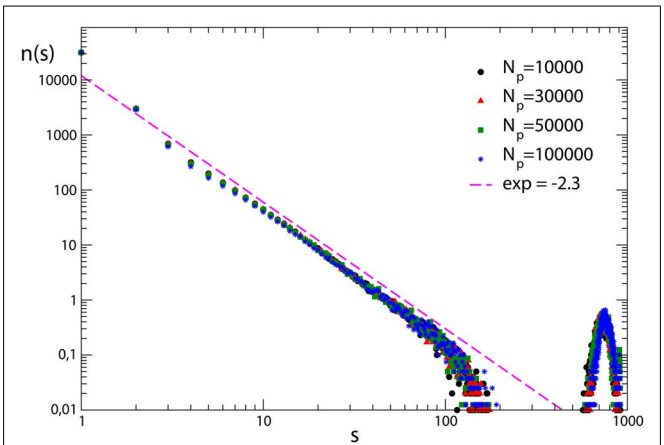

FIGURE 6 | Avalanche size distribution for 100 configurations of fully connected networks with N = 1000 neurons with $p_{in} = 0.05$. The different curves correspond to different durations of the plastic adaptation period N_p.

not depend on the synaptic strengths. The analysis of the effect of pruning on very large avalanches confirms this observation. Plastic adaptation of different duration is now applied to scale-free networks, leading to pruning of synapses. Supercritical behavior, that appears in the unpruned networks, survives when only few percentage of the synapses is removed. Conversely, a more extended pruning strongly affects connectivity and hampers the development of very large avalanches.

At time $t = 0$ a neuron is activated by an external stimulus initiating the avalanche. This will continue until no neuron is at or above threshold. The number of avalanches lasting a time T, $n(T)$, as function of T also exhibits power law behavior (**Figure 7**) followed by an exponential cut-off. The scaling exponent is found to be $\tau = 2.1 \pm 0.2$ for all networks and equal and random initial conductances. Only for the fully connected networks the distribution exhibits a bump at long durations, due to the excess of large avalanches which all contribute to the tail of the distribution. The value of the exponent is found to be stable with respect to different parameters, provided that the number of pruned bonds N_{pb} is lower than the plateau for that value of α. Finally this value agrees within error bars with the value 2.0, exponent found experimentally by Beggs and Plenz (2003, 2004).

5. POWER SPECTRUM

The power spectrum of the time signal for the overall electrical activity can be calculated. The aim is to compare the scaling behavior of the numerical spectrum with the power law observed usually in medical data (Novikov et al., 1997; Freeman et al., 2000). For this purpose, the number of active neurons is monitored as function of time, which recalls the experimental condition in which electrodes are placed on the scalp in order to study the patient's spontaneous electrical activity. In neuronal networks neuronal activity consists in avalanches of all sizes generated in response to the external stimulus. Here the unit time is the time for the avalanche to propagate from one neuron to the next one. The power spectrum is calculated as the squared amplitude of the time Fourier transform as function of frequency, averaged over many initial configurations. Because of the definition of the numerical time unit, the frequency unit does not correspond to the experimental one in Hertz.

Figure 8 shows the spectrum for different networks and different values of N_p. We also show the magnetoelectroencephalography (similar to EEG) obtained from channel 17 in the left hemisphere of a male subject resting with his eyes closed, as measured in Novikov et al. (1997), having the exponent 0.795. For $N_p = 0$, i.e., without plasticity adaptation, the spectrum has a $1/f$ behavior, characteristic of SOC. For values of N_p different from zero, but before the N_{pb} plateau, one can distinguish two different regimes: a power law behavior with exponent $\beta = 0.8 \pm 0.1$ at high frequency, followed by a crossover toward white noise at low frequency. The difference between $\beta = 1$ for $N_p = 0$ and β ; 0.8 for higher N_p, suggests that plasticity reduces the relevance of small frequencies in the power spectrum, in better agreement with experimental EEG spectra (Novikov et al., 1997; Freeman et al., 2000). The stability of the exponent with respect to α has also been verified, finding consistently $\beta = 0.8 \pm 0.1$ at high frequency. The stability of the spectrum exponent suggests that an universal scaling characterizes a large class of brain models and physiological signal spectra for brain controlled activities. Medical studies of EEG focus on subtle details of a power spectrum (e.g., shift in peaks) to discern between various pathologies. These detailed structures however live on a background power law spectrum that shows universally an exponent of about 0.8, as measured for instance in Freeman et al. (2000) and Novikov et al. (1997). A similar exponent was also detected in the spectral analysis of the stride-to-stride fluctuations in the normal human gait which can directly be related to neurological activity (Hausdorff et al., 2001). The measured value for the power spectra exponent is in agreement with the expected

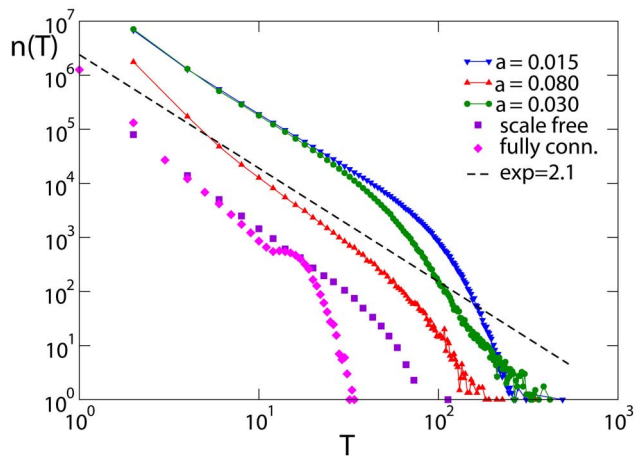

FIGURE 7 | Avalanche duration distribution for different networks with $p_{in} = 0.05$: the scale-free network ($N = 4000$); the fully connected network with $N_p = 50000$; the Apollonian networks for different values of α (9th generation, $N_p = 500$). Data are logarithmically binned. The dotted line has slope 2.1.

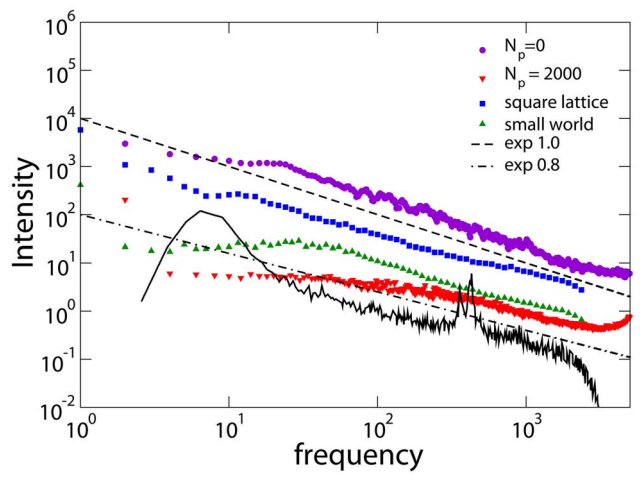

FIGURE 8 | Power spectra obtained for different networks: square lattice ($N = 10^6$, $\alpha = 0.03$, $N_p = 10$); small-world networks ($N = 10^6$, $\alpha = 0.05$, $N_p = 1000$, 1% rewired bonds); Apollonian networks for different N_p (9th generation, $\alpha = 0.020$). The experimental data (black line) are from Novikov et al. (1997) with frequency in Hertz. Experimental data are shifted in order to be in the same frequency range of numerical data.

relation $\beta = 3 - \tau$, being the scaling exponent of the avalanche duration distribution $\tau > 1$ (Jensen, 1998).

The scaling behavior of the power spectrum can be interpreted in terms of a stochastic process resulting from the superposition of multiple inputs taking Gaussian distributed random values (Hausdorff and Peng, 1996). The output signal sum of different and uncorrelated superimposed processes is characterized by a power spectrum with power law regime, crossing over to white noise at low frequencies and to brown noise to high frequencies. The low crossover frequency is related to the inverse of the longest characteristic time among the superimposed processes. $1/f$ noise characterizes a superposition of processes of different frequencies with similar amplitudes. In our case the scaling exponent is smaller than unity, suggesting that processes with high characteristic frequency are more relevant than processes with low frequency in the superposition (Hausdorff and Peng, 1996).

6. DISCUSSION

Several experimental evidences suggest that the brain behaves as a system acting at a critical point. This statement implies that the collective behavior of the network is more complex than the functioning of the single components. Moreover, the emergence of self-organized neuronal activity, with the absence of a characteristic scale in the response, unveils similarities with other natural phenomena exhibiting scale-free behavior, as earthquakes or solar flares (de Arcangelis et al., 2006b). For a wide class of these phenomena, self-organized criticality has indeed become a successful interpretive scheme. As in self-organized criticality, the threshold dynamics ensures time-scale separation (slow external drive and fast internal relaxation). This dynamics leads to criticality and therefore power law behavior (Jensen, 1998). The model belongs to the class of non-conservative models, since output neurons can drive charge outside the system. However the model presents a number of different features: The propagation of charge from one neuron to the connected one is non-uniform and non-isotropic. Moreover the connectivity network is not static but dynamically evolves following activity. In this scenario the plastic rules introduce a homeostatic regulatory mechanism between excitation and inhibition leading to critical behavior. The ensemble of these new ingredients is at the origin of the measured exponents, different from the typical exponents found in SOC models. It is interesting to notice that in fully connected networks the excess of very large avalanches hampers the synaptic depression mechanisms and therefore alters the self-organized regulation between excitation and inhibition. As a consequence, supercritical behavior is observed.

Extensive simulations of this activity-dependent model are derived for regular, small-world, scale-free, and fully connected lattices. The results are compared with experimental data. The first result is that an optimal value of the plasticity strength α exists with respect to the pruning process, optimizing information transmission. This remark could be interpreted as the evidence of a homeostatic mechanism between strengthening and weakening processes in the adaptation of real synapses. Moreover the avalanche size and duration distributions exhibit a power law behavior with stable exponents compatible with the values experimentally found for neuronal avalanches. These values appear to be independent of the model parameters and the specific connectivity network. This universal behavior is also in agreement with experimental results, which provide the same exponents for very different systems (dissociated neurons, cortex slices, and networks *in vivo*), evidently characterized by connectivity networks with different complexity. Solely the fully connected networks consistently exhibit supercritical behavior due to the high connectivity level which sustains large avalanche activity. The stability of the spectrum exponent suggests that a universal scaling characterizes a large class of brain models and physiological signal spectra for brain controlled activities. This work may open new perspectives to study pathological features of EEG spectra by including further realistic details into the neuron and synapse behavior.

REFERENCES

Andrade, J. S., Herrmann, H. J., Andrade, R. F. S., and da Silva, L. R. (2005). Apollonian networks: simultaneously scale-free, small world, Euclidean, space filling, and with matching graphs. *Phys. Rev. Lett.* 94, 018702.

Arieli, G. A., Sterkin, A., and Aertsen, A. (1996). Dynamics of ongoing activity: explanation of the large variability in evoked cortical responses. *Science* 273, 1868–1871.

Azouz, R., and Gray, C. M. (1999). Cellular mechanisms contributing to response variability of cortical neurons in vivo. *J. Neurosci.* 19, 2209–2223.

Bak, P. (1996). *How Nature Works. The Science of Self-Organized Criticality*. New York: Springer.

Bartolomei, F., Bosma, I., Klein, M., Baayen, J. C., Reijneveld, J. C., Postma, T. J., Heimans, J. J., van Dijk, B. W., de Munck, J. C., de Jongh, A., Cover, K. S., and Stam, C. J. (2006). Disturbed functional connectivity in brain tumour patients: evaluation by graph analysis of synchronization matrices. *Clin. Neurophysiol.* 117, 2039–2049.

Beggs, J. M., and Plenz, D. (2003). Neuronal avalanches in neocortical circuits. *J. Neurosci.* 23, 11167–11177.

Beggs, J. M., and Plenz, D. (2004). Neuronal avalanches are diverse and precise activity patterns that are stable for many hours in cortical slice cultures. *J. Neurosci.* 24, 5216–5229.

Clauset, A., Shalizi, C. R., and Newman, M. E. J. (2009). Power-law distributions in empirical data. *SIAM Rev.* 51, 661.

de Arcangelis, L., and Herrmann, H. J. (2010). Learning as a phenomenon occurring in a critical state. *Proc. Natl. Acad. Sci. U.S.A.* 107, 3977.

de Arcangelis, L., Perrone Capano, C., and Herrmann, H. J. (2006a). Self-organized criticality model for brain plasticity. *Phys. Rev. Lett.* 96, 028107.

de Arcangelis, L., Godano, C., Lippiello, E., and Nicodemi, M. (2006b). Universality in solar flare and earthquake occurrence. *Phys. Rev. Lett.* 96, 051102.

Eguiluz, V. M., Chialvo, D. R., Cecchi, G. A., Baliki, M., and Apkarian, A. V. (2005). Scale-free brain functional networks. *Phys. Rev. Lett.* 94, 0181021–0181024.

Freeman, W. J., Rogers, L. J., Holmes, M. D., and Silbergeld, D. L. (2000). Spatial spectral analysis of human electrocorticograms including the alpha and gamma bands. *J. Neurosci. Methods* 95, 111.

Gireesh, E. D., and Plenz, D. (2008). Neuronal avalanches organize as nested theta- and beta/gamma-oscillations during development of cortical layer 2/3. *Proc. Natl. Acad. Sci. U.S.A.* 105, 7576–7581.

Hausdorff, J. M., Ashkenazy, Y., Peng, C. K., Ivanov, P. C., Stanley, H. E., and Goldberger, A. L. (2001). When human walking becomes random walking: fractal analysis and modeling of gait rhythm fluctuations. *Physica A* 302, 138.

Hausdorff, J. M., and Peng, C. K. (1996). Multiscaled randomness: a possible source of 1/f noise in biology. *Phys. Rev. E* 54, 2154.

Jensen, H. J. (1998). *Self-Organized Criticality*. Cambridge: Cambridge University Press.

Levina, A., Herrmann, J. M., and Geisel, T. (2007). Dynamical synapses causing self-organized criticality in neural networks. *Nat. Phys.* 3, 857.

Maeda, E., Robinson, H. P., and Kawana, A. (1995). The mechanisms of generation and propagation of synchronized bursting in developing networks of cortical neurons. *J. Neurosci.* 15, 6834–6845.

Mazzoni, A., Broccard, F. D., Garcia-Perez, E., Bonifazi, P., Ruaro, M. E., and Torre, V. (2007). On the dynamics of the spontaneous activity in neuronal networks. *PLoS ONE* 5, e439. doi:10.1371/journal.pone.0000439

Novikov, E., Novikov, A., Shannahoff-Khalsa, D., Schwartz, B., and Wright, J. (1997). Scale-similar activity in the brain. *Phys. Rev. E* 56, R2387.

Pasquale, V., Massobrio, P., Bologna, L. L., Chiappalone, M., and Martinoia, S. (2008). Self-organization and neuronal avalanches in networks of dissociated cortical neurons. *Neuroscience* 153, 1354–1369.

Pellegrini, G. L., de Arcangelis, L., Herrmann, H. J., and Perrone Capano, C. (2007). Modelling the brain as an Apollonian network. *Phys. Rev. E* 76, 016107.

Petermann, T., Thiagarajan, T. C., Lebedev, M. A., Nicolelis, M. A., Chialvo, D. R., and Plenz, D. (2009). Spontaneous cortical activity in awake monkeys composed of neuronal avalanches. *Proc. Natl. Acad. Sci. U.S.A.* 106, 15921–15926.

Ponten, S. C., Bartolomei, F., and Stam, C. J. (2007). Small-world networks and epilepsy: graph theoretical analysis of intracerebrally recorded mesial temporal lobe seizures. *Clin. Neurophysiol.* 118, 918.

Roerig, B., and Chen, B. (2002). Relationships of local inhibitory and excitatory circuits to orientation preference maps in ferret visual cortex. *Cereb. Cortex* 12, 187–198.

Rubinov, M., Knock, S. A., Stam, C. J., Michelojannis, S., Harris, A. W. F., Williams, L. M., and Breakspear, M. (2009). Small-world properties of nonlinear brain activity in schizophrenia. *Hum. Brain Mapp.* 30, 403.

Segev, R., Benveniste, M., Hulata, E., Cohen, N., Palevski, A., Kapon, E., Shapira, Y., and Ben-Jacob, E. (2002). Long term behavior of lithographically prepared in vitro neuronal networks. *Phys. Rev. Lett.* 88, 118102.

Shefi, O., Golding, I., Segev, R., Ben-Jacob, E., and Ayali, A. (2002). Morphological characterization of in vitro neuronal networks. *Phys. Rev. E* 66, 021905.

Staley, K. J., Longacher, M., Bains, J. S., and Yee, A. (1998). Presynaptic modulation of CA3 network activity. *Nat. Neurosci.* 1, 201–209.

Stam, C. J., Jones, B. F., Nolte, G., Breakspear, M., and Sceltens, P. H. (2007). Small-world networks and functional connectivity in Alzheimer's disease. *Cereb. Cortex* 17, 92.

Stevens, C. F., and Tsujimoto, T. (1995). Estimates for the pool size of releasable quanta at a single central synapse and for the time required to refill the pool. *Proc. Natl. Acad. Sci. U.S.A.* 92, 846–849.

Watts, D. J., and Strogatz, S. H. (1998). Collective dynamics of "small-world" networks. *Nature* 393, 440.

Conflict of Interest Statement: The authors declare that the research was conducted in the absence of any commercial or financial relationships that could be construed as a potential conflict of interest.

Received: 11 January 2012; accepted: 03 March 2012; published online: 28 March 2012.

Citation: de Arcangelis L and Herrmann HJ (2012) Activity-dependent neuronal model on complex networks. Front. Physio. ***3****:62. doi: 10.3389/fphys.2012.00062*

This article was submitted to Frontiers in Fractal Physiology, a specialty of Frontiers in Physiology.

frontiers in
PHYSIOLOGY

ORIGINAL RESEARCH ARTICLE
published: 20 August 2012
doi: 10.3389/fphys.2012.00331

Critical fluctuations in cortical models near instability

Matthew J. Aburn[1,2]*, C. A. Holmes[1], James A. Roberts[2], Tjeerd W. Boonstra[3,4] and Michael Breakspear[2,3,5]

[1] *School of Mathematics and Physics, The University of Queensland, Brisbane, QLD, Australia*
[2] *Systems Neuroscience Group, Queensland Institute of Medical Research, Brisbane, QLD, Australia*
[3] *The Black Dog Institute and School of Psychiatry, University of New South Wales, Sydney, NSW, Australia*
[4] *Research Institute MOVE, VU University Amsterdam, Amsterdam, Netherlands*
[5] *The Royal Brisbane and Women's Hospital, Brisbane, QLD, Australia*

Edited by:
Andreas Daffertshofer, VU University Amsterdam, Netherlands

Reviewed by:
Dimitris Kugiumtzis, Aristotle University of Thessaloniki, Greece
Hussein M. Yahia, INRIA, France

****Correspondence:***
Matthew J. Aburn, School of Mathematics and Physics, The University of Queensland, St Lucia, Brisbane, QLD 4072, Australia.
e-mail: m.aburn@uq.edu.au

Computational studies often proceed from the premise that cortical dynamics operate in a linearly stable domain, where fluctuations dissipate quickly and show only short memory. Studies of human electroencephalography (EEG), however, have shown significant autocorrelation at time lags on the scale of minutes, indicating the need to consider regimes where non-linearities influence the dynamics. Statistical properties such as increased autocorrelation length, increased variance, power law scaling, and bistable switching have been suggested as generic indicators of the approach to bifurcation in non-linear dynamical systems. We study temporal fluctuations in a widely-employed computational model (the Jansen–Rit model) of cortical activity, examining the statistical signatures that accompany bifurcations. Approaching supercritical Hopf bifurcations through tuning of the background excitatory input, we find a dramatic increase in the autocorrelation length that depends sensitively on the direction in phase space of the input fluctuations and hence on which neuronal subpopulation is stochastically perturbed. Similar dependence on the input direction is found in the distribution of fluctuation size and duration, which show power law scaling that extends over four orders of magnitude at the Hopf bifurcation. We conjecture that the alignment in phase space between the input noise vector and the center manifold of the Hopf bifurcation is directly linked to these changes. These results are consistent with the possibility of statistical indicators of linear instability being detectable in real EEG time series. However, even in a simple cortical model, we find that these indicators may not necessarily be visible even when bifurcations are present because their expression can depend sensitively on the neuronal pathway of incoming fluctuations.

Keywords: neural mass model, Hopf bifurcation, critical fluctuations, autocorrelation

INTRODUCTION

Computational models of neocortex and other brain structures have proved very useful for a range of research problems in neuroscience (Braun and Mattia, 2010; Friston and Dolan, 2010). Interpreting empirical data using dynamical models is particularly fruitful in neuroimaging, where underlying processes are obscured by the low temporal resolution of fMRI or the coarse spatial source resolution of electroencephalography (EEG)/MEG. This allows testing of hypotheses about internal dynamical mechanisms (e.g., Freyer et al., 2012) and, through model inversion, the estimation of neural and connectivity parameters that cannot be observed directly (Friston et al., 2003). In contrast to modeling at the microscopic scale, where the range of dynamics of healthy neurons is known to include non-linear behavior such as limit cycles, modeling at the larger scale of mesoscopic neural masses, or neural fields often assumes that the dynamics at this scale operate close to a stable fixed point where input fluctuations result in only small and brief perturbations of the population state. This premise is predicated on the *diffusion approximation* that states that correlations amongst neuronal inputs are reduced as the size of the population increases (for review, see Deco et al., 2008). This approach enables the calculation of spectra from the composition of transfer functions, a powerful technique that allows physiological parameters to be estimated from non-invasive functional neuroimaging (Friston et al., 2003) and neurophysiological (van Albada et al., 2010) data.

Dynamic instabilities in models at the larger scale of neural masses have typically been associated with the pathological activity of epileptic seizures (Wendling et al., 2000; Robinson et al., 2002; Breakspear et al., 2006). However, empirical data shows that such instabilities may also underlie healthy neural activity (Freyer et al., 2009, 2011). Indeed, the Jansen–Rit neural mass model (Jansen and Rit, 1995) and its derivatives (Wendling et al., 2002; David and Friston, 2003; Zavaglia et al., 2006; Moran et al., 2007; Sotero et al., 2007; Spiegler et al., 2010) reach bifurcations where fixed points become linearly unstable while still within the healthy physiological range of parameters. In fact, oscillations in the model output that have been identified with normal cortical alpha activity have been shown to arise from limit cycle activity following a supercritical Hopf bifurcation (Grimbert and Faugeras, 2006; Spiegler et al., 2010).

The term "linear instability" here does not necessarily imply that the dynamics of the system as a whole lose stability. Indeed, in the case of the supercritical Hopf bifurcation, stability of

the attractor is maintained as it deforms continuously from a stable fixed point to a stable limit cycle, which then increases in size in the phase space. Hence, there is no discontinuous transition. The distinction is that the dominant dynamics in the system are no longer linear. The presence of quadratic and higher order flow terms that become significant in the neighborhood of a bifurcating fixed point have a profound influence on the system's statistical properties and its response to stochastic perturbations.

The putative presence of linear instabilities in healthy, mesoscopic cortical activity is ultimately an empirical question that must be answered with reference to the theory of non-linear stochastic dynamical systems. For a wide range of systems, statistical measures such as increased autocorrelation, increased variance, and bistable switching have been proposed as generic indicators that the system is losing linear stability on approaching a bifurcation (Scheffer et al., 2009; Kelso, 2010). Increased autocorrelation length is a direct consequence of critical slowing down, which occurs as the strength of attraction to a stable fixed point becomes weaker before changing to equally weak repulsion. Long-range correlations may also reveal a transition from exponential to power law relaxation in the vicinity of linear instabilities as a result of the higher order (non-linear) flow terms.

Within neuroscience, statistical indicators of bifurcations have been studied at a range of scales, in both computational models and empirical analyses. In the context of single neuron models, increase of variance close to a bifurcation and the spectral peak near a Hopf bifurcation have been examined (Steyn-Ross et al., 2006). Spectral features and variance close to instability have been explored in large-scale mean field corticothalamic models (Robinson et al., 1997, 2002; Roberts and Robinson, 2012) and mean field models of the brainstem and hypothalamus (Robinson et al., 2010). Slowing down, instability, and bifurcations have also been studied at the highest level of brain function, particularly in human movement. For example, increased variance and critical slowing have been observed in human bimanual motor control (Kelso et al., 1986; Scholz et al., 1987) and are explained by a simplified phenomenological model of coordination (Haken et al., 1985).

In addition to the analyses of empirical data contained within these computational studies, signatures of transitions in neuroimaging data have been the subject of a number of predominantly empirical studies. Amplitude fluctuations of human brain oscillations have been shown to have long time autocorrelations with power law decay in EEG (Linkenkaer-Hansen et al., 2001), consistent with effects expected near linear instability. Scale-free cortical activity has also been reported in surface electrocorticogram (ECoG) activity, although the significance, scaling coefficient, and likely mechanisms remain contested (Bedard et al., 2006; Miller et al., 2009; He et al., 2010). Similarly, Stam and de Bruin (2004) reported scale-free fluctuations in the degree of synchronization between surface EEG recordings. These findings are consistent with prior reports of intermittent non-linear structure within (Stam et al., 1999) and between (Breakspear and Terry, 2002) surface EEG channels. More recently, Freyer et al. (2009) found that 10 Hz oscillations showed intermittent switching between two distinct bistable modes, although the dwell times within each mode followed a stretched exponential, not a power law decay.

The objectives of the present study are to examine linear instabilities in the Jansen–Rit model, a closed set of equations describing the activity of a small cortical region and one of the simplest cortical neural mass models. At the same time it is a base upon which many extensions and derivative models have been built (Wendling et al., 2002; David and Friston, 2003; Zavaglia et al., 2006; Moran et al., 2007; Sotero et al., 2007; Spiegler et al., 2010). The phenomena which we report in this simple model therefore highlight the possibility of similar behavior in a wider class of models. We focus on one key indicator of linear instability (autocorrelation length) and one important bifurcation (supercritical Hopf). Time series for each neural population in the model are generated for sets of parameters approaching a bifurcation. We then test whether the autocorrelation indicator of proximity to bifurcation is reliably detectable in the time series of the pyramidal population and also examine scaling properties of fluctuations in this time series. In this way we explore whether simple bifurcations at the population scale have the potential to contribute to indicators such as lengthened autocorrelation times and power law scaling of fluctuations reported in human EEG data.

MATERIALS AND METHODS

JANSEN–RIT NEURAL MASS MODEL

Building on the earlier work of Lopes da Silva et al. (1974) and Wilson and Cowan (1972), Jansen and Rit developed a simple computational model of a small cortical region (Jansen et al., 1993; Jansen and Rit, 1995). The model produces an output signal similar to spontaneous EEG alpha oscillations, and also shows responses similar to evoked potentials following pulsatile input. The Jansen–Rit model is a closed set of differential equations that describe the local average states of three interconnected neural populations (**Figure 1**), excitatory interneurons, pyramidal cells, and inhibitory interneurons. Here we follow David and Friston (2003) in identifying the excitatory interneurons in the model with layer IV spiny stellate cells. The spiny stellate and pyramidal neurons are both excitatory and both populations receive external input, although only the pyramidal cells project out of the local region.

Each second order equation in the model corresponds to a population of synapses and their postsynaptic dendritic processes (Freeman, 1992; Deco et al., 2008). Critically damped second order linear filters describe the time course of the population mean of postsynaptic potentials, further dispersed due to variability of parameters within each population. This mean behavior summarizes both synaptic and dendritic dynamics of the individual neurons. For excitatory and inhibitory synapses respectively these filters are expressed by the differential operators

$$L_{\mathrm{e}} = \frac{1}{H_{\mathrm{e}}\kappa_{\mathrm{e}}}\left(\frac{d^2}{dt^2} + 2\kappa_{\mathrm{e}}\frac{d}{dt} + \kappa_{\mathrm{e}}^2\right), \tag{1}$$

$$L_{\mathrm{i}} = \frac{1}{H_{\mathrm{i}}\kappa_{\mathrm{i}}}\left(\frac{d^2}{dt^2} + 2\kappa_{\mathrm{i}}\frac{d}{dt} + \kappa_{\mathrm{i}}^2\right), \tag{2}$$

where the scalar parameters H_{e} and H_{i} determine the maximum amplitude of the postsynaptic population response to excitatory

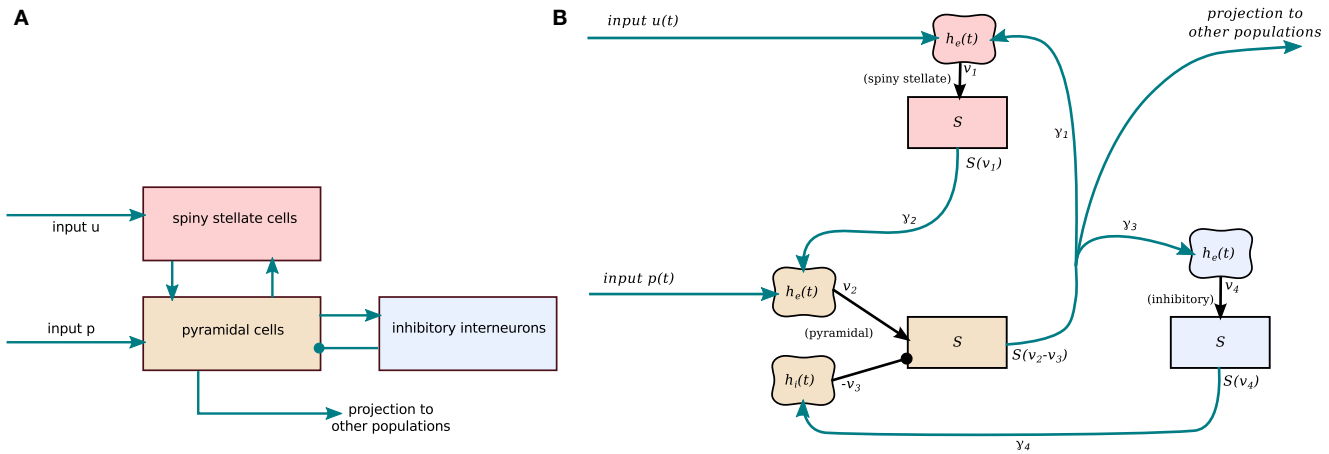

FIGURE 1 | Schematic connectivity of the Jansen–Rit model. (A) Basic connectivity diagram showing the three neuronal populations, their excitatory (arrows) and inhibitory (circle) connections, and inputs from outside the local cortical region (u and p). **(B)** A block diagram then summarizes how this translates directly to a mathematical model: linear filter boxes labeled $h_e(t)$ and $h_i(t)$ model the mean response of excitatory and inhibitory synapse populations respectively, including their postsynaptic dendritic filtering. Sigmoid boxes (denoted S) represent conversion of mean summed soma membrane potential to mean output firing rate. Connectivity constants γ_1 to γ_4 model the number and strength of connections between populations.

and inhibitory inputs, respectively. The rate constants κ_e and κ_i determine the time scale of these population responses. As the synaptic filters are linear, synapses with different source or target populations can be merged where synapses are assumed to have the same aggregate properties. For example Jansen and Rit (1995) consolidated their original model to just three second order equations, as it was implicitly assumed that excitatory and inhibitory interneuron populations would always have identical states up to a scaling constant. Following synaptodendritic filtering, fluctuations in membrane potential sum in the cell soma and lead to changes in the average population firing rate. The sigmoid function

$$S(v) = \frac{2e_0}{1 + \exp[\rho_1(\rho_2 - v)]}, \tag{3}$$

describes how the mean firing rate of a neural population depends on the mean soma membrane potential v, incorporating the dispersion of responses due to variability in the parameters and underlying neuronal states (Marreiros et al., 2008). Parameters e_0, ρ_2, and ρ_1 determine the maximum firing rate, threshold potential, and sensitivity, respectively.

We express the Jansen–Rit model as a set of four second order differential equations, thus allowing both pyramidal and spiny stellate populations separately to receive extrinsic input. We follow the variable and parameter names of Moran et al. (2007). The dynamical variables v_1, v_2, and v_4 represent the positive contributions to population mean soma potentials by excitatory synapses targeting spiny stellate, pyramidal, and inhibitory interneuron populations, respectively. Variable v_3 represents the negative contribution to the mean soma potential of the pyramidal population originating from inhibitory synapses. Thus the resulting mean soma potential of the pyramidal population is $v_2 - v_3$. This is taken as the main output of the model (Jansen and Rit, 1995; David et al., 2005) because the size and orientation of the apical dendrites of pyramidal neurons mean that pyramidal activity is most closely associated with EEG signals. These equations are given by

$$L_e v_1 = \gamma_1 S(v_2 - v_3) + \langle u \rangle + \sigma_u \xi_u(t), \tag{4}$$

$$L_e v_2 = \gamma_2 S(v_1) + \langle p \rangle + \sigma_p \xi_p(t), \tag{5}$$

$$L_i v_3 = \gamma_4 S(v_4), \tag{6}$$

$$L_e v_4 = \gamma_3 S(v_2 - v_3). \tag{7}$$

Equation 4 describes excitatory synaptic input targeting the spiny stellate population. Eqs 5 and 6 describe excitatory and inhibitory synaptic input to the pyramidal population, respectively. Equation 7 describes excitatory synaptic input to the inhibitory interneuron population. Parameters $\langle u \rangle$ and $\langle p \rangle$ are the mean per neuron external input firing rates to the cortical region, targeting spiny stellate, and pyramidal populations, respectively. Langevin white noise terms $\xi_u(t)$ and $\xi_p(t)$ in the extrinsic input represent the fluctuations in the input firing rates, with σ_u and σ_p denoting their standard deviations. Scalar connectivity constants γ_1 to γ_4 represent at the population scale the number and strength of connections between the three neural populations.

This system of equations is equivalent to a single eight-dimensional stochastic first order differential system:

$$d\boldsymbol{v} = \boldsymbol{f}(\boldsymbol{v})dt + G\, d\boldsymbol{W}(t), \tag{8}$$

where matrix elements of G determine the cross-correlation of noise inputs to the pyramidal and spiny stellate populations. This is the equation that we integrate numerically.

Table 1 lists the values of parameters used for all simulations in this study; they are the standard parameter values introduced by Jansen and Rit (1995).

Jansen and Rit (1995) themselves focused on numerical simulations of this non-linear model. Through a survey of the simulated

Table 1 | Jansen–Rit standard parameter values.

Parameter	Value	Description
H_e	3.25 mV	Maximum amplitude of the excitatory postsynaptic population response
H_i	22.0 mV	Maximum amplitude of the inhibitory postsynaptic population response
κ_e	$100\,s^{-1}$	Rate constant for postsynaptic population response to excitatory input
κ_i	$50\,s^{-1}$	Rate constant for postsynaptic population response to inhibitory input
e_0	$2.5\,s^{-1}$	Half of the maximum population mean firing rate
ρ_2	6.0 mV	Population mean firing threshold potential
ρ_1	$0.56\,mV^{-1}$	Firing rate sigmoid function voltage sensitivity parameter
γ_1	135	Connectivity constant: pyramidal to spiny stellate
γ_2	108	Connectivity constant: spiny stellate to pyramidal
γ_3	33.75	Connectivity constant: pyramidal to inhibitory interneurons
γ_4	33.75	Connectivity constant: inhibitory interneurons to pyramidal

behavior with physiologically realistic parameters, they observed a variety of noise-driven rhythmic behaviors consistent with human alpha and beta rhythms. Wendling et al. (2000) studied the emergence of "spike-wave" oscillations resembling epileptic activity when the ratio of excitation to inhibition was increased. Bifurcations in this model where subsequently examined by Grimbert and Faugeras (2006) who treated the input p as the bifurcation parameter in order to understand better the original simulation results of Jansen and Rit (limit cycle beyond a Hopf bifurcation causing alpha oscillations) and Wendling et al. (the emergence of a large amplitude non-harmonic oscillator near a sniper bifurcation). More recently, Spiegler et al. (2010) performed a more general bifurcation analysis that included time scale parameters and analyzed the presence of qualitatively different oscillatory regimes.

BIFURCATION PARAMETERS

In the original model (Jansen et al., 1993), both pyramidal and excitatory interneuron populations were the targets of extrinsic inputs, with the two inputs being always proportional (fully correlated). In the model of Jansen and Rit (1995), all extrinsic input was delivered to the pyramidal neurons only, with external stimulation of the other population dropped.

David and Friston (2003) revisited the Jansen–Rit model, in particular explicitly identifying the "excitatory interneuron" population of the original model with spiny stellate cells in layer IV of the neocortex. Their motivation was to send extrinsic input to the layer IV spiny stellate cells in the model rather than to the pyramidal cells. This was arguably a more realistic model of connectivity for input representing thalamocortical sensory afferents. However the equations as published retained the pyramidal-only input of the original Jansen–Rit model.

Moran et al. (2007), in the context of Dynamic Causal Modeling (DCM, a framework for model selection and parameter estimation), extended the Jansen–Rit model with several innovations, including firing rate adaptation, recurrent inhibition, and a differently shaped sigmoid function. In particular Moran et al. did change the target of the extrinsic input to be the spiny stellate population, as foreshadowed by David and Friston (2003). We refer to this model as the Moran–Friston model hereafter.

For the present study we minimally extend the Jansen–Rit model, so that extrinsic input can be delivered either to the pyramidal population (as in Jansen and Rit, 1995), the spiny stellate excitatory population (as in Moran et al., 2007) or more realistically a combination of the two. In this way, the system input can be varied continuously from the Jansen–Rit design to the Moran–Friston design or anywhere in between. In addition, for the case of input to both populations, these two inputs can be chosen as uncorrelated, fully correlated, or partially correlated in their fluctuations. Hence we study the bifurcations of this model as input is varied in the combined (u, p) plane. This subset of parameter space includes a one-dimensional space explored by Jansen and Rit containing a supercritical Hopf bifurcation studied by Grimbert and Faugeras (2006) that is within the physiological range of parameters. We present the bifurcation analysis in Section "Bifurcation diagram."

NUMERICAL SIMULATION AND ANALYSIS

The model is a system of stochastic differential equations (SDEs) with additive noise. Equation 8 is integrated numerically using the Heun algorithm, which is applicable to SDEs in Stratonovich form (Rümelin, 1982). This ensures that noise amplitude is scaled in appropriate proportion to the square root of the integration time step. We use an integration time step of 0.2 ms. The first transient 5 s of each simulation is discarded from further analysis.

As reviewed in the introduction, the approach to linear instabilities in systems of equations such as Eqs 4–7 is widely assumed to cause changes in the autocorrelation length and/or a peak in the power spectral density function (in the case of a Hopf bifurcation). This is because it is often assumed that the linear treatment of these systems – which predicts both an enhancement of spectral peaks and a lengthening of the autocorrelation time – can be extrapolated from the setting when the system is linearly stable to when it is in the neighborhood of a bifurcation.

To estimate the normalized autocorrelation function of the resulting time series we first normalize each time series to a mean of 0 and standard deviation of 1, and then compute the cross-correlation of the series with itself applying unbiased normalization,

$$\hat{R}_{\mathrm{xx,unbiased}}(m) = \frac{1}{N-m} \sum_{n=0}^{N-m-1} x_{n+m} x_{\mathrm{n}} \; (m \geq 0)\,, \tag{9}$$

where m is the lag expressed as number of samples (Orfanidis, 1996). In each case we compute autocorrelation at lag times from 0 to 1/4 of the total time series length for further analysis. Since time series are generated in the vicinity of Hopf bifurcations with

natural frequency about 11 Hz, the autocorrelation functions all have a strong 11 Hz component. Because we are primarily interested in the decay of the amplitude of this autocorrelation over a longer time scale, each simulation is repeated 16 times with identical parameters to generate 16 sample paths each of duration 600 or 1,800 s. The autocorrelation function is calculated as described above for each sample path separately. The decay is then quantified by calculating the modulus of the Hilbert transform of the normalized autocorrelation functions computed above. The pointwise mean and standard deviation of this autocorrelation amplitude across 16 sample paths are then plotted. Power spectra are estimated using the Welch algorithm with Hamming window and a segment length of 80,000 samples or 16 s.

The full MATLAB code implementing the model, integration, and time series analyses is available from the authors on request.

RESULTS

BIFURCATION DIAGRAM

From the earlier bifurcation analysis of Grimbert and Faugeras (2006) the model is known to have a supercritical Hopf bifurcation when the pyramidal input $p = 89.8\,\mathrm{s}^{-1}$ and the other parameters are set to the values used by Jansen and Rit (1995). This assumed no input to the excitatory (spiny stellate) population. We label this bifurcation point H1; it has mean input firing rate $\langle p\rangle = 89.8\,\mathrm{s}^{-1}$ to the pyramidal population and zero input to the spiny stellate population (i.e., $\langle u\rangle = 0$, $\sigma_u = 0$). This maps directly back to the original Jansen–Rit model with pyramidal-only input. Matching the effective noise level used by Jansen and Rit (correcting a scaling error in the original paper) is achieved by allowing p to fluctuate with standard deviation $\sigma_p = 0.5390\,\mathrm{s}^{-1}$.

To examine the difference between cases where input is provided in different ratios to the spiny stellate population and pyramidal population, we continue the bifurcation point H1 in the (u, p) plane in parameter space, using the numerical continuation package MATCONT (Dhooge et al., 2003).

Figure 2 shows the bifurcation diagram in the (u, p) plane. This plane is a two-dimensional slice through the larger parameter space of the model, so that a curve in this plane corresponds to a surface in parameter space. The Hopf curve is almost horizontal for $u > 0$, implying that the level of pyramidal cell stimulation required to reach the supercritical Hopf bifurcation in the model ($p \sim 75$–$90\,\mathrm{s}^{-1}$) is roughly independent of the level of spiny stellate cell stimulation for $u \gtrsim 0$. For comparison with H1, we select point H2 on this same surface of supercritical Hopf points, but this time with greater mean input to the spiny stellate population ($\langle u\rangle = 270\,\mathrm{s}^{-1}$) than to the pyramidal population ($\langle p\rangle = 73\,\mathrm{s}^{-1}$). The magnitude of fluctuations $\sqrt{\sigma_u^2 + \sigma_p^2}$ in the input is kept the same as at H1, with a standard deviation of $\sigma_u = 0.5203\,\mathrm{s}^{-1}$ in the spiny stellate input and $\sigma_p = 0.1407\,\mathrm{s}^{-1}$ in the pyramidal input.

AUTOCORRELATION INDICATOR BEHAVES DIFFERENTLY AT H1 AND H2

For each of the bifurcation points we simulate the dynamics at four locations in parameter space: the approach to the bifurcation from the linearly stable side (two points), at the bifurcation point (one point), and beyond the bifurcation (one point). In each case the output pyramidal time series $(v_2 - v_3)$ is the focus of our analysis.

Each simulation is performed separately with parameter values fixed at these different values, rather than performing a single dynamic simulation with sliding parameters. This approach allows the time series analyzed at a fixed parameter value to be approximately stationary (provided the total time simulated is long enough) so that statistics for the process at that parameter point can be estimated from a finite time series. Where variance is considered as an indicator of instability this approach also avoids any spurious short-time increases in variance due to the dynamically shifting range of the system in phase space, as distinct from increased noise-driven variance at the new parameter values (Kuehn, 2011).

To determine the effect of proximity to a bifurcation on the fluctuation statistics, we analyze the approach and passage through bifurcations H1 and H2. **Figure 3** shows the results for bifurcation H1. An exemplar pyramidal time series (**Figure 3A**) reveals a fluctuating oscillatory system, whose power spectrum (**Figure 3B**) peaks at the frequency of the Hopf instability, namely 11 Hz. The series of panels in **Figure 3C** shows that when approaching and passing point H1 (from left-to-right), the autocorrelation time stays approximately constant.

For comparison, the corresponding analyses for bifurcation H2 are shown in **Figure 4**. By eye, the fluctuation envelope of the amplitude appears smoother. As is evident in **Figure 4C**, the autocorrelation amplitude decays much more slowly as the system approaches the bifurcation. At the bifurcation point H2 the autocorrelation remains above 20% of its zero-lag value at a lag of 15 s.

The variance of the output pyramidal time series increases as the bifurcation H1 is approached, with standard deviations of 0.4550, 0.5344, 0.5630, and 0.6110 mV at the four parameter points respectively. Approaching H2 this also occurs, with standard deviations of 0.1454, 0.2160, 0.2582, and 0.3449 mV respectively for the output time series. It is notable that in the vicinity of point H2, the standard deviation of the simulated pyramidal output time series is between 1.8 and 3.1 times smaller than in the vicinity of point H1, while autocorrelation times are roughly 7 times longer than at H1.

As expected for a Hopf bifurcation in a stochastic system the dynamics change gradually and continuously through the bifurcation (Rowat and Greenwood, 2011). The amplitude of oscillations increases when moving toward and beyond the bifurcation point as revealed by increased variance of the output time series. Close to the bifurcation point this reflects weakening of the stability of the (fixed point) attractor while beyond the bifurcation point it reflects increasing size of the (limit cycle) attractor. The increase in power at 11 Hz is visible in the power spectrum (**Figure 3B**).

The comparison of **Figures 3C** and **4C** shows that autocorrelation is a useful and clearly visible indicator of linear instability in the vicinity of point H2, but not for point H1. This is despite these being points on the same surface of bifurcations with the same variance of input fluctuations.

We conjecture that the key difference between H1 and H2 is the orientation of the input fluctuations in phase space with respect to the two-dimensional center manifold of the bifurcation, which determines the specific directions in which linear stability is weakening. When close to the equilibrium point, the center manifold

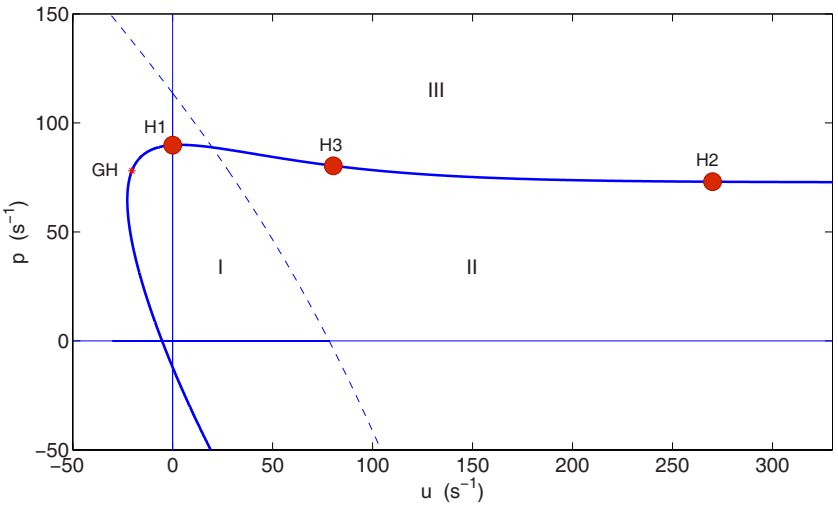

FIGURE 2 | Bifurcation diagram in the (*u*, *p*) parameter plane showing Hopf curve (thick, solid curve) and the location of the chosen Hopf bifurcation points H1, H2, and H3 on this curve. A generalized Hopf bifurcation (GH) marks the transition from subcritical Hopf points (the curve below GH) to supercritical Hopf points (the curve continuing beyond GH). Regions where $p < 0$ or $u < 0$ are non-physical. Below the Hopf curve (regions I and II) a stable fixed point exists, which gradually loses linear stability as the curve is approached. Above the Hopf curve (region III) this point has lost linear stability and become a stable limit cycle. The dashed line is a curve of fold bifurcation points. In region II a single stable fixed point exists. In region I the system is bistable with a second stable fixed point also existing, at lower excitation.

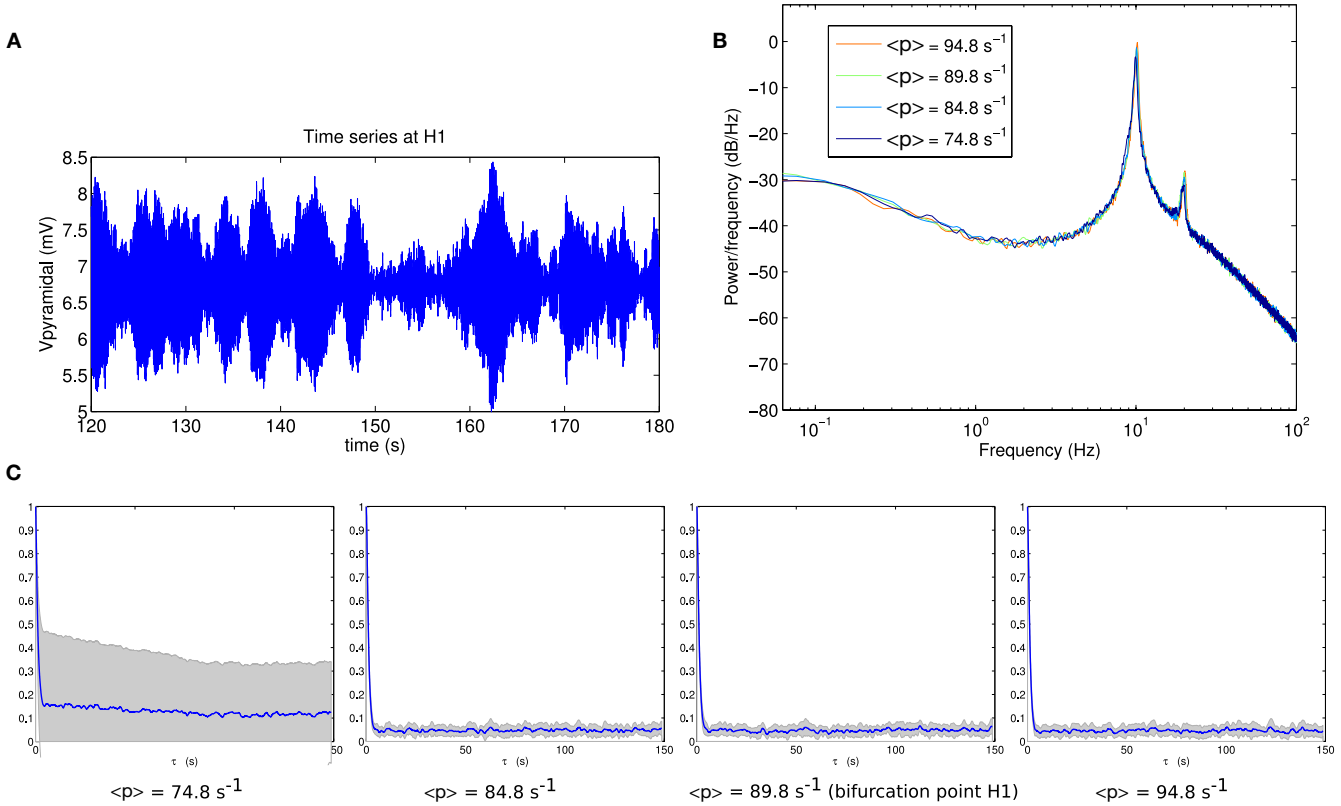

FIGURE 3 | (A) Example section of simulated time series at the bifurcation point H1. **(B)** Power spectrum at H1. **(C)** Autocorrelation amplitude at points in parameter space approaching the bifurcation point H1 ($<p> = 74.8\,s^{-1}$, $<p> = 84.8\,s^{-1}$), at the bifurcation point H1 ($<p> = 89.8\,s^{-1}$) and beyond the bifurcation point ($<p> = 94.8\,s^{-1}$). The line indicates the mean over 16 trials and the gray area indicates one standard deviation.

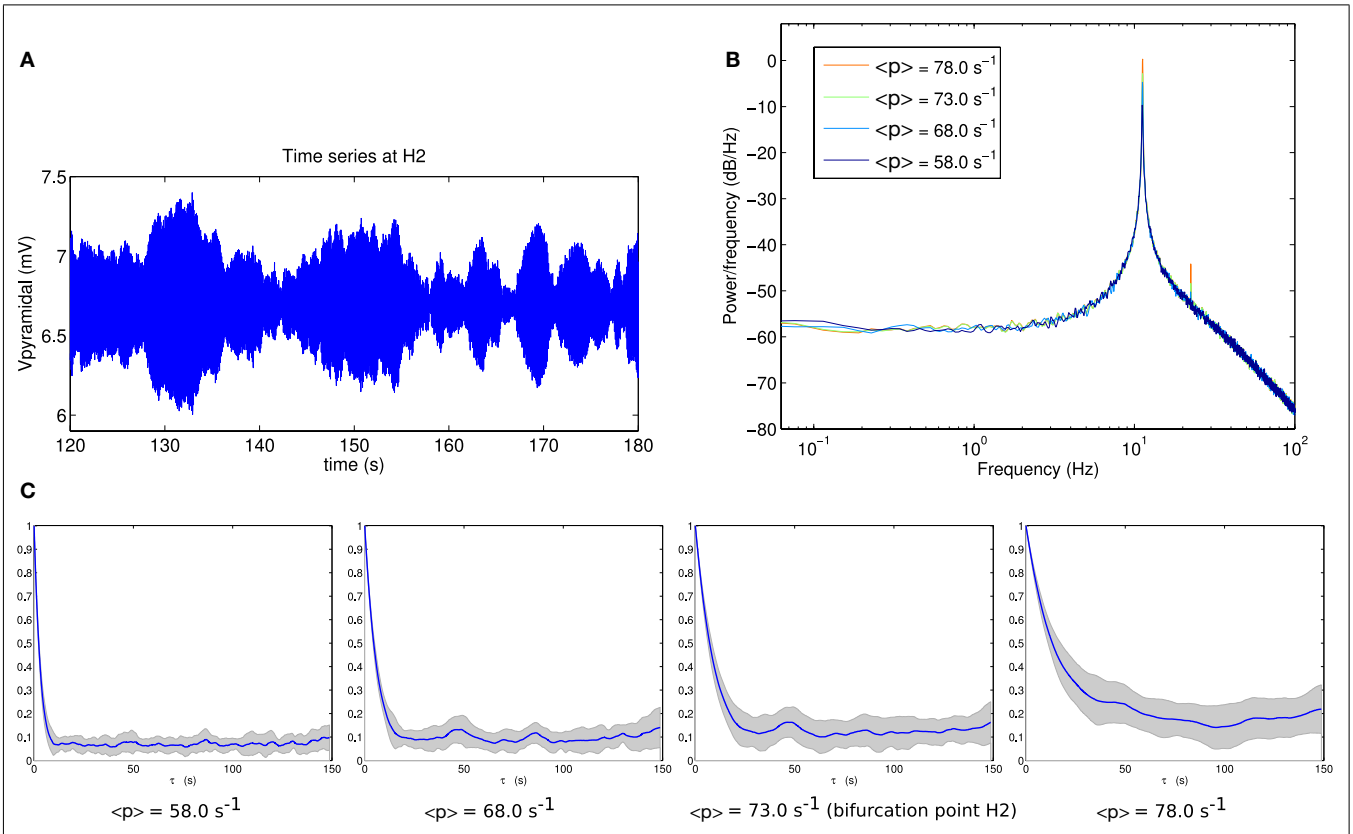

FIGURE 4 | (A) Example section of simulated time series at the bifurcation point H2. **(B)** Power spectrum at H2. **(C)** Autocorrelation amplitude at points in parameter space approaching the bifurcation point H2 ($<p> = 58.0\,s^{-1}$, $<p> = 68.0\,s^{-1}$), at the bifurcation point H2 ($<p> = 73.0\,s^{-1}$) and beyond the bifurcation point ($<p> = 78.0\,s^{-1}$). The line indicates the mean over 16 trials and the gray area indicates one standard deviation.

surface can be approximated by the center eigenspace of the bifurcation. Since the eigenvectors of the linearized system are far from orthogonal, the relevant reference plane to determine the noise component projected into the center eigenspace is the plane that is perpendicular to the stable eigenspace. For H1 the resulting projection of the noise vector onto this reference plane is $\cos\alpha = 0.0031$. For H2 the projection is $\cos\alpha = 0.0008$; i.e., the noise input has a projection onto that plane that is four times larger in the case of H1 than in the case of H2.

However, the comparison between points H1 and H2 does not by itself give strong support for this hypothesis, because there are several other factors that are significantly different between H1 and H2. In particular H2 has 3.1 times the total input firing rate of H1, so that on this basis the difference in autocorrelation could simply be due to greater level of excitation for point H2. This motivates the comparison constructed below.

AUTOCORRELATION DEPENDS ON ORIENTATION OF INPUT FLUCTUATIONS

In order to separate the effect of different mean firing rates from the effect of different noise orientation, we construct two new scenarios H3p and H3u, where the only difference between them is the noise orientation; all other parameters are kept identical. We choose point H3 on the same bifurcation line of supercritical Hopf points, but with equal mean input firing rates to pyramidal and spiny stellate populations (mean input firing rate per neuron of $\langle u\rangle = \langle p\rangle = 80.35\,s^{-1}$). We simulate two scenarios at point H3 to test the conjecture, with both scenarios using the same values for all model parameters, and in particular with both scenarios using the same mean input firing rates, as illustrated in **Figure 5**.

We define the scenario H3p as the case where only the pyramidal input is allowed to fluctuate about its mean, while spiny stellate input is held steady at its mean value, corresponding to the parameters $\langle p\rangle = 80.35\,s^{-1}$, $\sigma_p = 0.5390\,s^{-1}$, $\langle u\rangle = 80.35\,s^{-1}$, and $\sigma_u = 0\,s^{-1}$.

Scenario H3u is defined as the case where only the spiny stellate input is allowed to fluctuate, while pyramidal input is held steady, corresponding to the parameters $\langle p\rangle = 80.35\,s^{-1}$, $\sigma_p = 0\,s^{-1}$, $\langle u\rangle = 80.35\,s^{-1}$, and $\sigma_u = 0.5390\,s^{-1}$.

By using these two constructed scenarios, all parameters in the simulation are kept identical between scenarios H3p and H3u except for the direction of the fluctuations of input in phase space, which is rotated in phase space from the pyramidal direction to the spiny stellate direction. Rotating the vector of fluctuations independently from the vector of mean inputs is non-physiological. The simulated results of the non-physiological scenarios H3p and H3u are used to shed light on the reason for different autocorrelation in the original realistic scenarios H1 and H2.

Comparable analyses of these two scenarios are presented in **Figures 6** and **7**. The contrast between scenarios H3p and H3u

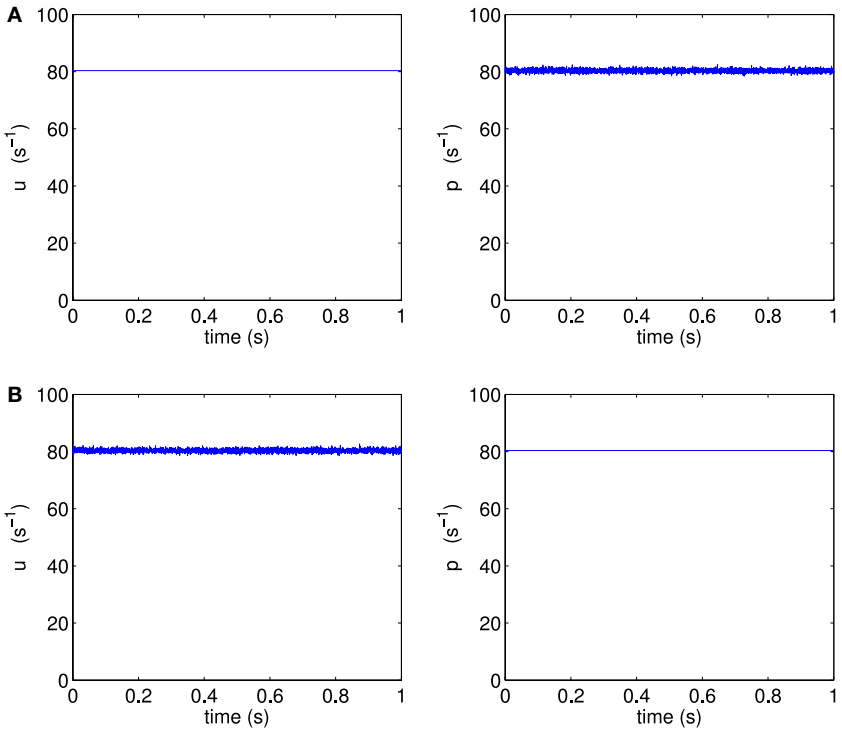

FIGURE 5 | One second of sample external inputs *u* and *p*, (A) for scenario H3p and (B) for scenario H3u.

is clear in **Figures 6C** and **7C**. When the fluctuations are in the input to the pyramidal population (scenario H3p), the decay of autocorrelation amplitude changes little as the bifurcation point is approached. By contrast, when the fluctuations are in the input to the spiny stellate population (scenario H3u) the indicator of increased autocorrelation length is very prominent. A large increase in autocorrelation heralds the transition to linear instability in scenario H3u with significant autocorrelation at lags of up to 450 s. This indicator is much less evident in scenario H3p.

It is also instructive to view the autocorrelation amplitude with log scaling of the delay axes. The results for the four scenarios (H1, H2, H3p, H3u) we have thus far considered are shown in **Figure 8**. Whereas the autocorrelation length stays almost invariant across the bifurcation in scenario H1 (**Figure 8A**), a clear increase is seen in scenario H2 (**Figure 8B**). Where scenario H3p shows a small, but systematic lengthening (**Figure 8C**), a progression through the same points in parameter space – but now with input fluctuations aligned with the stable eigenspace – can again be seen to lead to a dramatic increase (**Figure 8D**).

In both scenarios H3p and H3u the variance of the output pyramidal time series increases as the bifurcation point H3 is approached, with standard deviations of 0.4884, 0.4730, 0.5134, and 0.5339 mV for H3p and 0.0188, 0.0295, 0.0873, and 0.3033 mV for H3u. The standard deviation is starkly different between these two scenarios, with standard deviation between 2 and 22 times smaller in scenario H3u than in scenario H3p. Thus changing the noise input direction results in both reduced variance and increased autocorrelation length. Variance also increases more rapidly in scenario H3u than H3p as the bifurcation is approached.

Relating this to the orientation of input noise, the contrast in alignment is even greater between scenarios H3p and H3u than in the comparison of H1 and H2. For H3p the projection of the input noise onto the reference plane perpendicular to the stable eigenspace is $\cos\alpha = 0.003$, i.e., noise input has a non-negligible component perpendicular to the stable eigenspace of the bifurcation near the equilibrium point, whereas for H3u the projection is $\cos\alpha = 0.00006$, i.e., the projection of the noise input onto the reference plane is 50 times smaller in the case of H3u than H3p.

INPUT CORRELATION AND OUTPUT VARIABLE NOT IMPORTANT

The results presented above are calculated from the pyramidal time series. Applying the same process to time series for the other two populations in the model (spiny stellate and inhibitory) shows that in each case, the results for autocorrelation decay and variance show the same behavior as the pyramidal time series. This is important, as it rules out the possibility that the autocorrelation difference results from different amounts of filtering between the noise input and the measured output.

In the case of point H2, both pyramidal input and spiny stellate input have fluctuations. To check whether correlations between the two input fluctuations are important to the results we examine the two extreme cases of independent and perfectly correlated inputs. Cross-correlation of input fluctuations does not affect the results: autocorrelation amplitude of the pyramidal output decays

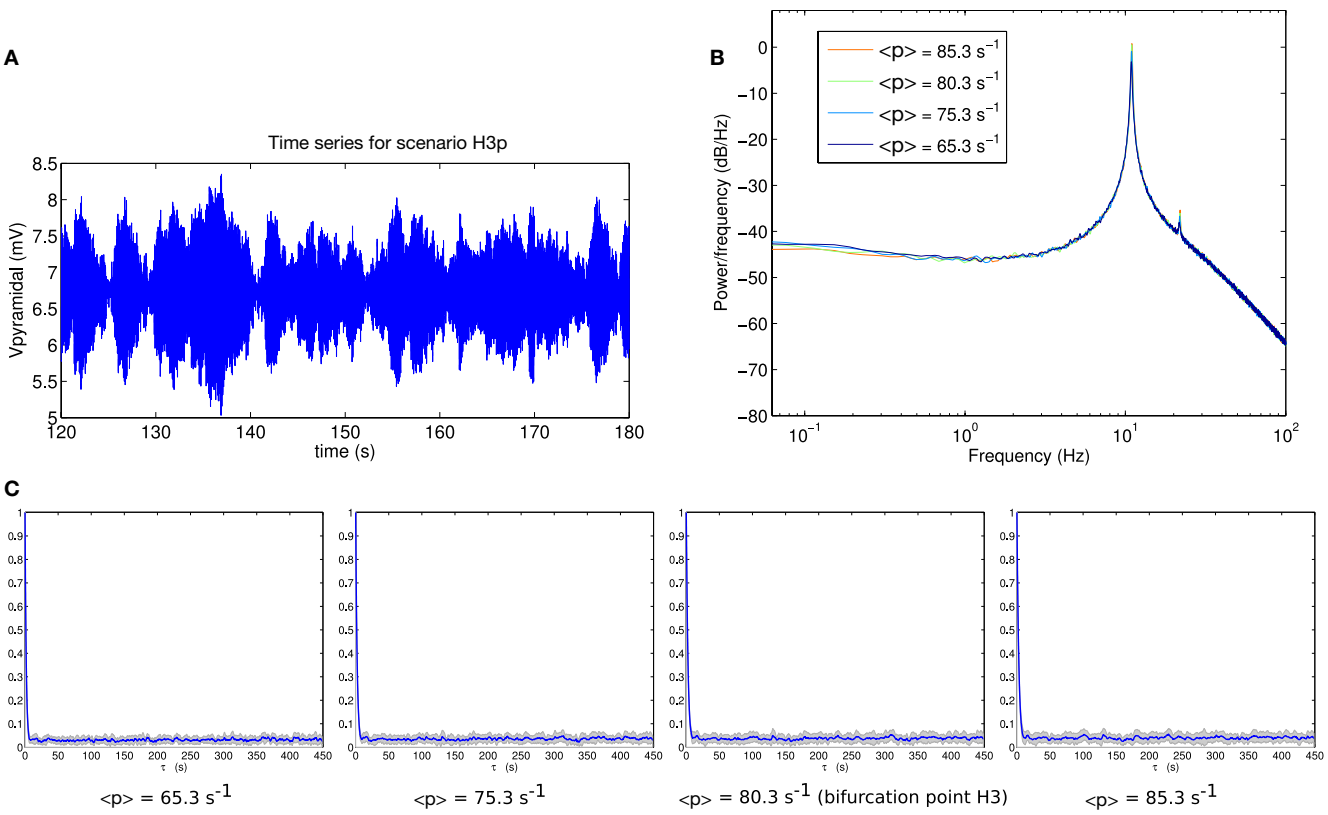

FIGURE 6 | (A) Example section of simulated time series for scenario H3p. **(B)** Power spectrum at H3. **(C)** Autocorrelation amplitude at points in parameter space approaching the bifurcation point H3 ($<p> = 65.3\ s^{-1}$, $<p> = 75.3\ s^{-1}$) at the bifurcation point H3 ($<p> = 80.3\ s^{-1}$) and beyond the bifurcation point ($<p> = 85.3\ s^{-1}$). The line indicates the mean over 16 trials and the gray area indicates one standard deviation.

over a similar time scale whether the inputs to the two populations are independent or perfectly correlated.

SCALING PROPERTIES OF OUTPUT FLUCTUATIONS

As reviewed earlier, long-tailed fluctuation distributions have been observed in the amplitude fluctuations of alpha (Freyer et al., 2009) and beta oscillations in scalp EEG data (Linkenkaer-Hansen et al., 2004). Therefore we study the statistical properties of fluctuations at and near the bifurcation points in scenarios H3u and H3p. In particular, we characterize fluctuations by the distributions of sizes and durations of excursions in the amplitude envelope of the detrended pyramidal time series. More specifically, we analyze the squared Hilbert amplitude, which is a measure of instantaneous power. We extract excursions above a threshold (sometimes termed "avalanches" in the literature) where each excursion is delineated by the time points at which the instantaneous power crosses the threshold from below and the next crossing from above. Fluctuation duration is thus the length of the time interval for which the power is above threshold, and we define fluctuation size to be the time integral of the instantaneous power over this interval (i.e., the area under the curve, a measure of energy in the fluctuation). We choose the threshold for each time series such that it approximately maximizes the number of identified fluctuations and falls in a regime where the fluctuation statistics are relatively insensitive to small changes in this value.

We analyze the fluctuation size and duration distributions following the methods of Clauset et al. (2009). For each set of fluctuation statistics we calculate the inverse cumulative distribution function and fit candidate distributions to the tail using the method of maximum likelihood: power law (the Pareto distribution), power law with exponential cutoff, lognormal, and exponential. Here the tail is all the data above a lower bound that we identify as the value that minimizes the Kolmogorov–Smirnov goodness-of-fit statistic between the power law model and the data (Clauset et al., 2009). This method of determining the range of the fit from the data strikes a balance between fitting too wide a range (i.e., outside the power law regime) and too narrow a range (i.e., throwing away data unnecessarily). We use the same fitting range for all four candidate distributions. We estimate a p-value for the fitted power law by comparing the data to 1,000 synthetic data sets drawn from a true power law, which accounts for whether the deviation between the data and the fitted power law is within the range expected for finite sampling of a true power law. The p-value is taken to be the fraction of synthetic data sets that deviate from the power law by at least as much as the data, and $p > 0.1$ indicates plausibility of the power law hypothesis (Clauset et al., 2009). We compare the fitted power law with alternative distributions using likelihood ratio tests. Significant deviation of the likelihood ratio from zero is tested using Vuong's methods (Vuong, 1989). For the nested hypothesis of power law versus power law with cutoff (the

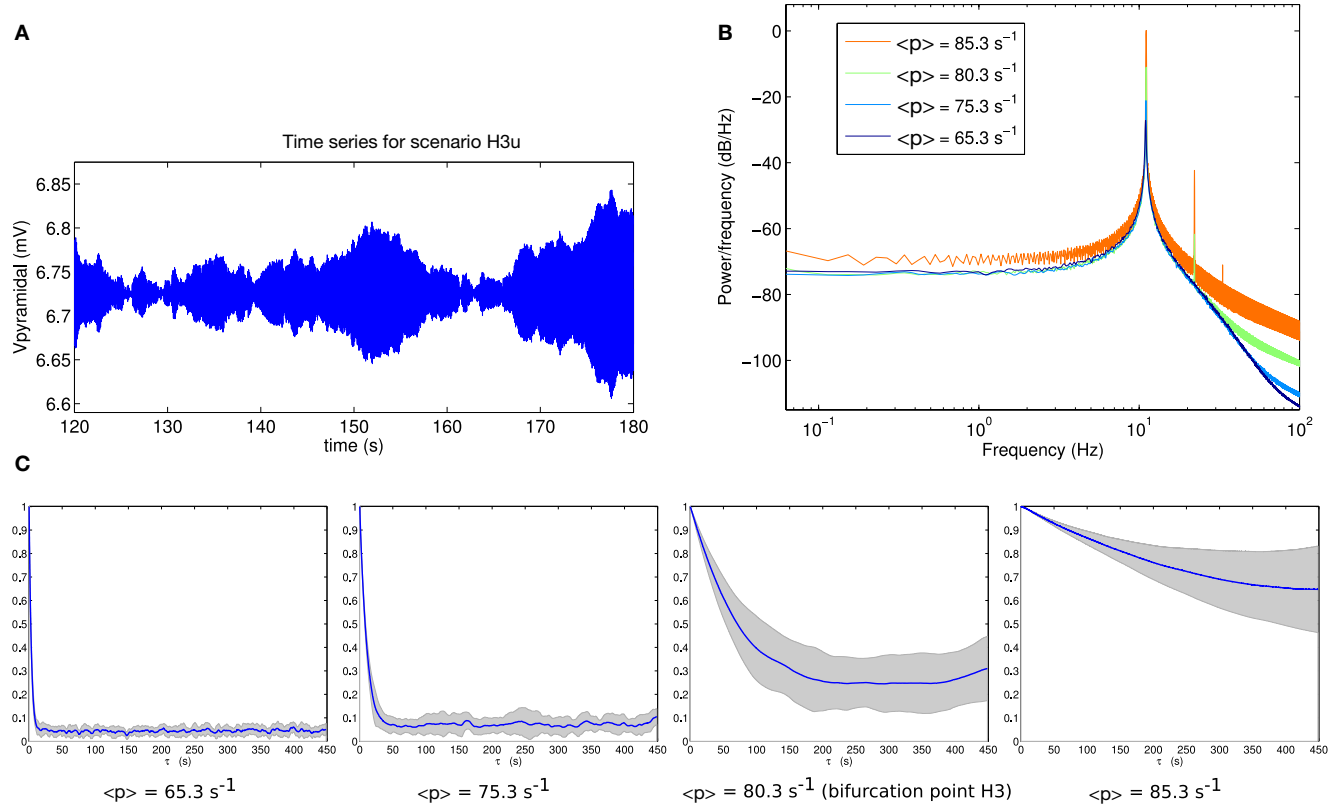

FIGURE 7 | (A) Example section of simulated time series for scenario H3u. Note the *y*-axis scale is much smaller than that of **Figure 6A**, reflecting much smaller output variance in this case. **(B)** Power spectrum at H3. **(C)** Autocorrelation amplitude at points in parameter space approaching the bifurcation point H3 ($\langle p \rangle = 65.3\,s^{-1}$, $\langle p \rangle = 75.3\,s^{-1}$), at the bifurcation point H3 ($\langle p \rangle = 80.3\,s^{-1}$) and beyond the bifurcation point ($\langle p \rangle = 85.3\,s^{-1}$). The line indicates the mean over 16 trials and the gray area indicates one standard deviation.

latter family includes the former), the null hypothesis is that the power law is best-fitting distribution. For all other tests, the null hypothesis is that both distributions are equally far from the true distribution.

Figure 9 shows the fluctuation distributions for H3u. The empirical distributions for both duration (**Figure 9A**) and area (**Figure 9B**) exhibit a scaling regime over approximately four orders of magnitude. The power law fits for duration and area have exponents 1.56 and 1.51, and p-values $p = 0.27$ and $p = 0.72$, respectively, and are thus consistent with the hypothesis that the true distribution is a power law. The fitted exponents depend weakly on the threshold value but the main finding of a broad scaling regime is unchanged. The lognormal and power law with exponential cutoff are *also* consistent with the data: the likelihood ratio tests do not distinguish between the lognormal and power law fits (duration: $p = 0.15$; area: $p = 0.26$), but favor the power law with exponential cutoff over both power law (duration: $p = 0.016$; area: $p = 0.047$) and lognormal (duration: $p = 0.003$; area: $p = 0.004$). The pure exponential distribution is strongly ruled out in all cases ($p \ll 0.001$) and so is not shown.

Approach to this bifurcation, shown in **Figure 10**, reiterates the autocorrelation results of Section "Autocorrelation Depends on Orientation of Input Fluctuations." Near H3u (**Figure 10A**), the long scaling regime of **Figure 9A** (black) is significantly diminished away from the bifurcation (red), with few fluctuations having durations >10 s. Here, the pure power law is ruled out ($p < 0.001$), and the power law with exponential cutoff is strongly favored over all the alternatives tested. For comparison, **Figure 9B** shows fluctuations at the same bifurcation when noise enters almost perpendicular to the center eigenspace (scenario H3p). At the bifurcation (black), there is no clear scaling regime, and the distribution is essentially unchanged by moving to a more stable point in parameter space (red). The power law fit is ruled out for both points ($p < 0.001$), and again the power law with cutoff is strongly favored. Thus, as in the autocorrelation cases (**Figures 7C** and **8C**), the fluctuation statistics clearly herald the approach to the bifurcation for H3u but only negligibly for H3p.

DISCUSSION

The relevance of these results to physiology is twofold. Firstly, we have demonstrated a fundamental limitation in the use of autocorrelation as an indicator of the loss of linear stability, a limitation which will apply when attempting to detect bifurcations from actual human EEG, EMG, and MEG time series. Secondly, the demonstration of both long autocorrelation times and scale-free temporal fluctuations in a simple, low-dimensional stochastic model informs the debate about whether the brain exhibits self-organized criticality, because it shows that these features can

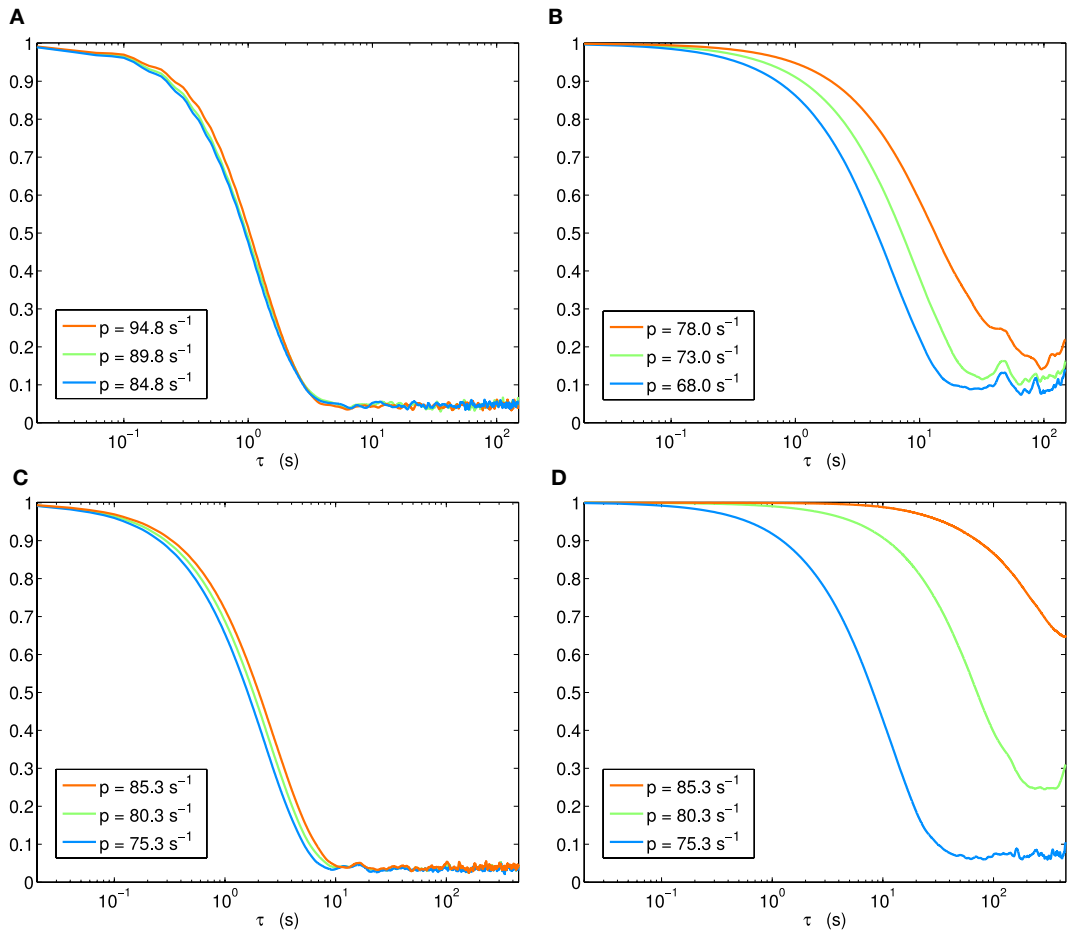

FIGURE 8 | Autocorrelation amplitude in log(delay)-linear(correlation) coordinates. Each panel shows step immediately before (blue), at (green), and beyond (orange) Hopf bifurcation. **(A)** Scenario H1, **(B)** H2, **(C)** H3p, **(D)** H3u.

also arise from mechanisms other than a multi-scale critical phase transition.

Close to the supercritical Hopf bifurcation in the Jansen–Rit model, we have shown that when lengthened autocorrelation times and scale-free fluctuations manifest in any one cell population as indicators of approach to the bifurcation, then they are indeed detectable in the pyramidal time series that is most closely associated with EEG signals. The standard parameters of the model provide sufficiently large coupling between the three neural populations that lengthened autocorrelation is evident in all three populations when it is present in any of them.

When considering long time autocorrelation and scale-free fluctuations that are present in human EEG time series this suggests that in addition to the possibility that these could arise in the brain at the point of phase transition in a complex, multi-scale system (Linkenkaer-Hansen et al., 2004; Stam and de Bruin, 2004), there may also be a role for low-dimensional stochastic dynamics at the population scale in generating these indicators.

More importantly, we have shown that even in a very simplistic cortical model, these indicators can already be subtle in their dependency on neuronal inputs. Longer autocorrelation times are not guaranteed to be evident in the output just because there is a bifurcation where linear stability is lost. In particular we have shown that a change of the orientation in phase space of small fluctuations in the input can be sufficient to enhance or almost completely remove this indicator.

Jansen and Rit (1995) suggested that input to excitatory interneurons could be removed from the model, as input to the pyramidal population from coupled columns was expected to have the same effect. Our results show that when fluctuations in the input are taken into account, the statistical properties of the model output are sensitive to the choice of which neural population receives the extrinsic input.

The Jansen–Rit model is representative of a broad class of models that mathematically can be expressed as a composition of sigmoid functions and second order linear filters. It is worth noting that neural field models (such as Jirsa and Haken, 1996; Robinson et al., 1997), when restricted to spatially uniform solutions, can also be expressed in this mathematical form, with an additional critically damped second order linear filter capturing the time characteristics of local axonal propagation with a population spread of sources and axon parameters (Robinson et al.,

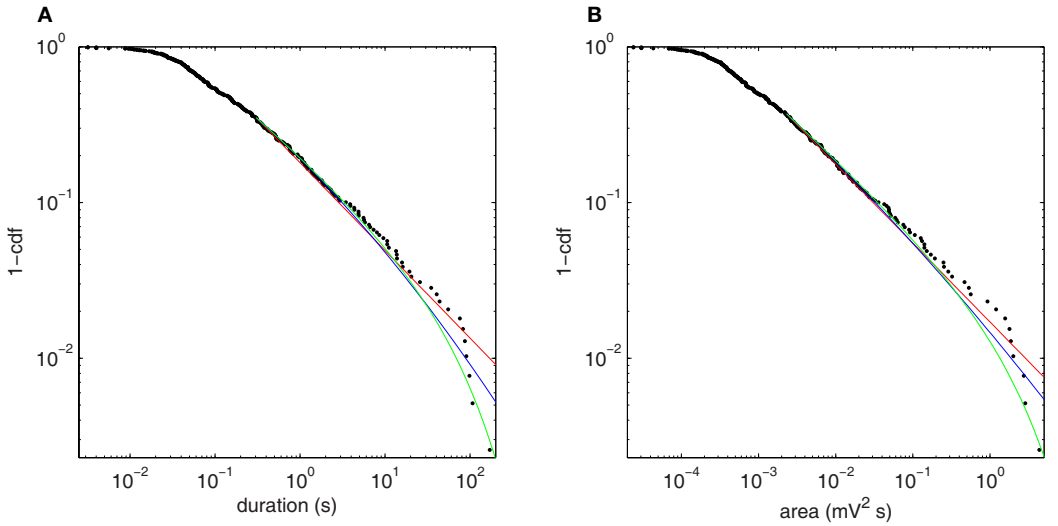

FIGURE 9 | Upper cumulative distributions of fluctuation statistics at the bifurcation point H3u, using squared Hilbert amplitude thresholded at 0.008 mV^2, with power law (red), power law with exponential cutoff (green), and lognormal (blue) fits plotted for the fitted range of the tail. (A) Fluctuation duration. **(B)** Fluctuation size as given by area under the curve.

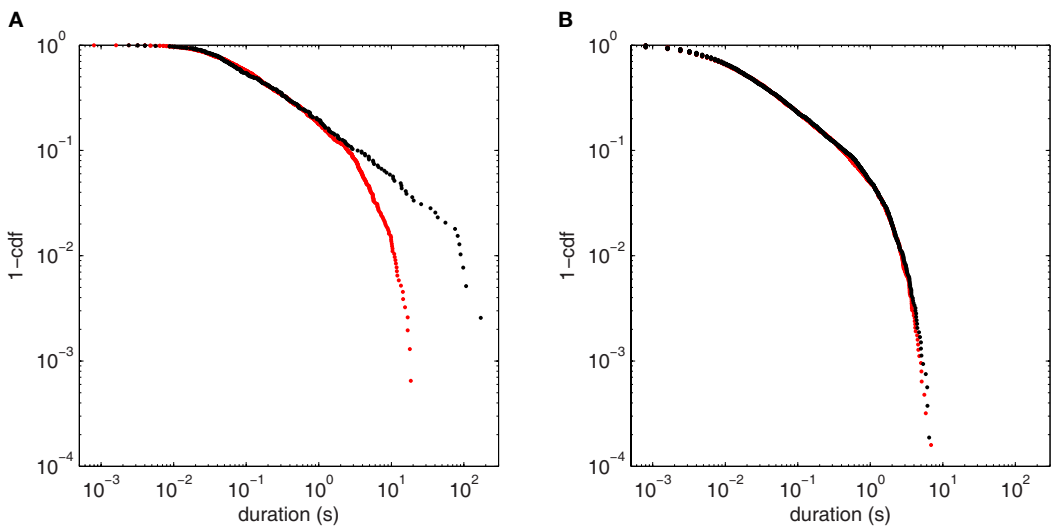

FIGURE 10 | Comparison of fluctuation duration distributions between points approaching ($p = 65.3\,s^{-1}$) and at the bifurcation point ($p = 80.3\,s^{-1}$) for the two noise input directions. (A) Point H3u (black, threshold = 0.008 mV^2) and nearby more stable point (red, threshold = 0.0002 mV^2). **(B)** Point H3p (black, threshold = 0.4 mV^2) and nearby more stable point (red, threshold = 0.18 mV^2).

1997). There are no particularities of the current model that suggest that the phenomena which we describe will be limited to this setting. The present results regarding fluctuation orientation hence speak broadly to the commonly employed neural mass and neural field models of large-scale neuronal activity.

OPPOSITE EFFECT ON AUTOCORRELATION AND VARIANCE

Autocorrelation and variance of the output signal have been suggested as generic indicators of the approach to local bifurcation, as standard linear analysis shows they are both expected to increase as the bifurcation is approached and the real part of bifurcating eigenvalues approaches zero. We also observed that changing the orientation of input fluctuations can result in autocorrelation increasing at the same time as variance is decreased. Insight into these phenomena can be gained by considering the behavior of a simple low-dimensional linear stochastic system. In the one-dimensional linear case of an Ornstein–Uhlenbeck process, $dx = -axdt + bdW$, the (normalized) autocorrelation is given by $\exp(-a\tau)$ and variance by $1/2\ b^2/a$, so both increase as the size of the eigenvalue a approaches zero. In particular, variance increases linearly with the variance of noise input b^2 (Gardiner, 2010). The same is true for a linearized two-dimensional

system near a Hopf bifurcation (Steyn-Ross et al., 2006). If we naively assume that aligning input noise with the center eigenspace increases the amount of noise affecting the slow dynamical system of the center manifold, we would expect variance to be greater when the angle with the center eigenspace plane was smaller, which was not the case. From consideration of the normal form transformation (Roberts, 2008) it is rather the plane perpendicular to the stable eigenspace that should be relevant in determining the magnitude of noise driving the slow dynamics. Because the eigenvectors of the linearized Jansen–Rit system are far from orthogonal, that reference plane is almost normal to the center eigenspace plane, resulting in the observed reversal of the expected relationship between noise orientation and variance.

It may be possible to study these bifurcation indicators more specifically in a normal form model by considering a full center manifold reduction. Close to the bifurcation non-linear terms can result in multiplicative noise in the slow dynamical system of the center manifold (Roberts, 2008). These occur in addition to the simpler additive noise that results directly from linear transformation of the input noise terms but so far we have yet to calculate the magnitude or importance of these multiplicative noise terms in the present system. Furthermore, any local analysis of the behavior close to the equilibrium point is valid only for the case of small noise, so that the state of the system remains local to the equilibrium point. That is not necessarily the case for this system, as suggested by larger output standard deviation near the bifurcation seen in the cases of H1 and H3p, which is comparable to the amplitude of the subsequent limit cycles. This implies that the system is exploring a wider region of phase space compared to the cases with high autocorrelation (H2 and H3u). Thus the structure of flow in the phase space further from the equilibrium point may be directly responsible for the quickly decaying autocorrelation in those cases. In particular if the center manifold curves away from the center eigenspace, then at a sufficient distance from the equilibrium point the directions of noise input which are "well aligned" and "poorly aligned" with the manifold may be reversed.

POWER LAW SCALING OF OUTPUT FLUCTUATIONS

Analyzing the distributions of fluctuation sizes and durations, we observe the presence of a long power law scaling regime that extends over four orders of magnitude with a rapid truncation at the far right hand tail at the bifurcation when input fluctuations are normal to the reference plane. This power law scaling is not observed when input fluctuations have a significant projection onto the reference plane. Further away from the bifurcation, the power law regime extends for less than one order of magnitude so that the lengthy power law tail provides a signature of proximity to the bifurcation in that scenario.

A range of simple dynamical mechanisms are known to permit production of scale-free fluctuation structure of this kind. A relaxation process with a fractional operator formally yields a power law (Pareto) probability distribution of fluctuation durations (Sokolov and Klafter, 2005). Multiplicative noise (which arises when reducing oscillation dynamics of the model to two dimensions) can also in specific cases result in power law probability distributions (Anteneodo and Riera, 2005). However, the cause of the power law scaling of the distributions of fluctuations in our system is not yet determined.

FUTURE WORK

This study considered autocorrelation in the output of a single Jansen–Rit model region, representing a small area of cortex of the order of 2–3 mm^2. For the question of potential detectability in EEG it remains to examine the effect on autocorrelation of combining the output of a large number of cortical regions, whose oscillations may be synchronized to a greater or lesser degree and where the output measurement function relating EEG to the combination of sources plays an important role.

Within the Jansen–Rit model we also observed indicators close to other bifurcation types, including switching between attractors in a bistable region near a cusp bifurcation and "flickering" or intermittent switching away from a stable fixed point in a monostable region near a sniper bifurcation, which are not explored further in this paper. Therefore it remains to examine the sensitivity of these and other indicators, such as mean switching times as bifurcations are approached, to noise orientation.

It is hoped that normal form analyses near the bifurcation will shed some light on the mechanism by which the input noise affects autocorrelation. A first step will be to examine a simpler normal form system displaying the same behavior, where exact control over the shape of the center manifold can be afforded, initially targeting the limiting case of small fluctuations. Such an analysis will serve to separate the generic local effects of the Hopf bifurcation from global behavior due to excursion of the state further from the equilibrium point.

Examination of a normal form system will also be key to determining the reason for the power law scaling of fluctuation statistics. The results presented in this paper show that some of the indicators of instability reported in human EEG also arise in the output of a simple neural mass model near linear instability.

While similar indicators can also emerge from a critical phase transition in a complex, multi-scale system, we have shown in the present study that some of the same indicators can arise in a very different way, from the low-dimensional stochastic dynamics at a single scale: the mesoscopic scale of interacting populations. As the field advances, it will become increasingly important to move away from a single umbrella notion of "criticality" in brain dynamics toward defining a number of exact, and possibly distinct, mechanisms responsible for correlations and scale-free fluctuations in the time and/or spatial domains. It is certainly possible at this stage that multiple mechanisms play a role.

ACKNOWLEDGMENTS

Michael Breakspear acknowledges the support of the Australian Research Council, the National Health and Medical Research Council and the Brain Network Recovery Group Grant JSMF22002082. Tjeerd W. Boonstra acknowledges support from the Netherlands Organization for Scientific Research (NWO #451–10-030). The authors thank Saeid Mehrkanoon for helpful technical advice.

REFERENCES

Anteneodo, C., and Riera, R. (2005). Additive-multiplicative stochastic models of financial mean-reverting processes. *Phys. Rev. E Stat. Nonlin. Soft Matter Phys.* 72, 026106.

Bedard, C., Kroeger, H., and Destexhe, A. (2006). Does the 1/f frequency scaling of brain signals reflect self-organized critical states? *Phys. Rev. Lett.* 97, 118102.

Braun, J., and Mattia, M. (2010). Attractors and noise: twin drivers of decisions and multistability. *Neuroimage* 52, 740–751.

Breakspear, M., Roberts, J. A., Terry, J. R., Rodrigues, S., Mahant, N., and Robinson, P. A. (2006). A unifying explanation of primary generalized seizures through nonlinear brain modeling and bifurcation analysis. *Cereb. Cortex* 16, 1296.

Breakspear, M., and Terry, J. R. (2002). Detection and description of non-linear interdependence in normal multichannel human EEG data. *Clin. Neurophysiol.* 113, 735–753.

Clauset, A., Shalizi, C. R., and Newman, M. E. J. (2009). Power-law distributions in empirical data. *SIAM Rev. Soc. Ind. Appl. Math.* 51, 661–703.

David, O., and Friston, K. J. (2003). A neural mass model for MEG/EEG: coupling and neuronal dynamics. *Neuroimage* 20, 1743–1755.

David, O., Harrison, L., and Friston, K. J. (2005). Modelling event-related responses in the brain. *Neuroimage* 25, 756–770.

Deco, G., Jirsa, V. K., Robinson, P. A., Breakspear, M., and Friston, K. (2008). The dynamic brain: from spiking neurons to neural masses and cortical fields. *PLoS Comput. Biol.* 4, e1000092. doi:10.1371/journal.pcbi.1000092

Dhooge, A., Govaerts, W., and Kuznetsov, Y. A. (2003). MATCONT: a MATLAB package for numerical bifurcation analysis of ODEs. *ACM Trans. Math. Softw.* 29, 141–164.

Freeman, W. (1992). "Predictions on neocortical dynamics derived from studies in paleocortex," in *Induced Rhythms in the Brain, Brain Dynamics Series*, Chap. 9, eds E. Basar and T. H. Bullock (Boston: Birkhäuser), 183–199.

Freyer, F., Aquino, K., Robinson, P. A., Ritter, P., and Breakspear, M. (2009). Bistability and non-Gaussian fluctuations in spontaneous cortical activity. *J. Neurosci.* 29, 8512.

Freyer, F., Roberts, J. A., Becker, R., Robinson, P. A., Ritter, P., and Breakspear, M. (2011). Biophysical mechanisms of multistability in resting-state cortical rhythms. *J. Neurosci.* 31, 6353.

Freyer, F., Roberts, J. A., Ritter, P., and Breakspear, M. (2012). A canonical model of multistability and scale-invariance in biological systems. *PLoS Comput. Biol.* doi: 10.1371/journal.pcbi.1002634

Friston, K. J., and Dolan, R. J. (2010). Computational and dynamic models in neuroimaging. *Neuroimage* 52, 752–765.

Friston, K. J., Harrison, L., and Penny, W. (2003). Dynamic causal modeling. *Neuroimage* 19, 1273–1302.

Gardiner, C. (2010). *Stochastic Methods: A Handbook for the Natural and Social Sciences, Springer Series in Synergetics Series*. New York: Springer.

Grimbert, F., and Faugeras, O. (2006). Bifurcation analysis of Jansen's neural mass model. *Neural Comput.* 18, 3052–3068.

Haken, H., Kelso, J. A. S., and Bunz, H. (1985). A theoretical model of phase transitions in human hand movements. *Biol. Cybern.* 51, 347–356.

He, B. J., Zempel, J. M., Snyder, A. Z., and Raichle, M. E. (2010). The temporal structures and functional significance of scale-free brain activity. *Neuron* 66, 353–369.

Jansen, B. H., and Rit, V. G. (1995). Electroencephalogram and visual evoked potential generation in a mathematical model of coupled cortical columns. *Biol. Cybern.* 73, 357–366.

Jansen, B. H., Zouridakis, G., and Brandt, M. E. (1993). A neurophysiologically-based mathematical model of flash visual evoked potentials. *Biol. Cybern.* 68, 275–283.

Jirsa, V. K., and Haken, H. (1996). Field theory of electromagnetic brain activity. *Phys. Rev. Lett.* 77, 960–963.

Kelso, J. A. S. (2010). Instabilities and phase transitions in human brain and behavior. *Front. Hum. Neurosci.* 4:23. doi:10.3389/fnhum.2010.00023

Kelso, J. A. S., Scholz, J. P., and Schöner, G. (1986). Nonequilibrium phase transitions in coordinated biological motion: critical fluctuations. *Phys. Lett. A* 118, 279–284.

Kuehn, C. (2011). A mathematical framework for critical transitions: bifurcations, fast-slow systems and stochastic dynamics. *Physica D* 240, 1020–1035.

Linkenkaer-Hansen, K., Nikouline, V. V., Palva, J. M., and Ilmoniemi, R. J. (2001). Long-range temporal correlations and scaling behavior in human brain oscillations. *J. Neurosci.* 21, 1370.

Linkenkaer-Hansen, K., Nikulin, V. V., Palva, J. M., Kaila, K., and Ilmoniemi, R. J. (2004). Stimulus-induced change in long-range temporal correlations and scaling behaviour of sensorimotor oscillations. *Eur. J. Neurosci.* 19, 203–218.

Lopes da Silva, F. H., Hoeks, A., Smits, H., and Zetterberg, L. H. (1974). Model of brain rhythmic activity. *Biol. Cybern.* 15, 27–37.

Marreiros, A. C., Daunizeau, J., Kiebel, S. J., and Friston, K. J. (2008). Population dynamics: variance and the sigmoid activation function. *Neuroimage* 42, 147–157.

Miller, K. J., Sorensen, L. B., Ojemann, J. G., and den Nijs, M. (2009). Power-law scaling in the brain surface electric potential. *PLoS Comput. Biol.* 5, e1000609. doi:10.1371/journal.pcbi.1000609

Moran, R. J., Kiebel, S. J., Stephan, K. E., Reilly, R. B., Daunizeau, J., and Friston, K. J. (2007). A neural mass model of spectral responses in electrophysiology. *Neuroimage* 37, 706–720.

Orfanidis, S. J. (1996). *Optimum Signal Processing*, 2nd Edn. New York: McGraw-Hill.

Roberts, A. J. (2008). Normal form transforms separate slow and fast modes in stochastic dynamical systems. *Physica A* 387, 12–38.

Roberts, J. A., and Robinson, P. A. (2012). Corticothalamic dynamics: structure of parameter space, spectra, instabilities, and reduced model. *Phys. Rev. E Stat. Nonlin. Soft Matter Phys.* 85, 011910.

Robinson, P. A., Rennie, C. J., Phillips, A. J. K., Kim, J. W., and Roberts, J. A. (2010). *Phase Transitions in Physiologically-Based Multiscale Mean-Field Brain Models, Modeling Phase Transitions in the Brain*. New York: Springer, 179–201.

Robinson, P. A., Rennie, C. J., and Rowe, D. L. (2002). Dynamics of large-scale brain activity in normal arousal states and epileptic seizures. *Phys. Rev. E Stat. Nonlin. Soft Matter Phys.* 65, 041924.

Robinson, P. A., Rennie, C. J., and Wright, J. J. (1997). Propagation and stability of waves of electrical activity in the cerebral cortex. *Phys. Rev. E Stat. Phys. Plasmas. Fluids Relat. Interdiscip. Topics* 56, 826.

Rowat, P. F., and Greenwood, P. E. (2011). Identification and continuity of the distributions of burst-length and interspike intervals in the stochastic Morris-Lecar neuron. *Neural Comput.* 23, 1–31.

Rümelin, W. (1982). Numerical treatment of stochastic differential equations. *SIAM J. Numer. Anal.* 19, 604–613.

Scheffer, M., Bascompte, J., Brock, W. A., Brovkin, V., Carpenter, S. R., Dakos, V., Held, H., van Nes, E. H., Rietkerk, M., and Sugihara, G. (2009). Early-warning signals for critical transitions. *Nature* 461, 53–59.

Scholz, J. P., Kelso, J. A. S., and Schöner, G. (1987). Nonequilibrium phase transitions in coordinated biological motion: critical slowing down and switching time. *Phys. Lett. A* 123, 390–394.

Sokolov, I. M., and Klafter, J. (2005). From diffusion to anomalous diffusion: a century after Einstein's Brownian motion. *Chaos* 15, 026103–026103.

Sotero, R. C., Trujillo-Barreto, N. J., Iturria-Medina, Y., Carbonell, F., and Jimenez, J. C. (2007). Realistically coupled neural mass models can generate EEG rhythms. *Neural Comput.* 19, 478–512.

Spiegler, A., Kiebel, S. J., Atay, F. M., and Knösche, T. R. (2010). Bifurcation analysis of neural mass models: Impact of extrinsic inputs and dendritic time constants. *Neuroimage* 52, 1041–1058.

Stam, C. J., and de Bruin, E. A. (2004). Scale-free dynamics of global functional connectivity in the human brain. *Hum. Brain Mapp.* 22, 97–109.

Stam, C. J., Pijn, J. P. M., Suffczynski, P., and da Silva, F. H. L. (1999). Dynamics of the human alpha rhythm: evidence for non-linearity? *Clin. Neurophysiol.* 110, 1801–1813.

Steyn-Ross, D. A., Steyn-Ross, M. L., Wilson, M. T., and Sleigh, J. W. (2006). White-noise susceptibility and critical slowing in neurons near spiking threshold. *Phys. Rev. E Stat. Nonlin. Soft Matter Phys.* 74, 051920.

van Albada, S. J., Kerr, C. C., Chiang, A. K. I., Rennie, C. J., and Robinson, P. A. (2010). Neurophysiological changes with age probed by inverse modeling of EEG spectra. *Clin. Neurophysiol.* 121, 21–38.

Vuong, Q. H. (1989). Likelihood ratio tests for model selection and non-nested hypotheses. *Econometrica* 57, 307–333.

Wendling, F., Bartolomei, F., Bellanger, J. J., and Chauvel, P. (2002). Epileptic fast activity can be explained by a model of impaired GABAergic dendritic inhibition. *Eur. J. Neurosci.* 15, 1499–1508.

Wendling, F., Bellanger, J. J., Bartolomei, F., and Chauvel, P. (2000).

Relevance of nonlinear lumped-parameter models in the analysis of depth-EEG epileptic signals. *Biol. Cybern.* 83, 367–378.

Wilson, H. R., and Cowan, J. D. (1972). Excitatory and inhibitory interactions in localized populations of model neurons. *Biophys. J.* 12, 1–24.

Zavaglia, M., Astolfi, L., Babiloni, F., and Ursino, M. (2006). A neural mass model for the simulation of cortical activity estimated from high resolution EEG during cognitive or motor tasks. *J. Neurosci. Methods* 157, 317–329.

Conflict of Interest Statement: The authors declare that the research was conducted in the absence of any commercial or financial relationships that could be construed as a potential conflict of interest.

Received: 26 March 2012; paper pending published: 09 May 2012; accepted: 29 July 2012; published online: 20 August 2012.
*Citation: Aburn MJ, Holmes CA, Roberts JA, Boonstra TW and Breakspear M (2012) Critical fluctuations in cortical models near instability. Front. Physio. **3**:331. doi: 10.3389/fphys.2012.00331*
This article was submitted to Frontiers in Fractal Physiology, a specialty of Frontiers in Physiology.

APPENDIX

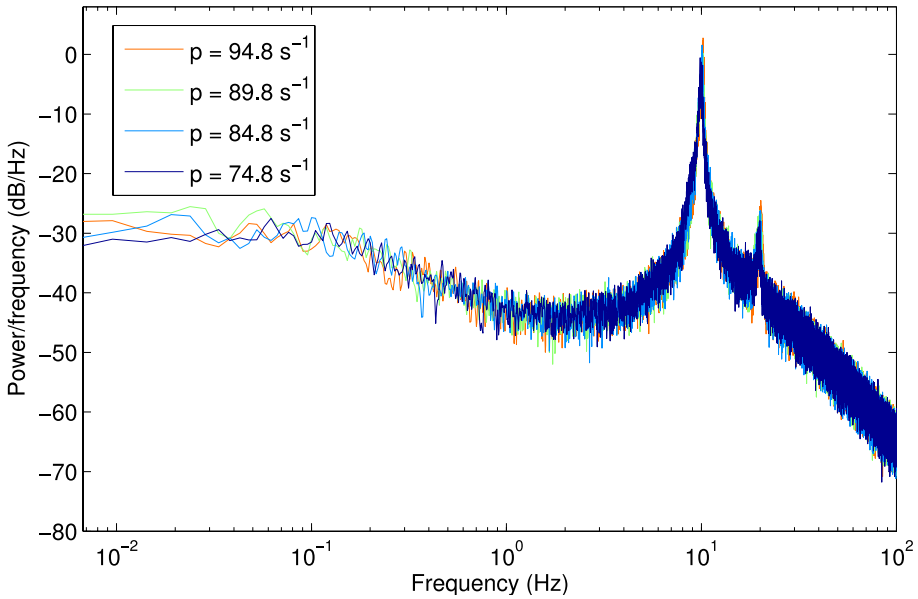

FIGURE A1 | Power spectrum at H1, using a larger window size of 150 s (750,000 samples) to show lower frequencies from 6.7 × 10^{-3} Hz.

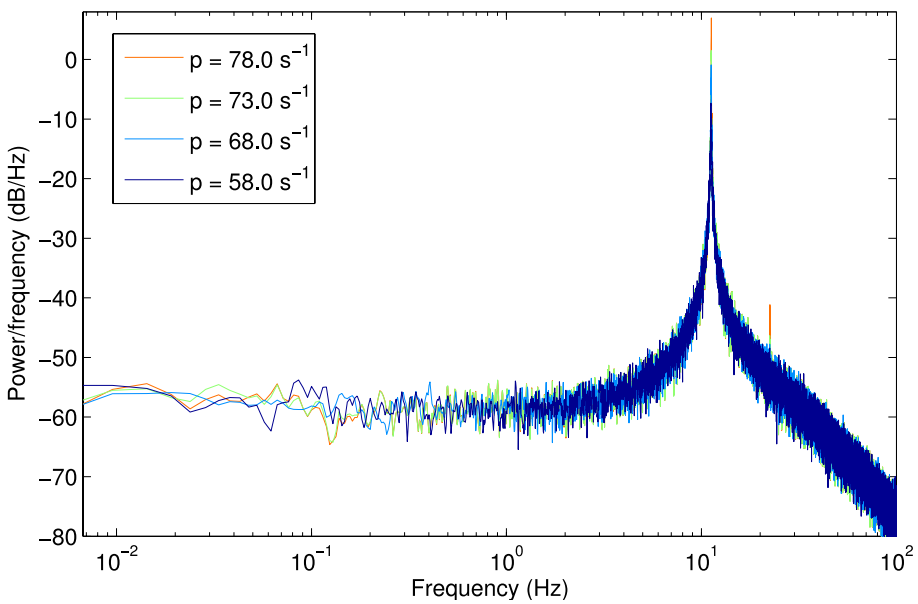

FIGURE A2 | Power spectrum at H2, using a larger window size of 150 s (750,000 samples) to show lower frequencies from 6.7 × 10^{-3} Hz.

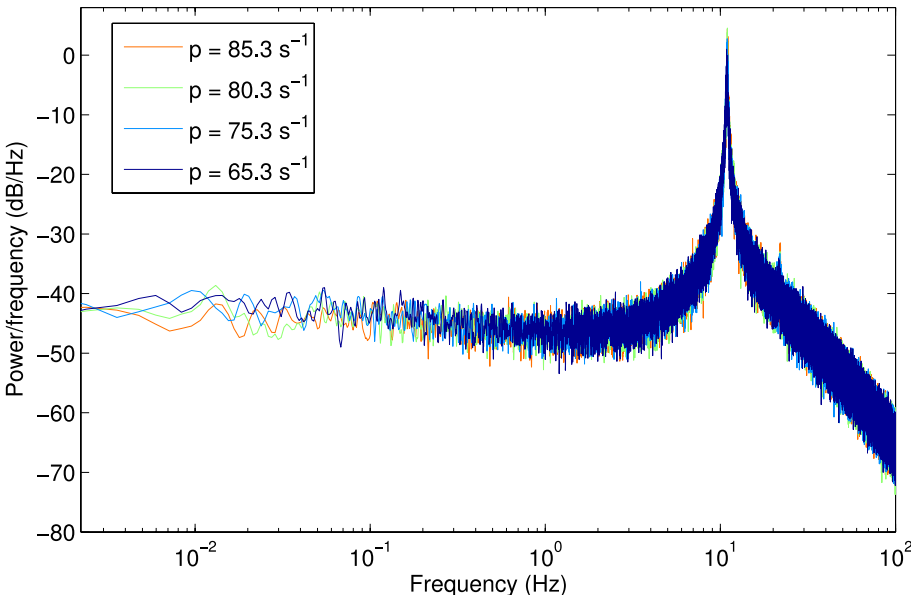

FIGURE A3 | Power spectrum for scenario H3p, using a larger window size of 450 s (2,250,000 samples) to show lower frequencies from 2.2 x 10^{-3} Hz.

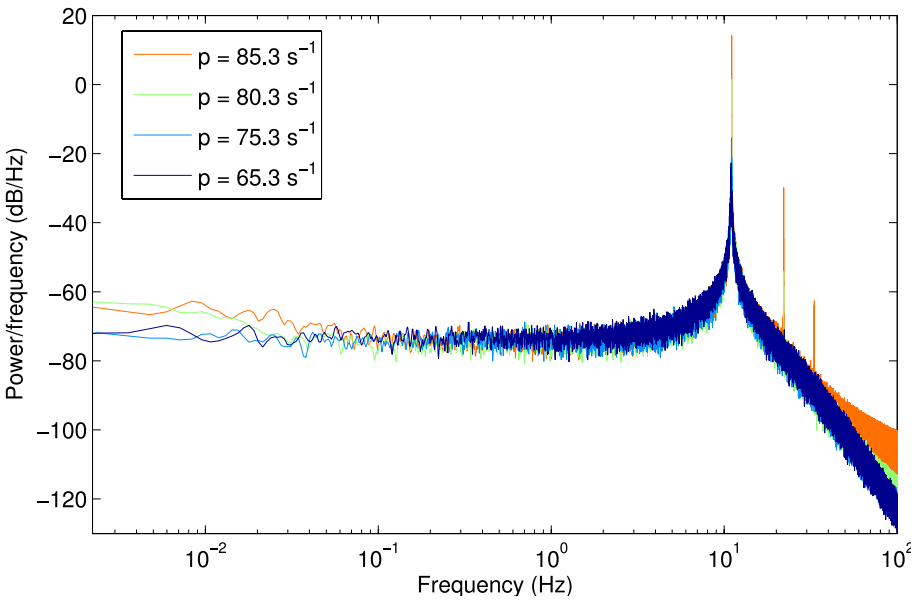

FIGURE A4 | Power spectrum for scenario H3u, using a larger window size of 450 s (2,250,000 samples) to show lower frequencies from 2.2 x 10^{-3} Hz.

frontiers in PHYSIOLOGY

HYPOTHESIS AND THEORY ARTICLE
published: 18 June 2012
doi: 10.3389/fphys.2012.00207

The blue-collar brain

Guy Van Orden[1]*, Geoff Hollis[2] and Sebastian Wallot[3]

[1] CAP Center for Cognition, Action and Perception, Department of Psychology, University of Cincinnati, Cincinnati, OH, USA
[2] Department of Psychology, Grant MacEwan University, Edmonton, AB, Canada
[3] MINDLab, Aarhus University, Aarhus, Denmark

Edited by:
Tjeerd W. Boonstra, University of New South Wales, Australia

Reviewed by:
Didier Delignieres, University Montpellier 1, France
Cees Van Leeuwen, Katholieke Universiteit Leuven, Belgium

***Correspondence:**
Guy Van Orden, CAP Center for Cognition, Action and Perception, Department of Psychology, University of Cincinnati, Cincinnati, OH 45221-0376, USA.
e-mail: guy.van.orden@uc.edu

Much effort has gone into elucidating control of the body by the brain, less so the role of the body in controlling the brain. This essay develops the idea that the brain does a great deal of work in the service of behavior that is controlled by the body, a blue-collar role compared to the white-collar control exercised by the body. The argument that supports a blue-collar role for the brain is also consistent with recent discoveries clarifying the white-collar role of synergies across the body's tensegrity structure, and the evidence of critical phenomena in brain and behavior.

Keywords: control, synergetics, self-organization, 1/f scaling, mind and body

INTRODUCTION

Lloyd Olsen shared fame in the 1940s with Mike the celebrity headless chicken. Mike's head was lost when he was five and a half months old while being prepared by Lloyd to become chicken dinner. Mike lived on without a head for 18 months, fed through an eyedropper and growing from two pounds, at his beheading, to eight pounds at his death. In the mean time he traveled widely performing in New York City, Los Angeles, Atlantic City, and elsewhere. Our interest in Mike is the demonstrated coordination among the processes of his body, despite lacking a head. What was left of Mike's brain – he probably still had a brainstem – would have marked a handkerchief somewhat less than a healthy sneeze. But he nonetheless retained the coordination among peripheral nervous system, organ systems, facia, muscles, and tendons, producing locomotion apparently indistinguishable from intact locomotion, even walking around and "pecking" right after losing his head.

To us Mike demonstrates that high-level control of the body has sources in addition to the central nervous system. An environment of constant red light, in a different demonstration, created feckless chickens. The steady-state environment obviated the chickens' connection to the daily cycles of sunrise and sunset, and the pace markers or zeitgebers of the body's circadian rhythm. Consequently the chickens suffered a breakdown of healthy coordination among the rhythms of physiology, including heart rate and cycles of deep body temperature, and the coupling of physiology with locomotor activities (Winget et al., 1968). Apparently, chicken physiology and behavior include necessary sources of control in the daily cycles of a circadian environment.

A sea squirt starts life as a rather simple tadpole-like creature, possessing a simple nervous system, and capable of locomotion and light detection. However, finding a surface upon which it can affix itself, the sea squirt will do so, and promptly ingest its nervous system (Birkeland et al., 1981). This sea squirt example, like the chicken examples, speaks again to sources of control of the body and behavior in addition to and distinct from the central nervous system. Deprivation of sleep cycles or nutrients illustrates this idea in human behavior. These deprivations destabilize human emotional control, increasing emotional lability. The effect is sufficiently reliable to have become a mainstay of the weekend initiation rituals of cults and extreme self-help programs. Initiates are kept awake in a common room without food for 24 h, which opens them up emotionally, becoming more receptive to the program being sold.

These examples all bear relationships to general theories of control, whether that of cybernetics or non-linear dynamics of self-organization (cf. Simon, 1973; Haken, 1977; Newell, 1990; Schiepek and Haken, 2006, respectively). The feckless chickens probably illustrate this relationship best. The faster changing processes of physiology are constrained in their coordination by the more slowly changing circadian rhythm – generally speaking, more slowly changing dynamics constrain faster dynamics, not vice versa. In self-organization, a key distinction between control and order parameters versus state dynamics is based on how fast one changes with respect to the other. Order parameters are defined to be particular configurations of state dynamics, which means they must change more slowly than state dynamics.

Thus the pacing of the phenomena of the body and brain, with respect to behavior, can tell us which processes constrain which in enacting behavior. Nonetheless, the idea that the body or behavior might control the brain, when first heard, may sound outrageous, depending on what you already believe about control, the brain, and behavior. The most widely held conventional belief is that the brain controls behavior, not the other way around. Yet, when compared with the lightening fast changes in the brain, the typically more slowly changing body suggests the exact opposite broad-stroke outline of control. The brain appears to take direction from the body, just as old school blue-collar workers took direction from white-collar counterparts in the front office.

This issue of Frontiers of Fractal Physiology is about critical phenomena of the brain. A close look at the critical phenomenon of *fractal time* suggests that the brain serves the blue-collar role in broad circumstances of on-going behavior. To understand this claim, we must first make explicit the links among related concepts of fractal physiology, criticality, non-linear dynamics, tensegrity, synergy, and control. The integrated ideas are that control of behavior originates in constraints on behavior changing on different timescales, and that constraints simultaneously sustain and are sustained by the emergent phenomena in which they participate.

HUMAN PERFORMANCE DATA

To begin we require an understanding of fractal time. Fractal time is a performance phenomenon, so in this section we re-examine the basic idea of measurement of human performance together with the idea of critical states separating qualitatively different modes of behavior. Following that we describe how fractal time appears in brains and behaviors and how the body has been proposed to be an excitable medium of self-organizing synergies. It is the synergies of the body that also constrain the brain during behavior. Finally, we summarize conclusions that appear to us to be the logical consequences of a blue-collar perspective on the brain.

Cognitive scientists may tell you that they study human performance of specific cognitive functions such as memory, language, or motor control. In actual practice we study the measurements of a person performing a "memory" task, a "language" task, or a "motor" task. Yet all task performances are motor performances and language is ubiquitous in the instructions to participants, which must tax memory to be remembered when performing the somewhat arbitrary laboratory task. So most of the time, and maybe all of the time, the scientists who study cognitive activities study the coordination over time among memory, language, and motor activities.

In particular, scientists are concerned with the reliable changes that they observe in the measurements that they take, which is true of cognitive scientists as well. The measurements that we take in cognitive science range from millisecond-precise durations of event times in human activities to nominal measurements that tally which category an observed behavior is assumed to represent. In all cases it is patterns of change or variation in the measured values that are scrutinized and interpreted to motivate interesting conclusions and to test the hypotheses that stem from scientific theories.

Early in the twentieth century scientists derived powerful statistical tools with which to carve out the patterns in data, based on idealized assumptions about the central tendencies of data and uniform dispersion of data values around a central tendency – as though an average behavior of a system could be found reliably at the center of the noisily dispersed measured values, falling equally on all sides, though less densely, outward from the center. With hindsight as a crystal ball, the twentieth century the picture of data was neatly generalized to become chaos theory or non-linear dynamical systems theory. Linear patterns of change in data, in which related changes were also proportional changes, one to another, were neatly absorbed as special cases of broader categories of non-linear disproportional change and discontinuous change.

In bifurcation theory, a tiny external change can break a balanced symmetry of possible outcomes, resulting in a qualitative change called a bifurcation. Bifurcation theory concerns the relation between locally continuous or incremental changes in control parameters and the abrupt fast qualitative restructuring that they may provoke. The tipping point of a bifurcation is a critical point and the behavior of systems near critical points is called criticality. The empirical foci of this essay are the observed scale-free behaviors of body and brain, predicted to occur near the critical bifurcation points of complex systems.

SCALE-FREE BEHAVIOR OF THE BRAIN AND THE BODY

Multicellular living things comprise nested structures. The toes and fingers at the small-scale periphery of the human skeleton are composed of small toe and finger bones coupled by small articulating joints. Toes and fingers are nested within the next scale of rigid bones of arms and legs that are coupled by larger articulating joints. Arms and legs in turn sprout from the trunk of the human body and are connected to the trunk by rotating joints at the hips and shoulders. Similarly, viewing a tree we can see that leaves are nested within the structure of small branches that are nested, in turn, within the structure of larger and yet larger branches that culminate in its largest branches, sprouting from the tree trunk.

The anatomy of blood vessels throughout the body, the detailed anatomy of a kidney, and the airways of a lung all comprise nested tree-structures across multiple scales – an arrangement called fractal structure that is studied using the mathematical tools of fractal geometry. The scaling relations that define the spatial organization of living things indicate their fractal composition. In a scaling relation, the size of a structure is inversely proportional to how often structures of that same size recur. For example, within limits, the diameter of each blood vessel is inversely proportional to the total number of blood vessels of that same diameter that will be found in the body (West, 2006).

The structure of the body provides specific physical limits on possible behavior. Scaling relations seen in the body are accompanied by scaling relations in the temporal unfolding of behavior. However, these constraints are not unidirectional. Physical structure and temporal behavior are mutually dependent. Typical physiological and neural development in young children (e.g., Hausdorff et al., 1999; Thelen et al., 2001) and change due to neurodegenerative disorders (e.g., Schmit et al., 2006), as well as musculature change in adults (e.g., Schmit et al., 2005), all shape the temporal structure of behavior. Likewise, behavior shapes both small-scale neural structure (e.g., Maguire et al., 2000) and larger scale muscular and cardiovascular structure, with exercise for instance.

Event times of both human physiology and human behavior compose temporal scaling relations. In the scaling relations of event times, the magnitude of changes in the duration of event times is inversely proportional to how often a change of that magnitude recurs. **Figure 1** portrays a physiological data series of brain activity to illustrate a scaling relation of fractal time. Across the top of **Figure 1** we present raw electroencephalogram (EEG) data

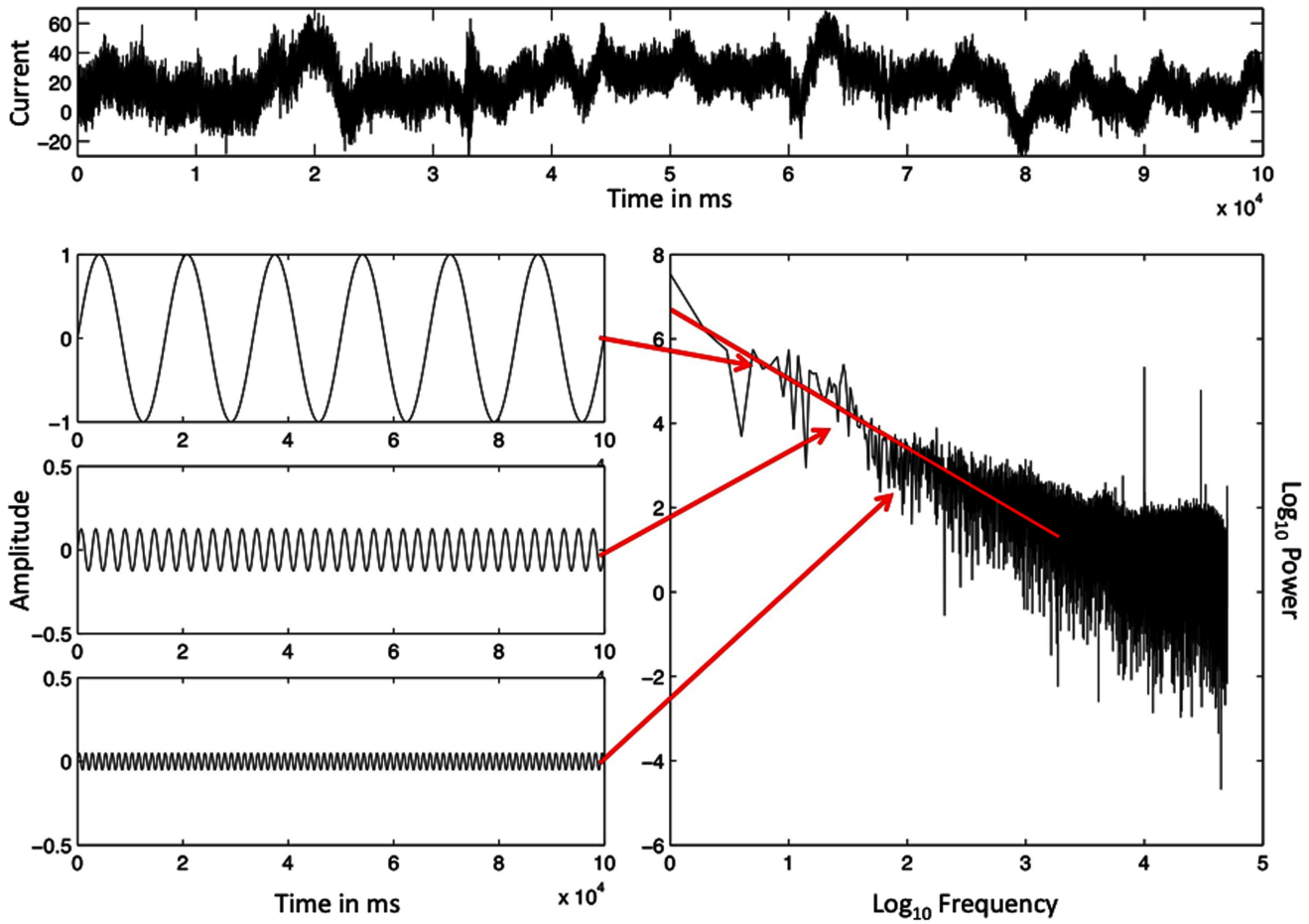

FIGURE 1 | The ordered series of a single EEG-electrode record, sampled at 500 Hz (top) and the illustration of a spectral analysis of this record (bottom, right). Specific frequencies and magnitudes of change (bottom, left) are used to approximate the rough graph of the EEG data (top), and the outcome is the spectral portrait (lower right) on log–log axes. The spectral slope $-\alpha = -1.08$ is close to idealized 1/f noise ($-\alpha = -1.00$). The Y-axes in the illustrated sine waves have been adjusted to make smaller amplitude sine waves visible.

from a volunteer, collected from an electrode on his scalp while he performed the task of repeatedly estimating a 1 s time interval.

The bottom, left side of **Figure 1** portrays a subset of the periodic sine waves used to simulate the aperiodic EEG signal. Arrows extend from each sine wave to its paired coordinate point in a power spectral graph, appearing below the raw EEG data. The amplitude and frequency of each sine wave become the two coordinates of a single point in the power spectral graph. The amplitude of the sine wave (squared) corresponds to the power or magnitude of changes in the data values that the sine wave simulates. The frequency of the sine wave estimates how often the changes of that magnitude recur.

Frequency of change and magnitude of change are the coordinate X- and Y-axes of the power spectral graph (after logarithmic transformations). Thus the power spectral graph presents a relation between the magnitude, or power, of the changes and the corresponding frequency of changes of that magnitude. The regression line, also portrayed in **Figure 1**, summarizes this relationship. The slope of the line in **Figure 1** indicates scale-free behavior because power is proportional to frequency. Data like these are called scale-free because the data pattern will look similar whether the vantage point of the analysis zooms in, to a finer scale, or zooms out, to a coarser scale.

The scale-free pattern of the data in **Figure 1** is further illustrated in **Figure 2** by repeatedly zooming in to examine the middle half of the time-series of the EEG data. Each tighter frame on the EEG data reveals another self-similar pattern in the variation. This self-similar pattern is the predominant pattern of variation in EEG data and begs to be explained with a high priority. An explanation may begin with the apparent fact of the fractal pattern, that the same pattern is observed whether the focus is one half of the original data, one fourth of the original data, one eighth of the original data, and so on.

Another fact begging for explanation is that, similar to the brain data, human performance data reveal a scale-free pattern (cf. Gilden, 2001), although it is possible to manipulate both patterns, to become more like white noise or brown noise (Van Orden et al., 2011; van Rooij and Van Orden, 2011). The performance data of the same volunteer, whose brain data appear in **Figures 1** and **2**, are portrayed in **Figure 3**. Each Y-value of a data point in

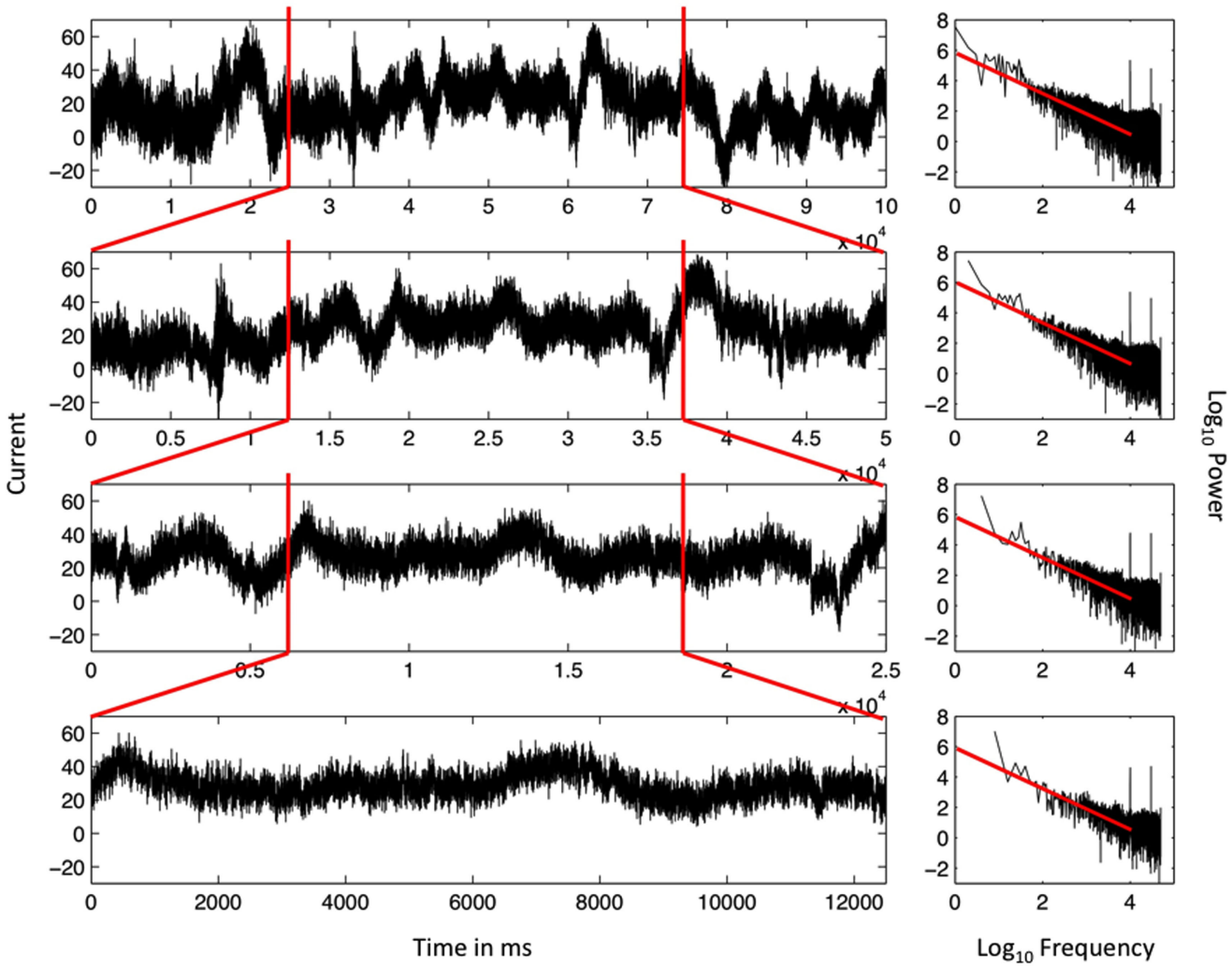

FIGURE 2 | Ordered series of the single EEG-electrode recording from Figure 1 (top, left) and the resulting spectral plot (right) on log–log axes. The top panel includes 16 min of continuous EEG recordings. All other panels are subsets of the original data series. The first and last quarters of each data series are both deleted in each iteration, yielding eventually a data series that ran for 2 min (bottom). The scaling relation remains very similar for each nested series, close to idealized 1/f noise, and demonstrating the statistical self-similarity of the data series.

the raw data series of **Figure 3** is the estimate produced by the volunteer of the duration of 1 s – the volunteer pressed a key to mark the time of each second's passing. The raw data are portrayed across the top of **Figure 3**. Each datum is portrayed in the order in which it was collected; the data value from the first estimated event time is leftmost on the X-axis of the raw data and the data value of the last estimated event time is rightmost on the X-axis.

A subset of the sine waves that were used to simulate the raw behavioral data series is portrayed on the left side of **Figure 3**. Each sine wave yielded two coordinates defining a point on the power spectral graph, again below the data series graph. Arrows connect each sine wave to its point coordinates. The amplitude of each sine wave (squared) estimates the size of changes in data values, and the frequency of the sine wave estimates how often changes of that size recur. The logarithms of frequency and size of change (power) are again the respective coordinate X- and Y-axes of the power spectral plot, and the summary regression line again has a slope near minus 1, which translates into a scaling exponent a close to positive 1.

Repeatedly measured data values, whether from brain activity or behavior, are generally scale-free with exponents $a \sim 1$, consistent with our examples (for brain see Buzsáki, 2006; for behavior see Newell and Slifkin, 1998; Gilden, 2001, 2009; Riley and Turvey, 2002). This fact, plus the idea of intuitive brain-to-body control, has led to speculation that the scale-free behavior of the brain causes the scale-free variation in behavior, in whole or in part (Raichle and Gusnard, 2005). The speculation is likely false however because the priority of control, as we mentioned already rests on relatively slowly changing constraints and the scale-free behavior of the body includes several orders-of-magnitude slower changes than the co-occurring brain activity. However, it

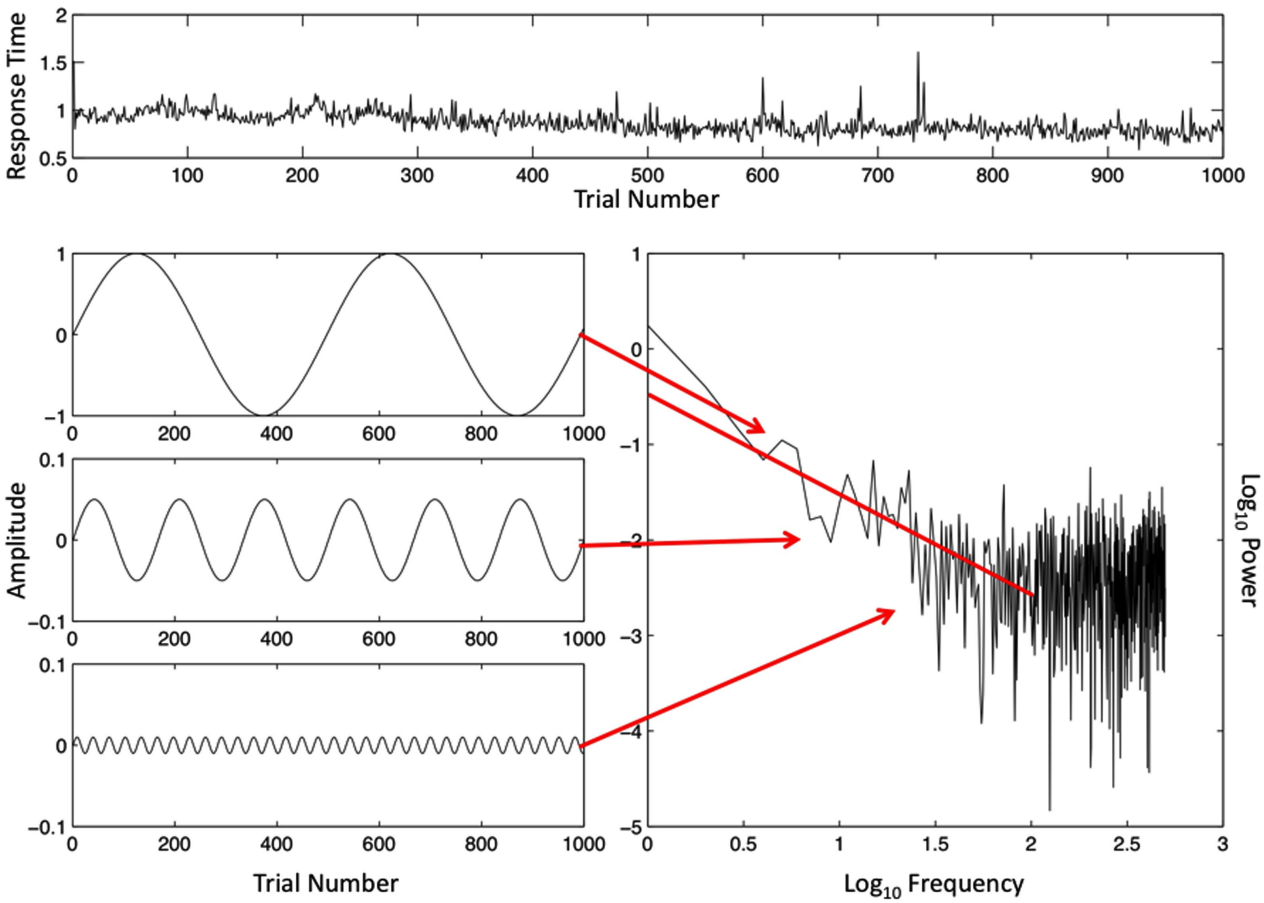

FIGURE 3 | The ordered trial-series of 1000 intervals between the button presses defining time estimates of 1 s (top) and an illustration of a spectral analysis of this time-series (bottom, right). Specific frequencies and magnitudes of change (lower left) are used to approximate the rough graph of the behavioral button-press data (top), and the outcome of the spectral analysis (lower right) on log–log axes. The spectral slope $-\alpha = -0.99$ is close to idealized 1/f noise ($-\alpha = -1.00$). The Y-axes in the illustrated sine waves have been adjusted to make smaller amplitude sine waves visible.

is precisely these fast time scales of brain activity that have been emphasized in the control of behavior. For control to flow this way, from faster to slower time scales, control would require an extra source of influence, in addition to brain dynamics, to amplify the activity of the brain in such a way that it could affect the dynamics of behavior.

Brain activity in the EEG record displays scale-free properties. This means at least two things: first, the magnitude of fluctuations of fast time scales in nervous activity is not sufficient to single-handedly account for behavioral control. Second, the faster time scales in the brain are constrained by its slower time scales (i.e., long-range traveling waves and neuroplasticity) as well as by the slower time scales on which behavior unfolds. Since the dynamics of brain and behavior both display scaling over a certain temporal range, this might indicate they are measures of the same process at different granularities. Although there is a relevant distinction between behavior and brain activity insofar as our measurement tools allow us to sample their changes at different rates, the issue of a fundamental distinction between "behavior" and "brain activity" is less important than the point that slower changes constrain faster changes.

We created an idealized illustration of how the range of scale-free behavior observed across the time scales of behavior and brain might look together on the same graph, using the duration of the sine wave periods that would suffice to simulate the time scales of variation in repeated measurements of behavior and brain. The idealization appears in **Figure 4**. The behavioral data fill out the slower region of low-frequency high-power change on the logarithmic X- and Y-axes; the longest data set, to our knowledge, coming from a study lasting over a year (Delignieres et al., 2004). The powerful amplitudes of change in the behavioral data are several orders-of-magnitude larger than those of the brain data. The low amplitude changes of the brain are thus too weak and change too fast to be the causes of the much slower and more strongly varying changes of the body in behavior. Perhaps then the activities of the body somehow "cause" those of the brain.

PRESENCE OF MIND

Low amplitude changes of the brain are too weak and change too fast to be causes of the much slower and much more strongly varying changes in the body. This claim might sound odd when adopting an overly exclusive "brain controls the body" way of

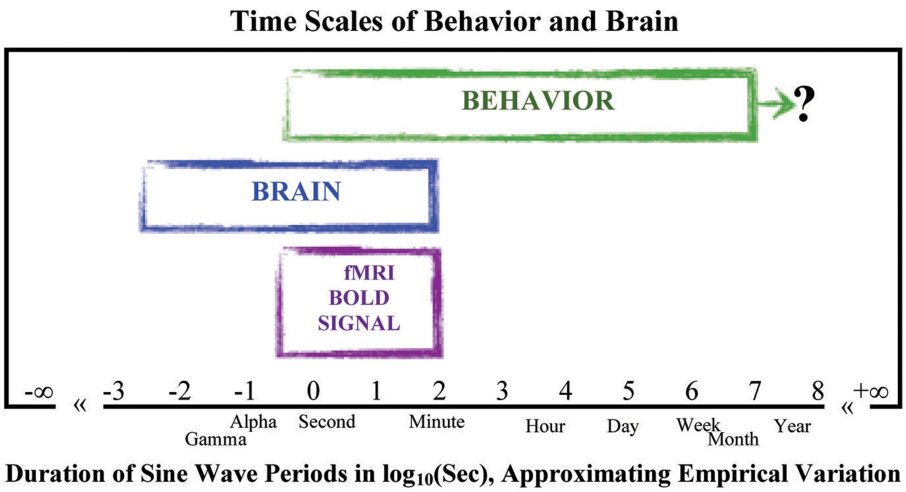

FIGURE 4 | Time scales of behavior and brain were estimated from the time scales implicated in sine wave simulations of variation across repeated measurements (as in Figure 4). Landmarks of durations (day, week, etc.) or brain activity (Alpha, Gamma) are placed near their values in log10(Sec). This figure also includes the span of brain activity observed in the BOLD signal of brain metabolism used in fMRI studies, all to give context to the contrast between the span of time scales observed of behavior and the span of time scales observed of the brain (for reviews see Gilden, 2001; Buzsáki, 2006; Van Orden et al., 2011; van Rooij and Van Orden, 2011). The question mark to the right of the behavioral span symbolizes the fact that no upper bound short of death has yet been discovered in longitudinal studies estimating the presence of scaling relations in the variation across measurements of behavior.

thinking. But it is not odd at all from an engineering perspective. Some engineered systems produce scaling relations in their behavior and the scaling relation characterizes a kind of marriage among different functions of "memory" and "context." The consequences concern how engineered processes on very different timescales constrain each other in their interaction.

Very slowly changing constraints could appear to be static if seen from the perspective of a very rapidly changing process. But the slow and fast changes are of course concurrent. On the one hand, concurrence allows very slowly changing constraints to serve a kind of memory function for more rapidly changing constraints. Slowly changing constraints remind a rapidly changing process of the constraints coming from the slow timescale, which may change only slightly, or not at all, from the constraints on previous cycles. Slower changes are in this way a means for faster changes to "remember" what they need to know about the status of all the more slowly changing constraints in the system (Keshner, 1982).

On the other hand, very slowly changing constraints also function as a relatively stable context, a slowly changing platform on which rapidly changing dynamics are staged. In this emphasis, the very slowly changing constraints limit the degrees of freedom available to a faster changing process, thus restricting the degrees of freedom for what can happen on faster time scales. The faster changing dynamics must evolve within the limited degrees of freedom that the context leaves available.

The crucial importance of memory and context is reflected in how the brain consumes energy. The brain alone accounts for 20% of the body's energy consumption (Clarke and Sokoloff, 1999). Yet in a task performance the range of changes in energy consumption in the brain's activity spans less than 1% of total bodily energy consumption (Raichle, 2010). In other words, our present state of knowledge about energy consumption implies that a complex brainy task requires little- or no-more energy than simply relaxing with eyes closed. This pattern of energy use is consistent with a brain that is primarily about updating and maintaining predictive aspects of history and current events from the lived perspective of the actor.

The facts about energy consumption make clear the importance of the brain "knowing" its place in the world, at any given time. This knowledge could be sustained in positive feedback loops of glutamate cycling (Davia, 2005), and it is estimated that between 60 and 80% of the overall energy consumption of the brain occurs in glutamate cycling (Raichle, 2010). If an actor's history and context – presence of mind – are sustained in the energy patterns of feedback loops, then the amount of energy dedicated to this blue-collar task is consistent with the importance of support for on-going perception and action. Whether viewed as history or context, the slower the change, the more constant, or stably constraining is the influence of the past.

Slower dynamics thus constrain faster dynamics, which allows the flow of visible or audible, or otherwise available, context to constrain the dynamics the brain. The flow of invariants across perception occurs on the slower time scales of change in brain activity (see **Figure 4**), supplying constraints that reduce the degrees of freedom for what may happen next. The residual degrees of freedom allowed by a visible checkerboard, for example, slowly changing its position across the visual field on which flickering rings create expanding or contracting traveling waves (1/32 or 1/48 Hz), gives structure to the activity in visual cortex. These slowly changing constraints reveal a more spatially precise picture of retinotopic organization, compared to previous attempts (Engel et al., 1993, 1994, 1997).

We suggest that the brain is primarily about maintaining presence of mind. In our meaning, "presence of mind" includes the present configuration of the body as it is currently entwined in meaningful relations with the present configuration of the world. Relations among configurations are all themselves changing relatively slowly (compared to the brain). Slower changes provide constraints to the brain in the shape of the pattern of energy flow in the brain. Constraints provide knowledge about possible futures, and they are had for free in the immediate status of relations between the body and the world (Stepp and Turvey, 2009).

A THIRD CATEGORY OF PHENOMENA

Behavior and brain share the same scaling relation, which they also share with other measured signals of physiology such as heart rate, colon contraction, transduction at the retina, neural firing, and many others (Glass, 2001). We believe there are fundamental consequences of this shared scaling relation. There are practical advantages for a system to maintain scaling relations in its patterns of change, these advantages place practical constraints on the development of species and organisms, and have staggering consequences for cognitive science.

An empirical scaling relation with scaling exponent $a \sim 1$ is approximately the mathematical scaling relation called fractal time, 1/f scaling, or pink noise. It is called pink noise due to a resemblance to the empirical spectral portrait of pink light, which concentrates power in the lower frequencies of red light relative to the higher frequencies of blue light. Pink noise is observed of complex systems near the critical points of bifurcations. By staying near to its critical points, a system sustains a poised attitude, ready at any moment to change the organization of its behavior.

Subtle changes in the relation between the task and the performer are often met by qualitative changes in the organization of performance. The relation between task and performer even shapes the expression of learning disabilities (Hendriks and Kolk, 1997). Encouraged to read aloud very quickly, developmental dyslexics make errors consistent with a deficit in the "lexical" process in reading, producing symptoms of a type of dyslexia that is defined by visual/phonological errors and semantic errors (e.g., POND → /pool/, BUSH → /tree/). When encouraged to read aloud accurately, the same dyslexics produce symptoms of a different type of dyslexia, exhibiting the ponderous letter-by-letter, or syllable-by-syllable reading associated with a "non-lexical" process of reading.

Human performance may undergo a bifurcation between speed versus accuracy conditions, self-organizing a different dynamical system suited for speed than for accuracy (cf. Dutilh et al., 2011; Wijnants et al., in press). This hypothesis is consistent with the two types of dyslexic performance, one under speed conditions and the other under accuracy conditions. These speed-versus-accuracy types also closely parallel the two types of acquired dyslexia that were featured conspicuously in a double dissociation of reading processes that kicked off modern cognitive neuropsychology (Marshall and Newcombe, 1973, 1977). And extreme speed conditions also induce errors by intact readers that resemble the errors defining acquired dyslexias (Kello and Plaut, 2000).

Different task demands elicit the symptoms of different types of aphasia from the same brain-damaged individual(s) (Kolk et al., 1985; Kolk and Heeschen, 1992; Hofstede and Kolk, 1994; Kolk and Hofstede, 1994). This would seem to require brain-to-body control, if only to guarantee performance will satisfy the task requirements described in instructions to a brain-damaged individual. Brain-to-body control could occur if the weaker and faster changes of the brain could be susceptible locally, as when a weak external perturbation can change the next stronger source of constraint. Local susceptibility of this sort could be passed up the hierarchy of constraints, each pace of change in turn, to usurp the stronger and slower dynamics of the body and change the course of behavior.

This is a reasonable way to imagine the white-collar control of behavior by the brain, capitalizing on the relatively unstable dynamics near critical points. But brain-to-body control is not the focus of this essay. Our goal is to shine more light on the blue-collar work of the brain. Blue-collar work exploits the relatively stable dynamics near critical points, which may at first seem to contradict what we just supposed to be the basis for white-collar control – that is, susceptibility stemming from relatively unstable dynamics near critical points.

Yet a critical state has the unique feature of being simultaneously the locus of stability and instability, regular and random variation, universal and singular structures – both together or neither alone – a third kind of behavior (Keshner, 1982; Ulanowicz, 2006; Nicolis and Rouvas-Nicolis, 2007; Sporns, 2007; Tsonis, 2008; Van Orden et al., 2011). Before complexity science the variation in measured values was divided exclusively between the regular changes of explainable variance and the random changes of measurement error, signal versus noise. But pink noise is neither signal nor noise, or it is both, as already noted, and so it cannot be classified within the conventional dichotomy. Pink noise is a third category of behavior, a widely acknowledged game-changing phenomenon of complexity science. It is the simultaneous presence of instability together with stability that defines a critical state.

Thus our thesis: if white-collar control can be said to exploit the instability of a critical state then blue-collar work depends upon stability. Brain-to-body control by the faster changing dynamics of the brain exploits the instability near a critical state to change the course of the slower dynamics of the body. Blue-collar work exploits constraints supplied by the more slowly changing "ghost" parameter dynamics of criticality that lend stability to the faster changing dynamics of the brain.

Additional sources of constraints for brain dynamics include the repetitively similar behavioral trajectories of organ systems, the expressed modes of physiological processes, the repetitive movements of human gait, as well as cognitive problems that persist over time or constraints due to intentions that remain unsatisfied. These few examples illustrate the reservoir of constraints present in the generally more slowly changing dynamics of behavior compared to brain. We next describe the structural composition of the body that self-organizes as movement trajectories of the body in behavior.

TENSEGRITY STRUCTURE OF THE BODY

A mollusk's body naturally self-organizes survivable relationships with its environment. While slowly treading water, for instance, the mollusk abruptly recruits interneurons within a self-ordering

central pattern generator, allowing a rapid escape from a predator (Nishikawa et al., 2007). In doing so, the central pattern generator illustrates the soft-assembly of a synergy.

Synergies are "softly" (temporarily) assembled dynamical processes. Temporary soft-assembly allows changes in control to stay apace with the changing demands for reorganization of behavior. Perpetually changing demands exist at the perpetually changing interface of an organism with its environment. Central pattern generators stay apace by re-organizing their network connectivity (Harris-Warrick and Marder, 1991; Morton and Chiel, 1994; Hooper, 2001). The changing relationship with an environment is sometimes served by previously inhibitory connections that now become excitatory connections, by neurons that are recruited into networks in which they did not participate before, or by the fusion of previously separate networks.

The spontaneous dynamics of the brain's so-called default network will change depending on what the participant just heard. The volunteer's investment of attention to a task and other task demands can also change the soft-assembled organization of brain activity among the regions of the default network (Hasson et al., 2009). Almost any change pertaining to ordinary standing around will yield uniquely soft-assembled postural dynamics (Riley et al., 2012). The body and brain thus create of themselves unlimited solutions, apace with the idiosyncratic local contexts in which they find themselves.

The organism at its changing interface with the environment requires this flexible self-control, and context-sensitive soft-assembly appears to be the vital organizing principle of brain architecture (Nikolić, 2010). Organism-wide synergies emerge across a tensegrity structure. The tensegrity structure is formed by a taught web of muscles and fascia to fully connect the parts of the skeleton, appearing to wrap it like a mummy. Similar to tensegrity structures in architecture (e.g., Tomassian, 1997) or robotics and biology (e.g., Tur and Juan, 2009), the skeleton supplies the struts while the muscles, ligaments, and fascia form the tension lines eliminating slack from the tensegrity structure (Levin, 2002). The taught web of tension lines ensures that movement at any one place in the tensegrity structure has consequences throughout the structure, creating a robust mechanical holism that even survives damage that has left the body paralyzed (Carello et al., 2008). The neuromusculoskeletal structure of the body, in the guise of this tensegrity structure, is an excitable medium of self-organizing constraints to sustain the coordinated movements of the body.

Synergies allow the tensegrity structure to behave in some ways but not others, and control works as a process of elimination. Synergies are webs of constraints that limit how the body can change in coordination. Respiratory and cardiovascular processes change together with a change of locomotor gait, for example, ensuring the right amount of oxygen to the cells at the right time (e.g., Gonzales et al., in press). Behavioral processes in a skilled tennis player are constrained to run for the ball and make forehand shots, backhand shots, and to serve and return serves. A swimmer is constrained by synergies to breath out through the nose and breath in through the mouth apace with the strokes of swimming. A web of constraints in each case delimits the possibilities for coordination among the processes of the body, in the actions at hand.

Synergies and tensegrity structure also harvest energy from the temporary contexts of the body (Kugler and Turvey, 1987). Some good configurations of the body with its environment exploit potential energy from inertial forces or from gravity in on-going movement (Bernstein, 1967; Kugler and Turvey, 1987; Dickinson et al., 2000; Turvey, 2007; Wijnants et al., in press). Other good configurations knit the body together, head to foot, in the endlessly novel solutions of postural control (Riccio and Stoffregen, 1988). We are two legged creatures who must balance a large heavy head on a thin neck and, to maintain balance, our center of mass should not exceed its base of support, approximately circumscribed within a perimeter around the feet. Lest we tip over, remote preflexes must anticipate all overt movements (Belen'kii et al., 1967). And yet walking is also falling because the body moves outside of its center of mass in each step, utilizing the potential energy from gravity in the process.

EVIDENCE OF SYNERGY

The taught tension-line coupling across the tensegrity structure allows the body to perform as a single functional unit. To do so, synergies tailor the available degrees of freedom for coordinated changes among the processes of the body. In a classic example, the lips must be in contact to say the/b/in/bob/ (Kelso et al., 1984). Synergy ensures this contact by coupling neuromuscular processes to exclude all non-contact relations between the lips at the time that contact is required. As we already noted, the taught web of tension lines ensures that change at any one place in the tensegrity structure has consequences throughout the structure, allowing synergies to contribute to presence of mind, supplying a way of knowing about the body and brain penultimate to an action itself.

Prior to saying the/b/in/bob/, the exclusion of unlikely configurations retains sufficient degrees of freedom prior to action, to allow the lips to compensate for each other, if something goes wrong (e.g., Scholz and Schöner, 1999; Latash et al., 2002; Riley et al., 2012). Thus, to test for control by synergy, simply perturb on-going speech and look whether compensation occurs in the coupled articulators. In the classic study, a speaker's attempt to say the/b/in/bob/was perturbed by a sudden, unexpected, downward tug on the speaker's jaw. Ultrafast compensation began within 5–10 ms – faster than the brain can compute and return a new plan of articulation (Wallot and Van Orden, in press) – and the lower lip, not the jaw, stretched upward to form a new configuration of contact, producing a fully intelligible pronunciation of/bob/with no audible distortion (Kelso et al., 1984; see also Folkins and Zimmermann, 1982; Abbs and Gracco, 1984).

Ultrafast compensation reconfigured the bilabial and laryngeal gestures (at least), producing compensatory lip gestures to respect abstract phonology as well as compensations in the kinematics of the larynx (Saltzman et al., 1998; see also Bauer et al., 1995). In the theoretical language of cognitive psychology, bi-level coupling of kinematic micro-dynamics and linguistic macro-dynamics is a coupling between body and mind. Synergies in speech generally include coupling across different levels of organization (van Lieshout, 2004) and coupling across multiple levels of organization solves the essential problem of speech production – the on-line coordination of about 70 muscles to stay within narrow trajectories of legible meaningful speech (e.g., van Lieshout et al., 2007).

In other evidence of synergetic control, the perturbation is again sufficient to prompt a change in degrees of freedom for reorganization of human performance. Dual-task paradigms can be interpreted according to whether performing one task perturbs the performance of another task (Riley et al., 2012). For instance, pressure to respond quickly in a cognitive task can perturb and decrease the stability of motor-task performance, compared to performing the motor task by itself (Temprado et al., 1999, 2001). Other times, a concurrent cognitive task is sufficient to change the organization of the motor performance (Pellecchia et al., 2005; Shockley and Turvey, 2005, 2006). In the latter case, dynamical models suggest that a higher-order synergy envelops cognitive and motor performance (Fuchs et al., 1996). However, the motor task of walking on a treadmill takes priority over a concurrent cognitive performance, lest the participant fall, yielding a reorganization of cognitive performance. The same dynamics of locomotion are present with or without the cognitive task, while cognitive dynamics are reorganized in the dual-task (Kiefer et al., 2009).

In concurrent observations of brain and behavior, changes that anticipate reorganization are seen in the repeated measurements of both brain and behavior, and the coincident changes strictly resemble those that precede known physical examples of bifurcations called phase transitions (Fuchs et al., 1992; Kelso and Fuchs, 1995). Reorganization across a bifurcation point is preceded by patterns of change called critical slowing, critical instability, and eventually the sudden-jump in a bifurcation. The time delay from the sudden-jump reorganization of the brain to the sudden-jump reorganization of behavior is also about right, given our speculation about brain-to-body control, occurring within the time required for a single jolt of activation running from brain to behavior (Fabre-Thorpe et al., 2001; Thorpe, 2002; Riley et al., 2012; Wallot and Van Orden, in press).

The coupling of processes in synergy is a refinement of the idea of coordinative structures in motor coordination, the previous solution to the notorious degrees of freedom problem of behavior (Turvey, 2007): there exist incalculably more possible configurations of the possible states of the body than there are smoothly and appropriately coordinated ways to make behavior (Bernstein, 1967). Tensegrity structure and synergies reduce the degrees of freedom of the body, limiting the possible configurations to task, and context appropriate "symphonies" of movement for coordinated change in behavior (Haken, 1977; Kugler et al., 1980, 1982; Kelso, 1995, 1998, 2009; Juarrero, 1999; Van Orden et al., 2011; Riley et al., 2012).

Another test for the presence of a synergy is to look for reduced degrees of freedom in the processes that are entailed in a behavior (e.g., Riley et al., 2011). For instance, the reduced degrees of freedom observed of one process may anticipate the reduced degrees of freedom of another process not yet enacted. Raising an arm requires anticipation by remote muscles on the opposite side of the body prior to any change in the arm's position – else the body would tip over. If the arm movement were made to signal a cognitive choice then the preflex of the remote muscles would "signal" the same choice. If so then the fact of the reduced degrees of freedom in the anticipatory preflex corroborates the synergy of the soft-assembled choice response.

One widely used cognitive task includes a judgment of whether a visually presented letter string correctly spells a word in a reference language – that is, standing before a screen on which letter-strings will appear, raise one arm for each American English "word" and the other arm for "non-words." Event times as "response times" by anticipatory preflexes can be measured in the onset of change in electromyographic activity in the right or left thigh, the right or left paraspinal muscles of the lower back, or the right or left shoulder muscles. If the preflexes reliably distinguish words from non-words instead of leaving the available degrees of freedom open, to accommodate either arm response, then the predicted, anticipatory, synergetic reduction in the degrees of freedom would be confirmed.

Moreno et al. (2011) conducted this experiment, and the side of the body of the preflex reliably distinguished the word from the non-word letter-strings. The observed reduced degrees of freedom in the corresponding preflexes corroborated synergetic control. Otherwise, they observed typical average "word" decision times of about 649 ms in the arm movement data and an identical advantage for "word" over "non-word" response times in each of the anticipatory preflexes. On average, the preflex "word" response times preceded the arm "word" response time by 120 ms at the shoulder, 189 ms at the trunk, and fully 225 ms at the thigh. Synergies appear to have soft-assembled a multilevel whole-body "American English word versus non-word judgment device" (cf. Fowler and Turvey, 1980; Turvey, 1990, 2007; Hollis et al., 2009; Kello and Van Orden, 2009; Kloos and Van Orden, 2009).

Synergies self-organize apace with the flow of context and behavior. This is sufficient to update on-going constraints that anticipate the requirements for oncoming behavior. Invariant or smoothly changing aspects of the world yield invariant or smoothly changing constraints at a pace that is slower than brain dynamics. These constraints inform behavior by limiting the degrees of freedom about what can happen next, leaving open the possible kinematic changes that the body may enact in behavior. A muscle contraction here or a postural adjustment there are nonetheless always constrained by, and constraining of, the total configuration of the behaving body – the organism as an integrated whole.

SUMMARY CONCLUSIONS

We began this essay with several examples of control that did not require an intact central nervous system. Mike the celebrity chicken may now be seen to illustrate the importance of tensegrity as an organizing principle of behavior. Taught tension lines across skeletal struts imbue the body with the self-organizing properties of excitable media. Chickens who lose their circadian coordination among physiology and behavior illustrate a coupling to the environment that contributes to control and regulation of health and wellbeing. The sea squirt is perhaps the ultimate illustration of how a nervous system can be necessary (although not sufficient) for some aspects of being, and dispensable for other aspects.

The blue-collar contribution brings together the concepts of timescale, constraint, synergy, and criticality to understand how the brain supports on-going behavior, to anticipate forthcoming behavior. Constraints that reduce the degrees of freedom for behavior unfold on different timescales, and the more slowly

changing constraints have priority over faster change constraints. Control in this sense in non-specific, a practically unlimited set of possible actions is reduced to a smaller subset, shaped by the contemporary states of physiological processes, environmental regularities, and the idiosyncratic history of the organism. The smaller subset is sustained in a state of criticality, lacking only a contingent discriminating circumstance to enact one of the possible actions (Järvilehto, 1998; Hollis et al., 2009; Van Orden et al., 2011; Riley et al., 2012; Wallot and Van Orden, in press).

Criticality is thus essential; it is no accident that the body and the brain stay near to critical states. Systems that stay near critical states are called metastable systems and the advantages of metastability are legion. A metastable system can commit to a region of the state space of possibilities for action, without otherwise narrowing its options. This allows a healthy codetermination of action by the actor's history and context together with the momentary contingencies that choose the behavior that is enacted. This codetermination is also another pairing of regularity and randomness or order and disorder, like those that characterize pink noise and other aspects of complex systems.

Cognitive science is well underway as complexity science, with wide implications for how to conceptualize and investigate human nature. Already, changes in the organization of behavioral activity, as evidenced by the measured dynamics, are revealing of the nature of an organ or organism (e.g., Lipsitz and Goldberger, 1992; Vaillancourt and Newell, 2002; Van Orden et al., 2011; Dixon et al., 2012; Riley et al., 2012). Regarding investigation, however, all aspects of widely applied measurement protocols must be reconsidered, given the capacity of the participant to mirror our protocols in soft-assembly. In other words, for distinct component functions of memory, language, or motor control, substitute constraints that can create or pick out the behaviors that we give these names to. Practically, this way of thinking promotes research that systematically varies a hierarchy of time scaled contexts. A systematic understanding of control, and how it changes in different contexts, will be had by observing changes in the organization of behaviors estimated by scaling relations or order parameters.

ACKNOWLEDGMENTS

Supported by NSF grants BCS #0843133 and DHB #0728743 to Guy Van Orden. Sebastian Wallot acknowledges funding from the Marie Curie TESIS network. We thank the MIND*Lab* at Aarhus University and the UNIK initiative of the Danish Ministry for Research and Innovation.

Guy Van Orden's journey into complexity science started with the question, "How would I ever know that I am wrong?" This statement was aimed at what is today called classical cognitive science. Guy reasoned that the answer was not found in particular outcomes of studies, but in how mathematics was used to describe observations. In particular, the identification of components of the mind hinges on independent sources of variability, which can be identified using linear statistics. However, the pervasiveness of interaction effects in behavioral data suggested to him that independent sources of variability are an exception case of human behavior.

In his later work, complexity science provided Guy with an alternative framework, and in particular the concepts of pink noise and criticality were of twofold importance. Pink noise showed what violations of independent contributions of variability look like and criticality offered an alternative set of concepts and statistics to build a science of phenomena that deviate from the classical assumptions. This article highlights some of his last thoughts on the role of critical fluctuations in brain and behavior, and sketches out new routes for a complexity science of cognition.

Guy passed away on May 11th 2012. Guy was unique and wonderful in his roles as scientist, mentor, and colleague. He will be sorely missed.

REFERENCES

Abbs, J. H., and Gracco, V. L. (1984). Control of complex motor gestures: orofacial muscle responses to load perturbations of lip during speech. *J. Neurophysiol.* 51, 705–723.

Bauer, A., Jancke, L., and Kalveram, K. T. (1995). Mechanical perturbation of jaw movements during speech: effects on articulation and phonation. *Percept. Mot. Skills* 80, 1108–1112.

Belen'kii, V., Gurfinkel, V., and Pal'tsev, Y. (1967). Elements of control of voluntary movements. *Biophysics (Oxf.)* 12, 154–156.

Bernstein, N. A. (1967). *Coordination and Regulation of Movements*. New York: Pergamon Press.

Birkeland, C., Cheng, L., and Lewis, R. A. (1981). Mobility of dideminid ascidian colonies. *Bull. Mar. Sci.* 31, 170–173.

Buzáki, G. (2006). *Rhythms of the Brain*. New York: Oxford University Press.

Carello, C., Silva, P. L., Kinsella-Shaw, J. M., and Turvey, M. T. (2008). Muscle-based perceptions: theory, research and implications for rehabilitation. *Rev. Bras. Fisioter* 12, 339–350.

Clarke, D. D., and Sokoloff, L. (1999). "Circulation and energy metabolism of the brain," in *Basic Neurochemistry, Molecular, Cellular and Medical Aspects*, 6th Edn, eds B. W. Agranoff and G. J. Siegel (Philadelphia: Lippincott-Raven), 637–670.

Davia, C. J. (2005). "Life, catalysis and excitable media: a dynamic systems approach to metabolism and cognition," in *The Physical Basis for Consciousness*, ed. J. Tuszynski (Heidelberg: Springer), 229–260.

Delignieres, D., Fortes, M., and Ninot, G. (2004). The fractal dynamics of self-esteem and physical self. *Nonlinear Dynamics Psychol. Life Sci.* 8, 479–510.

Dickinson, M. H., Farley, C. T., Full, R. J., Koehl, M. A. R., Kram, R., and Lehman, S. (2000). How animals move: an integrative view. *Science* 288, 100–106.

Dixon, J. A., Holden, J. G., Mirman, D., and Stephen, D. G. (2012). Multifractal dynamics in the emergence of cognitive structure. *Top. Cogn. Sci.* 4, 51–62.

Dutilh, G., Wagenmakers, E. J., Visser, I., and van der Maas, H. L. J. (2011). A phase transition model for the speed-accuracy trade-off in response time experiments. *Cogn. Sci.* 35, 211–250.

Engel, S. A., Glover, G. H., and Wandell, B. A. (1997). Retinotopic organization in human visual cortex and the spatial precision of functional MRI. *Cereb. Cortex* 7, 181–192.

Engel, S. A., Rumelhart, D. E., Wandell, B. A., Lee, A. T., Glover, G. H., Chichilnisky, E. J., and Shadlen, M. N. (1994). fMRI of human visual cortex. *Nature* 369, 525.

Engel, S. A., Rumelhart, D. E., Wandell, B. A., Lee, A. T., Glover, G. H., Chichilnisky, E. J., Shadlen, M. N., and Newsome, W. T. (1993). Functional MRI measurements of human striate cortex topography. *Soc. Neurosci. Abst.* 19, 335.

Fabre-Thorpe, M., Delorme, A., Marlot, C., and Thorpe, S. (2001). A limit to the speed of processing in ultra-rapid visual categorization of novel natural scenes. *J. Cogn. Neurosci.* 13, 1–10.

Folkins, J. W., and Zimmermann, G. N. (1982). Lip and jaw interaction during speech: responses to perturbation of lower-lip movement prior to bilabial closure. *J. Acoust. Soc. Am.* 71, 1225–1233.

Fowler, C. A., and Turvey, M. T. (1980). Immediate compensation for bite-block vowels. *Phonetica* 37, 306–326.

Fuchs, A., Jirsa, V. K., Haken, H., and Kelso, J. A. S. (1996). Extending the HKB-model of coordinated movement to oscillators with different eigenfrequencies. *Biol. Cybern.* 74, 21–30.

Fuchs, A., Kelso, J. A. S., and Haken, H. (1992). Phase transitions in the human brain: spatial mode dynamics. *Int. J. Bifurcat. Chaos* 2, 917–939.

Gilden, D. L. (2001). Cognitive emissions of 1 / f noise. *Psychol. Rev.* 108, 33–56.

Gilden, D. L. (2009). Global model analysis of cognitive variability. *Cogn. Sci.* 33, 1441–1467.

Glass, L. (2001). Synchronization and rhythmic processes in physiology. *Nature* 410, 277–284.

Gonzales, L. M., Hessler, E. E., and Amazeen, P. G. (in press). Perceptual constraints on frequency ratio performance in motor-respiratory coordination. *Ecol. Psychol.*

Haken, H. (1977). *Synergetics: An Introduction. Nonequilibrium Phase Transitions and Self-Organization in Physics, Chemistry, and Biology*. Berlin: Springer-Verlag.

Harris-Warrick, R. M., and Marder, E. (1991). Modulation of neural networks for behavior. *Annu. Rev. Neurosci.* 14, 39–57.

Hasson, U., Nusbaum, H. C., and Small, S. L. (2009). Task-dependent organization of brain regions active during rest. *Proc. Natl. Acad. Sci. U.S.A.* 106, 10841–10846.

Hausdorff, J. M., Zemany, L., Peng, C.-K., and Goldberger, A. L. (1999). Maturation of gait dynamics: stride-to-stride variability and its temporal organization in children. *J. Appl. Physiol.* 86, 1040–1047.

Hendriks, A. W., and Kolk, H. H. J. (1997). Strategic control in developmental dyslexia. *Cogn. Neuropsychol.* 14, 321–366.

Hofstede, B. T. M., and Kolk, H. J. (1994). The effects of task variation on the production of grammatical morphology in Broca's aphasia: a multiple case study. *Brain Lang.* 46, 278–328.

Hollis, G., Kloos, H., and Van Orden, G. (2009). "Origins of order in cognitive activity," in *Chaos and Complexity in Psychology*, eds S. J. Guastello, M. Koopmans, and D. Pincus (Cambridge: Cambridge University Press), 206–241.

Hooper, S. L. (2001). "Central pattern generators," in *Encyclopedia of Life Sciences* (Chichester: John Wiley & Sons), Available at: http://www.ELS.net [doi 10.1038/npg.els.0000032]

Järvilehto, T. (1998). The theory of the organism-environment system: I. Description of the theory. *Integr. Psychol. Behav. Sci.* 33, 321–334.

Juarrero, A. (1999). *Dynamics in Action: Intentional Behavior as a Complex System*. Cambridge, MA: MIT Press.

Kello, C. T., and Plaut, D. C. (2000). Strategic control in word reading: evidence from speeded responding in the tempo naming task. *J. Exp. Psychol. Learn Mem. Cogn.* 26, 719–750.

Kello, C. T., and Van Orden, G. (2009). Soft-assembly of sensorimotor function. *Nonlinear Dynamics Psychol. Life Sci.* 13, 57–78.

Kelso, J. A. S. (1995). *Dynamic Patterns: The Self-Organization of Brain and Behavior*. Cambridge, MA: MIT Press.

Kelso, J. A. S. (1998). "From Bernstein's physiology of activity to coordination dynamics," in *Progress in Motor Control, Vol. 1, Bernstein's Traditions in Movement Studies*, ed. M. L. Latash (Champaign, IL: Human Kinetics), 203–219.

Kelso, J. A. S. (2009). "Synergies: atoms of brain and behavior," in *Progress in Motor Control: A Multidisciplinary Perspective*, ed. D. Sternad (New York: Springer), 83–91.

Kelso, J. A. S., and Fuchs, A. (1995). Self-organizing dynamics of the human brain: critical instabilities and Sil'nikov chaos. *Chaos* 5, 64–69.

Kelso, J. A. S., Tuller, B., Vatikiotis-Bateson, E., and Fowler, C. A. (1984). Functionally specific articulatory cooperation following jaw perturbations during speech: evidence for coordinative structures. *J. Exp. Psychol. Hum. Percept. Perform.* 10, 812–832.

Keshner, M. S. (1982). 1/f noise. *Proc. IEEE* 70, 212–218.

Kiefer, A. W., Riley, M. A., Shockley, K., Villard, S., and Van Orden, G. (2009). Walking changes the dynamics of cognitive estimates of time intervals. *J. Exp. Psychol. Hum. Percept. Perform.* 35, 1532–1541.

Kloos, H., and Van Orden, G. (2009). "Soft-assembled mechanisms for the unified theory," in *Toward a Unified Theory of Development: Connectionism and Dynamic Systems Theory Re-Considered*, eds J. P. Spencer, M. Thomas, and J. McClelland (New York: Oxford University Press), 253–267.

Kolk, H. H. J., and Heeschen, C. (1992). Agrammatism, paragrammatism and the management of language. *Lang. Cogn. Process.* 7, 89–129.

Kolk, H. H. J., and Hofstede, B. T. M. (1994). The choice for ellipsis: a case study of stylistic shifts in an agrammatic speaker. *Brain Lang.* 47, 507–509.

Kolk, H. H. J., Van Grunsven, M. H. F., and Keyser, A. (1985). "On parallelism between production and comprehension in agrammatism," in *Agrammatism*, ed. M. Kean (New York: Academic Press), 165–206.

Kugler, P. N., Kelso, J. A. S., and Turvey, M. T. (1980). "On the concept of coordinative structures as dissipative structures: I. Theoretical lines of convergence," in *Tutorials in Motor Behavior*, eds G. E. Stelmach and J. Requin (New York: North-Holland), 3–47.

Kugler, P. N., Kelso, J. A. S., and Turvey, M. T. (1982). "On coordination and control in naturally developing systems," in *The Development of Movement Control and Coordination*, eds J. A. S. Kelso and J. E. Clark (New York: Wiley), 5–78.

Kugler, P. N., and Turvey, M. T. (1987). *Information, Natural Law, and the Self-Assembly of Rhythmic Movement*. Hillsdale, NJ: Lawrence Erlbaum Associates.

Latash, M. L., Scholz, J., and Schöner, G. (2002). Motor control strategies revealed in the structure of motor variability. *Exerc. Sport Sci. Rev.* 30, 26–31.

Levin, S. N. (2002). The tensegrity-truss as a model for spine mechanics: biotensegrity. *J. Mech. Med. Biol.* 2, 375–388.

Lipsitz, L. A., and Goldberger, M. D. (1992). Loss of 'complexity' and aging. *JAMA* 267, 1806–1809.

Maguire, E. A., Gadian, N. G., Johnsrude, I. S., Good, C. D., Ashburner, J., Frackowiak, R. S., and Frith, C. D. (2000). Navigation-related structural changes in the hippocampi of taxi drivers. *PNAS* 97, 4398–4403.

Marshall, J. C., and Newcombe, F. (1973). Patterns of paralexia: a psycholinguistic approach. *J. Psycholinguist. Res.* 2, 175–199.

Marshall, J. C., and Newcombe, F. (1977). "Variability and constraint in acquired dyslexia," in *Studies in Neurolinguistics*, Vol. 3, eds H. Whitaker and H. A. Whitaker (New York: Academic Press), 257–283.

Moreno, M. A., Stepp, N., and Turvey, M. T. (2011). Whole body lexical decision. *Neurosci. Lett.* 490, 126–129.

Morton, D. W., and Chiel, H. J. (1994). Neural architectures for adaptive behavior. *Trends Neurosci.* 17, 413–420.

Newell, A. (1990). *Unified Theories of Cognition*. Cambridge, MA: Harvard University Press.

Newell, K. M., and Slifkin, A. B. (1998). "The nature of movement variability," in *Motor Behavior and Human Skill: A Multidisciplinary Approach*, ed. J. P. Piek (Champaign, IL: Human Kinetics), 143–160.

Nicolis, G., and Rouvas-Nicolis, C. (2007). "Complex systems," in *Scholarpedia*, 2, 1473. Available at: http://www.scholarpedia.org/article/ [accessed April 24, 2009].

Nikolić, D. (2010). The brain is a context machine. *Rev. Psychol.* 17, 33–38.

Nishikawa, K., Biewener, A. A., Aerts, P., Ahn, A. N., Chiel, H. J., Daley, M. A., Daniel, T. L., Full, R. J., Hale, M. E., Hedrick, T. L., Lappin, A. K., Nichols, T. R., Quinn, R. D., Satterlie, R. A., and Szymik, B. (2007). Neuromechanics: an integrative approach for understanding motor control. *Integr. Comp. Biol.* 47, 16–54.

Pellecchia, G., Shockley, K., and Turvey, M. T. (2005). Concurrent cognitive task modulates coordination dynamics. *Cogn. Sci.* 29, 531–557.

Raichle, M. E. (2010). Two views of brain function. *Trends Cogn. Sci. (Regul. Ed.)* 14, 180–190.

Raichle, M. E., and Gusnard, D. A. (2005). Intrinsic brain activity sets the stage for expression of motivated behavior. *J. Comp. Neurol.* 493, 167–176.

Riccio, G. E., and Stoffregen, T. A. (1988). Affordances as constraints on the control of stance. *Hum. Mov. Sci.* 7, 265–300.

Riley, M. A., Richardson, M. J., Shockley, K., and Ramenzoni, V. C. (2011). Interpersonal synergies. *Front. Move. Sci. Sport Psychol.* 2:38. doi:10.3389/fpsyg.2011.00038

Riley, M. A., Shockley, K., and Van Orden, G. (2012). Learning from the body about the mind. *Top. Cogn. Sci.* 4, 21–34.

Riley, M. A., and Turvey, M. T. (2002). Variability and determinism in motor behavior. *J. Mot. Behav.* 34, 99–125.

Saltzman, E., Löfqvist, A., Kay, B., Kinsella-Shaw, J., and Rubin, P. (1998). Dynamics of intergestural timing: a perturbation study of lip-larynx coordination. *Exp. Brain Res.* 123, 412–424.

Schiepek, G., and Haken, H. (2006). *Synergetik in der Psychologie. (Synergetics in Psychology)*. Göttingen: Hogrefe.

Schmit, J. M., Regis, D., and Riley, M. A. (2005). Dynamic patterns of

postural sway in ballet dancers and track athletes. *Exp. Brain Res.* 163, 370–378.

Schmit, J. M., Riley, M. A., Dalvi, A., Sahay, A., Shear, P. K., Shockley, K. D., and Pun, R. Y. K. (2006). Deterministic center of pressure patterns characterize postural instability in Parkinsons's disease. *Exp. Brain Res.* 168, 357–367.

Scholz, J. P., and Schöner, G. (1999). The uncontrolled manifold concept: identifying control variables for a functional task. *Exp. Brain Res.* 126, 289–306.

Shockley, K., and Turvey, M. T. (2005). Encoding and retrieval during bimanual rhythmic coordination. *J. Exp. Psychol. Learn Mem. Cogn.* 31, 980–990.

Shockley, K., and Turvey, M. T. (2006). Dual-task influences on strategic retrieval and coordination dynamics. *Psychon. Bull. Rev.* 13, 985–990.

Simon, H. A. (1973). "The organization of complex systems," in *Hierarchy Theory: The Challenge of Complex Systems*, ed. H. H. Pattee (New York: Braziller), 1–27.

Sporns, O. (2007) "Complexity," in *Scholarpedia*, 2, 1623. Available at: http://www.scholarpedia.org/article/Complexity [accessed April 24, 2009].

Stepp, N., and Turvey, M. T. (2009). On strong anticipation. *Cogn. Syst. Res.* 11, 148–164.

Temprado, J. J., Zanone, P. G., Monno, A., and Laurent, M. (1999). Attentional load associated with performing and stabilizing preferred bimanual patterns. *J. Exp. Psychol. Hum. Percept. Perform.* 25, 1579–1594.

Temprado, J. J., Zanone, P. G., Monno, A., and Laurent, M. (2001). A dynamical framework to understand performance trade-offs and interference in dual tasks. *J. Exp. Psychol. Hum. Percept. Perform.* 27, 1303–1313.

Thelen, E., Schöner, G., Scheier, C., and Smith, L. B. (2001). The dynamics of embodiment: a field theory of infant perseverative reaching. *Behav. Brain Sci.*, 24, 1–34.

Thorpe, S. J. (2002). Ultra-rapid scene categorization with a wave of spikes. *Lect. Notes Comput. Sci.* 2525, 1–15.

Tomassian, R. (1997). *The Stiff, the Sagging, the Supple: The Possibility of Flexible Integrity in Architecture.* Masters thesis, University of Cincinnati, Cincinnati.

Tsonis, A. A. (2008). *Randomicity: Rules and Randomness in the Realm of the Infinite.* London: Imperial College Press.

Tur, J. M. M., and Juan, S. H. (2009). Tensegrity frameworks: dynamic analysis review and open problems. *Mech. Mach. Theory* 44, 1–18.

Turvey, M. (1990). Coordination. *Am. Psychol.* 45, 938–953.

Turvey, M. T. (2007). Action and perception at the level of synergies. *Hum. Mov. Sci.* 26, 657–697.

Ulanowicz, R. E. (2006). *A Third Window: Natural Life beyond Newton and Darwin.* West Conshohocken, PA: Templeton Press.

Vaillancourt, D. E., and Newell, K. M. (2002). Changing complexity in human behavior and physiology through aging and disease. *Neurobiol. Aging* 23, 1–11.

van Lieshout, P. H. H. M. (2004). "Dynamical systems theory and its application in speech," in *Speech Motor Control in Normal and Disordered Speech*, eds B. Maassen, R. Kent, H. Peters, P. van Lieshout, and W. Hulstijn (Oxford: Oxford University Press), 51–82.

van Lieshout, P. H. H. M., Bose, A., Square, P. A., and Steele, C. M. (2007). Speech motor control in fluent and dysfluent speech production of an individual with apraxia of speech and Broca's aphasia. *Clin. Linguist. Phon.* 21, 159–188.

Van Orden, G., Kloos, H., and Wallot, S. (2011). "Living in the pink: intentionality, wellness, and complexity," in *Handbook of the Philosophy of Science, Vol. 10, Philosophy of Complex Systems*, ed. C. A. Hooker (Amsterdam: Elsevier), 639–684.

van Rooij, M., and Van Orden, G. (2011). It's about space, it's about time, neuroeconomics and the brain sublime. *J. Econ. Perspect.* 25, 31–56.

Wallot, S., and Van Orden, G. (in press). Ultrafast cognition. *J. Conscious. Stud.*

West, B. J. (2006). *Where Medicine Went Wrong. Rediscovering the Path to Complexity*. London: World Scientific.

Wijnants, M. L., Cox, R. F. A., Hasselman, F., Bosman, A. M. T., and Van Orden, G. (in press). A trade-off study revealing nested timescales of constraint. *Front. Fractal Physiol.*

Winget, C., Card, D., and Pope, J. (1968). Circadian oscillations of three parameters at defined light intensities and color. *J. Appl. Physiol.* 24, 401–406.

Conflict of Interest Statement: The authors declare that the research was conducted in the absence of any commercial or financial relationships that could be construed as a potential conflict of interest.

Received: 28 January 2012; accepted: 24 May 2012; published online: 18 June 2012.

*Citation: Van Orden G, Hollis G and Wallot S (2012) The blue-collar brain. Front. Physio. **3**:207. doi: 10.3389/fphys.2012.00207*

This article was submitted to Frontiers in Fractal Physiology, a specialty of Frontiers in Physiology.